Disorder in quantum many-body physics: from strange metal to spin glass systems

A DISSERTATION PRESENTED
BY
MARIA D. TIKHANOVSKAYA
TO
THE DEPARTMENT OF PHYSICS

IN PARTIAL FULFILLMENT OF THE REQUIREMENTS
FOR THE DEGREE OF
DOCTOR OF PHILOSOPHY
IN THE SUBJECT OF
PHYSICS

HARVARD UNIVERSITY
CAMBRIDGE, MASSACHUSETTS
DECEMBER 2024

Thesis advisor: Professor Subir Sachdev Maria D. Tikhanovskaya

Disorder in quantum many-body physics: from strange metal to spin glass systems

Abstract

This dissertation investigates the role of disorder in quantum many-body systems, focusing on strange metals and spin glass systems.

For strange metals, we analyze the low-frequency spectra of complex Sachdev-Ye-Kitaev (SYK) models at arbitrary densities, combining analytical and numerical methods. Building on these insights, we study the overdoped random $t-J$ model, demonstrating that strange metal behavior persists across the entire doping range. We also show that the critical metal develops an instability to a low-doping spin-glass phase, and compute the critical doping value. Furthermore, we explore the chaotic properties of a distinct strange metal model—the large N theory of a critical Fermi surface—and establish that it exhibits maximal quantum chaos.

For spin glass systems, we examine the low-energy spectrum and Parisi replica-symmetry-breaking function in the quantum Ising model with infinite-range random exchange interactions with the presence of transverse and longitudinal fields. In the spin glass phase, we find that the local spin spectra are gapless and provide a detailed analysis of the phase diagram. Additionally, we investigate the quantum spherical p-rotor model in an external field, showing that the spin glass phase remains robust across a wide range of field strengths. The potential experimental applications of these findings are also discussed.

Contents

To my parents - Tatyana and Dmitrii.

Acknowledgments

A Ph.D. is a long journey, and I could not have made it without the incredible people and support network who helped along the way.

First of all, I would like to express my deepest gratitude to my advisor, Professor Subir Sachdev. His guidance, support and encouragement at all stages of my graduate studies have been invaluable. Subir was not just a great mentor; he genuinely cared about my growth as a scientist and as a person. He supported all my ambitions, from taking on challenging projects to exploring fellowship and internship opportunities. When I decided to branch out into new scientific directions, Subir did not just approve, he was genuinely excited for me.

Beyond academic support, Subir also created a welcoming and supportive environment for everyone in the group. From group lunches and check-ins during the COVID-19 years to hosting parties at his house, he made sure that we stayed connected. I know people say that having a good advisor is a matter of luck, but having Subir as my advisor felt like an extraordinary gift.

The start of my Ph.D. was nothing but smooth; it took time to find a research direction that truly clicked. During those early days, I was lucky to have the support of Professors Mikhail Lukin and

Daniel Jafferis. They introduced me to fascinating topics in atomic physics, quantum information, and their connections to black hole physics. Prof. Jafferis, who also served on my committee, provided thoughtful feedback on my work that consistently pushed me to think deeper and expand my understanding of the field in ways I hadn't expected.

I am deeply grateful to my third committee member, Prof. Amir Jacoby. His support over the years has been invaluable and I am especially glad I took his laboratory class (which I was initially reluctant to take, but ended up being very glad I did). It gave me the opportunity to learn from his perspective on superconductivity and experimental physics as a whole.

I am deeply grateful to my collaborators on Harvard projects over the years: Maine Christos, Haoyu Guo, Darshan Joshi, Eric Mascott, Dirk Morr, Alex Nikolaenko, Aavishkar Patel, Rhine Samajdar, and Grisha Tarnopolsky. Each of you has taught me so much about what it means to be a scientist. I would not be the scientist I am today without your insights, support, and collaboration. Truly, thank you.

I also want to thank other members of Subir Sachdev's group: Serhii Kryhin, Chenyuan Li, Henry Shackleton, Julia Steinberg, and Yanting Teng. From joining the group just before the pandemic to staying connected and seeing the unique paths we have each taken, it has been a journey filled with challenges, friendship, and growth. Despite the difficulties of graduate school, I am grateful for the support we have shared along the way.

During graduate school, one of my professional career highlights was visiting the Kavli Institute for Theoretical Physics in Santa Barbara, California. The half-a-year program at KITP made me realize how nice California is. Still, more importantly, I met incredible collaborators: Prof. Matthew P. A. Fisher, Ali Lavasani, and Prof. Sagar Vijay. I am incredibly grateful for Ali, who was extremely patient while I was learning a new programming language and a new field. He was always there for me, and I will always be grateful for his time - whether for several-hour meetings or climbing adventures we took together. I am also thankful for the cohort of the graduate fellows - Jake Bringewatt, Margarita

Davydova, Chris O'Connor, Andy Liu, Yuhan Liu, Åsmund Folkestad, Emanuele Sayed, Dinh Duy Vu, and Zixia Wei. Thank you for all the adventures we took together.

During graduate school, I had the opportunity to serve as a teaching fellow for six different courses, ranging from introductory undergraduate physics to more advanced graduate-level classes in condensed matter physics and statistical mechanics. I was fortunate to collaborate with exceptional professors and instructors, including Girma Hailu, Daniel Jafferis, Vinny Manoharan, Prineha Narang, Subir Sachdev, and Greg Kestin. These experiences not only deepened my understanding of the material but also helped me develop my skills in teaching, communicating complex topics clearly, and engaging with students. I am grateful for the many talented students I had the pleasure of working with, and I have even stayed in touch with a few and followed their unique paths (Maryam, Zack, and Sabrina – hello!).

The graduate program would not be the same without the incredible people behind it: Liz Alcock, Jacob Barandes, Lisa Cacciabaudo, and Silke Exner. I am constantly amazed by how much they manage and how quickly and efficiently everything gets done. Beyond providing essential support for the program, they are always there for students, offering a listening ear when personal or professional challenges arise. I would especially like to thank Jacob Barandes for his tremendous support. He patiently listened to me for hours as I navigated my challenges, and his guidance made all the difference. Jacob, you are an amazing person, and I am truly grateful for everything.

Another important highlight of graduate school for me was the privilege of being a student researcher at Google. This experience has pushed my boundaries once again. This fantastic opportunity was given to me by mbrenner. His extraordinary way of looking at research and having fun with it is something I had to learn and still am learning. He is the man who never has an opening in his schedule, yet he is always present for people when they need him. Thank you, Michael, for your support and, honestly, for changing my life. My experience at Google has taught me many new tools and a lot about AI. I could not overcome the challenges of learning so much without the support of the

incredible team - Dan, Eun-Ah, Haining, James, Martyna, Nayantara, Paul, Subhashini, and Yasaman.

My transition to a different field later in my Ph.D. program was intriguing but challenging. I had the privilege to meet incredible professors and scientists who made this transition possible and who convinced me that, despite my questions and fears, my passion for learning and my background would be enough to make it work. One of the people who inspired me to make this transition is Prof. Haim Sompolinsky. His love for what he does and incredible vision of the field gave me that I was making the right choice. Haim is one of the people who can deeply scientifically inspire, but he has always been incredibly friendly to me and constantly offered help whenever I needed it (and I needed it a lot!). Thank you, Haim, for everything you have done for me.

As unique and fulfilling as the scientific part of the Ph.D. has been, I have to thank many people outside of my professional life - friends and family - who supported me on this journey, never let me give up, and made me believe in myself.

Thank you to my closest friends: Iris Cong, Margarita Davydova, Chris Fourie, Sandra Gonzalez Sanchez, Hannah Gibson, Joyce Kwan, Alex Khudorozkov, Christina Lasota, Pem Lasota, Nate Leitao, Ethan Rouen, Rohini Pande, Furkan Ozturk, and Lauren Sather. I am so grateful for everything you have done for me and for all the adventures we have shared. A special thank you to Chris for your incredible support over the years—it is hard to put into words how much I appreciate your friendship. I also want to thank my climbing partner, Ethan, for always pushing me to challenge myself in the gym, which has had such a positive impact on other parts of my life. I am excited to see where life takes all of you, and I cannot wait to stay in touch. I love you all.

More recently, I have been fortunate to form incredible friendships with Maine Christos, Oriana Diessel, Katharina Duecker, and Martyna Plomecka. These amazing people have shown me the importance of opening up and trusting others, and how it is possible to form deep connections in a short amount of time. I am truly grateful to each of you, and I am excited to continue growing our friendships.

I would also like to thank Yasaman Bahri, Jenny Coulter, Nicolo Foppiani, Monica Kang, Amir Karamlou, Ethan Lake, Dom Leggett, Ali Lavasani, Rhine Samajdar, Konstantinos Sfairopoulos, Julia Steinberg, Roxy Paans, Kristine Rezai, Wenjie Ji some of whom were mentioned above. Thank you for being there for me during different stages of my Ph.D., always accepting me for who I am, and supporting me no matter what. I am excited to stay in touch and see each other more often.

My special thank you goes to my family. My mom, Tatyana Tikhanovskaya, and my dad, Dmitrii Tikhanovsky, have always had my back over the years. Despite the 7- to 8-hour time difference, they never hesitated to take my calls during the early years of my Ph.D. program, always ready to listen to my concerns and help in any way they could. I will be forever grateful for their sacrifices and constant love.

My support system over the years has also included my brother, Valera Tikhanovsky, my sister, Alina Tikhanovskaya, and other family members—Rusina Tikhanovskaya, Nadya Tikhanovskaya, Inna Lopatkina, and my nieces - Vera, Albina and Lilya. They have been there for me every step of the way, and I am deeply grateful for all they have done for me.

My acquired family has been an incredible support over the past several years. My husband, Sasha Brownsberger, has introduced me to and taught me countless things that are impossible to fully describe. I am deeply grateful for everything Sasha has done for me, and I am excited for all the adventures that lie ahead for us.

My American family—Maya Ramirez, Bob Brownsberger, Max Brownsberger, and the Copeland family—taught me that it is possible to build a home far from home. They have done so much for me, and words cannot fully express my gratitude. I will always cherish their kindness and support.

Finally, I want to thank my furry friends—Campbell, Holly, Rogue, Ari, Biscuit, Rag, and Seed. These creatures were a constant source of comfort, offering love when I needed it the most.

Citations to Previous Work

Several chapters of this thesis are based on published articles. In particular,

Chapter 2 has appeared as Maria Tikhanovskaya, Haoyu Guo, Subir Sachdev, and Grigory Tarnopolsky, Physical Review B 103(7), 075141 (2021)

Chapter 3 has appeared as Maria Tikhanovskaya, Haoyu Guo, Subir Sachdev, and Grigory Tarnopolsky, Physical Review B 103(7), 075142 (2021)

Chapter 4 has appeared as Maria Tikhanovskaya, Subir Sachdev, and Aavishkar Patel, Physical Review Letters, 129(6), 060601 (2022)

Chapter 5 has appeared as Maine Christos, Darshan Joshi, Subir Sachdev, and Maria Tikhanovskaya, Proceedings of the National Academy of Sciences, 119(29), e2206921119 (2022)

Chapter 6 has appeared as Maria Tikhanovskaya, Subir Sachdev, and Rhine Samajdar, Physical Review X Quantum 5 (2), 020313 (2024)

1

Introduction

1.1 Phases of the high temperature superconducting materials

Since the 1980s, the phenomenon of high-temperature superconductivity has captured the attention of the condensed matter physics community. The experimental discovery of these materials, beginning with the cuprates, revolutionized our understanding of superconductivity and initiated intense theoretical and experimental efforts to uncover the underlying mechanisms. Over the decades, signif-

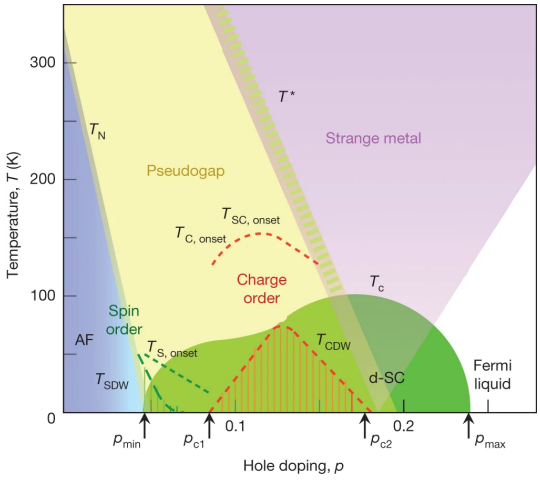

Figure 1.1: Schematic cuprate phase diagram as a function of hole doping. The figure is taken from[167].

icant progress has been made, and high-temperature superconductors continue to serve as a source of inspiration for much of modern condensed matter physics. These materials have deepened our understanding of quantum phase transitions, strongly correlated electron systems, and emergent phenomena. For instance, studies of high-temperature superconductors have influenced research into quantum criticality, strange metals, and topological phases of matter. The phase diagram of high-temperature superconducting materials (see Fig. 1.1) is intricate and rich in physical phenomena. It features a variety of distinct phases, including the Mott insulating phase, the pseudogap phase, the superconducting dome, and the strange metal regime.

This dissertation is primarily concerned with studying mean-field models that capture the key properties of the strange metal regime, the conventional Fermi liquid phase, and the spin glass phases. This chapter introduces the essential concepts underlying conventional and strange metals from the perspective of mean-field theory models. Additionally, we discuss the fundamental aspects of spin glasses. These theoretical approaches aim to illuminate emergent behaviors in high-temperature superconductors and related systems, contributing to a broader understanding of strongly correlated electron systems.

1.2 Conventional and strange metals

1.2.1 Fermi liquid

The Landau Fermi liquid theory provides a foundational framework for understanding the behavior of conventional metals. This theory elegantly captures the properties of strongly correlated electronic systems by introducing the concept of quasiparticles — effective particles that behave like non-interacting fermions but embody the collective excitations of a many-body system. In the low temperature limit, the real part of the self-energy behaves as $\mathrm{Re}\Sigma(\omega) \sim \omega$, and the quasiparticle decay rate behaves as

$$\mathrm{Im}\Sigma(\omega) \sim \omega^2 + T^2 \tag{1.1}$$

which in turn implies that the resistivity of the Fermi liquid grows quadratically with temperature

$$\rho(T) = A + BT^2 \tag{1.2}$$

as $T \to 0$. Deviations from this behavior in resistivity and in quasiparticle decay rate lead to theories of non-Fermi liquid which we briefly discuss below.

1.2.2 Non-Fermi liquid

Theories of non-Fermi liquid arise when the behavior of the metal at low temperatures cannot be explained by the Fermi liquid theory. Strange metal is a metallic state and is within a subclass of non-Fermi liquids. An important property of a strange metal that strongly deviates from the Fermi liquid is its linear-in-temperature resistivity. DC resistivity in strange metals behaves as $\rho(T) \sim A + BT$ as $T \to 0$.

There have been a vast amount of proposals to explain why certain compounds do not behave as

predicted by the theory of normal metals in certain regimes of the phase diagram. In this section we focus on several models of non-Fermi liquid and discuss their main properties.

Sachdev-Ye model.

The Sachdev-Ye (SY) model [156] is the model of $SU(\mathcal{M})$ spins with the interactions of the following form

$$H = -\frac{1}{\sqrt{N\mathcal{M}}} \sum_{i<j} J_{ij} S_i \cdot S_j, \tag{1.3}$$

where S_i and S_j are the spin-operators in the $SU(\mathcal{M})$ group and J_{ij} is the random interactions between the operators taken from the normal distribution of the form

$$P(J_{ij}) \sim \exp\left(-\frac{J_{ij}^2}{2J^2}\right). \tag{1.4}$$

The model has intrigued scientists in recent years especially with the development of the Sachdev-Ye-Kitaev model [105,121], specifically, its connection to the black hole physics.

From the condensed matter prospective, the SY model provides deep insights into the physics of metals that do not behave 'normal', i.e. those that do not show the resistivity to grow quadratically with temperature at temperatures much lower than the Debye temperature. The original discovery of this model was in the presence of the gapless state produced by the quantum fluctuations on top of the spin glass state. In the leading order, the local dynamic spin-susceptibility in the gapless state behaves as

$$\overline{\chi(\omega)} \sim \log(1/|\omega|) + i\pi/2\,\mathrm{sgn}(\omega). \tag{1.5}$$

A notable feature of the form of the susceptibility above is that it matches the phenomenologically proposed marginal Fermi liquid [178] - the behavior that was experimentally observed in many cuprate compounds. This theory generally assumes that the real and imaginary parts of electron self-energy in the system behave as $\mathrm{Re}\Sigma(\omega) \sim \omega \log|\omega|$ and $\mathrm{Im}\Sigma(\omega) \sim |\omega|$, respectively, in contrast to the Fermi

liquid self-energy (1.1).

In Chapter 2, we investigate corrections to the leading order in this model. We show not only that they can be computed analytically, but also that they match the numerical solution at small frequencies.

Random $t-J$ model.

The random $t-J$ model is described by the following Hamiltonian:

$$H = \sum_{\langle ij\rangle,l,\alpha} t_{ij} c^{\dagger}_{il\alpha} c_{jl\alpha} + h.c. + \sum_{\langle ij\rangle,\alpha\beta} J_{ij} \left(S_{i\alpha\beta} S_{j\beta\alpha} - \frac{1}{M} S_{i\alpha\alpha} S_{j\beta\beta} \right), \tag{1.6}$$

where the interactions between the electron operators $c_{il\alpha}$ have the form

$$t_{ij} = \frac{t}{\sqrt{Mz}}, \tag{1.7}$$

and z is the coordination number of the Bethe lattice. The spin operators $S_{i\alpha\beta}$ are coupled by J_{ij} which are random variables taken from the Gaussian distribution with $\overline{J_{ij}} = 0$ and $\overline{J_{ij}^2} = J^2/Mz$.

In Chapter 3 we study this model and, similarly to Chapter 2, analytically compute the subleading corrections to the low frequency behavior of the spectral density and optical conductivity. We show that the subleading corrections match the full numerical solution of the model for a range of low frequencies.

Large-N theory of critical Fermi surface.

The third model that is discussed in this thesis is a 2-dimensional model with Yukawa interactions

that can be described by the following Lagrangian density:

$$\mathcal{L} = \sum_{r=\pm}\sum_{j=1}^{N} \psi^{\dagger}_{r,j}(\partial_\tau - ir\partial_x - \partial_y^2)\psi_{r,j} + \sum_{r=\pm}\sum_{l=1}^{M}\sum_{ij=1}^{N} \frac{g_{ijl}}{N} r^s \psi^{\dagger}_{r,i}\psi_{r,j}\varphi_l + \frac{1}{2}\sum_{i=1}^{M}(\partial_y\varphi_i)^2\,, \tag{1.8}$$

where fermions $\psi_{r,i}$ and bosons φ_l are coupled via Yukawa interactions $g_{ijl} = g^*_{jil}$. Fermions have a Fermi surface and the number of flavors is N, while bosons have M flavors. r denotes a specific patch of the Fermi surface.

In Chapter 4 we study this model in the large N limit from a prospective of quantum chaos. We compute the out-of-time-ordered correlation function and show that this model is maximally chaotic.

Recent advances in the theoretical understanding of strange metals, particularly through investigations of the two-dimensional Yukawa-SYK model, have been remarkable. In [141], the authors developed a theory that captures the universal properties of strange metals. Specifically, they proposed a physically viable framework to explain the presence of the strange metal regime in high-temperature superconducting materials.

More recently, numerical studies at large scales of the model were performed, using Hybrid Monte Carlo method [142,143]. In these studies, the authors observed well-defined signatures of strange metal regime, such as linear-in-temperature resistivity, and the 'plankian' transport scattering rate in an extended regime away from the quantum critical point. These findings offer profound insights into the physics of high-temperature superconductors and further establish the relevance of SYK-family models as a robust framework for exploring the behavior of cuprates and strange metals.

Furthermore, in [117], the authors examined the instabilities of the strange metal regime to superconductivity, providing deeper insight into the physics of cuprates.

1.2.3 From strange metal to spin glass

Finally, in Chapter 5, we expand on the analysis of the random *t-J* model introduced in Section 1.2.2. Using a combination of numerical and analytical techniques, we demonstrate that the critical solution persists across the entire overdoped region. It was later shown in numerical studies of the Yukawa-SYK model [142,143] that the critical behavior of the model persists over a large region of the phase diagram providing additional evidence for the presence of critical regime in the overdoped part of the cuprate phase diagram.

We identify a well-defined phase transition separating the non-Fermi liquid phase from the spin glass phase. Our results show that the Fermi liquid phase is not a viable solution within this model which confirms the experimental observations [34,70,11].

The system we studied is the overdoped random $t-J$ model, characterized by the following Hamiltonian:

$$H = \frac{1}{\sqrt{N}} \sum_{i \neq j=1}^{N} t_{ij} c_{i\alpha}^{\dagger} c_{j\alpha} + \frac{1}{\sqrt{N}} \sum_{i<j=1}^{N} J_{ij} \vec{S}_i \cdot \vec{S}_j - \mu \sum_i c_{i\alpha}^{\dagger} c_{i\alpha} \,, \tag{1.9}$$

where, as before, S_i are operators in $SU(M)$ group with random interactions J_{ij} that follow a Gaussian distribution as defined in. Operator $c_{i\alpha}$ is the electron annihilation operator and t_{ij} is the complex random hopping (1.7), and μ is the chemical potential.

By fixing the interaction parameters while varying the temperature T and doping p, we aim to identify the critical parameter values that signify the transition between the non-Fermi liquid and spin glass phases. To achieve this, we represent spins S_i and electrons $c_{i\alpha}$ as fractional particles

$$c_{i\alpha} = b^{\dagger} f_{i\alpha} \,, \;\; S_i^a = f_{i\alpha}^{\dagger} \frac{\sigma^a_{\alpha\beta}}{2} f_{i\beta} \,, \tag{1.10}$$

with the constraint, $f_{i\alpha}^{\dagger} f_{i\alpha} + b_i^{\dagger} b_i = 1$. Doping p is defined as the value that allows to satisfy the

self-consistency equations

$$\langle f^\dagger f\rangle = \frac{1}{2} - \frac{1}{2}p, \quad \langle b^\dagger b\rangle = p, \tag{1.11}$$

where compared to Chapter 5, we chose the specific physical values for $k = 1/2$ and $\kappa = 1/2$.

Doping, in this context, is defined as the relative density of fractionalized particles. Within this framework, we observe that the spin correlation exponent varies continuously with doping, and the resistivity displays a linear dependence on temperature.

Additionally, we investigated the instability of the non-Fermi liquid regime toward the spin glass phase. Our analysis revealed that the spin glass phase remains stable in the low-doping regime, with the doping value at which the transition occurs depending on the interaction strength J at a fixed temperature.

1.3 Spin glasses

Spin glass systems, characterized by their intrinsic disorder, have been extensively studied across various scientific disciplines. Their applications span fields such as economics [118,18], quantum optics [112], neuroscience [58], and machine learning [87]. Spin glass behavior has also been proposed in the context of experimental investigations of cuprates [55,138]. From the perspective of quantum information science, a recent experiment on the maximal independent set problem [48] has drawn intriguing parallels to spin glass dynamics.

Despite their broad relevance, many fundamental questions about spin glasses remain unanswered, presenting opportunities for further exploration through traditional approaches of condensed matter theory.

Spin glasses are systems of spins with random interactions, which lead to complex behavior. These interactions present significant challenges for analysis, particularly in finite-dimensional systems. However, in the systems where the range of interactions becomes infinite, the complexity is reduced, and

many spin glass systems become solvable.

In this dissertation, we focus on two distinct spin glass systems: the infinite-range Ising spin glass model in transverse and longitudinal fields, and the quantum spherical p-rotor model. We explore their fundamental properties, analyze their behavior, and discuss the experimental motivation.

1.3.1 Sherrington-Kirkpatrick model

Before discussing the quantum Ising spin glass model, it is helpful to introduce the Sherrington-Kirkpatrick (SK) model [161]. It is one of the most well-studied models among spin glass systems. The Hamiltonian of the model has the following form:

$$H = -\frac{1}{\sqrt{N}} \sum_{ij} J_{ij} S_i S_j, \tag{1.12}$$

where N is the total number of spins in the system. The couplings J_{ij} are randomly sampled from the Gaussian distribution

$$P(J_{ij}) = \sqrt{\frac{N}{2\pi J^2}} \exp\left(-\frac{N}{2J^2} \left(J_{ij} - \frac{J_0}{2N} \right)^2 \right) \tag{1.13}$$

with J_0 and J^2 being the mean and variance of the distribution respectively. This model can be solved using the replica method.

The replica method is a useful technique in solving models with infinite range random interactions. The approach is to evaluate the free energy using the following formula:

$$\overline{\log Z} = \lim_{n \to 0} \frac{1}{n} \log \overline{Z^n}. \tag{1.14}$$

This method allows us to evaluate the free energy by computing the averaged value of the partition function, instead of the averaged value of the logarithm of the partition function.

The solution of the model is the phase diagram when the system is exposed to the external magnetic field H. The phase diagram is presented in Fig. 1.2. The curve separating the two phases is obtained by studying the stability of the SK model[43]. The curve represents the transition between the two states: stable (paramagnet) and unstable (spin glass). The spin glass phase is described by the replica symmetry breaking (RSB) solution. It is important to note that the RSB solution is present for a large range of the external magnetic fields and for a large range of temperatures.

The spin glass phase has different notable properties that are important to mention:

- The spin glass phase has a complex energy landscape that consists of many local minima. The number of the minima grows exponentially with the system size

$$\mathcal{N} \sim e^{N\Sigma}, \tag{1.15}$$

  where Σ is the complexity (configurational entropy)[26].

- The barriers between these minima are infinite for the infinite-range model in the thermodynamic limit and, therefore, the system would never equilibrate. Ergodicity is broken in this case. However, in a finite dimensional system the barriers between metastable states are always finite.

- 'Glassy dynamics' usually refers to systems that take an extremely long time to reach equilibrium. Glassy dynamics is usually observed slightly above and below the glass transition.

Motivated by these phenomena and the capabilities of modern quantum simulators to investigate the dynamics of disordered many-body systems, in Chapter 6 we explored the impact of adding a longitudinal field term to the SK model. This addition allows us to study its phase diagram with the additional parameter. The inclusion of the longitudinal field is particularly relevant, as quantum simulators inherently exhibit a longitudinal field component that cannot be entirely eliminated. We

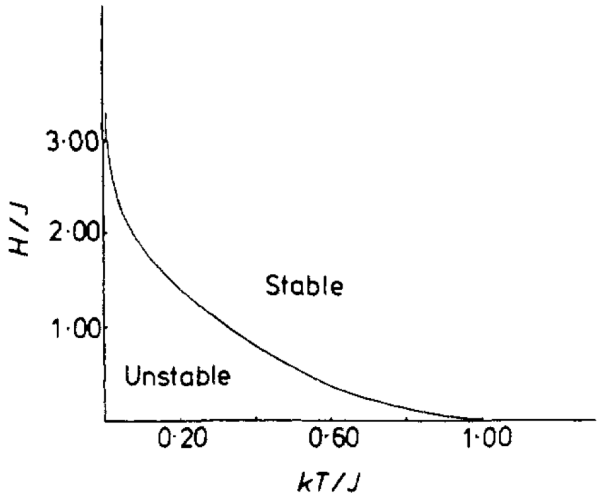

Figure 1.2: Almeida-Thouless line. The line represents the phase transition in the SK model in the external magnetic field H. The figure is taken from [43].

find that the external field does not eliminate the spin glass phase, opening up possibilities for a variety of applications.

1.3.2 Infinite range quantum Ising spin glass

In Chapter 6 we examine the equilibrium dynamics of the infinite-range Ising spin glass that is exposed to the external field h. The Hamiltonian of the system

$$H = \sum_{i<j} J_{ij} Z_i Z_j - g \sum_i X_i - h \sum_i Z_i, \tag{1.16}$$

where $i, j = 1 \ldots N$ denote the lattice sites. The interaction between the spin sites is given by J_{ij} which is taken as independent random numbers drawn from the distribution

$$P(J_{ij}) \propto \exp\left[-\frac{N J_{ij}^2}{2 J^2}\right]. \tag{1.17}$$

In Chapter 6 we investigate the behavior of the bilocal field in imaginary time

$$Q_{ab}(\tau_1, \tau_2) \sim \frac{1}{N} \sum_i Z_{ia}(\tau_1) Z_{ib}(\tau_2), \tag{1.18}$$

where a, b are replica indecies. We show that even for $h \neq 0$, the spectrum of the model is gapless

$$\mathrm{Im} Q_r(\omega) \sim \omega \tag{1.19}$$

which is further explored in detail. Additionally, we compute the phase diagram and demonstrate that the spin glass phase persists across a wide range of external field values.

1.3.3 Spherical quantum p-rotor model

The spherical quantum p-rotor model has been extensively studied due to its ability to capture out-of-equilibrium dynamics, a challenging task in many systems. However, it is also valuable to investigate this model in equilibrium, as it provides important insights into its fundamental behavior.

The spherical p-rotor model in external field h is described by the following partition function

$$Z[J_{i_1 \ldots i_p}] = \int \mathcal{D}\sigma_i(\tau) \ \exp\left[- \int_0^\beta d\tau \left(\frac{1}{2g} \dot{\sigma}_i(\tau) \dot{\sigma}_i(\tau) \right.\right. \tag{1.20}$$

$$\left.\left. + \sum_{i_1 < \ldots < i_p} J_{i_1 \ldots i_p} \sigma_{i_1}(\tau) \ldots \sigma_{i_p}(\tau) - h \sum_i \sigma_i(\tau) \right) \right]. \tag{1.21}$$

Each $\sigma_i(\tau)$ is a real continuous variable and $\dot{\sigma}_i(\tau) \equiv d\sigma_i / d\tau$. The spherical constraint in this model reads

$$\sum_{i=1}^{N} \sigma_i(\tau) \, \sigma_i(\tau) = N. \tag{1.22}$$

The interaction couplings between the rotors are $J_{i_1 \ldots i_p}$, and similarly to the SK model, all of these

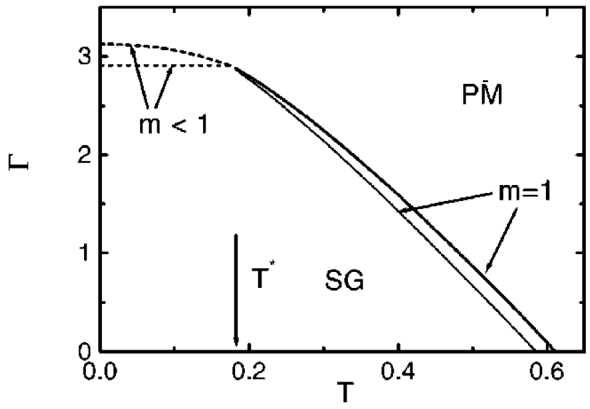

Figure 1.3: The phase diagram of the spherical $p = 3$-spin model. The parameter $\Gamma = \hbar^2/(MJ)$. The solid lines depict the second-order phase transition between the paramagnetic (PM) phase and spin glass (SG) phase, and the dashed lines represent the first-order phase transition. The figure is taken from [38].

couplings are taken to be independent random variables with distribution

$$P(J_{i_1\ldots i_p}) \propto \exp\left[-\frac{N^{p-1}}{p!}\frac{J_{i_1\ldots i_p}^2}{J^2}\right], \tag{1.23}$$

where p is the number of the coupled rotors and J^2 is the mean of the Gaussian distribution. Although the local constraint does not have a direct physical interpretation, the model can provide with valuable insights into the physics of spin glasses.

Numerical studies of the model without an external field ($h = 0$) have been conducted previously [38,7] and the phase diagram of the $p = 3$ model is shown in Fig. 1.3.

In Chapter 6, we extend these investigations by incorporating a longitudinal field, demonstrating that the phase diagram of this modified model includes a finite region corresponding to the spin glass phase. We also emphasize the relevance of these findings for advancing the study of spin glass systems using quantum simulators.

1.4 Organization of the thesis

The thesis is organized as follows. In Chapter 2 we study a class of SYK models. Specifically, we analytically find power-law corrections to the leading order in susceptibility and compare them to the exact numerical solution. In Chapter 3 we study the power-law corrections in a random $t-J$ model by extending the analysis from Chapter 2. In Chapter 4 we analyze a chaotic theory non-Fermi liquid and study its chaotic properties with an emphasis on computing the out-of-time-ordered correlation function. In Chapter 5 we return to studying the random $t-J$ model with an emphasis on describing the phase diagram in the model. Finally, in Chapter 6, we study and describe a set of spin glass models: SK model and p-spherical spin glass model. We analyze their phases while varying parameters in the Hamiltonians.

2

Excitation spectra of Sachdev-Ye-Kitaev models

2.1 Introduction

There has been much recent interest in solvable models [156,105,154] in the Sachdev-Ye-Kitaev (SYK) class as descriptions of compressible quantum many body systems without quasiparticle excitations. These

are models with random and all-to-all interactions, and their low energy limit has the structure of 0+1 dimensional conformal field theory [139]. Instead of quasiparticles, there are infinite towers of primary operators [147,121,104,75], all but a few of which have irrational scaling dimensions and these describe the long time dynamics of all local observables. We will examine a number of models of bosons and/or fermions in this paper, and the boson or fermion, $a = \mathfrak{b}, f$, has a zero temperature ($T = 0$) spectral density as a function of frequency, ω, of the form (for the case with $q = 4$-particle terms in the Hamiltonian)

$$\rho_a(\omega) = \begin{cases} \dfrac{g_{a+}(\omega)}{\sqrt{\omega}}, & \omega > 0 \\ \dfrac{g_{a-}(-\omega)}{\sqrt{-\omega}}, & \omega < 0 \end{cases} . \tag{2.1}$$

Here $g_{a\pm}(\omega \to 0) =$ constant, and the main purpose of the present article is to describe the small ω expansions of $g_{a\pm}(\omega)$ for a number of models of physical interest. These expansions depend upon the scaling dimensions and operator product expansions of the irrelevant primary operators, and are also constrained by Luttinger-like theorems [63,42,78] and an emergent time reparameterization symmetry [121,104]. We will compare conformal theory predictions with accurate numerical solutions of the SYK equations carried out directly on the real ω axis at $T = 0$ (as in the original paper of Ref. [156]), and find excellent agreement.

A related analysis has been carried out by Maldacena and Stanford [121]. They examined the particle-hole symmetric Majorana SYK model, using numerical solutions of the SYK equations in imaginary time. All of our numerical analysis will be carried out in real time, using real frequency spectral functions: we will show that this allows higher precision, and enables us to identify various subleading and non-linear corrections. We also examine fermionic and bosonic models without particle-hole symmetry—the scaling dimensions for the particle-hole asymmetric fermionic models were obtained in Ref. [78].

Our results will also apply to the random quantum magnets with SU(M) symmetry which were studied in Ref. [156] in the limit of large M. Such models are of interest to condensed matter physics because of their 'Mottness': they have constraints associated with strong on-site interactions, in contrast to the infinite-range interactions of the SYK models. For these magnets, we compute the dynamic local spin susceptibility $\chi_L(\omega)$. This quantity is potentially of experimental interest as a description of a quantum critical point in a disordered magnetic system studied by neutron scattering [96,8,2,159,59]. The time reparameterization mode is the leading irrelevant operator determining the frequency dependence of χ_L, and we find

$$\mathrm{Im}\chi_L(\omega) \sim \tanh\left(\frac{\omega}{2T}\right)\left[1 - \mathcal{C}\gamma\,\omega\tanh\left(\frac{\omega}{2T}\right) - \ldots\right], \tag{2.2}$$

where the specific heat per spin component $= \gamma T$, and $\mathcal{C}$ is a dimensionless number which is specified in (2.107) and (2.108) for our models. The leading term in (2.2) has been obtained earlier [139]. We obtain here the term proportional to $\mathcal{C}$: this is the contribution of the time reparameterization mode *i.e.* the boundary graviton in the holographic dual. Notice that this term has a prefactor of ω without a corresponding factor of $1/T$: this indicates the violation of scaling induced by an irrelevant operator. We show a plot of $\mathrm{Im}\chi_L$ in Fig. 2.1; it is curious that this resembles observations in Refs. [8,2], and it would be worthwhile to investigate this further, especially in systems with greater randomness. Similar spectra should also apply to anomalous density fluctuations in the model of Ref. [93], and density fluctuations have been investigated in momentum-resolved electron energy-loss spectroscopy (M-EELS) [132,88] but for $\omega \gg T$.

In the limit of $T \to 0$, (2.2) predicts a discontinous spectral density at zero frequency. We have computed higher order terms at $T = 0$ for the particle-hole symmetric case (see Eq. (2.105))

$$\mathrm{Im}\chi_L(\omega) \sim \mathrm{sgn}(\omega)\left[1 - \mathcal{C}\gamma|\omega| - \frac{7}{16}(\mathcal{C}\gamma)^2|\omega|^2 - \mathcal{C}'|\omega|^{2.77354\ldots} + \frac{37}{48}(\mathcal{C}\gamma)^3|\omega|^3 - \ldots\right], \tag{2.3}$$

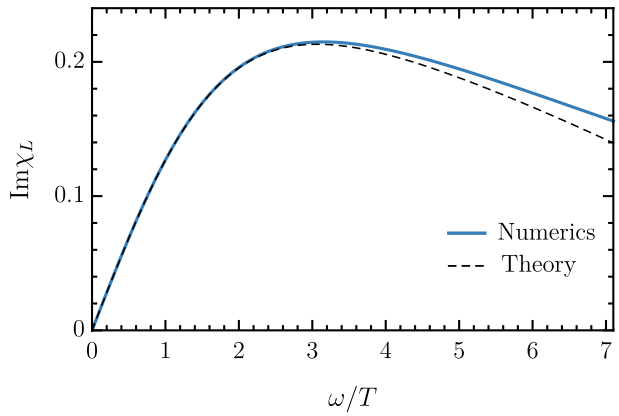

Figure 2.1: Plot of the local dynamic spin susceptibility. The blue solid line is obtained from numerical solution of the Schwinger-Dyson equations (2.16) for $T/J = 0.1$. The black dashed line is analytical result in (2.2) for $\mathcal{C}\gamma T \simeq 0.05$ with three higher order terms in (2.3) included with their $T = 0$ expressions.

where the $|\omega|^2$ and $|\omega|^3$ terms are non-linear corrections from the time reparameterization mode, and $\mathcal{C}'$ mode is a linear contribution of a second irrelevant operator with scaling dimension $h = 3.77354\ldots$. The $T > 0$ form of the $\mathcal{C}'$ term can be deduced from imaginary part of (A.55).

We have attempted to write this paper in a self-contained manner for condensed matter physicists. We will begin in Section 2.2 by defining the models of interest, and recalling the leading conformally invariant results. A diagrammatic analysis of the conformal perturbation theory is presented in Section 2.3, where we obtain the scaling dimensions of all primary operators, and identify the operators associated with time reparameterization and an emergent U(1) gauge invariance. Section 2.4 employs an alternative functional approach of Kitaev and Suh [104] which allows efficient treatment of particle-hole asymmetry, non-linear corrections and non-zero temperatures. Section 2.5 transforms our results from imaginary time to the spectral densities on the real frequency axis. Section 2.6 extends our analysis to models of bosonic random rotors, which has appeared in some recent studies of quantum phase transitions. Finally, our main numerical results are presented in Section 2.7, where we compare numerical solutions of the SYK equations on the real frequency axis with the predictions of the conformal perturbation analysis.

The formalism developed in this paper for the SYK models will be applied to the *t-J* in a companion paper [175]. We will dope the large M SU(M) insulating quantum magnets described in the present paper by mobile charge carriers. The resulting theory of fractionalized particles, the spinons and holons, is described [92] by a set of Schwinger-Dyson equations similar to those presented in Section 2.2. The companion paper [175] presents the conformal corrections to a variety of gauge-invariant observables, including the electron spectral functions and the optical conductivity.

2.2 Conformal solutions for the SYK models

We begin by recalling the less-familiar models considered originally in Ref. [156], as these will connect directly to the *t-J* models considered in the companion paper [175]. These are SU(M) spin models with Hamiltonian

$$H_J = \sum_{\langle ij\rangle,\alpha\beta} J_{ij}\left(S_{i\alpha\beta}S_{j\beta\alpha} - \frac{1}{M}S_{i\alpha\alpha}S_{j\beta\beta}\right). \tag{2.4}$$

Here $\alpha = 1\ldots M$ is a SU(M) spin index, $S_{i\alpha\beta} = S^{\dagger}_{i\beta\alpha}$ is the spin operator on site i, and the $1/M$ term (which will be dropped in large M limit) is added to ensure it transform in the adjoint of SU(M). Here, we have chosen [139] to place the sites i on a high-dimensional lattice with co-ordination number z, and the J_{ij} are nearest-neighbor exchange interactions and Gaussian random variables with

$$\overline{J_{ij}} = 0, \quad \overline{J_{ij}^2} = \frac{J^2}{Mz} \tag{2.5}$$

We will examine the model H_J in the limit of large z, followed by large M. Alternatively, we can consider the model on a N-site cluster, with all-to-all random exchange interactions; this was the model considered in Ref. [156], and the large N limit leads to the same saddle-point equations as the large z limit. However, the large z limit allows us to consider transport properties of electrons in a lattice [139,81] using a *t-J* model, which we will described in paper II.

The properties of the SU(M) spin models depend upon the representation of SU(M) realized by the states on each site, i. The most common choices correspond to the formulations in terms of fermionic and bosonic *spinons*. The fermionic spinon case corresponds to the representation with a single column of boxes in the SU(M) Young tableaux, with the spin operator

$$S_{i\alpha\beta} = f^\dagger_{i\alpha} f_{i\beta}. \tag{2.6}$$

expressed in terms of fermionic spinons $f_{i\alpha}$. This induces a U(1) gauge symmetry

$$f_{i\alpha}(\tau) \to f_{i\alpha}(\tau) e^{i\varphi_i(\tau)}, \tag{2.7}$$

The physical Hilbert space must be U(1) gauge-symmetric, which implies that the gauge charge is conserved, and we consider the representation

$$\sum_\alpha f^\dagger_{i\alpha} f_{i\alpha} = \kappa M, \tag{2.8}$$

with κM boxes in the Young tableaux. We will take the large M limit at fixed κ.

Similarly, the bosonic spinon case corresponds to a different SU(M) representation with a Young tableaux of a single row of boxes, and the spin operator

$$S_{i\alpha\beta} = \mathfrak{b}^\dagger_{i\alpha} \mathfrak{b}_{i\beta}, \tag{2.9}$$

with the U(1) gauge charge constraint

$$\sum_\alpha \mathfrak{b}^\dagger_{i\alpha} \mathfrak{b}_{i\alpha} = \kappa M\,. \tag{2.10}$$

The fermionic spinon representation defined by (2.6) and (2.8) and the bosonic spinon representation

defined by (2.9) and (2.10) are the same only for $\kappa M = 1$.

Along with the SU(M) spin models recalled above, our results apply also to the complex SYK model (with a $q = 4$ fermion Hamiltonian)

$$H_{\text{SYK}} = \frac{1}{2N^{3/2}} \sum_{i,j,k,\ell=1}^{N} J_{ij;k\ell} f_i^\dagger f_j^\dagger f_k f_\ell - \mu_f \sum_i f_i^\dagger f_i \tag{2.11}$$

where $J_{ij;k\ell}$ are independent random numbers with $\overline{|J_{ij;k\ell}|^2} = J^2$. The advantage of this model is that only a single large N limit is required, and there is no analog of the subsequent large M limit required for the models above. But, as we discussed in Section 2.1, this simplicity comes at a cost: we loose the Mottness that is present in the spin (and t-J) models, and is important for condensed matter applications. The analog of the fermion constraint in (2.8) is now

$$\langle f_i^\dagger f_i \rangle = \kappa \,, \tag{2.12}$$

with no sum over i. Analogously to the fermionic SYK model we can define bosonic SYK model as

$$H_{\text{SYK}} = \frac{1}{2N^{3/2}} \sum_{i,j,k,\ell=1}^{N} J_{ij;k\ell} \mathfrak{b}_i^\dagger \mathfrak{b}_j^\dagger \mathfrak{b}_k \mathfrak{b}_\ell - \mu_{\mathfrak{b}} \sum_i \mathfrak{b}_i^\dagger \mathfrak{b}_i \,, \tag{2.13}$$

along with the constraint

$$\langle \mathfrak{b}_i^\dagger \mathfrak{b}_i \rangle = \kappa \,. \tag{2.14}$$

We remark that the bosonic models defined above have $\mathfrak{b}^\dagger \partial_\tau \mathfrak{b}$ kinetic term in the Lagrangian formalism.

All of the above models have a common set of saddle point equations, which we now describe. We

introduce two-point Green's function in imaginary time, τ, at a finite temperature T:

$$G_f(\tau) = -\langle \mathrm{T}_\tau\big(f(\tau)f^\dagger(0)\big)\rangle\,, \quad G_b(\tau) = -\langle \mathrm{T}_\tau\big(\mathfrak{b}(\tau)\mathfrak{b}^\dagger(0)\big)\rangle\,. \tag{2.15}$$

In both cases the large N Dyson-Schwinger equations look identical and read for $\tau \in (0,\beta)$

$$G_a(i\omega_n) = \frac{1}{i\omega_n + \mu_a - \Sigma_a(i\omega_n)}, \quad \Sigma_a(\tau) = J^2 G_a(\tau)^{q/2} G_a(\beta-\tau)^{q/2-1}\,, \tag{2.16}$$

where the index $a = f, \mathfrak{b}$ denotes fermions or bosons, $\beta = 1/T$ is the inverse temperature, μ_a is the chemical potential and we assume that q is even integer. The models described above have $q = 4$, but we will also present some results for general q. For the fermionic case the Matsubara frequencies is $\omega_n = \frac{2\pi}{\beta}(n+\frac{1}{2})$ and for the bosonic $\omega_n = \frac{2\pi}{\beta}n$. The two-point Green's function satisfies the KMS (Kubo-Martin-Schwinger) conditions $G_a(\tau) = \zeta_a G_a(\beta+\tau)$, where $\zeta_{\mathfrak{b}} = 1$ and $\zeta_f = -1$.

It is well-known that the equations (2.16) admit conformal solution in the IR region, where $1/J \ll \tau \ll \beta - 1/J$

$$\begin{aligned} G_a^c(\tau) &= -b_a^\Delta \left(\frac{\beta J}{\pi}\sin\frac{\pi\tau}{\beta}\right)^{-2\Delta} e^{2\pi\mathcal{E}_a(\frac{1}{2}-\frac{\tau}{\beta})}\,, \\ \Sigma_a^c(\tau) &= -J^2 b_a^{1-\Delta} \left(\frac{\beta J}{\pi}\sin\frac{\pi\tau}{\beta}\right)^{-2(1-\Delta)} e^{2\pi\mathcal{E}_a(\frac{1}{2}-\frac{\tau}{\beta})}\,, \end{aligned} \tag{2.17}$$

where $\Delta = 1/q$, $\mathcal{E}_a$ is the asymmetry parameter which implicitly depends on μ, and the dimensionless constant prefactor b_a is

$$b_f = \frac{(1-2\Delta)\sin 2\pi\Delta}{4\pi\cos\big(\pi(\Delta+i\mathcal{E}_f)\big)\cos\big(\pi(\Delta-i\mathcal{E}_f)\big)}\,, \quad b_{\mathfrak{b}} = \frac{(1-2\Delta)\sin 2\pi\Delta}{4\pi\sin(\pi(\Delta+i\mathcal{E}_{\mathfrak{b}}))\sin(\pi(\Delta-i\mathcal{E}_{\mathfrak{b}}))}\,. \tag{2.18}$$

When we work in frequency space, it turns out to be convenient to use the asymmetry angles θ_a related

to $\mathcal{E}_a$ by

$$e^{2\pi\mathcal{E}_a} = \zeta_a \frac{\sin(\theta_a + \pi\Delta)}{\sin(\theta_a - \pi\Delta)}, \quad e^{-2i\theta_f} = \frac{\cos\big(\pi(\Delta + i\mathcal{E}_f)\big)}{\cos\big(\pi(\Delta - i\mathcal{E}_f)\big)}, \quad e^{-2i\theta_{\mathfrak{b}}} = -\frac{\sin(\pi(\Delta + i\mathcal{E}_{\mathfrak{b}}))}{\sin(\pi(\Delta - i\mathcal{E}_{\mathfrak{b}}))}, \tag{2.19}$$

therefore we can find

$$b_a = \zeta_a \frac{(1-2\Delta)}{\pi} \frac{\sin(\theta_a + \pi\Delta)\sin(\theta_a - \pi\Delta)}{\sin 2\pi\Delta}. \tag{2.20}$$

Notice that $\mathcal{E}_{\mathfrak{b}} = 0$ for $\theta_{\mathfrak{b}} = \pi/2$ and $\mathcal{E}_f = 0$ for $\theta_f = 0$. Also $\pi\Delta < \theta_{\mathfrak{b}} < \pi/2$ and $-\pi\Delta < \theta_f < \pi\Delta$.

Below, we will study the structure of the conformal corrections to the large z and large M saddle point of H_J in (2.4), and the large N saddle-point of H_{SYK} in (2.11). The Schwinger-Dyson equations at the saddle point are identical in the two models, so the conformal corrections will also be the same. However, once we go beyond the saddle point, and examine four-point correlators, there will be differences between the two models. We will not address these differences here.

2.3 Conformal perturbations

In this section we describe a useful view point on the SYK models as a conformal field theory (CFT) perturbed by infinite set of irrelevant operators. Although this approach is not rigorous and has caveats, which we mention below, it clarifies understanding of some results and can correctly predict $1/(\beta J)$ and $1/(\beta J)^2$ corrections to the free energy (see Appendix A.1). We will turn to a more complete approach to similar results in Section 2.4.

For simplicity, in this section we consider only the fermionic SYK model (2.11) with zero chemical potential $\mu = 0$, as the generalization to $\mu \neq 0$ is described in Section 2.4. It was shown in Refs.[73,108,106] that this model has an infinite set of bilinear primary operators $O_b^{\text{A}}(\tau)$ and $O_b^{\text{S}}(\tau)$, which

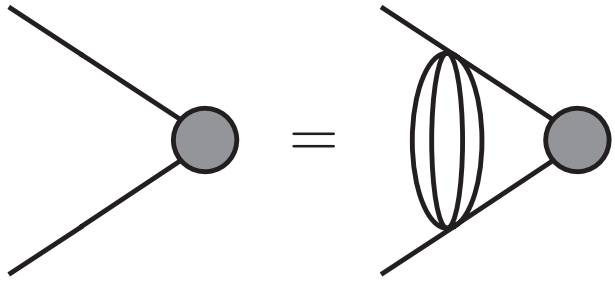

Figure 2.2: Diagrammatic representation of the Dyson-Schwinger equations (2.22), after dropping the bare terms. The internal loop has $q-2$ powers of G^c (this diagram is for $q=6$).

can be schematically represented as $O^{\mathrm{A}}_{b_n} = f_i^\dagger \partial_\tau^{2n+1} f_i$ and $O^{\mathrm{S}}_{b_n} = f_i^\dagger \partial_\tau^{2n} f_i$ for $n = 0, 1, 2, \ldots$. To compute the scaling dimensions of the operators $O_b^{\mathrm{A/S}}(\tau)$ we consider three point functions

$$v_b^{\mathrm{A/S}}(\tau_1, \tau_2, \tau_0) = \langle f(\tau_1) f^\dagger(\tau_2) O_b^{\mathrm{A/S}}(\tau_0) \rangle \,. \tag{2.21}$$

Then we can derive the Dyson-Schwinger equations for the three point functions in the IR region, and we can drop the bare terms to obtain[73]

$$v_b^{\mathrm{A/S}}(\tau_1, \tau_2, \tau_0) = \int d\tau_3 d\tau_4 K_{\mathrm{A/S}}(\tau_1, \tau_2; \tau_3, \tau_4) v_b^{\mathrm{A/S}}(\tau_3, \tau_4, \tau_0) \,, \tag{2.22}$$

where the kernels $K_{\mathrm{A/S}}$ are

$$K_{\mathrm{A/S}}(\tau_1, \tau_2; \tau_3, \tau_4) = -\left(\frac{q}{2} \pm \left(\frac{q}{2} - 1\right)\right) J^2 G^c(\tau_{13}) G^c(\tau_{24}) G^c(\tau_{34})^{q-2} \,. \tag{2.23}$$

Diagramatically the equations (2.22) are represented in Fig.2.2. Emergent conformal symmetry in the IR region fixes the functional form of the three-point functions up to the structure constants c_b^{A} and c_b^{S}

$$v_b^{\mathrm{A}}(\tau_1, \tau_2, \tau_0) = \frac{c_b^{\mathrm{A}} b^\Delta \, \mathrm{sgn}(\tau_{12})}{|J\tau_{12}|^{2\Delta - h} |J\tau_{10}|^h |J\tau_{20}|^h}, \quad v_b^{\mathrm{S}}(\tau_1, \tau_2, \tau_0) = \frac{c_b^{\mathrm{S}} b^\Delta \, \mathrm{sgn}(\tau_{10}) \mathrm{sgn}(\tau_{20})}{|J\tau_{12}|^{2\Delta - h} |J\tau_{10}|^h |J\tau_{20}|^h} \,. \tag{2.24}$$

It can be shown that for arbitrary h the three-point functions $v_h^{\mathrm{A/S}}$ satisfy the equation [121,104,108,106]

$$\int d\tau_3 d\tau_4 K_{\mathrm{A/S}}(\tau_1,\tau_2;\tau_3,\tau_4) v_h^{\mathrm{A/S}}(\tau_3,\tau_4,\tau_0) = k_{\mathrm{A/S}}(h) v_h^{\mathrm{A/S}}(\tau_1,\tau_2,\tau_0)\,, \tag{2.25}$$

where $k_{\mathrm{A/S}}(h)$ are given by the formulas

$$\begin{aligned} k_{\mathrm{A}}(h) &= \frac{\Gamma(2\Delta-h)\Gamma(2\Delta+h-1)}{\Gamma(2\Delta-2)\Gamma(2\Delta+1)}\left(1-\frac{\sin(\pi h)}{\sin(2\pi\Delta)}\right)\,, \\ k_{\mathrm{S}}(h) &= \frac{\Gamma(2\Delta-h)\Gamma(2\Delta+h-1)}{\Gamma(2\Delta-1)\Gamma(2\Delta)}\left(1+\frac{\sin(\pi h)}{\sin(2\pi\Delta)}\right)\,. \end{aligned} \tag{2.26}$$

This formula can be verified by taking the limit $|\tau_0|\to\infty$ in (2.25) and then evaluating the integrals over $\tau_{3,4}$. Therefore comparing (2.25) with (2.22), we have to set

$$k_{\mathrm{A}}(h) = 1, \quad k_{\mathrm{S}}(h) = 1\,, \tag{2.27}$$

and these equations define the anomalous scaling dimensions of the operators $O_h^{\mathrm{A/S}}(\tau)$.

The SYK model can be viewed as some conformal field theory perturbed by this infinite set of irrelevant primary operators. In the case of zero chemical potential $\mu = 0$ there is an exact particle-hole symmetry and thus only O_h^{A} operators can appear in the action. This situation exactly coincides with the case of the Majorana SYK model, where instead of complex fermions f_i we have Majorana fermions χ_i. Therefore in what follows we omit letter "A" for brevity and write for the effective action of the Majorana SYK model

$$S_{\mathrm{SYK}} = S_{\mathrm{CFT}} + \sum_h g_h \int_0^\beta d\tau O_h(\tau)\,, \tag{2.28}$$

where O_h have anomalous dimensions $h = h_0, h_1, h_2, h_3, \ldots$ and $h_0 = 2, h_1 \simeq 3.77, h_2 \simeq 5.68$, etc, which are found from the equation $k_{\mathrm{A}}(h) = 1$. (A notational aside: we will often use the subscript i

to represent the subscript h_i *e.g.* $g_{h_2} \equiv g_2$.)

The expression for the full two point function reads

$$G(\tau_{12}) = -\frac{1}{Z}\int D\chi \frac{1}{N}\chi_i(\tau_1)\chi_i(\tau_2)e^{-S_{\text{SYK}}}\,, \tag{2.29}$$

therefore using conformal perturbation theory we find

$$\begin{aligned} G(\tau_{12}) =& G^c(\tau_{12}) + \sum_h g_h \int d\tau_3 \frac{1}{N}\langle \chi_i(\tau_1)\chi_i(\tau_2)O_h(\tau_3)\rangle \\ &- \frac{1}{2}\sum_{h,h'} g_h g_{h'} \int d\tau_3 d\tau_4 \frac{1}{N}\langle \chi_i(\tau_1)\chi_i(\tau_2)O_h(\tau_3)O_{h'}(\tau_4)\rangle + \dots\,, \end{aligned} \tag{2.30}$$

where we used that $G^c(\tau_{12}) = -\frac{1}{N}\langle \chi_i(\tau_1)\chi_i(\tau_2)\rangle$ and averaging of the correlation functions is implicitly performed with S_{CFT} action and involves only connected diagrams. The higher correlation functions are fixed by conformal invariance up to the structure constants c_h and $c_{h_1h_2h_3}$:

$$\begin{aligned} &\frac{1}{N}\langle \chi_i(\tau_1)\chi_i(\tau_2)O_h(\tau_3)\rangle = \frac{c_h b^\Delta \operatorname{sgn}(\tau_{12})}{|J\tau_{12}|^{2\Delta-h}|J\tau_{13}|^h|J\tau_{23}|^h}\,, \\ &\frac{1}{N}\langle \chi_i(\tau_1)\chi_i(\tau_2)O_{h_1}(\tau_3)O_{h_2}(\tau_4)\rangle = \sum_h \frac{c_h c_{hh_1h_2} b^\Delta \operatorname{sgn}(\tau_{12})|\tau_{14}|^{h_{12}}}{|J\tau_{12}|^{2\Delta}|J\tau_{34}|^{h_1+h_2}|\tau_{13}|^{h_{12}}} x^h\, {}_2F_1(h, h+h_{12}, 2h, x)\,, \end{aligned} \tag{2.31}$$

where $h_{12} = h_1 - h_2$ and $x = \frac{\tau_{12}\tau_{34}}{\tau_{13}\tau_{24}}$. Alternatively they can be found from the Operator Product Expansion (OPE)

$$\begin{aligned} &\frac{1}{N}\chi_i(\tau_1)\chi_i^\dagger(\tau_2) = \frac{b^\Delta \operatorname{sgn}(\tau_{12})}{|J\tau_{12}|^{2\Delta}} + \frac{1}{N}\sum_h \frac{c_h b^\Delta \operatorname{sgn}(\tau_{12})}{|J\tau_{12}|^{2\Delta-h}}\mathcal{C}_h(\tau_{12},\partial_2)O_h(\tau_2)\,, \\ &O_{h_1}(\tau_1)O_{h_2}(\tau_2) = \frac{N\delta_{hh'}}{|J\tau_{12}|^{2h}} + \sum_{h''} c_{h_1h_2h_3}|J\tau_{12}|^{h_3-h_1-h_2}\mathcal{C}_{123}(\tau_{12},\partial_2)O_{h_3}(\tau_2)\,, \end{aligned} \tag{2.32}$$

where $b = \frac{1}{2\pi}(1-2\Delta)\tan(\pi\Delta)$ and the operators $\mathcal{C}_h$ and $\mathcal{C}_{123}$ generate all descendants and are determined by the functional form of the three-point functions. The structure constants c_h are [121]

$$c_h^2 = \frac{1}{(q-1)b^\Delta} \cdot \frac{(h-1/2)}{\pi\tan(\pi h/2)} \frac{\Gamma(h)^2}{\Gamma(2h)} \cdot \frac{1}{k'_{\rm A}(h)}\,, \tag{2.33}$$

and $c_{hh'h''}$ have much more complicated form and were computed in Refs. [76,75]. The OPE formulas (2.32) should not include $h_0 = 2$ operator, since it was shown in [121] that this operator breaks conformal symmetry in the SYK model. Moreover we notice that c_h is divergent for $h_0 = 2$. Nevertheless let us assume that we deal with unbroken CFT and can include O_{h_0} operator in the OPE formulas assuming limit $h_0 \to 2$ [*].

For the first order correction to the two point function at zero temperature $\beta = \infty$ we find

$$\delta G_h(\tau_{12}) = g_h \int_{-\infty}^{+\infty} d\tau_3 \frac{c_h b^\Delta \operatorname{sgn}(\tau_{12})}{|J\tau_{12}|^{2\Delta-h}|J\tau_{13}|^h|J\tau_{23}|^h} = -G^c(\tau_{12})\frac{\alpha_h}{|J\tau_{12}|^{h-1}}\,, \tag{2.34}$$

where α_h and g_h are related as

$$g_h^2 = J^2(q-1)b^\Delta k'_{\rm A}(h)\frac{(h-1/2)}{\pi\tan(\pi h/2)}\frac{\Gamma(h)^2}{\Gamma(2h)}\alpha_h^2\,. \tag{2.35}$$

We notice that g_0 has to be divergent for $h_0 = 2$ in order for α_0 to be finite. Also we remark that all $g_h \propto J$ are dimensionful couplings, whereas α_h are dimensionless constants. The analysis in Section 2.4 establishes that α_0 is indeed finite, and we will confirm this in our numerical results.

[*] Perhaps this approach can be justified if the SYK model is considered as a limit of some conformal SYK model for which $h_0 = 2 - \varepsilon_0$ and $\varepsilon_0 \to 0$, see [74] and Appendix H in [121].

For the second order correction we find using (2.31)

$$\delta^2 G_{hh'}(\tau_{12}) = -\frac{1}{2} g_h g_{h'} \int d\tau_3 d\tau_4 \frac{1}{N} \langle \chi_i(\tau_1)\chi_i(\tau_2) O_h(\tau_3) O_{h'}(\tau_4)\rangle \tag{2.36}$$

$$= -G^c(\tau_{12}) \frac{a_{hh'}\alpha_h\alpha_{h'}}{2|J\tau_{12}|^{h+h'-2}}\,, \tag{2.37}$$

where the coefficients $a_{hh'}$ are functions of h, h' and Δ and we will find some of them explicitly in the Section 2.4 using resonance theory.

It is instructive to use these conformal perturbation methods to also compute the free energy. We describe this in Appendix A.1; one term is at variance with another discussion [35].

2.4 Kitaev-Suh resonance theory

In this section, we will review the renormalization and resonance formalism developed in [104,78,81], and extend it to nonlinear order. The theory provides a framework for understanding the corrections due to physics at higher energy scales in SYK-type models.

To linear order, the corrected Green's function in (2.30) $G(\tau) = -\langle \mathrm{T}_\tau f(\tau) f^\dagger(0)\rangle$ can be written as

$$G(\tau) = G^c(\tau)\left(1 - \sum_h \frac{\alpha_h}{(\beta J)^{h-1}} \mathcal{F}_h(\tau/\beta) + \dots\right). \tag{2.38}$$

Here recall that $G^c(\tau)$ is the conformal Green's function, β is inverse temperature and J denotes some UV energy scale, which is usually taken to be the SYK coupling. $\mathcal{F}_h$ is some universal scaling functions that will be computed later in (2.92). The sum runs over a set of discrete numbers $\{h_i\}$ that will be determined in Section 2.4.1. Although the resonance formalism is a direct consequence of Schwinger-Dyson equations, the structure of the corrections is consistent with the CFT interpretation of SYK-type model. The numbers $\{h_i\}$ can be interpreted as the scaling dimensions of primary operators $\{O_h\}$ in the SYK CFT that appears in the OPE of $f(\tau)f^\dagger(0)$. The dimensionless coefficients

α_h parameterize the deformation away from the SYK CFT, as in (2.28).

The exact values of α_h's require solving the full Schwinger-Dyson equations in the UV, and they are usually extracted from numerics.

In SYK-type models, operators O_0^{S} (there may be several) of scaling dimension $h_0^{\mathrm{S}} = 1$ and O_0^{A} of scaling dimension $h_0^{\mathrm{A}} = 2$ are special: they are conserved charges of $U(1)$ and time-reparameterization symmetry respectively. These symmetries are emergent and spontaneously broken in the IR, but also explicitly broken by the deformation δS which lives in the UV. Therefore δS provides the effective action for the these pseudo-Nambu-Goldstone modes. For the time-reparameterization symmetry, this is the well-known Schwarzian action.

The resonance formalism was first developed in [104] for Majorana SYK, where the Green's function is always antisymmetric in time and $\mathcal{F}_h$ is obtained for generic temperature. In [78], the formalism was extended to complex SYK model which has a $U(1)$ symmetry, and $\mathcal{F}_h$ is obtained at zero temperature for generic $U(1)$ charge. In [81], the theory was further extended to the *t-J* model, a couple system of both fermions and bosons, and the scaling function $\mathcal{F}_h$ was obtained for generic temperature and $U(1)$ charge. In all these previous works, the correction is only calculated for linear order in α_h, which only provides information about the spectral weight $\rho_a(\omega)$ around $\omega = 0$. In this paper, we will extend the formalism to arbitrary nonlinear order in α_h, which shows excellent agreement with large-q expansion and numerics at finite q: it can now extrapolate the spectral weight $\rho_a(\omega)$ up to finite ω/J.

2.4.1 Linear order correction

We summarize previous works on linear order resonance theory [104,78,81]. Our discussion will be based on the Schwinger-Dyson equation, abstractly written as

$$G = G_*[\Sigma], \quad \Sigma = \Sigma_*[G] + \sigma. \tag{2.39}$$

Here G and Σ are regarded as bi-local fields and G_* and Σ_* are functionals that define the saddle point. σ is a bi-local field referred as the UV source. The conformal solution (G^c, Σ^c) is exact if $\sigma = 0$. In the bosonic and fermionic SYK$_q$ models, $G_*[\Sigma](\tau_1, \tau_2) = -(1/\Sigma)(\tau_1, \tau_2)$ (in the sense of functional inverse), and $\Sigma_*[G](\tau_1, \tau_2) = (-)^{\epsilon_a} J^2 G(\tau_1, \tau_2)^{q/2} \left(-G(\tau_2, \tau_1)\right)^{q/2-1}$, and $\sigma(\tau_1, \tau_2) = (\partial_{\tau_1} - \mu)\delta(\tau_1 - \tau_2)$. σ is referred as UV source because it contains high frequency Fourier components. We also note that the self-energy Σ is shifted from the usual definition by σ.

If we are interested in the IR physics $J^{-1} \ll |\tau| \lesssim \beta$, the UV source σ can be treated as small perturbation, the small parameter being the ratio between IR and UV scales $1/(\beta J)^{h-1}$ or $1/|J\tau|^{h-1}$. To calculate the linear response, we expand the SD equations (2.39) around the conformal saddle point (G^c, Σ^c) to linear order:

$$G = G^c + \delta G, \quad \Sigma = \Sigma^c + \delta\Sigma. \tag{2.40}$$

and obtain

$$\delta G = W_\Sigma \delta\Sigma, \quad \delta\Sigma = W_G \delta G + \sigma \tag{2.41}$$

where we defined W_Σ and W_G as

$$W_\Sigma = \left.\frac{\delta G_*}{\delta \Sigma}\right|_{\Sigma^c}, \qquad W_G = \left.\frac{\delta \Sigma_*}{\delta G}\right|_{G^c}. \tag{2.42}$$

Finally a simple analysis yields[78]:

$$\delta G = (1 - \underbrace{W_\Sigma W_G}_{K_G})^{-1} W_\Sigma \sigma, \quad \delta\Sigma = (1 - \underbrace{W_G W_\Sigma}_{K_\Sigma})^{-1} \sigma. \tag{2.43}$$

Here we defined two kernels $K_G = W_\Sigma W_G$ and $K_\Sigma = W_G W_\Sigma$. We remark that K_G is exactly the one-rung diagrams that one needs to sum to compute the four-point functions [121,104]. By construction the

nonzero spectra of K_G and K_Σ are the same.

In what follows we are going to adopt a convenient notation used in Ref.[78] for writing functions which have discontinuity at $\tau = 0$ and different behaviour for negative and positive τ. Namely, we write all functions as two component vectors, where the first component is for $\tau > 0$ and the second one is for $\tau < 0$. We refer to this as a plus/minus basis. For example the conformal solution for the Green's function $G_a^c(\tau)$ and self-energy $\Sigma_a^c(\tau)$ at zero temperature can be written as

$$G_a^c(\tau) = -\begin{pmatrix} e^{\pi\mathcal{E}_a}, & \tau > 0 \\ \zeta_a e^{-\pi\mathcal{E}_a}, & \tau < 0 \end{pmatrix} \frac{b_a^\Delta}{|J\tau|^{2\Delta}}\,, \quad \Sigma_a^c(\tau) = -\begin{pmatrix} e^{\pi\mathcal{E}_a}, & \tau > 0 \\ \zeta_a e^{-\pi\mathcal{E}_a}, & \tau < 0 \end{pmatrix} \frac{J^2 b_a^{1-\Delta}}{|J\tau|^{2(1-\Delta)}}\,, \tag{2.44}$$

where the constant b_a is given in (2.20) and $\zeta_\mathfrak{b} = 1$ and $\zeta_f = -1$. In what follows we suppress index $a = f, \mathfrak{b}$ in various functions for brevity and only keep ζ factors where it's needed.

To proceed in analysis, we notice that the conformal saddle point possesses $\mathrm{SL}(2, R)$ symmetry, and therefore we can break up (2.43) into irreducible representations of $\mathrm{SL}(2, R)$ labelled by h, and a convenient basis for this purpose at zero temperature is

$$\delta G(\tau) = \delta\vec{G}|J\tau|^{1-h}G^c(\tau), \quad \delta\Sigma(\tau) = \delta\vec{\Sigma}|J\tau|^{1-h}\Sigma^c(\tau), \quad \sigma(\tau) = \sum_h \vec{\sigma}_h|J\tau|^{1-h}\Sigma^c(\tau)u(\tau)\,, \tag{2.45}$$

where $\delta\vec{G} = (\delta G_+, \delta G_-)^{\mathrm{T}}$, $\delta\vec{\Sigma} = (\delta\Sigma_+, \delta\Sigma_-)^{\mathrm{T}}$ and $\vec{\sigma}_h = (\sigma_{h+}, \sigma_{h-})^{\mathrm{T}}$ are all two components columns according to our new notations and the source $\sigma(\tau)$ is written in the IR region with the window function $u(\tau)$ and positive real numbers h (for details about this representation of the soruce σ see Ref.[104]). In this basis, W_Σ, W_G and K_G, K_Σ become 2×2 dimensional matrices. So for the fermionic and bosonic SYK_q models (2.16), we can find

$$\delta\Sigma_*(\tau)|_{G^c} = \left(\frac{q}{2}\frac{\delta G(\tau)}{G^c(\tau)} + \left(\frac{q}{2} - 1\right)\frac{\delta G(-\tau)}{G^c(-\tau)}\right)\Sigma^c(\tau) \tag{2.46}$$

and using the basis (2.45) we write it as

$$\delta\Sigma_*(\tau)|_{G^c} = W_G \delta\vec{G} |J\tau|^{1-h} \Sigma^c(\tau)\,, \tag{2.47}$$

where W_G becomes a 2×2 matrix given by the formula

$$W_G = \begin{pmatrix} q/2 & q/2-1 \\ q/2-1 & q/2 \end{pmatrix}. \tag{2.48}$$

To find expression for the operator W_Σ we are going to use the Fourier transform written in our convenient plus/minus basis

$$\begin{pmatrix} a_+|\tau|^{-\alpha}, & \tau>0 \\ a_-|\tau|^{-\alpha}, & \tau<0 \end{pmatrix} e^{i\omega\tau} d\tau = \begin{pmatrix} a'_+|\omega|^{\alpha-1}, & \omega>0 \\ a'_-|\omega|^{\alpha-1}, & \omega<0 \end{pmatrix}, \quad \begin{pmatrix} a'_+ \\ a'_- \end{pmatrix} = M(\alpha) \begin{pmatrix} a_+ \\ a_- \end{pmatrix}, \tag{2.49}$$

where the 2×2 matrix $M(\alpha)$ has the form

$$M(\alpha) = \Gamma(1-\alpha) \begin{pmatrix} i^{1-\alpha} & i^{\alpha-1} \\ i^{\alpha-1} & i^{1-\alpha} \end{pmatrix}, \quad M(\alpha)^{-1} = \frac{\Gamma(\alpha)}{2\pi} \begin{pmatrix} i^{-\alpha} & i^{\alpha} \\ i^{\alpha} & i^{-\alpha} \end{pmatrix}. \tag{2.50}$$

In the Fourier space the basis (2.45) takes the form

$$\delta G(i\omega) = F(h)\delta\vec{G}|\omega/J|^{h-1} G^c(i\omega), \quad \delta\Sigma(i\omega) = \Phi(h)\delta\vec{\Sigma}|\omega/J|^{h-1}\Sigma^c(i\omega)\,, \tag{2.51}$$

where the matrices $F(h)$ and $\Phi(h)$ are

$$F(h) = -i\sqrt{\frac{\Gamma(2\Delta)}{\Gamma(2-2\Delta)}}b^{\frac{1}{2}}\begin{pmatrix} e^{i\theta} & 0 \\ 0 & -e^{-i\theta}\end{pmatrix} M(2\Delta-1+h)\begin{pmatrix} e^{\pi\mathcal{E}} & 0 \\ 0 & \zeta e^{-\pi\mathcal{E}}\end{pmatrix},$$
$$\Phi(h) = -i\sqrt{\frac{\Gamma(2-2\Delta)}{\Gamma(2\Delta)}}b^{\frac{1}{2}}\begin{pmatrix} e^{-i\theta} & 0 \\ 0 & -e^{i\theta}\end{pmatrix} M(1-2\Delta+h)\begin{pmatrix} e^{\pi\mathcal{E}} & 0 \\ 0 & \zeta e^{-\pi\mathcal{E}}\end{pmatrix}. \tag{2.52}$$

and we used formulas for $G^c(i\omega)$ and $\Sigma^c(i\omega)$ in the Fourier space at zero temperature:

$$G^c(i\omega) = -\frac{iC}{J}\begin{pmatrix} e^{-i\theta} \\ -e^{i\theta}\end{pmatrix}|\omega/J|^{2\Delta-1}, \quad \Sigma^c(i\omega) = -\frac{iJ}{C}\begin{pmatrix} e^{i\theta} \\ -e^{-i\theta}\end{pmatrix}|\omega/J|^{1-2\Delta}, \tag{2.53}$$

where we defined $C \equiv \sqrt{\Gamma(2-2\Delta)/\Gamma(2\Delta)}b^{\Delta-\frac{1}{2}}$. Notice that there are no ζ factors in (2.53). The operator W_Σ connects linear corrections $\delta\Sigma$ and δG as $\delta G = W_\Sigma \delta\Sigma$ and has a simple form in the Fourier space

$$\delta G_*(i\omega)|_{\Sigma^c} = G^c(i\omega)^2\delta\Sigma(i\omega). \tag{2.54}$$

Thus using (2.51) and $G^c(i\omega)\Sigma^c(i\omega) = -1$ we find

$$F(h)\delta\vec{G} = -\Phi(h)\delta\vec{\Sigma} \tag{2.55}$$

and therefore W_Σ acts on $\delta\vec{\Sigma}$ as a matrix $W_\Sigma(h) = -F(h)^{-1}\Phi(h)$ and is given by the formula[78]:

$$W_\Sigma(h) = \frac{\Gamma(2\Delta-1+h)\Gamma(2\Delta-h)}{\Gamma(2\Delta)\Gamma(2\Delta-1)\sin(2\pi\Delta)}\begin{pmatrix} \sin(\pi h+2\theta) & -\sin(2\pi\Delta)+\sin(2\theta) \\ -\sin(2\pi\Delta)-\sin(2\theta) & \sin(\pi h-2\theta)\end{pmatrix}. \tag{2.56}$$

We notice that the matrix $W_\Sigma(h)$ has the same form for bosonic and fermionic SYK models and the only difference is the range of asymmetry angle θ in these two cases. The matrix $K_G(h)$ is a product of two matrices $W_\Sigma(h)$ and W_G, so $K_G(h) = W_\Sigma(h) W_G$. Therefore (2.43) reads

$$\delta G = \frac{1}{1 - K_G(h)} W_\Sigma(h) \sigma. \tag{2.57}$$

For generic h, $1 - K_G(h)$ is non-singular and therefore the response δG is negligible at IR scales. We need to remember that a physical source σ is supported only in the UV, and we expect a non-singular response δG is also constrained in the UV region. To get an IR response, $1 - K_G(h)$ should be singular, so the possible h's that appear in (2.38) is selected by the condition

$$\det(1 - K_G(h)) = 0\,. \tag{2.58}$$

For the particle-hole symmetric case, $\mu = 0$, this equation is equivalent to $k_{\mathrm{A/S}}(h) = 1$ where $k_{\mathrm{A/S}}(h)$ are defined in (2.26).

For the resonant values of $h = h_*$, the apparent singluarity in (2.57) is regulated by the window function $u(\tau)$ which restricts σ to be supported only on UV scales. Following [104,78] we obtain

$$\delta G(\tau) = \sum_{h=h_*} \frac{1}{K_G'(h)} W_\Sigma(h) \vec{\sigma}_h |J\tau|^{1-h} G^c(\tau)\,, \tag{2.59}$$

where the sum goes over all resonances h_* which are the solutions of (2.58). The derivative of matrix $K_G'(h)$ is

$$\frac{1}{K_G'(h)} = \frac{v_h w_h}{k_G'(h)}\,, \tag{2.60}$$

where v_h and w_h are the corresponding right and left eigenvectors of $K_G(h)$ respectively which have

eigenvalue $k_G(h) = 1$ and normalized as $w_h v_h = 1$. Finally, we can rewrite (2.59) into the form

$$\begin{aligned} \delta G(\tau) &= -\sum_{h=h_*} \alpha_h v_h \frac{G^c(\tau)}{|J\tau|^{h-1}}\,, \\ \alpha_h &= -\frac{w_h W_\Sigma(h)\vec{\sigma}_h}{k'_G(h)}\,. \end{aligned} \tag{2.61}$$

We remark that the values of $\vec{\sigma}_h$ and thus α_h are not accessible in the IR because a physical UV source such as $\sigma(\tau) = (\partial_\tau - \mu)\delta(\tau)$ is highly singular and the task of decomposing it into asymptotic power-laws perhaps is equivalent to solving the full Schwinger-Dyson equations. Below in the Section 2.7 we present numerical results for α_h of the first few resonances in the bosonic and fermionic SYK$_4$ models. The UV parameters α_h depend on the asymmetry angle θ and q [†]. Below we present explicit formulas for the eigenvalues and eigenvectors of the matrix $K_G(h)$:

$$\begin{aligned} k_{\mathrm{A/S}}(h,\theta) &= \frac{\Gamma(2\Delta-h)\Gamma(2\Delta+h-1)}{\Gamma(2\Delta+1)\Gamma(2\Delta-1)}\left(2\Delta - 1 + \frac{\cos(2\theta)\sin(\pi h)}{\sin(2\pi\Delta)} \mp \sqrt{P}\right), \\ v_h^{\mathrm{A/S}}(\theta) &= \frac{1}{1+(2\Delta-1)\frac{\sin(\pi h)}{\sin(2\pi\Delta)}}\begin{pmatrix} \frac{\sin(2\theta)}{\sin(2\pi\Delta)}(2\Delta-1-\cos(\pi h)) \pm \sqrt{P} \\ 1 + \frac{\sin(2\theta)}{\sin(2\pi\Delta)} + (2\Delta-1)\frac{\sin(\pi h - 2\theta)}{\sin(2\pi\Delta)} \end{pmatrix}, \end{aligned} \tag{2.62}$$

where

$$P = \sin(2\theta)^2\left(1 - \frac{\sin(\pi h)^2}{\sin(2\pi\Delta)^2}\right) + \left(\cos(2\theta) + (2\Delta-1)\frac{\sin(\pi h)}{\sin(2\pi\Delta)}\right)^2. \tag{2.63}$$

Also $w_h^{\mathrm{A/S}}(\theta)$ can be expressed through $v_h^{\mathrm{S/A}}(\theta)$ as $w_h^{\mathrm{A/S}}(\theta) = v_h^{\mathrm{S/A}}(-\theta)^{\mathrm{T}}\sigma_z / (v_h^{\mathrm{S/A}}(-\theta)^{\mathrm{T}}\sigma_z v_h^{\mathrm{A/S}}(\theta))$, where σ_z is the third Pauli matrix and one can check that $w_h^{\mathrm{A/S}} v_h^{\mathrm{S/A}} = 0$. We notice that for $\theta = 0$ the eigenvalues $k_{\mathrm{A/S}}(h)$ in (2.62) coincide with definition (2.26). Though for non-zero asymmetry angle θ there is no symmetry under $\tau \to -\tau$ we still label eigenvalues and eigenvectors with A/S indices. We

[†] We notice that α_0 for $h_0 = 2$ resonance in the Majorana SYK model was computed numerically in Ref. [121] and denoted there as α_G. Moreover α_G was defined with respect to $\mathcal{J} = 2^{(1-q)/2}\sqrt{q}J$ and therefore for $q = 4$ we have $\alpha_0 = \sqrt{2}\alpha_G$

denote by $h^{A/S}$ solutions of the equations $k_{A/S}(h,\theta)=1$ and numerate them as $h_0^{A/S}, h_1^{A/S}, h_2^{A/S}, \dots$. For these solutions we denote α_h as $\alpha_0^{A/S}, \alpha_1^{A/S}, \dots$ and similarly $v_0^{A/S}, v_1^{A/S}, \dots$. In Fig.2.3 we plot $h^{A/S}$ and corresponding $k'_{A/S}(h^{A/S})$ for the fermionic and bosonic SYK$_4$ models as functions of the asymmetry angles θ_f and $\theta_\mathfrak{b}$. We remark that in the fermionic model for $\theta_f = \pi/6$ some solutions of the equation $k_S(h) = 1$ (red lines) go into solutions of $k_A(h) = 1$ (blue lines), nevertheless we still denote the dimension of the whole line by h^A. In bosonic case this happens for $\theta_\mathfrak{b} = \pi/3$. The resonances $h_0^A = 2$ and $h_0^S = 1$ are related to reparametrization and $U(1)$ symmetries respectively and don't depend on the asymmetry angles θ_f or $\theta_\mathfrak{b}$. According to the eq. (2.61) the mode $h_0^S = 1$ gives a constant correction to the Green's function and represents a response of the asymmetry parameter $\mathcal{E}$ (or θ) to a change of the chemical potential μ. Therefore in the conformal two-point function (2.44) this mode is already taken into account. Moreover it was shown in[78] that the $h_0^S = 1$ resonance leads to the Luttinger relations:

$$
\begin{aligned}
Q &\equiv \frac{1}{2} - \frac{1}{NM}\sum_{i\alpha}\langle f^\dagger_{i\alpha} f_{i\alpha}\rangle = \frac{\theta_f}{\pi} + \Big(\frac{1}{2}-\Delta\Big)\frac{\sin\big(2\theta_f\big)}{\sin(2\pi\Delta)}\,,\\
S &\equiv \frac{1}{NM}\sum_{i\alpha}\langle \mathfrak{b}^\dagger_{i\alpha}\mathfrak{b}_{i\alpha}\rangle = \frac{\theta_\mathfrak{b}}{\pi} + \Big(\frac{1}{2}-\Delta\Big)\frac{\sin(2\theta_\mathfrak{b})}{\sin(2\pi\Delta)} - \frac{1}{2}\,.
\end{aligned}
\tag{2.64}
$$

We notice an interesting behaviour of the operator h_1^A in the bosonic SYK model. For $\theta_\mathfrak{b} > 0.284\pi$ (exact value $\theta_{\mathfrak{b}1} = \frac{1}{2}\cos^{-1}(\frac{-2}{3\pi})$) the resonance h_1^A is less than $h_0^A = 2$ mode and becomes the leading contribution to the Green's function. At $\theta_\mathfrak{b} = \pi/3$ we have $h_1^A = 3/2$ and for $\theta_\mathfrak{b} = 0.360\pi$ (exact value $\theta_{\mathfrak{b}2} = \frac{1}{2}\cos^{-1}(\frac{-2}{\pi})$) we find that $h_1^A = 1$ and therefore we should expect violation of the Luttinger relations (2.64). We indeed confirm this numerically below in the Section 2.7. For $\theta_\mathfrak{b} > 0.360\pi$ the resonance h_1^A becomes less than one and therefore gives divergent contribution to the Green's function for large τ. In terms of the discussion of the Section 2.3 this means that the operator $O_{h_1^A}$ becomes relevant and thus it violates basis of the analysis of the Sections 2.3 and 2.4. Interestingly

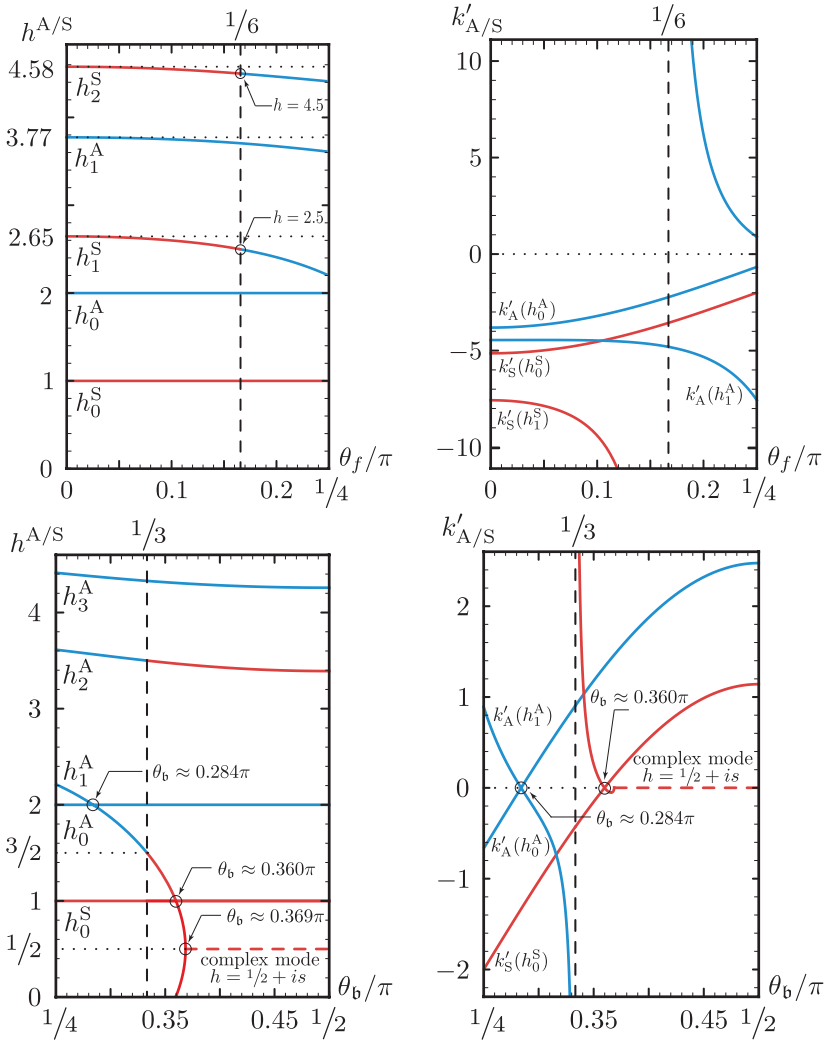

Figure 2.3: Plots of the resonance values $h^{A/S}$ and corresponding $k'_{A/S}(h^{A/S})$ for the fermionic and bosonic $q = 4$ SYK models as functions of the asymmetry angles θ_f and θ_b. $h^{A/S}$ are solutions of the equations $k_{A/S}(h, \theta) = 1$, where $k_{A/S}$ are defined in (2.62). The red and blue lines are solutions of the equation $k_S(h) = 1$ and $k_A(h) = 1$ respectively.

for $\theta_{\mathfrak{b}} > 0.360\pi$ we see that another operator of dimension $1 - h_1^{\mathrm{A}}$ appears and both operators merge at $\theta_{\mathfrak{b}} = 0.369\pi$ (exact value $\theta_{\mathfrak{b}3} = \frac{1}{2}\cos^{-1}(\frac{1}{2} - \frac{3}{8\pi})$) and $h = 1/2$ and go to the complex plane. This is a well-known scenario, discussed in [94,65,68]. In the context of the SYK-like models it was also found in [64].

We chose normalization of $v_h^{\mathrm{A/S}}$ in (2.62) such that at $\theta = 0$ it is $v_h^{\mathrm{A/S}} = (\pm 1, 1)^{\mathrm{T}}$ and $w_h^{\mathrm{A/S}} = \frac{1}{2}(\pm 1, 1)$ for arbitrary h and thus the value of α_0 for $h_0^{\mathrm{A}} = 2$ mode is in agreement with the previous works [121,104].

We remark that for the fermionic SYK model at zero chemical potential $\mu = 0$ ($\theta_f = 0$) we have

$$\alpha_h^{\mathrm{S}} = \frac{\sigma_{h+}^{\mathrm{S}} - \sigma_{h-}^{\mathrm{S}}}{k_{\mathrm{S}}'(h)} = 0\,, \tag{2.65}$$

where we used that the source $\sigma(\tau)$ has to be antisymmetric under $\tau \to -\tau$ due to the particle-hole symmetry. Thus in this case only h^{A} operators contribute to the two-point function.

2.4.2 Nonlinear order corrections

In this section we present the generalization of the above resonance formalism to linear in α_h order. In the CFT interpretation, we are computing corrections to Green's functions due to double insertion of irrelevant operators, for example $\iint \mathrm{d}\tau_3 \mathrm{d}\tau_4 \langle f(\tau_1) f^\dagger(\tau_2) O_h(\tau_3) O_{h'}(\tau_4)\rangle$, which is expected to be proportional to $1/|\tau_{12}|^{2\Delta+h+h'-2}$. In terms of the Schwinger-Dyson equation, this corresponds to double insertion of the UV source σ. We will develop a recursive procedure that enables computation of correction up to arbitrary order.

For simplicity, we will restrict to zero temperature and comment on finite temperature later. Our

strategy is to treat (2.39) as a perturbation problem and expand G, Σ to n-th order in σ:

$$\begin{aligned} G &= G^c + \delta G + \delta^2 G + \cdots + \delta^n G\,, \\ \Sigma &= \Sigma^c + \delta\Sigma + \delta^2\Sigma + \cdots + \delta^n\Sigma\,. \end{aligned} \tag{2.66}$$

Expand (2.39) accordingly and match order by order, we have

$$\delta^k G = \delta^k G_*[\Sigma]\,, \quad \delta^k\Sigma = \delta^k\Sigma_*[G], \quad k \geq 2. \tag{2.67}$$

We can calculate $\delta^k G$ and $\delta^k\Sigma$ order by order recursively. To do so we rewrite the above equation as

$$\delta^k G = W_\Sigma \delta^k\Sigma + \bar{\delta}^k G_*[\Sigma]\,, \quad \delta^k\Sigma = W_G \delta^k G + \bar{\delta}^k\Sigma_*[G]\,, \tag{2.68}$$

where we have explicitly separated out the pieces depending on $\delta^k G$ and $\delta^k\Sigma$, which are all linear. The rest are written as $\bar{\delta}^k G_*$ and $\bar{\delta}^k\Sigma_*$, and they depend nonlinearly on the corrections of order 1 through $k-1$. We can readily write down the solution for $\delta^k G$, $\delta^k\Sigma$:

$$\delta^k G = \frac{1}{1 - W_\Sigma W_G}\left[W_\Sigma \bar{\delta}^k\Sigma_*[G] + \bar{\delta}^k G_*[\Sigma]\right], \tag{2.69}$$

$$\delta^k\Sigma = \frac{1}{1 - W_G W_\Sigma}\left[W_G \bar{\delta}^k G_*[\Sigma] + \bar{\delta}^k\Sigma_*[G]\right]. \tag{2.70}$$

The starting point of the recursion is the $\delta G,\ \delta\Sigma$ computed from linear resonance theory. Because all $\delta^k G$ and $\delta^k\Sigma$ are powerlaws in both time and frequency domain, the expansion of $\bar{\delta}^k G_*,\ \bar{\delta}^k\Sigma_*$ and the action of $W_\Sigma,\ W_G$ can be carried out analytically and automated on a computer. At finite temperature, the recursion is harder to implement because $\delta^k G$ and $\delta^k\Sigma$ are usually hypergeometric functions whose complexity increases with k.

As an example, we find the second order correction for the bosonic and fermionic SYK$_q$ model.

The Schwinger-Dyson equations (2.39) take the form

$$G_*[\Sigma](i\omega) = \frac{-1}{\Sigma(i\omega)}, \qquad \Sigma_*[G](\tau) = (-)^{\varepsilon_a} J^2 G(\tau)^{q/2} G(-\tau)^{q/2-1}. \tag{2.71}$$

In the subsection (2.4.1) we derive the linear order response for the resonance h

$$\delta_h G(\tau) = -\alpha_h v_h \frac{G^c(\tau)}{|J\tau|^{h-1}}\,, \tag{2.72}$$

where $v_h = (v_{h+}, v_{h-})$ is the right eigenvector of the matrix $K_G(h) = W_\Sigma(h) W_G$ with the eigenvalue $k_G(h) = 1$, so $K_G(h) v_h = v_h$. Using (2.71) we can calculate

$$\bar{\delta}^2 G_* = -\sum_{h,h'} \frac{\delta_h \Sigma(i\omega)\delta_{h'}\Sigma(i\omega)}{\Sigma^c(i\omega)^3} = \sum_{h,h'} \frac{\delta_h G(i\omega)\delta_{h'} G(i\omega)}{G^c(i\omega)}\,, \tag{2.73}$$

where we used that $G^c(i\omega)\Sigma^c(i\omega) = -1$ and $\delta_h G(i\omega) = G^c(i\omega)^2 \delta_h \Sigma(i\omega)$ and the sum over h and h' goes over all resonances. Using (2.51) we find for the linear order response in the Fourier space

$$\delta_h G(i\omega) = -\alpha_h F(h) v_h |\omega/J|^{h-1} G^c(i\omega)\,, \tag{2.74}$$

where the matrix $F(h)$ is given in (2.52) and acts on the vector v_h. Therefore we find

$$\frac{\delta_h G(i\omega)\delta_{h'} G(i\omega)}{G^c(i\omega)} = \alpha_h \alpha_{h'} \big(F(h) v_h \cdot F(h') v_{h'}\big) |\omega/J|^{h+h'-2} G^c(i\omega)\,, \tag{2.75}$$

where we introduced a special notation $v_h \cdot v_{h'} \equiv (v_{h+} v_{h'+}, v_{h-} v_{h'-})$. Finally we go back to the coordinate space and obtain for the second variation of $\bar{\delta}^2 G_*$:

$$\frac{\bar{\delta}^2 G_*(\tau)}{G^c(\tau)} = \sum_{h,h'} F(h+h'-1)^{-1} \big(F(h) v_h \cdot F(h') v_{h'}\big) \frac{\alpha_h \alpha_{h'}}{|J\tau|^{h+h'-2}}\,. \tag{2.76}$$

The second variation of $\Sigma_*[G_c]$ reads

$$\frac{\bar{\delta}^2\Sigma_*(\tau)}{\Sigma^c(\tau)} = \frac{q-2}{8}\Big(q\frac{\delta_h G(\tau)\delta_{h'}G(\tau)}{G^c(\tau)G^c(\tau)} + (q-4)\frac{\delta_h G(-\tau)\delta_{h'}G(-\tau)}{G^c(-\tau)G^c(-\tau)} + q\frac{\delta_h G(\tau)\delta_{h'}G(-\tau)}{G^c(\tau)G^c(-\tau)} + q\frac{\delta_h G(-\tau)\delta_{h'}G(\tau)}{G^c(-\tau)G^c(\tau)}\Big) \tag{2.77}$$

and using our vector notations for $v_h = (v_{h+}, v_{h-})$ and $\bar{v}_h = (v_{h-}, v_{h+})$ we obtain

$$\frac{\bar{\delta}^2\Sigma_*(\tau)}{\Sigma^c(\tau)} = \sum_{h,h'}\frac{1}{8}(q-2)\big(q(v_h+\bar{v}_h)\cdot(v_{h'}+\bar{v}_{h'}) - 4\bar{v}_h\cdot\bar{v}_{h'}\big)\frac{\alpha_h\alpha_{h'}}{|J\tau|^{h+h'-2}}\,. \tag{2.78}$$

Therefore the full second correction to $G(\tau)$ reads

$$\frac{\delta^2 G(\tau)}{G^c(\tau)} = -\frac{a_{hh'}\alpha_h\alpha_{h'}}{|J\tau|^{h+h'-2}}\,, \tag{2.79}$$

where the two component vector $a_{hh'}$ is given by the formula

$$a_{hh'} = -\big(1 - W_\Sigma(h+h'-1)W_G\big)^{-1}\Big(F(h+h'-1)^{-1}\big(F(h)v_h\cdot F(h')v_{h'}\big) + \frac{1}{8}(q-2)W_\Sigma(h+h'-1)\big(q(v_h+\bar{v}_h)\cdot(v_{h'}+\bar{v}_{h'}) - 4\bar{v}_h\cdot\bar{v}_{h'}\big)\Big)\,. \tag{2.80}$$

The general formula for the two point function can be written as

$$G(\tau) = G^c(\tau)\Big(1 - \sum_h\frac{\alpha_h v_h}{|J\tau|^{h-1}} - \sum_{h,h'}\frac{a_{hh'}\alpha_h\alpha_{h'}}{|J\tau|^{h+h'-2}} - \sum_{h,h',h''}\frac{a_{hh'h''}\alpha_h\alpha_{h'}\alpha_{h''}}{|J\tau|^{h+h'+h''-3}} - \dots\Big)\,, \tag{2.81}$$

where v_h, $a_{hh'}$, $a_{hh'h''}$, etc are two-component vectors. For example for $h_0^{\mathrm{A}} = 2$ mode and $q = 4$ case

we find

$$v_0^{\mathrm{A}} = \begin{pmatrix} 1 - \frac{3}{2}\sin(2\theta) \\ 1 + \frac{3}{2}\sin(2\theta) \end{pmatrix}, \quad a_{00}^{\mathrm{A}} = \begin{pmatrix} \frac{3}{16}(17\cos(4\theta) - 5 + 24\sin(2\theta)) \\ \frac{3}{16}(17\cos(4\theta) - 5 - 24\sin(2\theta)) \end{pmatrix}. \tag{2.82}$$

For the fermionic SYK$_q$ model at zero chemical potential we have $\theta = 0$ and we omit all upper subscripts A for brevity, since as we explained in (2.65) modes h^{S} don't contribute to the two-point function in this case. Then $v_b = (1,1)^{\mathrm{T}}$ and also $a_{bb'} \propto (1,1)^{\mathrm{T}}$, $a_{bb'b''} \propto (1,1)^{\mathrm{T}}$ etc, and we can omit vector notations so the coefficients $a_{bb'}$, $a_{bb'b''}$, etc become just real numbers and thus the leading terms for the two-point function can be written as

$$G(\tau) = G^c(\tau)\left(1 - \frac{\alpha_0}{|J\tau|} - \frac{\alpha_1}{|J\tau|^{b_1-1}} - \frac{a_{00}\alpha_0^2}{|J\tau|^2} - \frac{2a_{01}\alpha_0\alpha_1}{|J\tau|^{b_1}} - \frac{a_{11}\alpha_1^2}{|J\tau|^{2b_1-2}} - \frac{a_{000}\alpha_0^3}{|J\tau|^3} + \dots\right), \tag{2.83}$$

where $b_0 = 2$ and $b_1 \simeq 3.77$. Using (2.80) for $v_b = (1,1)$ and $\theta = 0$ we find explicitly

$$a_{00} = \frac{(2\Delta+1)(2-2\Delta-\cos(2\pi\Delta))}{8\Delta\cos^2(\pi\Delta)}. \tag{2.84}$$

In general it is possible to obtain corrections up to an arbitrary order. As an example for the cubic order in α_0 the result takes the form for $\theta = 0$

$$a_{000} = \frac{(\Delta+1)(2\Delta+1)(6\Delta-8+\cos(2\pi\Delta))}{24\Delta^2\cos^2(\pi\Delta)}. \tag{2.85}$$

We checked that the results for $a_{bb'}$ and a_{000} in (2.80) and (2.85) for $\theta = 0$ exactly match with the large q and $q \to 2$ expansions discussed in Appendices A.2 and A.3.

2.4.3 Finite Temperature Generalization

The results described above are only applicable at zero temperature. To generalize to finite temperature, we use the $U(1)$ and time-reparameterization symmetry of the conformal saddle point equations. In presence of the symmetry, $G,\ \Sigma, W_G,\ W_\Sigma$ are all covariant under time-reparameterization and $U(1)$. Therefore, the coefficients α_b should be temperature independent, and all we need is the finite temperature form of the scaling function $\mathcal{F}_b$.

As we already discussed in the Section 2.3 in general for the complex fermions with the particle-hole symmetry the three-point function has two independent structures [108,99]

$$\left\langle f(\tau_1) f^\dagger(\tau_2) O_b(\tau_0) \right\rangle = \frac{b^\Delta \left(c_b^{\mathrm{A}} \operatorname{sgn}(\tau_{12}) + c_b^{S} \operatorname{sgn}(\tau_{10}) \operatorname{sgn}(\tau_{20}) \right)}{|\frac{\beta J}{\pi} \sin \frac{\pi \tau_{12}}{\beta}|^{2\Delta - b} |\frac{\beta J}{\pi} \sin \frac{\pi \tau_{10}}{\beta}|^{b} |\frac{\beta J}{\pi} \sin \frac{\pi \tau_{20}}{\beta}|^{b}}\,, \tag{2.86}$$

where c_b^{A} and c_b^{S} are independent structure constants and the sign function is antiperiodic on the thermal circle $\operatorname{sgn}(\tau + \beta) = -\operatorname{sgn}(\tau)$. This form is consistent with higher-dimensional CFT results for fermions (see for example [137,89]) and gives correct statistics for the fermionic and bosonic fields, when one of the field is moved over the full thermal circle. For non-zero chemical potential this result was generalized in [81] and takes the form

$$\left\langle f(\tau_1) f^\dagger(\tau_2) O_b(\tau_0) \right\rangle = -G_f^c(\tau_{12}) \frac{c_b^{\mathrm{A}} + c_b^{S} \operatorname{sgn}(\tau_{12}) \operatorname{sgn}(\tau_{10}) \operatorname{sgn}(\tau_{20})}{|\sin \frac{\pi \tau_{12}}{\beta}|^{-b} |\frac{\beta J}{\pi} \sin \frac{\pi \tau_{10}}{\beta} \sin \frac{\pi \tau_{20}}{\beta}|^{b}}\,, \tag{2.87}$$

where we used conformal Green's functions $G_f^c(\tau)$ to write the three-point function compactly. For the bosonic case we have to replace $G_f^c(\tau)$ by $G_{\mathfrak{b}}^c(\tau)$. For a domain $\tau \in [-\beta, \beta]$ the formulas for the conformal two-point functions are

$$G_f(\tau) = -e^{\pi \mathcal{E}_f \operatorname{sgn}(\tau)} \frac{b_f^\Delta \operatorname{sgn}(\tau)}{|\frac{\beta J}{\pi} \sin \frac{\pi \tau}{\beta}|^{2\Delta}} e^{-\frac{2\pi \mathcal{E}_f}{\beta} \tau}, \quad G_{\mathfrak{b}}(\tau) = -e^{\pi \mathcal{E}_{\mathfrak{b}} \operatorname{sgn}(\tau)} \frac{b_{\mathfrak{b}}^\Delta}{|\frac{\beta J}{\pi} \sin \frac{\pi \tau}{\beta}|^{2\Delta}} e^{-\frac{2\pi \mathcal{E}_{\mathfrak{b}}}{\beta} \tau}. \tag{2.88}$$

Appearance of the factors $\exp\left(-\frac{2\pi\mathcal{E}}{\beta}\tau\right)$ in the three-point functions can be derived by applying $U(1)$ transformation on f and $f^\dagger$, assuming O_b is neutral under $U(1)$. One can check that the expression (2.87) agrees with (2.31) upon taking $\beta \to \infty$ limit and setting $\mathcal{E}_f = c_b^{\mathrm{S}} = 0$. We also remark that the three-point functions (2.87) represent a basis for the kernel K_G. This A/S basis is related to previously used plus/minus basis by some transformation matix.

Analogously to the discussion in the Section 2.3 the linear correction to the two-point function can be computed as

$$\delta_b G(\tau_{12}) = g_b \int_0^\beta d\tau_0 \left\langle f(\tau_1) f^\dagger(\tau_2) O_b(\tau_0) \right\rangle , \tag{2.89}$$

where we recall that $g_b \propto J$ is dimensionful coupling. The correction is split on two parts $\delta_b G(\tau) = \delta_b G_{\mathrm{A}}(\tau) + \mathrm{sgn}(\tau)\delta_b G_{\mathrm{S}}(\tau)$ and to match our result (2.61) for zero-temperature we have

$$\frac{\delta_b G_{\mathrm{A}}(\tau)}{G^c(\tau)} = -\frac{1}{2}(v_{b+} + v_{b-})\frac{\alpha_b}{(\beta J)^{b-1}} f_b^{\mathrm{A}}(\tau), \quad \frac{\delta_b G_{\mathrm{S}}(\tau)}{G^c(\tau)} = -\frac{1}{2}(v_{b+} - v_{b-})\frac{\alpha_b}{(\beta J)^{b-1}} f_b^{\mathrm{S}}(\tau) , \tag{2.90}$$

where

$$f_b^{\mathrm{A}}(\tau_{12}) \propto \int_0^\beta d\tau_0 \frac{|\sin\frac{\pi\tau_{12}}{\beta}|^b}{|\sin\frac{\pi\tau_{10}}{\beta}\sin\frac{\pi\tau_{20}}{\beta}|^b}, \quad f_b^{\mathrm{S}}(\tau_{12}) \propto \int_0^\beta d\tau_0 \frac{|\sin\frac{\pi\tau_{12}}{\beta}|^b \mathrm{sgn}(\tau_{10})\mathrm{sgn}(\tau_{20})}{|\sin\frac{\pi\tau_{10}}{\beta}\sin\frac{\pi\tau_{20}}{\beta}|^b} . \tag{2.91}$$

The function $\mathcal{F}_b(\tau/\beta)$ defined in (2.38) reads

$$\mathcal{F}_b(\tau/\beta) = \frac{1}{2}(v_{b+} + v_{b-}) f_b^{\mathrm{A}}(\tau) + \frac{1}{2}(v_{b+} - v_{b-}) f_b^{\mathrm{S}}(\tau)\mathrm{sgn}(\tau) . \tag{2.92}$$

Using results from [104,81] for the integrals in (2.91) and fixing proportionality constants such that

$f_h^{A/S}(\tau) \to (\beta/|\tau|)^{h-1}$ in the limit $\beta \to \infty$ we obtain

$$f_h^{A}(\tau) = \frac{(2\pi)^{h-1}\Gamma(h)^2}{2\sin\frac{\pi h}{2}\Gamma(2h-1)}\left(A_h(e^{i\frac{2\pi\tau}{\beta}}) + A_h(e^{-i\frac{2\pi\tau}{\beta}})\right), \tag{2.93}$$

$$f_h^{S}(\tau) = \frac{(2\pi)^{h-1}\Gamma(h)^2}{2\cos\frac{\pi h}{2}\Gamma(2h-1)}\left(iA_h(e^{i\frac{2\pi\tau}{\beta}}) - iA_h(e^{-i\frac{2\pi\tau}{\beta}})\right), \tag{2.94}$$

where $A_h(u) = (1-u)^h \mathbf{F}(h,h,1;u)$ and $\mathbf{F}$ is the regularized hypergeometric function. Our definition of A_h coincides with $A^{\pm}_{h,0}$ defined in [104] and [103], and we have dropped the $\pm$ notation because the two definitions in the references agree for our choice of parameter. Inside the unit circle $|u| \leq 1$ we can compute $A_h(u)$ using series expansion. We list results for $h_0^A = 2$ mode

$$f_0^{A}(\tau) = 2 + \frac{\pi - \frac{2\pi|\tau|}{\beta}}{\tan\frac{\pi|\tau|}{\beta}}, \quad f_0^{S}(\tau) = \frac{\pi}{\tan\frac{\pi|\tau|}{\beta}}. \tag{2.95}$$

One has to be careful computing $f_0^A(\tau)$ function since the prefactor in (2.93) diverges and we need to expand $A_h(u)$ to the next order in h, so for $h \to 2$ we have $A_h(u) = (1+u)/(1-u) - (h-2)((1+u)\log(1-u) - 2u)/(1-u) + \ldots$.

The above procedure is relatively simple for linear in α_h order. For nonlinear order the computation involves complicated products of hypergeometric functions and we leave it for future investigation.

2.5 Spectral densities

To numerically study the models discussed above, it is convenient to work with spectral density $\rho(\omega)$ instead of the Green's function. For the fermionic and bosonic SYK models we define it as follows

$$G(i\omega_n) = \int_{-\infty}^{+\infty} d\omega \frac{\rho(\omega)}{i\omega_n - \omega}. \tag{2.96}$$

This definition implies that $\int_{-\infty}^{+\infty} d\omega \rho(\omega) = 1$ and the spectral density can be found as

$$\rho(\omega) = -\frac{1}{\pi}\mathrm{Im}G_R(\omega)\,, \tag{2.97}$$

where $G_R(\omega)$ is the retarded Green's function. It is related to Matsubara function $G(i\omega_n)$ by analytic continuation from the upper-half complex ω plane, namely we have $G_R(\omega) = G(i\omega_n = \omega + i0)$, where $\omega_n \geq 0$. Using (2.53) we find for the conformal G_R^c and ρ^c, written in the plus/minus basis:

$$G_R^c(\omega) = \frac{C}{J}\begin{pmatrix} e^{-i\pi\Delta - i\theta} \\ -e^{i\pi\Delta - i\theta}\end{pmatrix}|\omega/J|^{2\Delta-1}, \quad \rho^c(\omega) = \frac{C}{\pi J}\begin{pmatrix} \sin(\pi\Delta+\theta) \\ \sin(\pi\Delta-\theta)\end{pmatrix}|\omega/J|^{2\Delta-1}\,. \tag{2.98}$$

Next using the Fourier transform (2.74) for the eq. (2.81) and making analytical continuation to the real frequencies we find the general formula for the retarded Green's function. Then using formula (2.97) we obtain the following expansion of the spectral density at low frequencies

$$\rho(\omega) = \rho^c(\omega)\left(1 - \sum_h \frac{\Gamma(2\Delta)\alpha_h v_h |\omega/J|^{h-1}}{\Gamma(2\Delta+h-1)} - \sum_{h,h'} \frac{\Gamma(2\Delta)\alpha_h\alpha_{h'}a_{hh'}|\omega/J|^{h+h'-2}}{\Gamma(2\Delta+h+h'-2)} - \dots\right)\,. \tag{2.99}$$

At the end of this section we derive an expression for the spin spectral density. The spin-spin correlator in imaginarty time is $Q(\tau) = -\langle \mathrm{T}_\tau(S(\tau)S(0))\rangle$ and using that $S = f^\dagger f$ or $S = \mathfrak{b}^\dagger\mathfrak{b}$ in the large M limit we find

$$Q(\tau) = -\zeta G(\tau)G(-\tau)\,. \tag{2.100}$$

Expressing Green's function $G(\tau)$ through the spectral density and using a similar formula for $Q(\tau)$

we find expression for the spin spectral density

$$\rho_Q(\omega) = \int_{-\infty}^{\infty} d\nu \rho(\nu)\rho(\nu-\omega)(n(\nu-\omega)-n(\nu))\,, \tag{2.101}$$

where $n(\omega) = 1/(e^{\beta\omega} - \zeta)$ is the Fermi or Bose distribution. At zero temperature we have $n(\omega) = -\zeta\theta(-\omega)$ and we obtain

$$\rho_Q(\omega) = -\zeta \int_0^{\omega} d\nu \rho(\nu)\rho(\nu-\omega)\,, \tag{2.102}$$

where it is valid for both positive and negative frequencies ω. Using (2.98) and (2.99) we find

$$\begin{aligned}\rho_Q(\omega) =& \rho_Q^c(\omega)\Bigg(1 - \sum_h \frac{\Gamma(4\Delta)\alpha_h(v_{h+}+v_{h-})|\omega/J|^{h-1}}{\Gamma(4\Delta+h-1)} \\ &- \sum_{h,h'} \frac{\Gamma(4\Delta)\alpha_h\alpha_{h'}(a_{hh'+}+a_{hh'-}-v_{h+}v_{h'-})|\omega/J|^{h+h'-2}}{\Gamma(4\Delta+h+h'-2)} - \dots\Bigg)\,,\end{aligned} \tag{2.103}$$

and the conformal spin spectral density is

$$\rho_Q^c(\omega) = \mathrm{sgn}(\omega)\frac{b^{2\Delta}}{J\Gamma(4\Delta)}|\omega/J|^{4\Delta-1}\,. \tag{2.104}$$

For comparison to numerical results, we can find for $q = 4$ fermionic SYK at $\theta_f = 0$ that the first few terms in ρ_{Q_f} for $\omega > 0$ are

$$\rho_{Q_f}(\omega) = \rho_{Q_f}^c(\omega)\left(1 - 2\alpha_0^A\left(\frac{\omega}{J}\right) - \frac{7}{4}(\alpha_0^A)^2\left(\frac{\omega}{J}\right)^2 - 0.44\alpha_1^A\left(\frac{\omega}{J}\right)^{2.77} + \frac{37}{6}(\alpha_0^A)^3\left(\frac{\omega}{J}\right)^3 + \dots\right), \tag{2.105}$$

where we used values of a_{00} and a_{000} from (2.84) and (2.85) and $h_1^{\mathrm{A}} \simeq 3.77$.

We generalize results for the spectral densities at finite temperature in the Appendix A.4. Here we only present finite temperature generalization of the eq. (2.103) for $\Delta = 1/4$, where only $h_0^{\mathrm{A}} = 2$

mode is retained

$$\rho_Q(\omega) = \frac{b^{1/2}}{J} \tanh\left(\frac{\beta\omega}{2}\right) \left(1 - \frac{2\alpha_0^{\mathrm{A}}\omega}{J} \tanh\left(\frac{\beta\omega}{2}\right) - \dots\right) , \tag{2.106}$$

and we used that $v_{0+} + v_{0-} = 2$. The coefficient of the correction term $2\alpha_0^{\mathrm{A}}/J$ can be related to the coefficient γ in specific heat $C = \gamma T$ by the Schwarzian action argument in [81], with the result

$$\mathcal{C}_f = \frac{2\alpha_0^{\mathrm{A}}/J}{\gamma} = \frac{24}{\pi\left[2\cos 2\theta_f + 3\pi\cos^2 2\theta_f\right]} . \tag{2.107}$$

For bosonic spinon theory, there is an extra sign because bosonic action differs from the fermionic version by a minus sign:

$$\mathcal{C}_{\mathfrak{b}} = \frac{2\alpha_0^{\mathrm{A}}/J}{\gamma} = -\frac{24}{\pi\left[2\cos 2\theta_{\mathfrak{b}} + 3\pi\cos^2 2\theta_{\mathfrak{b}}\right]} . \tag{2.108}$$

2.6 Random Quantum Rotor model

In this section we consider random quantum q-rotor model (or also known as quantum spherical q-spin model), where q is a positive integer number. The Hamiltonian of this model has the form

$$H = \sum_{i=1}^{N} \frac{\pi_i^2}{2M} + \sum_{i_1,\dots,i_q}^{N} J_{i_1\dots i_q}\varphi_{i_1}\cdots\varphi_{i_q} , \tag{2.109}$$

where M is the mass, π_i is the conjugate momentum to a real scalar spin variable φ_i so $[\varphi_i, \pi_j] = i\delta_{ij}$ and there is the spherical constraint $1/N\sum_{i=1}^{N}\langle\varphi_i^2\rangle = 1$. The couplings $J_{i_1\dots i_q}$ are independent Gaussian variables with zero mean and variance

$$\overline{J_{i_1\dots i_q}^2} = \frac{\tilde{J}^2}{qN^{q-1}} . \tag{2.110}$$

This model was first studied in [37,38] and similar models were considered in [135,66,176,57,124]. We define imaginary time Green's function at finite temperature

$$G(\tau) = \frac{1}{N}\sum_{i=1}^{N}\langle \mathrm{T}_\tau(\varphi_i(\tau)\varphi_i(0))\rangle\,. \tag{2.111}$$

Introducing replicas and averaging over disorder it is possible to derive Schwinger-Dyson equations for the function $G(\tau)$ in the large N limit

$$G(i\omega_n) = \frac{1}{\omega_n^2 + \lambda - \Sigma(i\omega_n)}, \quad \Sigma(\tau) = J^2 G(\tau)^{q-1}\,, \tag{2.112}$$

where $\omega_n = 2\pi n/\beta$ are Matsubara frequencies and λ is the Lagrange multiplier imposing the spherical constraint, also we assumed replica symmetric solution and made rescaling $\varphi \to \varphi/\sqrt{M}$, so the spherical constraint takes the form $G(\tau = 0) = M$ and also $J = \tilde{J}/M^{q/2}$. Similarly to the SYK models the equations (2.112) admit conformal solution in the IR region for a given J upon tuning M and thus λ to a critical value. The conformal solution reads

$$G^c(\tau) = \frac{b^\Delta}{|(\beta J/\pi)\sin(\pi\tau/\beta)|^{2\Delta}}\,, \tag{2.113}$$

where $\Delta = 1/q$ and dimensionless constant b coincides with $b_\mathfrak{b}$ in (2.20) computed for $\theta_\mathfrak{b} = \pi/2$. The analysis from the Section 2.4 can be applied to the random rotor model. The only difference is that the source term now is $\sigma(\tau) = \partial_\tau^2$. The correction to the conformal Green's function comes from $h^{\mathrm{A}}(\theta)$ modes computed at $\theta_\mathfrak{b} = \pi/2$. For $q = 4$ these modes are represented by blue lines in Fig. 2.3 and for $\theta_\mathfrak{b} = \pi/2$ we find $h_0^{\mathrm{A}} = 2$, $h_1^{\mathrm{A}} \simeq 4.26$, $h_2^{\mathrm{A}} \simeq 6.34$, etc. Symmetric modes h^{S} don't contribute to the two-point function due to the exact particle-hole symmetry (see discussion around eq. (2.65)). We notice that for $\theta_\mathfrak{b} = \pi/2$ there is a complex mode in the symmetric sector[66]. Though the complex mode formally does not affect the large N two-point function it presumably

makes the replica diagonal solution unstable and leads to replica symmetry breaking [‡]. We also remark that appearance of the complex modes in some non-Fermi liquid theories was noticed in [1]. In any case it is interesting to study conformal solution of the Schwinger-Dyson equations (2.112). The leading analytical corrections to the Green's function at zero temperature read

$$G(\tau) = G^c(\tau)\left(1 - \frac{\alpha_0}{|J\tau|} - \frac{a_{00}\alpha_0^2}{|J\tau|^2} - \frac{a_{000}\alpha_0^3}{|J\tau|^3} - \frac{\alpha_1}{|J\tau|^{h_1-1}} - \dots\right), \tag{2.114}$$

where we omitted subscripts A for brevity and for $q = 4$ we find $a_{00} = 9/4$ and $a_{000} = -65/4$ from (2.84) and (2.85) which are also valid for $\theta_{\mathfrak{b}} = \pi/2$ and $\Delta = 1/4$. We notice that in this case quadratic and cubic non-linear terms of $h_0 = 2$ mode are more dominant than linear correction of h_1 mode. In the Section 2.7 we will verify (2.114) numerically for $q = 4$ by computing spectral density at zero temperature. The spectral density $\rho(\omega)$ is defined as

$$G(i\omega_n) = \int_{-\infty}^{+\infty} d\omega \frac{\rho(\omega)}{\omega - i\omega_n} \tag{2.115}$$

and due to the particle-hole symmetry the spectral density is an odd function $\rho(-\omega) = -\rho(\omega)$. Using this we can write (2.115) in the form

$$G(i\omega_n) = \int_{-\infty}^{+\infty} d\omega \frac{\omega\rho(\omega)}{\omega^2 + \omega_n^2}, \tag{2.116}$$

and taking the large z limit we find $\int_{-\infty}^{+\infty} d\omega\omega\rho(\omega) = 1$. We also notice that unitarity implies that $\rho(\omega) > 0$ for $\omega > 0$. We will find numerically that $\alpha_0 \simeq -0.556$ for $q = 4$ case. We notice that it is negative, whereas for bosonic and fermionic SYK models α_0 is positive.

[‡] We thank Igor Klebanov for discussion of these issues and for pointing out to us the references [37,176].

2.7 Numerical results for spinon spectra

In this section we present numerical solutions of the real time Schwinger-Dyson equations at zero temperature for the bosonic and fermionic spinon models and also the random rotor model in case of $q = 4$. We study the corrections found analytically in the section 2.4 and provide numerical evidence that the conformal solutions and the corrections to the conformal solutions work very well for all parameters in fermionic model and for some range of parameters in bosonic model. We also numerically find values of the dimensionless coefficients α_b for the first terms in the sum (2.99) for a range of assymetry angles θ_f and θ_b and argue that the numerically found spectra of operators agree with the ones found analytically.

The first Schwinger-Dyson equation for bosonic and fermionic spinon models is

$$G_R(\omega)^{-1} = \omega + i0 + \mu - \Sigma_R(\omega)\,, \tag{2.117}$$

and using the second Schwinger-Dyson equation we can express the retarded self energy $\Sigma_R(\omega)$ though the spectral density $\rho(\omega)$, which is in turn related to $G_R(\omega)$ as $\rho(\omega) = -\frac{1}{\pi}\mathrm{Im}G_R(\omega)$. We solve these equations at zero temperature using iterations. The detailed derivation of the equations above and numerical technique is discussed in the Appendix A.5 and we notice that a similar numerical approach was used in [156].

At zero temperature we expect for the spectral density to diverge at small frequencies, therefore, the quantity of interest in this

$$\rho(\omega) = \begin{cases} \dfrac{g_+(\omega)}{\sqrt{\omega/J}}, & \omega > 0 \\ \dfrac{g_-(-\omega)}{\sqrt{-\omega/J}}, & \omega < 0 \end{cases} . \tag{2.118}$$

We are interested to find a solution of the SD equations that at zero frequency approaches the conformal solution. Therefore the function of interest $g_\pm(\omega)$ should approach a constant

$$g_\pm(0) = \frac{C}{\pi J}\sin(\pi/4 \pm \theta), \quad C = \left(\frac{-\zeta\pi}{\cos 2\theta}\right)^{1/4} \tag{2.119}$$

according to eqs. (2.98) and (2.99). We remark that these boundary conditions at $\omega = 0$ determine asymmetry angle θ of the numerical solution and the chemical potential is fixed to be $\mu = \Sigma_R(0)$ and is not an input parameter at zero temperature numerics. In contrast for the finite temperature numerics one fixes μ first and then can infer θ by analyzing numerical solution.

We are interested in the low frequency behavior of the numerical solution that is theoretically described in the section 2.4, for both fermionic and bosonic spinon models. We use the expansion of the spectral density at small frequencies (2.99) and rewrite the expression at $\Delta = 1/q = 1/4$ for the function $g_\pm(\omega)$ as follows

$$g_\pm(\omega) = g_\pm(0)\left(1 - \sum_h \frac{\sqrt{\pi}\alpha_h v_{h\pm}(\omega/J)^{h-1}}{\Gamma(h-1/2)} - \sum_{h,h'} \frac{\sqrt{\pi}\alpha_h\alpha_{h'}a_{hh'\pm}(\omega/J)^{h+h'-2}}{\Gamma(h+h'-3/2)} - \dots\right), \tag{2.120}$$

where $g_\pm(0)$ is given in (2.119). The coefficients α_h depend on asymmetry angles θ_f and θ_b and are different for fermionic and bosonic models. The eigenvectors $v_h = (v_{h+}, v_{h-})$ of the matrix K_G and vectors $a_{hh'}, a_{hh'h''}, \dots$ also depend on the asymmetry angles and are given by eqs. (2.62) and (2.80). For given asymmetry angle there are first few leading modes in (2.120) which dominate the low frequency expansion.

Let us start with the fermionic SYK model at zero chemical potential. In this case $\theta_f = 0$ and due to particle-hole symmetry all h^{S} modes don't contribute and also $g_+ = g_- = g$ and the leading terms

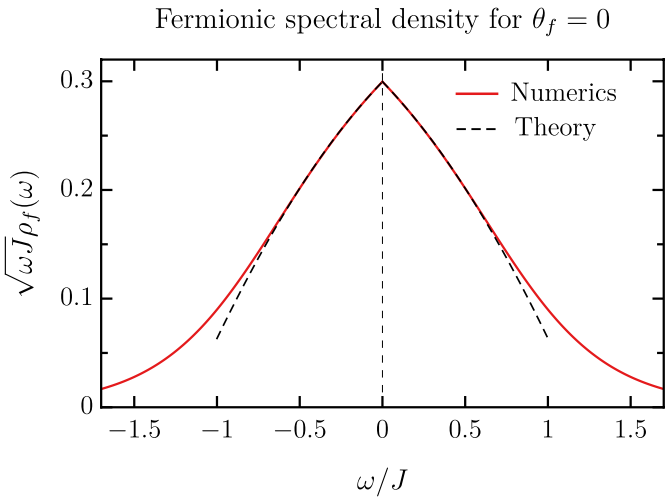

Figure 2.4: Plot of the fermionic SYK_4 spectral density for $\theta_f = 0$ at zero temperature. The red solid line is the numerical result obtained by solving the Schwinger-Dyson equations using iterations. The black dashed line is theoretical curve (2.121) ploted for $\alpha_0^{\mathrm{A}} = 0.2643$ and $\alpha_1^{\mathrm{A}} = 0.31$.

in (2.120) are

$$g_f(\omega) = \frac{1}{(4\pi^3)^{\frac{1}{4}} J}\left(1 - 2\alpha_0^{\mathrm{A}}\frac{\omega}{J} - 3(\alpha_0^{\mathrm{A}})^2\left(\frac{\omega}{J}\right)^2 - 0.68\alpha_1^{\mathrm{A}}\left(\frac{\omega}{J}\right)^{2.77} + \frac{26}{3}(\alpha_0^{\mathrm{A}})^3\left(\frac{\omega}{J}\right)^3 - \dots\right), \tag{2.121}$$

where we used that $v_b^{\mathrm{A}} = (1,1)$ and $h_1^{\mathrm{A}} \simeq 3.77$ and also $a_{00}^{\mathrm{A}} = 9/4$ and $a_{000}^{\mathrm{A}} = -65/4$ (see eqs. (2.84) and (2.85)) for $\Delta = 1/4$ and $\theta_f = 0$. Fitting numerical data we can find $\alpha_0^{\mathrm{A}} = 0.2643$ and $\alpha_1^{\mathrm{A}} \simeq 0.31 - 0.36$. We plot numerical result and theory (2.121) in Fig.2.4. One can see a really good agreement between theory and numerics at low frequencies. We notice that since α_1^{A} term is subleading we can not fix it with good precision, in contrast α_0^{A} can be fixed with high accuracy and our result agrees well with previous computation of this term in [121].

For non-zero chemical potential and thus non-zero asymmetry angle θ_f modes from the symmetric sector contribute to the spectral density and since $h_1^{\mathrm{S}} < 3$ the leading terms in low frequency expansion

of $g_{\pm}(\omega)$ are

$$g_{f\pm}(\omega) = \frac{\sin\left(\frac{\pi}{4} \pm \theta_f\right)}{J(\pi^3 \cos 2\theta_f)^{\frac{1}{4}}} \left(1 - 2\alpha_0^{\mathrm{A}} v_{0\pm}^{\mathrm{A}} \frac{\omega}{J} - \frac{\sqrt{\pi}\alpha_1^{\mathrm{S}} v_{1\pm}^{\mathrm{S}}}{\Gamma(h_1^{\mathrm{S}} - \frac{1}{2})} \left(\frac{\omega}{J}\right)^{h_1^{\mathrm{S}}-1} - \frac{4}{3}(\alpha_0^{\mathrm{A}})^2 a_{00\pm}^{\mathrm{A}} \left(\frac{\omega}{J}\right)^2 - \dots\right), \tag{2.122}$$

where explicit expressions for vectors v_0^{A} and a_{00}^{A} are given in (2.82) and vector v_1^{S} can be computed from (2.62) for a given value of h_1^{S}. The θ_f angle dependence of h_1^{S} is represented in Fig. 2.3.

We remark that since the series (2.120) is asymptotic [§] the relevance of higher order terms depends on the range of $\omega \in [0, \omega_{\max}]$ for which we approximate the exact result. That means that if we truncate series at order $p_{\max}$ the maximal frequency $\omega_{\max}$ for which this series gives reasonable approximation to the exact result is roughly determined by the condition that the term $(\omega_{\max}/J)^{p_{\max}}$ becomes comparable with the lower order terms in the series. Based on this and approximate values of the coefficients α_h for the fermionic SYK_4 model we keep only 2 or 3 leading terms written in (2.122).

We also notice that the coefficient α_0^{A} can be found by fitting the numerical curve by the linear correction

$$g_{\pm}^{\mathrm{lin}}(\omega) = g_{\pm}(0)\left(1 - 2\alpha_0^{\mathrm{A}}\left(1 \mp \frac{3}{2}\sin 2\theta_a\right)\frac{\omega}{J}\right). \tag{2.123}$$

We present the solutions of the equations (A.69) - (A.75) and the corresponding fitting of the analytical formula (2.122) in the Fig.2.5 for the fermionic spinon model and in the Fig.2.6 for the bosonic spinon model.

[§] This can be seen from $q = 2$ case, where the explicit formula (A.27) for $G(\tau)$ is available.

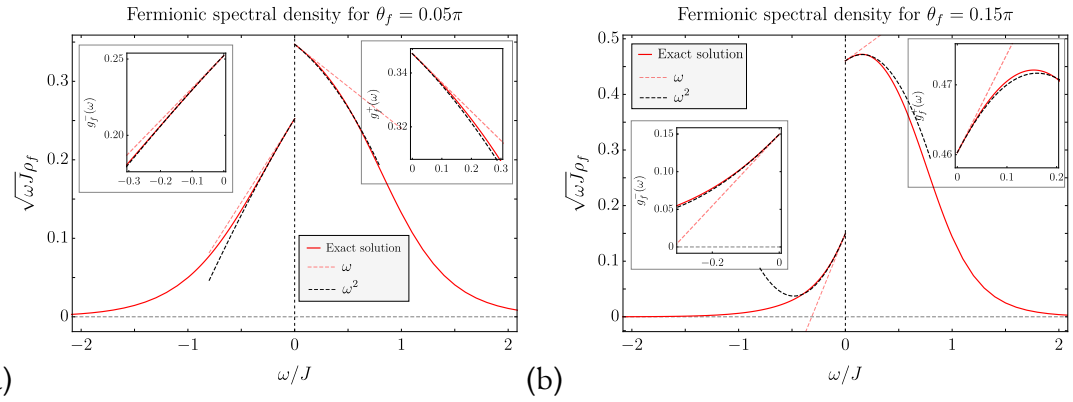

Figure 2.5: Spectral density plots at zero temperature for the fermionic spinon model. Main plots: the red solid lines are the numerical solution of the equations (A.69) - (A.75) for fermionic case at the value of the asymmetry parameter (a) $\theta_f = 0.05\pi$ and (b) $\theta_f = 0.15\pi$. The dashed lines are the fitting given by theoretical formula (2.122). The pink dashed lines are the linear fit given by (2.123) with (a) $\alpha_0^{\mathrm{A}} \simeq 0.29$ and (b) $\alpha_0 \simeq 0.68$. The black dashed lines are the fitting with the first four terms (nonlinear fitting is included) $g_{\pm}(\omega) = g_{\pm}(0)(1 + a\omega + b\omega^{h_1^{\mathrm{S}}-1} + c\omega^2)$ where (a) $h_1^{\mathrm{S}} \simeq 2.63$, $\alpha_1^{\mathrm{S}} \simeq 0.05$, and (b) $h_1^{\mathrm{S}} \simeq 2.53$, $\alpha_1^{S} \simeq 0.06$; and c is a coefficient that depends on α_0^{S}. Insets: zoomed in views of $g_f^{\pm}$ at small frequencies. The legend shows the powers of frequencies at which the series is terminated.

For the bosonic case the leading two operators are $h_0^{\mathrm{A}} = 2$ and h_1^{A} therefore we have

$$g_{\mathfrak{b}\pm}(\omega) = \frac{\sin\left(\frac{\pi}{4} \pm \theta_{\mathfrak{b}}\right)}{J(-\pi^3 \cos 2\theta_{\mathfrak{b}})^{\frac{1}{4}}} \left(1 - 2\alpha_0^{\mathrm{A}} v_{0\pm}^{\mathrm{A}} \frac{\omega}{J} - \frac{\sqrt{\pi}\alpha_1^{\mathrm{A}} v_{1\pm}^{\mathrm{A}}}{\Gamma(h_1^{\mathrm{A}} - \frac{1}{2})} \left(\frac{\omega}{J}\right)^{h_1^{\mathrm{A}}-1} - \frac{4}{3}(\alpha_0^{\mathrm{A}})^2 a_{00\pm}^{\mathrm{A}} \left(\frac{\omega}{J}\right)^2 - \frac{2\sqrt{\pi}\alpha_0^{\mathrm{A}}\alpha_1^{\mathrm{A}} a_{01\pm}^{\mathrm{A}}}{\Gamma(h_1^{\mathrm{A}} + \frac{1}{2})} \left(\frac{\omega}{J}\right)^{h_1^{\mathrm{A}}} - \frac{\sqrt{\pi}(\alpha_1^{\mathrm{A}})^2 a_{11\pm}^{\mathrm{A}}}{\Gamma(2h_1^{\mathrm{A}} - \frac{3}{2})} \left(\frac{\omega}{J}\right)^{2h_1^{\mathrm{A}}-2} - \dots \right). \tag{2.124}$$

For $\theta_{\mathfrak{b}} > 0.284\pi$ anomalous dimension h_1^{A} becomes less than $h_0^{\mathrm{A}} = 2$ and thus start dominating the expansion in (2.124).

The numerical approach we use in this section allows us to compute the coefficients α_h in the formula (2.122) with a very good precision. We use the function (2.122) as a fitting polynomial and find the dimensionless coefficients of each term. The results for the fermionic case are presented in the Fig.2.7 and for the bosonic case in the Fig.2.8. For the bosonic model, we see that the values of α_h becomes very large at some value of $\theta_{\mathfrak{b}}$. This value is close to $\theta_{\mathfrak{b}} = 0.284\pi$ where $h_0^{\mathrm{A}} = h_1^{\mathrm{A}}$ and $k'_{\mathrm{A}}(h) = 0$. We do not include the region where $h_1^{\mathrm{A}} \leq h_0^{\mathrm{S}} = 1$ since the numerical solution is not

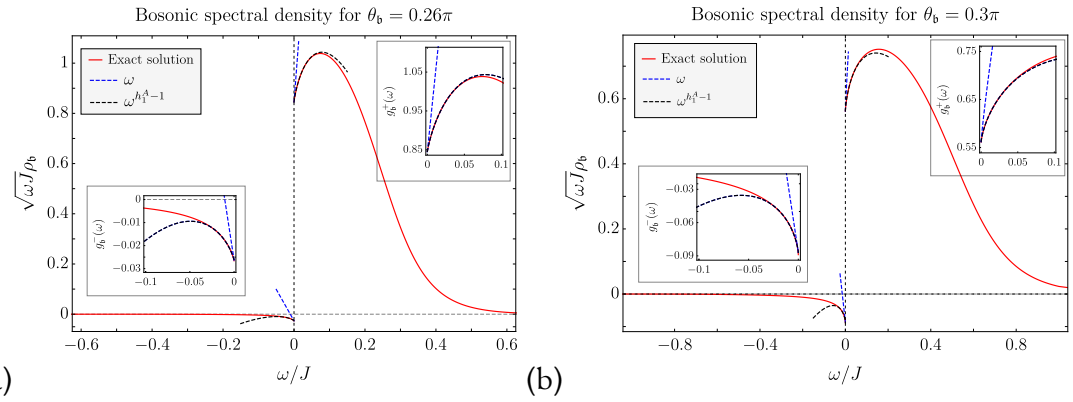

Figure 2.6: Spectral density plots at zero temperature for the bosonic spinon model. Main plots: the red solid lines are the numerical solution of the equations (A.69) - (A.75) for bosonic case at the value of the asymmetry parameter (a) $\theta_b = 0.26\pi$ and (b) $\theta_b = 0.3\pi$. The dashed lines are the fitting given by (2.122). The blue dashed line is the linear fit given by (2.123) with (a) $\alpha_0^A \simeq 21.9$ and (b) $\alpha_0^A \simeq 17.3$. The black dashed lines are the fitting of the function (2.122) with the first three terms $g_\pm(\omega) = g_\pm(0)(1 + a\omega + b\omega^{h_1^A-1})$ with (a) $h_1^A = 2.16$, $\alpha_1^A \simeq -12.2$ and (b) $h_1^A = 1.87$, $\alpha_1^A \simeq -8.5$. Insets: zoomed in views of $g_{b\pm}$ at small frequencies.

described by the conformal theory and is probably non-physical.

Even though the coefficients α_h cannot be computed analytically as discussed in the section 2.4, and therefore, the fitting functions cannot be exactly determined and has to include numerical results, there are ways to understand how well numerical solutions work by comparing them with pure theoretical predictions. One way to do this is to compute the ratio of coefficients in front of each term in (2.122). The general formula of the ratio of each term reads

$$r_h(\theta_a) = \frac{\sin(\pi\Delta - \theta_a)}{\sin(\pi\Delta + \theta_a)} \frac{v_{h-}}{v_{h+}} . \tag{2.125}$$

where v_h are the eigenvectors found in section 2.4, therefore, $v_{h\pm}$ are the components of the eigenvector that correspond to the positive and negative frequencies. We can compute this ratio both analytically and numerically (using the analytically found resonance values of h). The results of the first two terms are presented in the Fig.2.9 for the fermionic and bosonic models. We again note that for the bosonic model we do not include the region where h_1^A becomes less than one, since we cannot trust

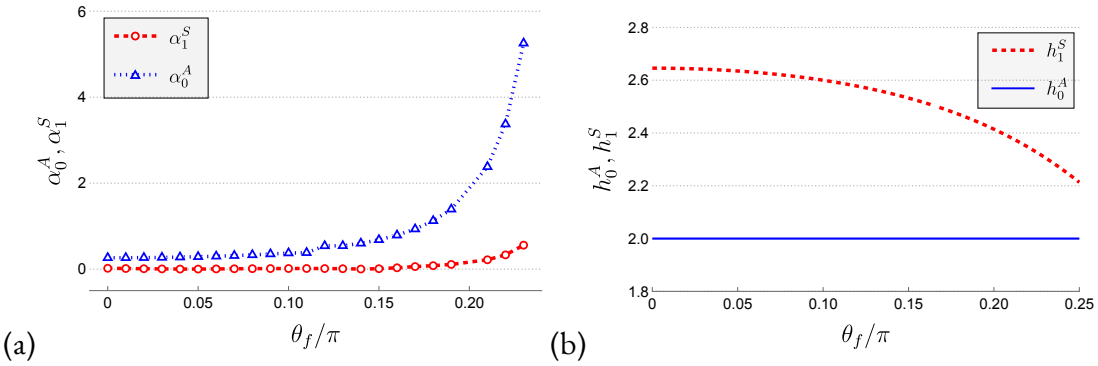

Figure 2.7: Numerically computed coefficients α_b (2.122) and theoretical values of the anomalous dimension of $\mathcal{O}_{b_1^S}$ operator in fermionic SYK. (a) The red circles are the numerical values of α_1^S – the coefficient die to the new operator with the anomalous dimension h_1^S, computed at different θ_f parameters; blue triangles are the numerical values of the coefficient α_0^A representing the linear correction, computed at different θ_f parameters. The lines are the linear interpolation between points. (b) Red dashed line is the plot of h_1^S given by the theoretical prediction, as a function of θ_f. The blue line is $h_0^A = 2$.

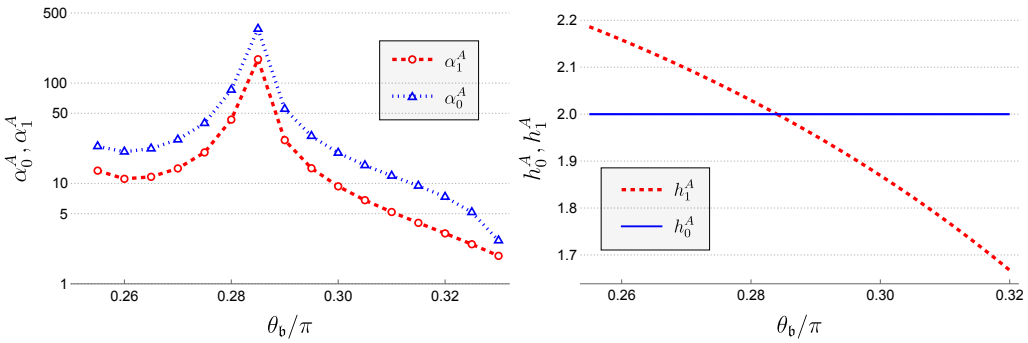

Figure 2.8: Numerically computed coefficients (absolute values) α_b and analytical values of the anomalous dimension of $\mathcal{O}_{b_1^A}$ operator in Bosonic SYK. Same as in the Fig.2.7 except: the left plot if in logarithmic scale. In the bosonic SYK case we notice that $h_1^A = h_0^A$ at $\theta_b \simeq 0.284\pi$. Near this value, the peak on the upper plot becomes prominent.

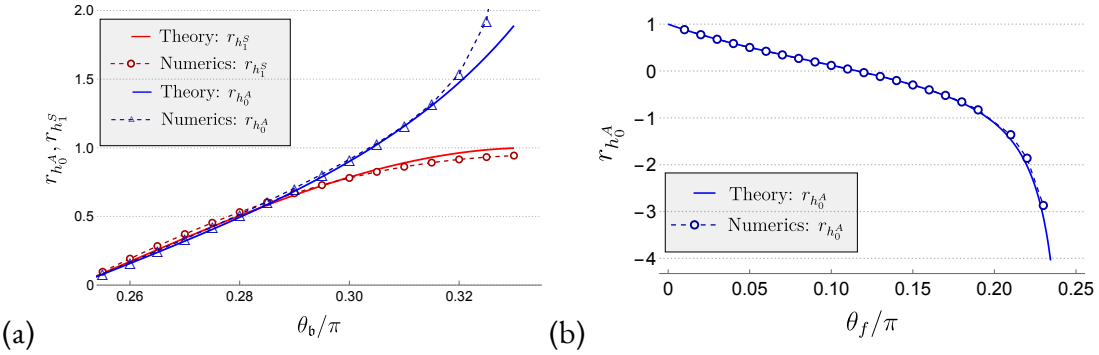

Figure 2.9: Plot of the function $r_b(\theta)$ defined in (2.125) for the bosonic and fermionic models. The blue and red solid lines are analytical relations of the coefficients of the positive and negative frequencies due to the $h_0^{\mathrm{A}} = 2$ and h_1^{A} terms respectively, and are given by the relation (2.125). (a) The red circles and blue triangles are numerical relations $r_{b_0^{\mathrm{A}}}(\theta_{\mathfrak{b}})$ and $r_{b_1^{\mathrm{A}}}(\theta_{\mathfrak{b}})$. (b) The blue circles are the numerical relation $r_{b_0^{\mathrm{A}}}$ at different $\theta_{\mathfrak{b}}$. Both: for the numerical fitting, we use $\omega_{max} = 7 \times 10^{-3}$ to obtain the closest to the theory result.

the solution in this region.

Another way to compare the numerical and theoretical results is to compute the Luttinger relations (2.64) for both models. Numerically we find $Q(\theta_f)$ and $S(\theta_{\mathfrak{b}})$ from the spectral density at zero temperature as $S = -\int_{-\infty}^{0} d\omega \rho_{\mathfrak{b}}(\omega)$ and $Q = \int_0^{\infty} d\omega \rho_f(\omega) - 1/2$ and compare them with the theory. The results for both models are presented in the Fig.2.10. We note that both solutions are close to the theoretical curves within $\Delta S, \Delta Q \sim 10^{-6}$ for each numerical point. As it was discussed in the section 2.4.1, at the asymmetry angle $\theta_{\mathfrak{b}} \simeq 0.36\pi$ where the anomalous dimension $h_1^{\mathrm{A}} \leq 1$ for the bosonic model, the Luttinger relation stops working. As we can see in the Fig.2.10(a), this indeed happens around $\theta_{\mathfrak{b}} \simeq 0.36\pi$ as predicted from the theory. It is unclear if solutions for angles $\theta_{\mathfrak{b}} > 0.36\pi$ are physical. Also one can provide a general argument why there is no conformal solution of the bosonic SYK at $\theta_{\mathfrak{b}} = \pi/2$. For the conformal solution at this angle we have $S = -\int_{-\infty}^{0} d\omega \rho_{\mathfrak{b}}(\omega) = 0$ and thus from unitarity $\rho_{\mathfrak{b}}(\omega) \leq 0$ for $\omega < 0$ we should conclude that $\rho_{\mathfrak{b}}(\omega) = 0$ for $\omega < 0$, but the conformal solution implies that $g_-(0) = -1/((4\pi^3)^{1/4} J)$ at $\theta_{\mathfrak{b}} = \pi/2$.

It is also instructive to find values of the charge Q and spin S as a function of the chemical potential μ_f and $\mu_{\mathfrak{b}}$ respectively rather than the asymmetry angle θ_f and $\theta_{\mathfrak{b}}$. Numerically we compute μ using

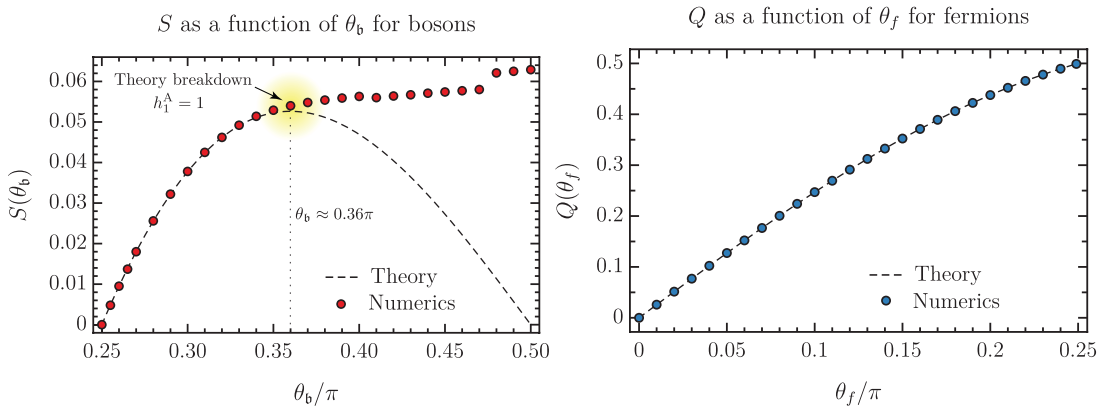

Figure 2.10: S as a function of $\theta_\mathfrak{b}$ for the bosonic model and Q as a function of θ_f for the fermionic model. The dashed lines are given by relations (2.64) and the red and blue points are obtained from numerical solution for the spectral density at zero temperature. For bosonic case we see that numerics deviates from theory at $\theta_\mathfrak{b} \simeq 0.36\pi$, this is the angle after which the anomalous dimension h_1^{A} is less than 1 and thus corresponds to relevant perturbation.

that $\mu = \mathrm{Re}\Sigma_R(\omega = 0)$ and the Kramers-Kronig relation

$$\mu = \int_{-\infty}^{+\infty} \frac{d\nu}{\pi} \frac{\mathrm{Im}(\Sigma_R(\nu) - \Sigma_R(0))}{\nu} \,. \tag{2.126}$$

Plot of the charge Q as the function of μ_f for the fermionic SYK is shown in the Fig.2.11(a) and we see that there is a maximum absolute value of the chemical potential $|\mu_{f\,\mathrm{max}}| \simeq 0.245J$. At this value $|Q_{\mathrm{max}}| \simeq 0.358$. A similar dependence of Q as a function of μ_f was found in [12,52]¶. In [12,52] a general phase diagram in (T, μ_f) space was investigated. It was showed that at $T = 0$ the SYK solution becomes unstable already when $Q \gtrsim 0.26$ and there is a first order phase transition to a low entropy phase. In the Fig.2.11(b) we plotted compressibility $K = dQ/d\mu_f$ as a function of Q. We see that it diverges at Q_{max}. For the bosonic SYK case we plotted $\theta_\mathfrak{b}$ as a function of $\mu_\mathfrak{b}$ in Fig. 2.12.

¶We thank Yingfei Gu for discussing his unpublished work with us.

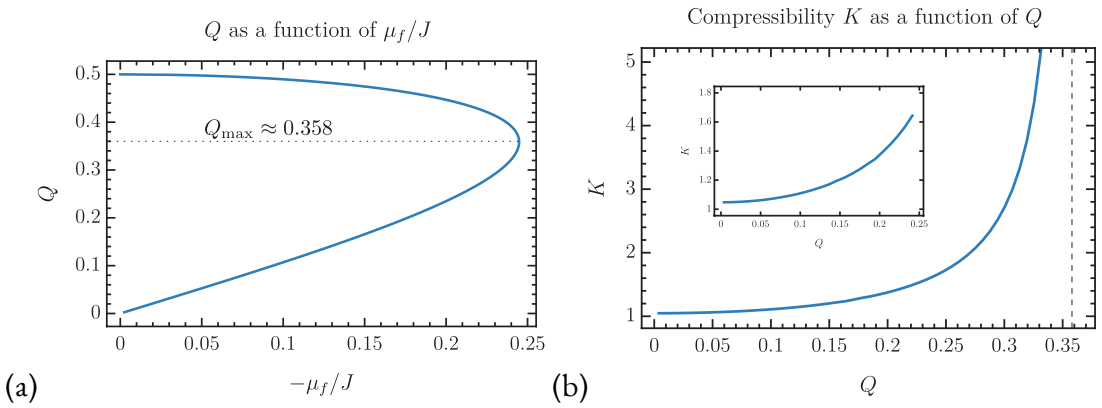

Figure 2.11: (a) Charge as a function of the chemical potential for the fermionic SYK at zero temperature. The blue line is the numerical solution of the Schwinger-Dyson equations $(\mathrm{A}.69)$ - $(\mathrm{A}.75)$ for the fermionic SYK at zero termperature for different values of the asymmetry angle. There is a maximal value of the chemical potential at which the value of the charge $Q_{\max} \simeq 0.358$. (b) Compressibility K as a function of charge for the fermionic spinon model at zero temperature (here we set $J = 1$). Compressibility diverges at $Q_{\max} \simeq 0.358$ $(\theta_f \simeq 0.153\pi)$. Inset: compressibility growth as small Q.

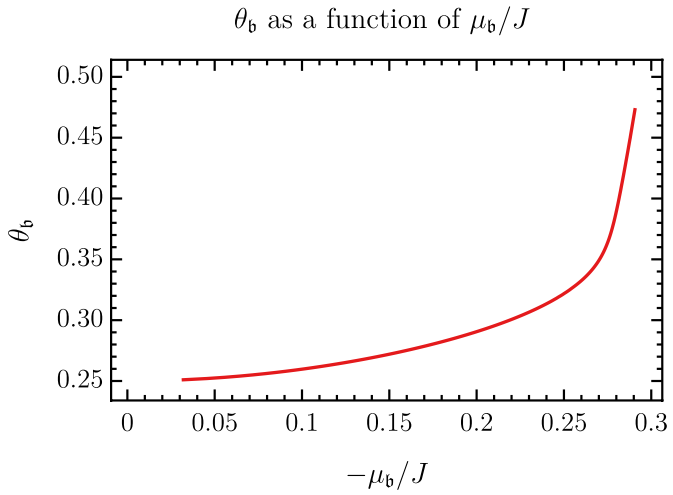

Figure 2.12: Asymmetry angle $\theta_{\mathfrak{b}}$ as a function of the chemical potential for the bosonic SYK at zero temperature.

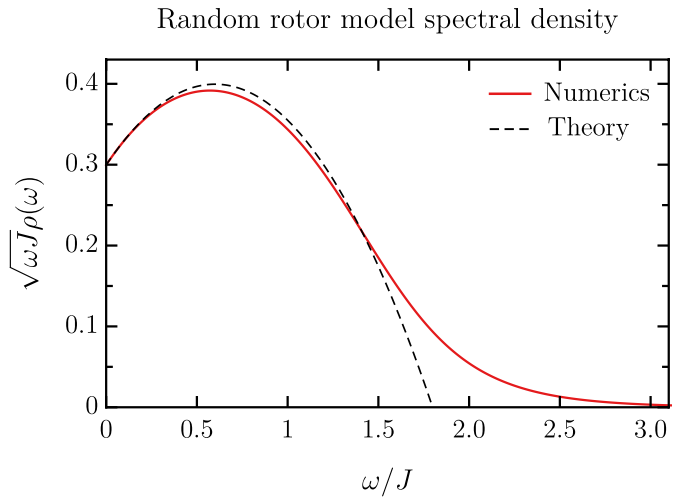

Figure 2.13: Plot of spectral density at zero temperature for the random quantum $q = 4$ rotor model. The red solid line is the numerical result obtained by solving the Schwinger-Dyson equations using iterations. The black dashed line is analytical curve (2.127) with only two leading terms ω and ω^2 plotted for $\alpha_0^{\mathrm{A}} = -0.556$.

Finally for the random quantum rotor model discussed in the Section 2.6 we use expansion

$$g_{\pm}(\omega) = \pm \frac{1}{(4\pi^3)^{\frac{1}{4}} J} \left(1 - 2\alpha_0^{\mathrm{A}} \frac{\omega}{J} - 3(\alpha_0^{\mathrm{A}})^2 \left(\frac{\omega}{J}\right)^2 + \frac{26}{3}(\alpha_0^{\mathrm{A}})^3 \left(\frac{\omega}{J}\right)^3 - \dots \right) . \tag{2.127}$$

We plot numerical result and analytical fit in Fig. 2.13. For the fit we used only two leading terms ω and ω^2. As we mentioned at the end of the Section 2.6 in this case the value of $\alpha_0^{\mathrm{A}} \simeq -0.556$ is negative. We also found that $M_{\mathrm{crit}} = \int_0^{+\infty} d\omega \rho(\omega) \simeq 0.88$ and we checked that $\int_{-\infty}^{+\infty} d\omega \omega \rho(\omega) = 0.9988$ which confirms validity of the numerical solution.

We conclude this section by finding numerically the spin spin spectral density $\rho_{Q_a}(\omega)$ using the spectral density representation (2.118) in (2.102). Changing variables in order to eliminate divergences of the integrand, we find a formula suitable for numerical evaluation

$$\rho_Q(\omega) = 2\mathrm{sgn}(\omega) \int_0^{1/\sqrt{2}} \frac{dx}{\sqrt{1-x^2}} \left(g_+(|\omega|x^2) g_-(|\omega|(1-x^2)) + g_-(|\omega|x^2) g_+(|\omega|(1-x^2)) \right) . \tag{2.128}$$

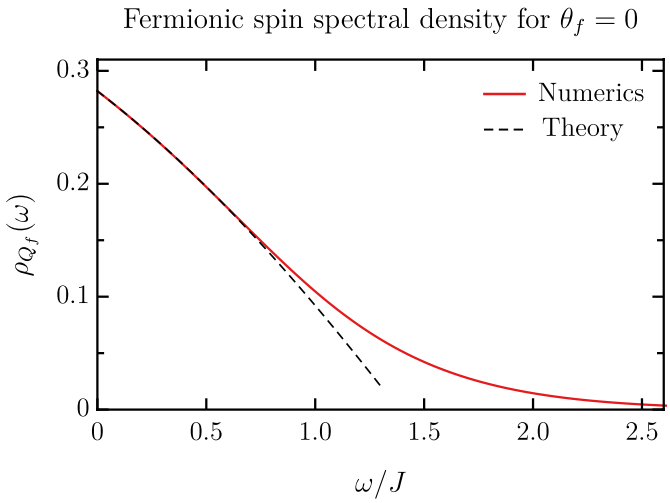

Figure 2.14: Plot of the fermionic spin spectral density for $\theta_f = 0$. The red solid line is the numerical result. The black dashed line is theoretical curve (2.105) ploted for $\alpha_0^{\mathrm{A}} = 0.2643$ and $\alpha_1^{\mathrm{A}} = 0.31$.

For the fermionic SYK model at $\theta_f = 0$ we plot both numerical solution and analytical formula for the spin spin spectral density in Fig.2.14, where for the black dashed line we used analytical formula (2.105) with $\alpha_0^{\mathrm{A}} \simeq 0.2643$ and $\alpha_1^{\mathrm{A}} \simeq 0.31$. We notice that the analytical fitting works very well at some range of frequencies where $\omega < 1$. Numerical solutions for the spin spin spectral densities for both fermionic and bosonic spinon models for various asymmetry angles θ_f and $\theta_{\mathfrak{b}}$ without the theoretical fitting are presented in the Fig.2.15.

2.8 Conclusions

The SYK equations in (2.16) describe the large N limit of the SYK models, and the large N limit followed by the large M limit of the SU(M) spin models described in Section 2.2. Despite their apparent simplicity, these equations contain a great deal of subtle scaling structure which we have reviewed and extended here. The predictions of the conformal perturbation theory agree very well with the real-frequency numerical analyses, including the cases with particle-hole asymmetry. Thus the low frequency behavior of the solutions of (2.16) can be declared to be well understood. Specifically, we

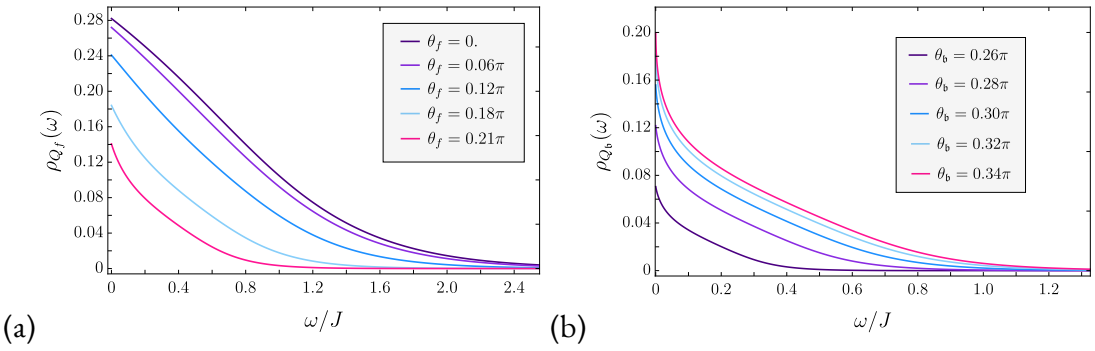

Figure 2.15: Plots of the numerically computed spin spectral densities (2.128) for (a) fermionic and (b) bosonic spinon models at different values of asymmetry angles.

have confirmed the Luttinger relations between the spectral asymmetry and the density; and we have shown that the low frequency corrections to the spectral density are controlled by the leading irrelevant operators, the most important of which is the time reparameterization operator.

All the analysis of the present paper is at $N = \infty$, and many other works [14,121,104,127,109,113] have addressed the nature of the $1/N$ corrections to the SYK saddle point. These are dominated by the fluctuations of a quantum 'graviton' associated with the time reparameterization mode, which leads to a breakdown of the conformal invariance described here at energy scales lower than J/N. We expect this breakdown to also apply to the SU(M) spin models.

From the condensed matter standpoint, it will be worthwhile to address the $1/M$ fluctuations of the SU(M) magnets in the $N = \infty$ theory. Upon considering the SYK model as a dynamic mean-field theory of correlated electrons, the $1/N$ corrections are finite size corrections which are not of interest in the thermodynamic limit. On the other hand, physical systems usually have only a SU(2) symmetry, and so the $1/M$ corrections are of greater interest. We expect that the conformal structure is preserved in the $1/M$ expansion, and the 'protected' scaling dimensions of the time-reparameterization mode ($b_0^{\rm A} = 2$) and of the U(1) gauge symmetry mode ($b_0^{\rm S} = 1$) hold to all orders in $1/M$. Renormalization group computations [180,153,92] have been used to argue that the gauge-invariant spin operator also has

a protected scaling dimension, and so none of the exponents in (2.2) will be modified in the $1/M$ expansion. It would be of interest to examine these conclusions directly in the $1/M$ expansion, and also determine the scaling dimensions of other possible gauge-invariant operators.

Finally, we note that we have extended the analyses of the present paper to the doped magnet, described by the SU(M) *t-J* model studied in Ref. [92]. These results will be described in paper II.

3

Excitation spectra of random $t - J$ models

3.1 Introduction

This paper extends our recent analysis in Ref. [174] from insulating spin models to metallic states of a random *t-J* model. This yields a rare solvable model of a metallic system without quasiparticle excitations, and so it is worthwhile to explore its properties in detail.

In the condensed matter literature, extensions of the Sachdev-Ye-Kitaev (SYK) models [156,105,154]

provide solvable theories of 'strange' and 'bad' metal behavior. Extensions which include single particle hopping [165,186,31,144,146] have regimes of intermediate temperature (T) with the paradigmatic linear-in-T resistivity, but with a bad metal resistivity *i.e.* larger than the quantum of resistance h/e^2 (in two dimensions). Upon lowering T, these models enter a disordered Fermi liquid regime with resistivity $\sim T^2$ and well-defined quasiparticles, once the resistivity becomes smaller than h/e^2. A strange metal regime, *i.e.* a linear-in-T resistivity smaller than h/e^2, only appears possible in special models with 'resonant' interactions [146].

In recent work, Joshi *et al.* [92] argued that a shortcoming of the above SYK models [165,186,31,144,146] is the absence of 'Mottness' *i.e.* a strong local repulsion between electrons that allows an interaction-driven insulator at commensurate densities. Mottness was present in the original Sachdev-Ye model [156] of an insulator, and this can be extended to metals by considering a SYK-like version of the *t-J* model with random exchange interactions [139,92,81,160]. Ref. [92] argued that upon tuning the electron density, such *t-J* models have critical points or phases in which the SYK criticality extends down to $T = 0$. They noted that such quantum critical theories provide an attractive description of the optimally doped cuprates, realizing deconfined criticality between an underdoped phase with spin glass order, and a Fermi liquid at large doping.

Ref. [92] also proposed a large M limit of a *t-J* model with SU(M) symmetry, when the solution reduces to a set of SYK-like saddle-point equations for the Green's functions of *fractionalized* particles carrying emergent U(1) gauge charges: these are the spinons and holons carrying the spin and charge of the underlying electrons, and they realize a deconfined critical state. The leading low frequency behaviors of the Green's functions were determined in Ref. [92]. Here, we shall provide a full numerical analysis of the saddle-point equations, and show that solutions with the proposed low frequency singularities do exist over some range of parameters. We shall also analytically compute the subleading corrections to the low frequency behavior, along the lines of Refs. [81,174], and show that it is consistent with our numerical results. We focus on gauge-invariant observables related to experimental probes

of the optimally doped cuprates.

With the knowledge of the Green's functions of the fractionalized particles, we can compute various physical gauge-invariant observables. We list the properties of the electron spectral weight, $\rho_e(\omega)$, the spin spectral density $\rho_Q(\omega)$, and the optical conductivity $\sigma(\omega)$ at frequency ω and at temperature $T = 0$ (J is the root-mean-square exchange interaction):

$$\begin{aligned}
\rho_e(\omega) &= A^{\pm}\left(1 - \sum_b A_b^{\pm}|\omega/J|^{b-1} - \sum_{bb'} A_{bb'}^{\pm}|\omega/J|^{b+b'-2} + \dots\right), \\
\rho_Q(\omega) &= B^{\pm}\left(1 - \sum_b B_b|\omega/J|^{b-1} - \sum_{bb'} B_{bb'}|\omega/J|^{b+b'-2} + \dots\right), \\
\mathrm{Re}\,\sigma(\omega) &= \sigma_0\left(1 - \sum_b C_b|\omega/J|^{b-1} - \sum_{bb'} C_{bb'}|\omega/J|^{b+b'-2} + \dots\right),
\end{aligned} \tag{3.1}$$

where $\pm$ superscripts refer to $\omega \gtrless 0$. Here the summation is over the spectrum of irrelevant operators, and A, B, C, σ_0's are coefficients that will be given in the main text in (3.69), (3.88) and (3.78). In the above expressions, we include the leading term arising from the conformal solution (the $\omega = 0$ result), and the subleading corrections organized according to conformal perturbation theory. Example of the latter includes a leading irrelevant operator with scaling dimension $h_1 < 2$ (see Fig. 3.3), and the time reparameterization mode (*i.e.* the boundary graviton in dual models of two-dimensional quantum gravity [121,122,104]) with scaling dimension $h_0 = 2$. We note that the presence of the mode with $h_1 < 2$ is a new feature of the doped *t-J* model, and was not present in the undoped antiferromagnet examined earlier [174]; the leading irrelevant operator in the latter case was the $h_0 = 2$ boundary graviton.

We can also extend the results in (3.1) to non-zero T: each term will be multiplied by a scaling function of ω/T. The expressions for these scaling functions are rather complicated at general scaling dimension h and are given in the body of the paper. But the scaling functions do simplify for the $h_0 = 2$ case. Including only these T-dependent corrections, the non-zero T form of (3.1) is, for $\omega, T \ll J (\beta \equiv 1/T)$

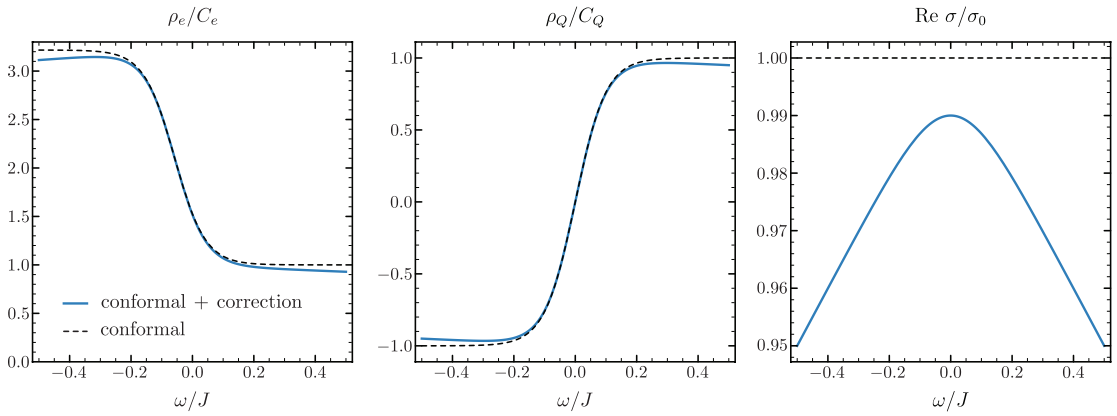

Figure 3.1: Plots of the functions in Eq. (E.91). We used $\beta J = 20$, $\theta_f = 0.1\pi$, $\theta_b = 0.3\pi$, $\alpha_0 = 0.05$.

Finally, we present the results for the d.c. resistivity, $\rho(T)$. Note from (3.1) that the zero frequency conductivity from the scaling limit solution is a constant *i.e.* the conformal solution yields a residual resistivity. So all the T dependence arises from corrections to conformality, and these are (from (3.83))

$$\rho(T) = \frac{1}{\sigma_0}\left(1 + \sum_b \alpha_b (v_{bf+} + v_{bf-} + v_{bb+} + v_{bb-}) R(b) \left(\frac{T}{J}\right)^{b-1} + \ldots\right) . \tag{3.2}$$

Here $R(b)$ is a known numerical function given in the main text. Note that the time reparameterization mode, with $b_0 = 2$, yields a linear-in-temperature correction. Further results on the numerical values of the coefficients in (3.1) and (3.2) appear in Section 3.5.

The outline of our paper is as follows. We define the *t-J* model in Section 3.2, along with its large M limit using fractionalized spinons and holons. We also present the SYK-like saddle-point equations and their conformal solutions. Section 3.3 turns to our new results on the operator spectrum and the associated corrections to conformality for the spinon and holon Green's functions. We also find regimes where the conformal solutions are unstable: this can happen by the appearance of operators with scaling dimension $b < 1$, and by complex values of b. Section 3.4 combines the fractionalized results of Section 3.3 to compute the spectral functions of various gauge invariant observables and their corrections to conformality. Finally, Section 3.5 computes the full numerical solution of the

saddle-point equations and compares them with our conformal expansions.

3.2 $t-J$ model and fractionalization

3.2.1 Model Hamiltonian

We consider the following Hamiltonian of the *t-J* model

$$H=\sum_{\langle ij\rangle,l,\alpha} t_{ij}c^{\dagger}_{il\alpha}c_{jl\alpha}+h.c.+\sum_{\langle ij\rangle,\alpha\beta} J_{ij}\left(S_{i\alpha\beta}S_{j\beta\alpha}-\frac{1}{M}S_{i\alpha\alpha}S_{j\beta\beta}\right). \tag{3.3}$$

Here $c_{il\alpha}$ is electron operator, with i denoting site, l denotes an auxiliary SU(M') orbital label, and α denotes SU(M) spin. The $S_{i\alpha\beta}=S^{\dagger}_{i\beta\alpha}$ is the spin operator on site i, and the $1/M$ term (which will be dropped in large M limit) is added to ensure it transform in the adjoint of SU(M).

We assume the system lives on a Bethe lattice of coordination number z with

$$t_{ij}=\frac{t}{\sqrt{Mz}}, \tag{3.4}$$

and J_{ij}'s are Gaussian random variables with

$$\overline{J_{ij}}=0,\quad \overline{J^2_{ij}}=\frac{J^2}{Mz}. \tag{3.5}$$

Implementing dynamical mean-field approximation ($z\to\infty$), and assuming a diagonal mean-field ansatz, the Hamiltonian induces the following interaction terms in the single-site action

$$S\supset\frac{t^2}{M}\sum_{l\alpha}\int_0^{1/T}\mathrm{d}\tau\mathrm{d}\tau'\sum_{l\alpha}c^{\dagger}_{l\alpha}G_c(\tau,\tau')c_{l\alpha}(\tau')-\frac{J^2}{2M}\sum_{\alpha\beta}\int_0^{1/T}\mathrm{d}\tau\mathrm{d}\tau' S_{\alpha\beta}(\tau)Q(\tau,\tau')S_{\beta\alpha}(\tau'). \tag{3.6}$$

Here the mean-field ansatz G_e and Q should satisfy the following self-consistency equations

$$G_e(\tau,\tau') = \frac{-1}{MM'}\sum_{l\alpha}\langle c_{l\alpha}(\tau)c^\dagger_{l\alpha}(\tau')\rangle\,, \quad Q(\tau,\tau') = \frac{1}{M^2}\sum_{\alpha\beta}\left\langle S_{\beta\alpha}(\tau)S_{\alpha\beta}(\tau')\right\rangle\,. \tag{3.7}$$

We also assume large M, M' limit with fixed

$$k = \frac{M'}{M}\,. \tag{3.8}$$

Taking a large M limit at fixed k ensures that we obtain saddle-point equations with a SYK-like structure for both fermionic and bosonic partons: consequently a critical state is realized in which the bosonic partons do not condense. In contrast, the large M limit with $M' = 1$ was studied in Ref. [139], and at low temperatures their bosonic partons condensed so that the ground state was always a Fermi liquid at non-zero doping.

The full action also contains WZW terms for slave particles and Langrangian multipliers, which will be detailed shortly.

3.2.2 Fermionic spinon + Bosonic holon

We fractionalize the model by introducing fermionic spinon and bosonic holon:

$$c_{il\alpha} = f_{i\alpha}b^\dagger_{il}, \quad S_{i\alpha\beta} = f^\dagger_{i\alpha}f_{i\beta}\,. \tag{3.9}$$

Here the boson b_{il} transforms in anti-fundamental of SU(M') such that the electron $c_{il\alpha}$ transforms in fundamental of SU(M'). This induces a U(1) gauge symmetry

$$f_{i\alpha}(\tau) \to f_{i\alpha}(\tau)e^{i\varphi_i(\tau)}, \quad b_{il}(\tau) \to b_{il}(\tau)e^{i\varphi_i(\tau)}. \tag{3.10}$$

For the theory to be consistent, the physical Hilbert space must be U(1) gauge-symmetric, which implies that the gauge charge is conserved, and we consider the representation

$$\sum_{\alpha} f_{i\alpha}^{\dagger} f_{i\alpha} + \sum_{l} b_{il}^{\dagger} b_{il} = \kappa M. \tag{3.11}$$

We also implement the doping density p by

$$\frac{1}{M'} \sum_{l} \langle b_{il}^{\dagger} b_{il} \rangle = p. \tag{3.12}$$

The full action is thus

$$\begin{aligned} S[f,b,\lambda] &= \int_0^{1/T} d\tau \left[\sum_{\ell} b_{\ell}^{\dagger} \left(\frac{\partial}{\partial \tau} + i\lambda \right) b_{\ell} + \sum_{\alpha} f_{\alpha}^{\dagger} \left(\frac{\partial}{\partial \tau} + \varepsilon_0 + i\lambda \right) f_{\alpha} - i\lambda \frac{M}{2} \right] \\ &\quad + \frac{t^2}{M} \sum_{\ell,\alpha} \int_0^{1/T} d\tau d\tau' f_{\alpha}^{\dagger}(\tau) b_{\ell}(\tau) G_c(\tau - \tau') b_{\ell}^{\dagger}(\tau') f_{\alpha}(\tau') \\ &\quad - \frac{J^2}{2M} \sum_{\alpha,\beta} \int_0^{1/T} d\tau d\tau' Q(\tau - \tau') f_{\alpha}^{\dagger}(\tau) f_{\beta}(\tau) f_{\beta}^{\dagger}(\tau') f_{\alpha}(\tau') \,. \end{aligned} \tag{3.13}$$

Introducing bilocal fields

$$G_f(\tau,\tau') = \frac{-1}{M} \sum_{\alpha} f_{\alpha}(\tau) f_{\alpha}^{\dagger}(\tau'), \quad G_b(\tau,\tau') = \frac{-1}{M'} \sum_{l} b_l(\tau) b_l^{\dagger}(\tau') \tag{3.14}$$

the saddle-point equations for the slave particles b_ℓ and f_α are given as follows,

$$G_b(i\omega_n) = \frac{1}{i\omega_n + \mu_b - \Sigma_b(i\omega_n)}, \tag{3.15}$$

$$\Sigma_b(\tau) = -t^2 G_f(\tau) G_f(-\tau) G_b(\tau), \tag{3.16}$$

$$G_f(i\omega_n) = \frac{1}{i\omega_n + \mu_f - \Sigma_f(i\omega_n)}, \tag{3.17}$$

$$\Sigma_f(\tau) = -J^2 G_f(\tau)^2 G_f(-\tau) + kt^2 G_f(\tau) G_b(\tau) G_b(-\tau). \tag{3.18}$$

Here μ_f and μ_b are chemical potentials, determined by ε_0 and the saddle point value of λ, and chosen to satisfy

$$\left\langle f^\dagger f \right\rangle = \kappa - kp \quad , \quad \left\langle b^\dagger b \right\rangle = p \, . \tag{3.19}$$

The electron Green's functions is a product

$$G_e(\tau) = -G_f(\tau) G_b(-\tau) \, .$$

Eqs.(3.15)-(3.18) admit the following infra-red (IR) conformal saddle point solution at zero temperature [92]

$$G_a^c(\tau) = -\begin{pmatrix} e^{\pi \mathcal{E}_a} \\ \zeta e^{-\pi \mathcal{E}_a} \end{pmatrix} \frac{b_a^{\Delta_a}}{|J\tau|^{2\Delta_a}}, \quad G_a^c(i\omega) = -\frac{iC_a}{J} \begin{pmatrix} e^{-i\theta_a} \\ -e^{i\theta_a} \end{pmatrix} |\omega/J|^{2\Delta_a - 1} \, , \tag{3.20}$$

where c in the superscript means conformal and subscript $a = b, f$ indexes boson and fermion respectively. We are following the convention of writing functions as two component vectors, where the first component is for $\tau > 0$ or $\omega > 0$, and the second one is for $\tau < 0$ or $\omega < 0$. Also $\mathcal{E}_b$, $\mathcal{E}_f$ and θ_b, θ_f are asymmetry parameters and angles and ζ factor is $\zeta_b = 1$ and $\zeta_f = -1$. To pass from the coordinate space to the frequency one we use the Fourier transform in our plus/minus basis

$$\begin{pmatrix} a_+ \\ a_- \end{pmatrix} |\tau|^{-\alpha} e^{i\omega\tau} d\tau = M(\alpha) \begin{pmatrix} a_+ \\ a_- \end{pmatrix} |\omega|^{\alpha - 1} \, , \quad M(\alpha) = \Gamma(1-\alpha) \begin{pmatrix} i^{1-\alpha} & i^{\alpha-1} \\ i^{\alpha-1} & i^{1-\alpha} \end{pmatrix} \, . \tag{3.21}$$

We will restrict our attention here to the the case where the boson and fermion scaling dimensions are $\Delta_f = \Delta_b = 1/4$, which is the case proposed for the deconfined critical point in Ref. [92]. The large M equations also admit a solution in a critical phase [92] with $1/4 < \Delta_f < 1/2$, $\Delta_f + \Delta_b = 1/2$ which we will not explicitly consider here: we expect similar results to also apply to this critical phase. For

the case $\Delta_f = \Delta_b = 1/4$, the pre-factors satisfy

$$\begin{aligned} &(t^2/J^2)C_f^2 C_b^2 \cos\big(2\theta_f\big) = \pi, \\ &C_f^4 \cos\big(2\theta_f\big) - k(t^2/J^2)C_f^2 C_b^2 \cos(2\theta_b) = \pi \end{aligned} \tag{3.22}$$

and we can find

$$C_f = \Big(\frac{\pi(1-\eta)}{\cos\big(2\theta_f\big)}\Big)^{1/4}, \quad C_b = \frac{J}{t}\Big(\frac{\pi}{\cos\big(2\theta_f\big)(1-\eta)}\Big)^{1/4}, \quad \eta \equiv -k\frac{\cos(2\theta_b)}{\cos\big(2\theta_f\big)}\,. \tag{3.23}$$

Positivity constraints on the spectral densities impose restrictions on asymmetry angles: $-\pi\Delta_f < \theta_f < \pi\Delta_f, \pi\Delta_b < \theta_b < \pi/2$. Therefore we see that $\eta > 0$ and since C_b and C_f are defined to be real positive numbers, we find another constraint for θ_b and θ_f:

$$\eta < 1\,. \tag{3.24}$$

For completeness we also list expressions for b_f and b_b:

$$b_f = \frac{\cos\big(2\theta_f\big)}{4\pi}(1-\eta), \quad b_b = \frac{\cos\big(2\theta_f\big)}{4\pi}\frac{\eta^2 J^4/t^4}{k^2(1-\eta)} \tag{3.25}$$

and the asymmetry parameters $\mathcal{E}_a$ are related to asymmetry angles θ_a as

$$e^{2\pi\mathcal{E}_a} = \frac{\sin(\theta_a + \pi\Delta_a)}{\sin(\theta_a - \pi\Delta_a)}\zeta, \quad e^{-2i\theta_a} = \frac{\sin\pi(i\tilde{\mathcal{E}}_a + \Delta_a)}{\sin\pi(i\tilde{\mathcal{E}}_a - \Delta_a)}, \tag{3.26}$$

where $\tilde{\mathcal{E}}_b = \mathcal{E}_b, \tilde{\mathcal{E}}_f = \mathcal{E}_f + 1/2$.

Thus all parameters of the IR solution are fully determined by the two asymmetry angles θ_f and θ_b. We can relate these angles to the boson and fermion densities by Luttinger constraints. According

to[63,78], for a SYK-type model with UV source σ we can define a U(1) charge at zero temperature

$$\mathcal{Q} = -\int_{-\infty}^{\infty} \mathrm{d}\tau \tau \sigma(\tau) G(-\tau)\,. \tag{3.27}$$

For the case of our model, $\sigma(\tau) = \delta'(\tau) - \mu\delta(\tau)$, which yields

$$\mathcal{Q} = \frac{G(0^+) + G(0^-)}{2}. \tag{3.28}$$

Matching this with the definition of Green's functions, we get

$$\mathcal{Q}_f = \left\langle f^\dagger f \right\rangle - \frac{1}{2}, \quad \mathcal{Q}_b = -\left\langle b^\dagger b \right\rangle - \frac{1}{2}\,. \tag{3.29}$$

Also the charge can be calculated entirely from the IR asymptotics, related to θ-parameter by

$$\mathcal{Q}(\theta) = -\frac{\theta}{\pi} - \left(\frac{1}{2} - \Delta\right) \frac{\sin(2\theta)}{\sin(2\pi\Delta)}\,. \tag{3.30}$$

Therefore, from (3.19), θ_f, θ_b satisfy the following Luttinger constraints[63,78]

$$\frac{\theta_f}{\pi} + \left(\frac{1}{2} - \Delta_f\right) \frac{\sin\left(2\theta_f\right)}{\sin\left(2\pi\Delta_f\right)} = \frac{1}{2} - \kappa + kp, \tag{3.31}$$

$$\frac{\theta_b}{\pi} + \left(\frac{1}{2} - \Delta_b\right) \frac{\sin(2\theta_b)}{\sin(2\pi\Delta_b)} = \frac{1}{2} + p\,. \tag{3.32}$$

3.2.3 Bosonic Spinon + Fermionic holon

We now discuss a fractionalization scheme that consists of bosonic spinons and fermionic holons,

$$c_{il\alpha} = \mathfrak{b}_{i\alpha} \mathfrak{f}^\dagger_{il}, \quad S_{i\alpha\beta} = \mathfrak{b}^\dagger_{i\alpha} \mathfrak{b}_{i\beta}\,, \tag{3.33}$$

with the gauge charge constraint

$$\sum_{\alpha} \mathfrak{b}_{i\alpha}^{\dagger}\mathfrak{b}_{i\alpha} + \sum_{l} \mathfrak{f}_{il}^{\dagger}\mathfrak{f}_{il} = \kappa M, \tag{3.34}$$

and filling density

$$\frac{1}{M'}\sum_{l}\langle \mathfrak{f}_{il}^{\dagger}\mathfrak{f}_{il}\rangle = p\,. \tag{3.35}$$

But most of our analysis will be carried out in the fractionalization scheme in Section 3.2.2. Following the similar discussion of the other scheme, we can now derive the action to be

$$\begin{aligned} S[\mathfrak{f},\mathfrak{b},\lambda] = &\int_0^{1/T} \mathrm{d}\tau \left[\sum_{\alpha}\mathfrak{b}_{\alpha}^{\dagger}\left(\frac{\partial}{\partial\tau}+i\lambda\right)\mathfrak{b}_{\alpha} + \sum_{\alpha}\mathfrak{f}_{l}\left(\frac{\partial}{\partial\tau}+\varepsilon_0+i\lambda\right)\mathfrak{f}_{l} - i\lambda\frac{M}{2}\right] \\ &+ \frac{t^2}{M}\sum_{l\alpha}\int_0^{1/T}\mathrm{d}\tau\mathrm{d}\tau'\mathfrak{f}(\tau)\mathfrak{b}_{\alpha}^{\dagger}(\tau)G_c(\tau,\tau')\mathfrak{b}_{\alpha}(\tau')\mathfrak{f}_{l}^{\dagger}(\tau') \\ &- \frac{J^2}{2M}\sum_{\alpha\beta}\int_0^{1/T}\mathrm{d}\tau\mathrm{d}\tau'\mathfrak{b}_{\alpha}^{\dagger}(\tau)\mathfrak{b}_{\beta}(\tau)Q(\tau,\tau')\mathfrak{b}_{\beta}^{\dagger}(\tau')\mathfrak{b}_{\alpha}(\tau')\,. \end{aligned} \tag{3.36}$$

The self consistency relations are

$$G_e(\tau,\tau') = \frac{-1}{MM'}\sum_{l\alpha}\langle c_{l\alpha}(\tau)c_{l\alpha}^{\dagger}(\tau')\rangle = \frac{-1}{MM'}\sum_{l\alpha}\left\langle \mathfrak{b}_{\alpha}(\tau)\mathfrak{f}_{l}^{\dagger}(\tau)\mathfrak{f}_{l}(\tau')\mathfrak{b}_{\alpha}^{\dagger}(\tau')\right\rangle\,, \tag{3.37}$$

$$Q(\tau,\tau') = \frac{1}{M^2}\sum_{\alpha\beta}\left\langle S_{\beta\alpha}(\tau)S_{\alpha\beta}(\tau')\right\rangle = \frac{1}{M^2}\sum_{\alpha\beta}\left\langle \mathfrak{b}_{\beta}^{\dagger}(\tau)\mathfrak{b}_{\alpha}(\tau)\mathfrak{b}_{\alpha}^{\dagger}(\tau')\mathfrak{b}_{\beta}(\tau')\right\rangle\,. \tag{3.38}$$

Introducing bilocal fields

$$G_{\mathfrak{b}}(\tau,\tau') = \frac{-1}{M}\sum_{\alpha}\mathfrak{b}_{\alpha}(\tau)\mathfrak{b}_{\alpha}^{\dagger}(\tau'), \quad G_{\mathfrak{f}}(\tau,\tau') = \frac{-1}{M'}\sum_{l}\mathfrak{f}_{l}(\tau)\mathfrak{f}_{l}^{\dagger}(\tau')\,, \tag{3.39}$$

and the corresponding self-energies $\Sigma_{\mathfrak{b}}(\tau,\tau')$, $\Sigma_{\mathfrak{f}}(\tau,\tau')$, we can obtain the saddle point equations

$$\begin{aligned} G_{\mathfrak{b}}(i\omega_n) &= \frac{1}{i\omega_n + \mu_{\mathfrak{b}} - \Sigma_{\mathfrak{b}}(i\omega_n)}\,, && (3.40)\\ G_{\mathfrak{f}}(i\omega_n) &= \frac{1}{i\omega_n + \mu_{\mathfrak{f}} - \Sigma_{\mathfrak{f}}(i\omega_n)}\,, && (3.41)\\ \Sigma_{\mathfrak{b}}(\tau) &= -kt^2 G_{\mathfrak{f}}(\tau)G_{\mathfrak{f}}(-\tau)G_{\mathfrak{b}}(\tau) + J^2 G_{\mathfrak{b}}(\tau)^2 G_{\mathfrak{b}}(-\tau)\,, && (3.42)\\ \Sigma_{\mathfrak{f}}(\tau) &= t^2 G_{\mathfrak{f}}(\tau)G_{\mathfrak{b}}(-\tau)G_{\mathfrak{b}}(\tau)\,, && (3.43) \end{aligned}$$

where we have substituted the self consistent relations

$$G_c(\tau) = G_{\mathfrak{f}}(-\tau)G_{\mathfrak{b}}(\tau), \quad Q(\tau) = G_{\mathfrak{b}}(\tau)G_{\mathfrak{b}}(-\tau)\,. \tag{3.44}$$

The chemical potentials should be adjusted to satisfy

$$\left\langle \mathfrak{f}^\dagger \mathfrak{f} \right\rangle = p, \quad \left\langle \mathfrak{b}^\dagger \mathfrak{b} \right\rangle = \kappa - kp\,. \tag{3.45}$$

Again we assume a conformal ansatz for the solution

$$G_a^c(\tau) = -\begin{pmatrix} e^{\pi\mathcal{E}_a} \\ \zeta e^{-\pi\mathcal{E}_a} \end{pmatrix} \frac{b_a^{\Delta_a}}{|J\tau|^{2\Delta_a}}, \quad G_a^c(i\omega) = -\frac{iC_a}{J}\begin{pmatrix} e^{-i\vartheta_a} \\ -e^{i\vartheta_a} \end{pmatrix} |\omega/J|^{2\Delta_a - 1}\,, \tag{3.46}$$

where c in the superscript means conformal and subscript $a = \mathfrak{b}, \mathfrak{f}$ indexes boson and fermion respectively. Assuming $\Delta_{\mathfrak{f}} = \Delta_{\mathfrak{b}} = 1/4$, the coefficients $C_{\mathfrak{b}}$ and $C_{\mathfrak{f}}$ satisfy

$$\begin{aligned} &(t^2/J^2)C_{\mathfrak{f}}^2 C_{\mathfrak{b}}^2 \cos(2\vartheta_{\mathfrak{b}}) = -\pi\,,\\ &C_{\mathfrak{b}}^4 \cos(2\vartheta_{\mathfrak{b}}) - k(t^2/J^2)C_{\mathfrak{b}}^2 C_{\mathfrak{f}}^2 \cos(2\vartheta_{\mathfrak{f}}) = -\pi \end{aligned} \tag{3.47}$$

and we find

$$C_{\mathfrak{b}} = \Big(\frac{\pi(1-\eta)}{-\cos(2\theta_{\mathfrak{b}})}\Big)^{1/4}, \quad C_{\mathfrak{f}} = \frac{J}{t}\Big(\frac{\pi}{-\cos(2\theta_{\mathfrak{b}})(1-\eta)}\Big)^{1/4}, \quad \eta \equiv -k\frac{\cos(2\theta_{\mathfrak{f}})}{\cos(2\theta_{\mathfrak{b}})}\,. \tag{3.48}$$

The unitarity constraints are $-\pi\Delta_{\mathfrak{f}} < \theta_{\mathfrak{f}} < \pi\Delta_{\mathfrak{f}}$, $\pi\Delta_{\mathfrak{b}} < \theta_{\mathfrak{b}} < \pi/2$ and the condition for real $C_{\mathfrak{b}}$ and $C_{\mathfrak{f}}$ is $\eta < 1$ as before.

The Luttinger constraints for $\theta_{\mathfrak{f}}, \theta_{\mathfrak{b}}$ are

$$\frac{\theta_{\mathfrak{f}}}{\pi} + \left(\frac{1}{2} - \Delta_{\mathfrak{f}}\right)\frac{\sin(2\theta_{\mathfrak{f}})}{\sin(2\pi\Delta_{\mathfrak{f}})} = \frac{1}{2} - p\,, \tag{3.49}$$

$$\frac{\theta_{\mathfrak{b}}}{\pi} + \left(\frac{1}{2} - \Delta_{\mathfrak{b}}\right)\frac{\sin(2\theta_{\mathfrak{b}})}{\sin(2\pi\Delta_{\mathfrak{b}})} = \frac{1}{2} + \kappa - kp\,. \tag{3.50}$$

If we ignore the Luttinger constraints, the saddle point equations above are identical to that of the other fractionalization scheme by substitution

$$G_f(\tau) \leftrightarrow G_{\mathfrak{b}}(\tau), \quad G_b(\tau) \leftrightarrow G_{\mathfrak{f}}(\tau), \quad 0 < \tau < 1/T, \tag{3.51}$$

and we transform $\tau < 0$ into $0 < \tau < \beta$ using KMS relation. In particular, when $\Delta_{\mathfrak{f}} = \Delta_b = \Delta_{\mathfrak{b}} = \Delta_f = 1/4$, we could identify the Green's functions in the two schemes by

$$\theta_{\mathfrak{f}} = \frac{\pi}{2} - \theta_b, \quad \theta_{\mathfrak{b}} = \frac{\pi}{2} - \theta_f, \quad C_{\mathfrak{f}} = C_b, \quad C_{\mathfrak{b}} = C_f. \tag{3.52}$$

However, we point out that (3.52) is incompatible with Luttinger constraints. For example, we can add (3.32) and (3.49) together and using (3.52) to see $\sin(2\theta_b) = 1$, which leads to $p = 0$, but (3.50) has no solution for $p = 0$. This reflects fact that at large M limit the two fractionalization schemes are two different theories, and they are identical only at $M = 2, M' = 1$.

3.3 Operator Spectrum and Corrections to Conformality

3.3.1 Corrections to Conformality

The saddle point solutions G_f and G_b of the *t-J* model can be viewed as a correlation functions in conformal field theory, which is deformed by infinite series of irrelevant operators[73,108,106]. Therefore the two-point functions receive corrections from these operators. We shall focus here on the fermionic spinon + bosonic holon model and the results can be easily generalized to the other case. The general expression for the two-point function at zero temperature reads

$$G(\tau) = G^c(\tau)\left(1 - \sum_b \frac{\alpha_b v_b}{|J\tau|^{b-1}} - \sum_{b,b'} \frac{a_{bb'}\alpha_b\alpha_{b'}}{|J\tau|^{b+b'-2}} - \sum_{b,b',b''} \frac{a_{bb'b''}\alpha_b\alpha_{b'}\alpha_{b''}}{|J\tau|^{b+b'+b''-3}} - \dots\right), \quad (3.53)$$

where v_b, $a_{bb'}$, $a_{bb'b''}$, etc are four-component vectors in b/f and $+/-$ basis, so

$$v_b = (v_{bb+}, v_{bb-}, v_{bf+}, v_{bf-})^{\mathrm{T}}.$$

For instance the fermionic Green's function for $\tau > 0$ reads

$$G_f(\tau) = G_f^c(\tau)\left(1 - \sum_b \frac{\alpha_b v_{bf+}}{|J\tau|^{b-1}} - \sum_{b,b'} \frac{a_{bb'f+}\alpha_b\alpha_{b'}}{|J\tau|^{b+b'-2}} - \sum_{b,b',b''} \frac{a_{bb'b''f+}\alpha_b\alpha_{b'}\alpha_{b''}}{|J\tau|^{b+b'+b''-3}} - \dots\right). \quad (3.54)$$

The real numbers α_b are the same for all components b/f and $+/-$. We are able to find these numbers only numerically. On the other hand the vectors v_b and anomalous dimensions b can be found analytically from solving the equation

$$K_G(b)v_b = v_b\,, \quad (3.55)$$

where the 4×4 matix $K_G(h) = W_\Sigma(h) W_G(h)$ is a product of two matrices $W_\Sigma(h)$ and W_G which in the $(b/f) \times (+/-)$ basis are given by formulas

$$W_\Sigma(h) = \frac{\sec(\pi h)}{(1-2h)} \begin{pmatrix} \sin(\pi h + 2\theta_b) & \sin(2\theta_b) - 1 \\ -\sin(2\theta_b) - 1 & \sin(\pi h - 2\theta_b) \end{pmatrix} \oplus \begin{pmatrix} \sin\big(\pi h + 2\theta_f\big) & \sin\big(2\theta_f\big) - 1 \\ -\sin\big(2\theta_f\big) - 1 & \sin\big(\pi h - 2\theta_f\big) \end{pmatrix}, \tag{3.56}$$

$$W_G = \begin{pmatrix} 1 & 0 & 1 & 1 \\ 0 & 1 & 1 & 1 \\ \eta & \eta & 2-\eta & 1-\eta \\ \eta & \eta & 1-\eta & 2-\eta \end{pmatrix}, \tag{3.57}$$

and we remind that $\eta = -k\cos(2\theta_b)/\cos\big(2\theta_f\big)$. We notice that the matrix $W_\Sigma(h)$ is block-diagonal in b/f space and W_G does not depend on h. For $\eta = 0$ the fermionic sector is independent on the bosonic one and its Green's function is exactly the same as in the complex SYK model.

The results described above are based on the Kitaev-Suh theory [104,81,174]. The derivation of the kernel K_G is done in [81]. The kernel K_G for bosonic spinon + fermionic holon case is obtained by substitution $\theta_f \to \theta_\mathfrak{b}$, $\theta_b \to \theta_\mathfrak{f}$, for details see Appendix B.2. The coefficients $a_{bb'}$, $a_{bb'b''}$ can be calculated using the recursion procedure described in [174]. We present explicit derivation of $a_{bb'}$ for the *t-J* model in Appendix B.2.

The linear order zero-temperature correction (3.53) was generalized to finite temperature in [81,174]. The result takes the form on the interval $\tau \in (0, \beta)$:

$$G_a(\tau) = G^c_a(\tau) \left(1 - \frac{v_{ba+} + v_{ba-}}{2} \frac{\alpha_b}{(\beta J)^{b-1}} f^{\mathrm{A}}_b(\tau) - \frac{v_{ba+} - v_{ba-}}{2} \frac{\alpha_b}{(\beta J)^{b-1}} f^{\mathrm{S}}_b(\tau) \right), \tag{3.58}$$

where $G^c_a(\tau)$ is the finite temperature conformal Green's function

$$G^c_a(\tau) = -b_a^{\frac{1}{4}} \left(\frac{\beta J}{\pi} \sin\frac{\pi\tau}{\beta}\right)^{-\frac{1}{2}} e^{2\pi\mathcal{E}_a(\frac{1}{2}-\frac{\tau}{\beta})}\,, \tag{3.59}$$

and the functions $f_b^{\mathrm{A/S}}(\tau)$ are given by the formula

$$\begin{aligned} f_b^{\mathrm{A}}(\tau) &= \frac{(2\pi)^{b-1}\Gamma(b)^2}{\Gamma(2b-1)\cos(\frac{\pi b}{2})}\left(A_b(e^{i\frac{2\pi\tau}{\beta}}) + A_b(e^{-i\frac{2\pi\tau}{\beta}})\right)\,, \\ f_b^{\mathrm{S}}(\tau) &= \frac{(2\pi)^{b-1}\Gamma(b)^2}{\Gamma(2b-1)\sin(\frac{\pi b}{2})}\left(iA_b(e^{i\frac{2\pi\tau}{\beta}}) - iA_b(e^{-i\frac{2\pi\tau}{\beta}})\right)\,, \end{aligned} \tag{3.60}$$

where $A_b(u) = (1-u)^b\mathbf{F}(b,b,1;u)$ and $\mathbf{F}$ is the regularized hypergeometric function. We stress that there are no vectors in the formula (3.58) and it is correct for both bosons and fermions $a = b, f$ with their corresponding conformal two-point functions $G^c(\tau)$ and components $v_{b\pm}$.

3.3.2 Operator Spectrum

In this subsection we describe solutions h of the equation (3.55). Such values of h correspond to scaling dimensions of the bilinear operators $\mathcal{O}_h$ in the *t-J* model [174]. We can rewrite the equation for h in the form

$$\det(1 - K_G(h)) = 0\,.$$

We label positive solutions of the above equation by $h_0, h_1, h_2, \ldots$ and notice that the sums in ((3.53)) are taken over this series. Several remarks are in order. First we notice that there are always two $h = 1$ solutions which are related to $U(1)$ global symmetry and $U(1)$ gauge symmetry. The $h = 1$ modes are not included in the series $h_0, h_1, h_2, \ldots$. The effect of these modes is already taken into account in the asymmetry parameters $\mathcal{E}_f$ and $\mathcal{E}_b$ in G^c_f and G^c_b [78,81]. Second there is another parameter-invariant solution $h = 2$ which corresponds to emergent time-reparametrization symmetry of the Eqs.(3.15)-

(3.18). We label this solution by h_0, so we always have $h_0 = 2$. The rest of the modes are ordered and their values depend on k, θ_f, θ_b, so we have

$$h_0 = 2, \quad h_1 \leq h_2 \leq h_3 \leq h_4 \leq \dots . \tag{3.61}$$

We will use notation α_i for α_{h_i} and v_i for v_{h_i}. The eigenvector v_0 has a simple form

$$v_0 = \begin{pmatrix} 1 - \frac{3}{2}\sin(2\theta_b) \\ 1 + \frac{3}{2}\sin(2\theta_b) \\ 1 - \frac{3}{2}\sin\big(2\theta_f\big) \\ 1 + \frac{3}{2}\sin\big(2\theta_f\big) \end{pmatrix} \tag{3.62}$$

and is not normalized to unity. We assume that all other vectors are normalized to unity, so $v_i^{\mathrm{T}} v_i = 1$ for $i = 1, 2, 3, \dots$.

Our interest is in modes which can be potentially smaller than the time-reparameterization mode $h_0 = 2$. In the *t-J* model the mode h_1 is less than $3/2$ for arbitrary parameters and thus it is always more relevant than $h_0 = 2$ mode. In addition, the mode h_2 can become smaller than h_0 for some regions of parameters. A qualitative plot of these potentially relevant operators for the fermionic spinon case of Section 3.2.2 is shown in Fig. 3.2 (the derivation is in Appendix. B.3). We remind the readers that θ_f and θ_b are constrained by unitarity $-\pi/4 < \theta_f < \pi/4$, $\pi/4 < \theta_b < \pi/2$. The mode h_1 (see Fig. 3.3) has $h_1 = 3/2$ at zero doping $p = 0$, and its scaling dimensions decreases as p grows, and it can become relevant $h_1 < 1$ or complex $h_1 = 1/2 + is$, $s \in \mathbf{R}$. At first glance, it seems that the low-energy properties would be dominated by this operator. However, as we will see in Section 3.5, the prefactor α_1 accompanying this mode is small compared to α_0 of the $h_0 = 2$ mode when doping p is small. A partial explanation is the coefficient α_1 is proportional to $k'_G(h_1)^{-1}$ (see (B.34)), and when p is small, h_1 is close to the pole at $k_G(3/2)$, so $k'_G(h_1)$ is large. Therefore, we expect time reparameterization mode

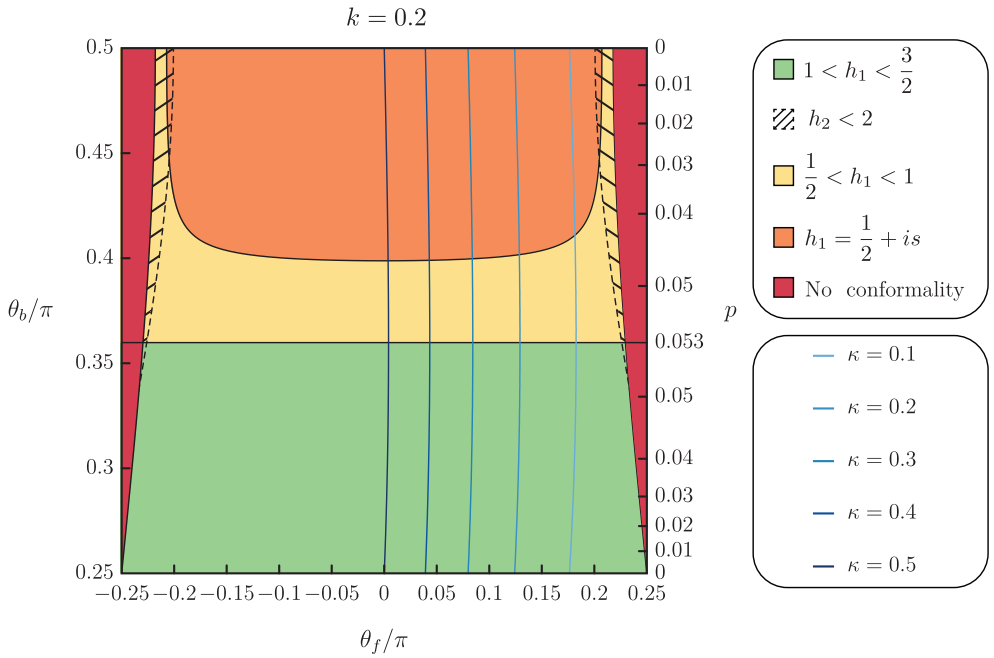

Figure 3.2: Scaling dimensions h of potentially dominant operators in the (θ_f, θ_b) plane. Here $k = 0.2$. Regions corresponding to different ranges of h are coded with different colors, with boundaries given by Eqs.(B.46),(B.47)-(B.50). There is a region dubbed "No conformality" meaning (3.24) is violated. On the right side, we also label different values of p obtained from the Luttinger constraint (3.32). In particular, the maximal $p_{\max} \simeq 0.053$ is reached when $\theta_b = \frac{1}{2}\arccos\left(\frac{-2}{\pi}\right)$. The colored lines are constant κ contours calculated from the Luttinger constraints (3.31),(3.32). Generally, the numerical solutions do not converge when $h_1 < 1$ or complex.

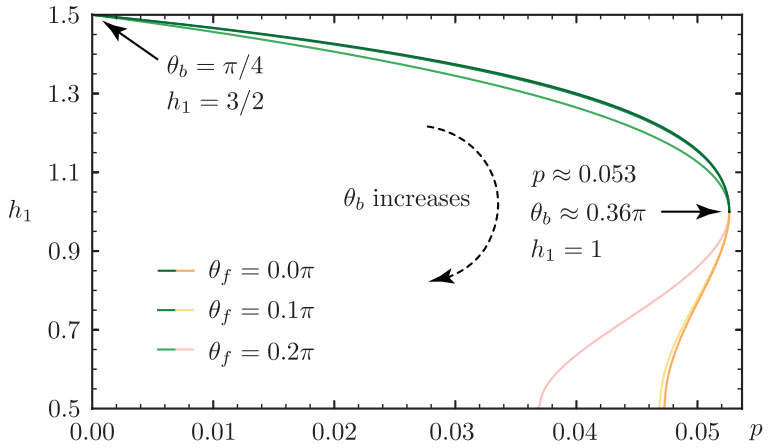

Figure 3.3: The scaling dimension h_1 plotted versus doping density p. The plot is obtained by taking three vertical cuts from Fig. 3.2 at $\theta_f = 0, 0.1\pi, 0.2\pi$. The scaling dimension $h_1 = 3/2$ when $p = 0$ and reaches $h_1 = 1$ when $p = p_{\max} \simeq 0.053$. Then h_1 starts to decrease with p until it reaches $h_1 = 1/2$ and becomes complex. Here we used $k = 0.2$.

$h_0 = 2$ to be important above some threshold temperature $T > T_1(p)$, where $T_1(p) \to 0$ as $p \to 0$. There is another potentially relevant operator h_2 which can move below 2, but it only appears in a restricted range of parameters.

The analysis of conformal corrections and operator spectrum in the bosonic spinon + fermionic holon case of Section 3.2.3 is very similar to the fermionic spinon + bosonic holon model. The kernel K_G can be obtained from the previous model by changing $\theta_f \to \theta_b, \theta_b \to \theta_f$ (see Appendix. B.2). The discussions of operators at $h = 1$ and $h = 2$ in the previous subsection still applie here. The analysis of other potentially relevant operators is shown in Fig. 3.4. In this case the second potentially relevant operator h_2 appears in a larger region of parameter space.

3.4 Gauge Invariant Observables

In this section we present results for some gauge invariant observables including electron spectral density $\rho_e(\omega)$, spin spectral density $\rho_Q(\omega)$ and optical conductivity Re $\sigma(\omega)$. We shall be focusing here on the fermionic spinon + bosonic holon fractionalization of Section 3.2.2.

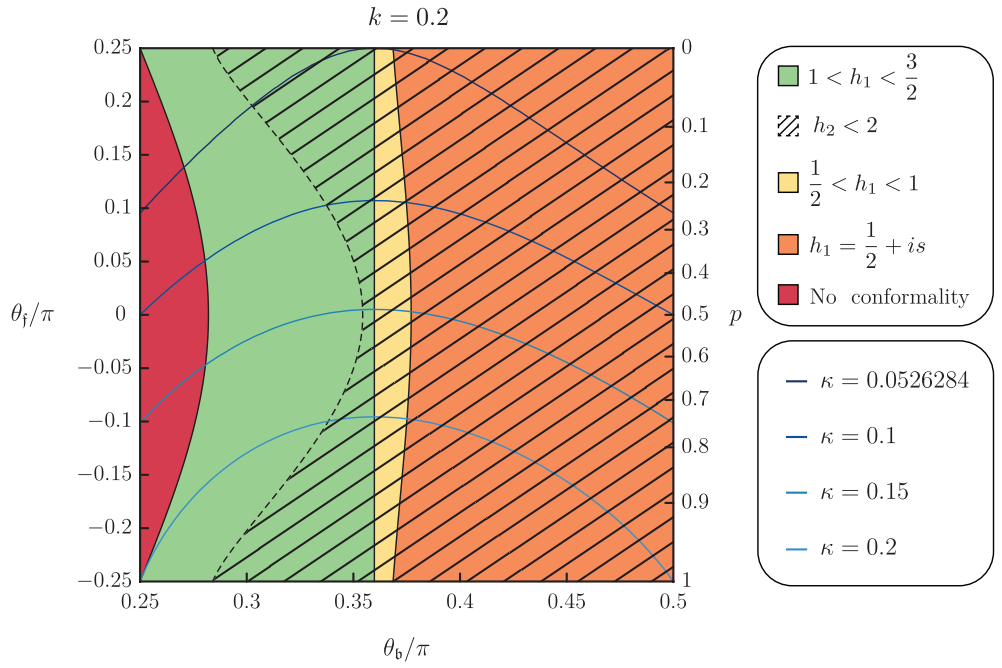

Figure 3.4: As in Fig. 3.2, but now for the bosonic spinon model.

3.4.1 Electron Spectral Density

The electron Green's function is a product of the spinon and holon Green's functions

$$G_e(\tau) = -G_f(\tau)G_b(-\tau)\,. \tag{3.63}$$

To obtain the electron spectral density, we shall first analytically continue to retarded-Green's function from imaginary time to the real one

$$G_{e,R}(t) = i\theta(t)(G_e(it+0) - G_e(it-0))\,, \tag{3.64}$$

where $\theta(t)$ is the Heaviside step function. Then we can find $G_{e,R}(\omega)$ in the frequency space and extract the spectral density as

$$\rho_e(\omega) = -\frac{1}{\pi}\mathrm{Im}G_{e,R}(\omega)\,. \tag{3.65}$$

The electron spectral density can also be written in terms of the spectral densities of spinon $\rho_f = -\frac{1}{\pi}\mathrm{Im}G_{f,R}$ and holon $\rho_b = -\frac{1}{\pi}\mathrm{Im}G_{b,R}$ as

$$\rho_e(\Omega) = \int_{-\infty}^{+\infty} \mathrm{d}\nu(n_F(\Omega+\nu) + n_B(\nu))\rho_f(\Omega+\nu)\rho_b(\nu)\,, \tag{3.66}$$

where $n_{F/B}(\omega) = 1/(e^{\beta\omega} - \zeta)$ is the Fermi or Bose distribution. We will perform the calculation at both zero temperature at finite temperature. At zero temperature we include nonlinear corrections, and at finite temperature we will restrict expressions to linear order corrections.

Zero temperature

Using (3.53) and (3.63), we can write the electron Green's function as

$$G_e(\tau) = G_e^c(\tau)\left(1 - \sum_b \frac{\alpha_b}{|J\tau|^{b-1}}(v_{bf} + \bar{v}_{bb}) - \sum_{bb'} \frac{\alpha_b\alpha_{b'}}{|J\tau|^{b+b'-2}}(a_{bb'f} + \bar{a}_{bb'b} - v_{bf}\bar{v}_{b'b}) - \dots\right). \tag{3.67}$$

Here $v_{bf(b)}$ means taking the fermionic (bosonic) component of the 4-component vector v_b, and similar meanings apply to $a_{bb'f(b)}$. $\bar{v}_{bb}$ means switching the $\pm$ components of v_{bb} and similar for $\bar{a}_{bb'b}$. $G_e^c(\tau)$ is the conformal electron Green's function

$$G_e^c(\tau) = -\begin{pmatrix} e^{\pi\mathcal{E}_e} \\ -e^{-\pi\mathcal{E}_e} \end{pmatrix}\frac{C_e}{|J\tau|}\,, \quad C_e = \frac{J}{t}\Big(\frac{-\cos(2\theta_b)}{4\pi}\Big)^{1/2}\,, \tag{3.68}$$

where $\mathcal{E}_e = \mathcal{E}_f - \mathcal{E}_b$ and we have used that $\Delta_f = \Delta_b = 1/4$. Analytically continuing to real-time and extract the spectral density, we obtain

$$\begin{aligned}\rho_e(\omega) = \rho_e^c(\omega)\Bigg(1 - \sum_b \frac{\alpha_b(v_{bf} + \bar{v}_{bb})}{\Gamma(b)} \left|\frac{\omega}{J}\right|^{b-1} \\ - \sum_{bb'} \frac{\alpha_b\alpha_{b'}(a_{bb'f} + \bar{a}_{bb'b} - v_{bf}\cdot\bar{v}_{b'b})}{\Gamma(b+b'-1)} \left|\frac{\omega}{J}\right|^{b+b'-2} - \dots\Bigg).\end{aligned} \tag{3.69}$$

Here $\rho_e^c(\omega)$ is the electron-spectral weight of the conformal solution

$$\rho_e^c(\omega) = \frac{C_e}{J}\begin{pmatrix} e^{\pi\mathcal{E}_e} \\ e^{-\pi\mathcal{E}_e}\end{pmatrix}, \tag{3.70}$$

where C_e is defined in (3.68).

Finite Temperature

We will work on the interval $0 < \tau < \beta$. The electron Green's function to linear order in α_b is

$$\begin{aligned}G_e(\tau) = G_e^c(\tau)\Bigg(1 - \sum_b \frac{\alpha_b}{2(\beta J)^{b-1}}\big((v_{bf+} + v_{bf-} + v_{bb+} + v_{bb-})f_b^{\mathrm{A}}(\tau) \\ + (v_{bf+} - v_{bf-} - v_{bb+} + v_{bb-})f_b^{\mathrm{S}}(\tau)\big) - \dots\Bigg),\end{aligned} \tag{3.71}$$

where the conformal electron Green's function at finite temperature is

$$G_e^c(\tau) = -C_e\Big(\frac{\beta J}{\pi}\sin\frac{\pi\tau}{\beta}\Big)^{-1} e^{2\pi\mathcal{E}_e(\frac{1}{2} - \frac{\tau}{\beta})}, \tag{3.72}$$

and the functions $f_b^{\mathrm{A}}(\tau)$ and $f_b^{\mathrm{S}}(\tau)$ are given in (3.60).

To find electron spectral density at finite temperature we analytically continue $G_e(\tau)$ to real time

using (3.64) and then take the Fourier transform to find $G_{e,R}(\omega)$ in the frequency space. Finally using (3.65) we find for the electron spectral density

$$\begin{aligned}\rho_e(\omega) =&\rho_e^c(\omega)\Bigg(1-\sum_h \frac{\alpha_h}{2(\beta J)^{h-1}}\Big((v_{hf+}+v_{hf-}+v_{hb+}+v_{hb-})\mathcal{R}_h^{\mathrm{A}}(\frac{\beta\omega}{2\pi}-\mathcal{E}_e)\\ &+(v_{hf+}-v_{hf-}-v_{hb+}+v_{hb-})\mathcal{R}_h^{\mathrm{S}}(\frac{\beta\omega}{2\pi}-\mathcal{E}_e)\Big)-\dots\Bigg),\end{aligned} \tag{3.73}$$

where the conformal electron spectral density is

$$\rho_e^c(\omega)=\frac{C_e\cosh\left(\frac{\beta\omega}{2}\right)}{J\cosh\left(\frac{\beta\omega}{2}-\pi\mathcal{E}_e\right)}, \tag{3.74}$$

and the functions $\mathcal{R}_h^{\mathrm{A}}(\omega)$ and $\mathcal{R}_h^{\mathrm{S}}(\omega)$ are

$$\begin{aligned}\mathcal{R}_h^{\mathrm{A}}(\omega)&=\frac{2\left(\frac{\pi}{2}\right)^h\Gamma(h)}{\sqrt{\pi}\sin\left(\frac{\pi h}{2}\right)\Gamma\left(h-\frac{1}{2}\right)}\mathrm{Re}\,{}_3\mathbf{F}_2\left(\begin{matrix}h,1-h,\frac{1}{2}+i\omega\\1,1\end{matrix};1\right),\\ \mathcal{R}_h^{\mathrm{S}}(\omega)&=\frac{2\left(\frac{\pi}{2}\right)^h\Gamma(h)}{\sqrt{\pi}\cos\left(\frac{\pi h}{2}\right)\Gamma\left(h-\frac{1}{2}\right)}\mathrm{Im}\,{}_3\mathbf{F}_2\left(\begin{matrix}h,1-h,\frac{1}{2}+i\omega\\1,1\end{matrix};1\right),\end{aligned} \tag{3.75}$$

where ${}_3\mathbf{F}_2$ is the regularized hypergeometric function. For derivation of similar to (3.73) results see [174]. Retaining only $h_0=2$ mode in (3.73) we find

$$\begin{aligned}\rho_e(\omega)=&\frac{C_e\cosh\left(\frac{\beta\omega}{2}\right)}{J\cosh\left(\frac{\beta\omega}{2}-\pi\mathcal{E}_e\right)}\\ &\times\left(1-\frac{\pi\alpha_0}{\beta J}\left(\frac{\beta\omega}{2\pi}-\mathcal{E}_e\right)\left(4\tanh\left(\frac{\beta\omega}{2}-\pi\mathcal{E}_e\right)-3(\sin(2\theta_f)-\sin(2\theta_b))\right)\right),\end{aligned} \tag{3.76}$$

where we have used the explicit expression (3.62) for the eigenvector v_0.

3.4.2 Conductivity

The Kubo formula for conductivity on Bethe lattice is derived in [81]:

$$\mathrm{Re}\,\sigma(\omega) = \frac{2\pi \mathcal{M}' e^2 t^2 a^{2-d}}{z} \int_{-\infty}^{+\infty} \mathrm{d}\Omega \rho_e(\Omega)\rho_e(\Omega+\omega) \frac{n_F(\Omega) - n_F(\Omega+\omega)}{\omega}\,, \tag{3.77}$$

where a is lattice constant and d is spatial dimension. We can evaluate the expression in three scenarios as below:

Zero temperature Optical conductivity

At zero temperature, we can evaluate the conductivity to nonlinear order in α_h using (3.69), the result is

$$\begin{aligned}\mathrm{Re}\,\sigma(\omega) = \sigma_0 \Bigg(1 &- \sum_h \frac{2\alpha_h}{\Gamma(h+1)} (v_{hf+} + v_{hf-} + v_{hb+} + v_{hb-}) |\omega/J|^{h-1} \\ &- \sum_{hh'} \frac{2\alpha_h \alpha_{h'} |\omega/J|^{h+h'-2}}{\Gamma(h+h')} [a_{hh'f+} + a_{hh'f-} + a_{hh'b+} + a_{hh'b-} \\ &- v_{hf+} v_{h'b-} - v_{hf-} v_{h'b+} - (v_{hf+} + v_{hb-})(v_{h'f-} + v_{h'b+})/2] \Bigg).\end{aligned} \tag{3.78}$$

Here σ_0 is the $T = 0$ DC conductivity given by

$$\sigma_0 = -\frac{\mathcal{M}' e^2 a^{2-d} \cos(2\theta_b)}{2z}\,, \tag{3.79}$$

where we used (3.70) for $\rho_e^c(\Omega)$.

Finite temperature optical conductivity at linear order

For the optical conductivity at finite temperature, we can analytically determine the contribution from the α_h correction. The result is

$$\mathrm{Re}\sigma(\omega) = \sigma_0 \left(1 - \sum_h \frac{\alpha_h}{(\beta J)^h}(v_{hf+} + v_{hf-} + v_{hb+} + v_{hb-})\Sigma_h\left(\frac{\beta\omega}{2\pi}\right) - \dots\right), \tag{3.80}$$

where

$$\Sigma_h(x) = \frac{2\left(\frac{\pi}{2}\right)^h \Gamma(h)}{\sqrt{\pi}\sin\left(\frac{\pi h}{2}\right)\Gamma\left(h-\frac{1}{2}\right)}\mathrm{Re}\,{}_3\mathbf{F}_2\left(\begin{matrix} h & 1-h & 1-ix \\ & 1 & 2 \end{matrix}; 1\right). \tag{3.81}$$

In particular, for the $h_0 = 2$ mode we have

$$\mathrm{Re}\sigma(\omega) = \sigma_0\left(1 - \frac{2\alpha_0\omega}{J}\coth\left(\frac{\beta\omega}{2}\right) - \dots\right). \tag{3.82}$$

Here we have used the eigenvectors (3.62). The detail of the calculation is in Appendix B.4.

Finite temperature DC conductivity

Using (3.80) we find for the finite temperature DC conductivity is

$$\sigma_{DC} = \sigma_0\left(1 - \sum_h \alpha_h(v_{hf+} + v_{hf-} + v_{hb+} + v_{hb-})R(h)\left(\frac{T}{J}\right)^{h-1} - \dots\right), \tag{3.83}$$

where $R(h) = \Sigma_h(0)$ and given by the formula

$$R(h) = -\frac{2\left(\frac{\pi}{2}\right)^{h-1}\cos\left(\frac{\pi h}{2}\right)\Gamma(h-1)}{\sqrt{\pi}h\Gamma\left(h-\frac{1}{2}\right)}. \tag{3.84}$$

A numerical plot of $R(h)$ is shown in Fig. 3.5. In particular, from the $h_0 = 2$ mode we can recover

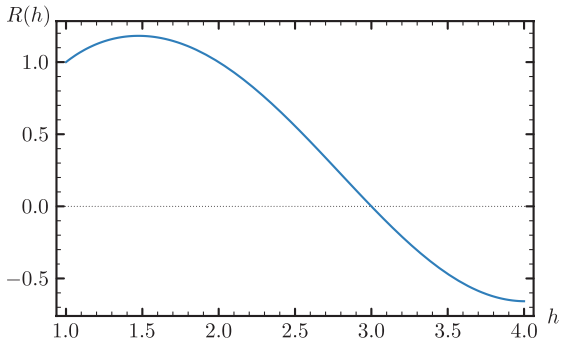

Figure 3.5: The function $R(h)$ defined in (3.84). Some special values are $R(1) = R(2) = 1$.

the linear resistivity obtained in [81]

$$\rho_{DC} = \frac{1}{\sigma_0}\left(1 + \frac{4\alpha_0 T}{J} - \dots\right), \tag{3.85}$$

where we have used the eigenvector (3.62). There is a factor of two difference from [81] because we have normalized the eigenvector differently.

3.4.3 Spin Spectral Density

In the large M limit, the spin-spin correlator factorizes as $Q(\tau) = G_f(\tau)G_f(-\tau)$, and the spin spectral density is defined as $\rho_Q = -\frac{1}{\pi}\mathrm{Im}Q_R(\omega)$. It can be expressed in terms of spinon spectral weight ρ_f as

$$\rho_Q(\omega) = \int_{-\infty}^{\infty} d\nu \rho_f(\nu)\rho_f(\nu-\omega)(n_F(\nu-\omega) - n_F(\nu)) . \tag{3.86}$$

The computation of this quantity is the same as the previous paper [174], and we report the results here.

Zero temperature

At zero temperature, the conformal spin spectral density is

$$\rho_Q^c(\omega) = \frac{C_Q}{J}\mathrm{sgn}\omega, \quad C_Q = \left(\frac{\cos\left(2\theta_f\right)}{4\pi}(1-\eta)\right)^{1/2}. \tag{3.87}$$

Including the conformal corrections, we have

$$\begin{aligned}\rho_Q(\omega) =& \rho_Q^c(\omega)\left(1 - \sum_h \frac{\alpha_h(v_{hf+} + v_{hf-})}{\Gamma(h)}\left|\frac{\omega}{J}\right|^{h-1}\right. \\ &\left. - \sum_{h,h'} \frac{\alpha_h\alpha_{h'}(a_{hh'f+} + a_{hh'f-} - v_{hf+}v_{h'f-})}{\Gamma(h+h'-1)}\left|\frac{\omega}{J}\right|^{h+h'-2} - \dots\right),\end{aligned} \tag{3.88}$$

Finite temperature

At finite temperature, we write the spin spectral weight to linear order in α_h as

$$\rho_Q(\Omega) = \rho_Q^c(\omega)\left(1 - \sum_h (v_{fh+} + v_{fh-})\frac{\alpha_h}{(\beta J)^{h-1}}\mathcal{R}_h^{\mathrm{A}}(\frac{\beta\omega}{2\pi}) - \dots\right), \tag{3.89}$$

where the conformal contribution to spin spectral weight is

$$\rho_Q^c(\omega) = \frac{C_Q}{J}\tanh\left(\frac{\beta\omega}{2}\right). \tag{3.90}$$

and the function $\mathcal{R}_h^{\mathrm{A}}(\omega)$ defined in (3.75). Considering only the correction from $h_0 = 2$ mode, we have

$$\rho_Q(\omega) = \frac{C_Q}{J}\tanh\left(\frac{\beta\omega}{2}\right)\left(1 - \frac{2\alpha_0\omega}{J}\tanh\left(\frac{\beta\omega}{2}\right) - \dots\right). \tag{3.91}$$

3.5 Numerical results for the $t-J$ model

In this section we numerically study the saddle point equations at zero temperature for the $t-J$ model, and use the solutions to constrain the coefficients of the conformal perturbations. We find that the contribution of the linear term from the $h_0 = 2$ mode dominates in the IR limit for the spin spectral density, but that the h_1 and h_0 modes are comparable in other observables. We focus on the case of fermionic spinon and bosonic holon model discussed in the Section 3.2.2. The solution in the case of bosonic spinon and fermonic holon can be derived and solved in a straightforward way using the approach discussed here by changing asymmetry angles $\theta_f \to \theta_\mathfrak{b}$ and $\theta_b \to \theta_\mathfrak{f}$.

The saddle point equations of interest at zero temperature are those in (3.15)-(3.18). To solve these equations numerically, we use an approach similar to the one used in the previous paper[174]. The detailed treatment of the equations is discussed in the Appendix B.1. Our focus is to solve the saddle point equations for bosonic and fermionic spectral densities first, and then present results for gauge invariant observables such as electron and spin spectral densities, and optical conductivity.

We focus on the asymmetry parameters of the model θ_f, θ_b that satisfy the Luttinger constraints. In this section we are interested in a particular case of $\Delta_b = \Delta_f = 1/4$, and thus we assume it everywhere. Therefore, we can write the Luttinger constraints (3.32) in the following form

$$\frac{\theta_f}{\pi} + \frac{1}{4}\sin\big(2\theta_f\big) = \frac{1}{2} - \kappa + kp, \tag{3.92}$$

$$\frac{\theta_b}{\pi} + \frac{1}{4}\sin(2\theta_b) = \frac{1}{2} + p\,. \tag{3.93}$$

The solutions with the constrains will correspond to the region crossed by one of the lines at chosen κ in the Fig. 3.2. Although there is a large region of asymmetry parameters where an analytical solution approximates a numerical result well, in this section we analyze only a portion of the full parameter space. We choose the asymmetry angles in the region of $\theta_b = 0.26\pi, 0.32\pi$ and $0 < \theta_f \leq 0.15\pi$.

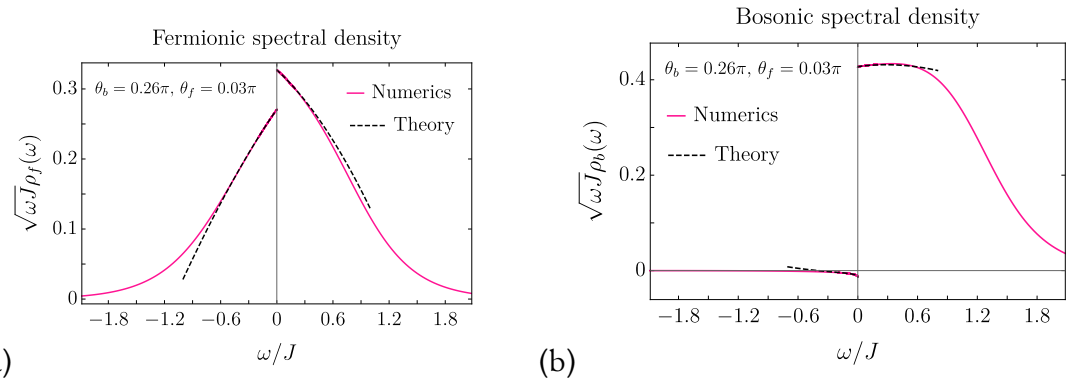

Figure 3.6: Fermioic (a) and bosonic (b) spectral densities as solutions of the equations (3.15)-(3.18). In both plots the chosen parameters: $\theta_b = 0.26\pi, \theta_f = 0.03\pi$. Solid magenta lines are the numerical solution for these parameters. Black dashed lines are given by analytical solution with nonlinear corrections. The values of the fitting parameters are given in the Fig. 3.8.

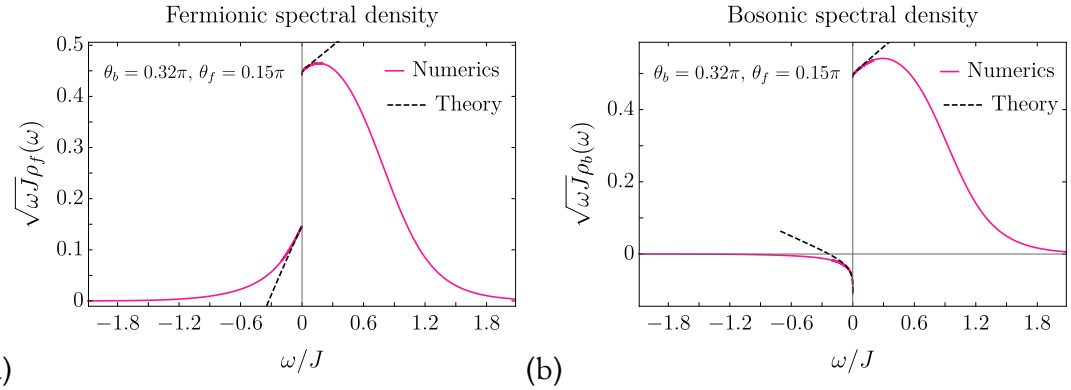

Figure 3.7: Fermioic (a) and bosonic (b) spectral densities as solutions of the equations (3.15)-(3.18). As in the Fig. 3.6 except the chosen parameters are $\theta_b = 0.32\pi, \theta_f = 0.15\pi$.

θ_f, θ_b	h_1	h_2	α_0	α_{h_1}	α_{h_2}
$0.03\pi, 0.26\pi$	1.47	2.49	0.25	-1.27	0.65
$0.08\pi, 0.26\pi$	1.47	2.49	0.31	-1.25	1.06
$0.13\pi, 0.26\pi$	1.47	2.49	0.48	-1.20	2.36
$0.14\pi, 0.26\pi$	1.47	2.49	0.54	-1.18	2.89
$0.15\pi, 0.26\pi$	1.47	2.48	0.62	-1.15	3.64
$0.03\pi, 0.32\pi$	1.23	2.42	0.27	-0.87	1.87
$0.08\pi, 0.32\pi$	1.23	2.42	0.33	-0.87	2.09
$0.13\pi, 0.32\pi$	1.22	2.41	0.52	-0.85	2.70
$0.14\pi, 0.32\pi$	1.22	2.40	0.59	-0.84	2.91
$0.15\pi, 0.32\pi$	1.22	2.39	0.67	-0.83	3.15

Figure 3.8: Approximate values of exponents h and coefficients α_h for different asymmetry angles θ_f, θ_b obtain by fits to the numerical solution.

We now show that the numerical solution with the constraints implied in small enough ω-region has behavior given by the results of the theoretical approach in the previous section. We discuss the behavior of fermionic and bosonic spectral densities as solutions of the saddle point equations (3.15)-(3.18) as well as gauge invariant observables such as electron, spin spectral densities and optical conductivity at zero temperature.

We first find the solution for bosonic $\rho_b(\omega)$ and fermionic $\rho_f(\omega)$ spectral densities of the equations (3.15)-(3.18) at zero temperature at various sets of parameters θ_f and θ_b and fixed $k = 0.2, t = J = 1$. The method of solving the equations at zero temperature is explained in detail in Appendix B.1 as well as in [174]. Amongst the range of parameters for which we solve the equations, we show two solutions that represent the behavior of the spectral densities at large ($\theta_b = 0.32\pi$, $\theta_f = 0.15\pi$) and small ($\theta_b = 0.26\pi, \theta_f = 0.03\pi$) asymmetry angles. The solutions are presented in Figs. 3.6,3.7, respectively.

The solutions found in this section compared to an analytical fit at small frequencies described in the previous sections and in Ref. [174]. Using the numerical solutions, we find the threshold of asymme-

try angles where it is still possible to get the solution as discussed in Appendix B.1. Below we describe a behavior of the gauge invariant observables and show that an analytical solution follows a numerical curve well enough at small frequencies.

Let us first rewrite the analytical expressions of the polynomials from section 3.4 that, as we show below, approximate the exact numerical solution at small frequencies. Following the notations in the previous sections, we use h_1, h_2 to denote the exponents in the fitting functions. We consider the polynomials for each of the gauge invariant observables truncated at the order of $h_2 - 1$ in frequency with all non-linear corrections included. A truncated expression for electron and spin spectral densities (3.69), (3.88) can be written as

$$\rho_{e,Q}(\omega) = \rho^c_{e,Q}(\omega) \left(1 - \sum_{h}^{h_2} \alpha_h A^{e,Q}_h |\omega/J|^{h-1} - \sum_{hh'}^{h_2} \alpha_h \alpha_{h'} A^{e,Q}_{hh'} |\omega/J|^{h+h'-2}\right). \tag{3.94}$$

We write the similar expression for optical conductivity $\sigma(\omega)$ truncating the full series (3.78) in a similar way

$$\sigma(\omega) = \sigma_0(\omega) \left(1 - \sum_{h}^{h_2} \alpha_h A^{\sigma}_h |\omega/J|^{h-1} - \sum_{hh'}^{h_2} \alpha_h \alpha_{h'} A^{\sigma}_{hh'} |\omega/J|^{h+h'-2}\right) \tag{3.95}$$

with different coefficients A^{σ}_h. In the above, $\rho^c_{e,Q}(\omega)$ are the electron and spin spectral weights of the conformal solutions (3.70), (3.87), and σ_0 is given by (3.79). The coefficients $A^{e,Q,\sigma}_h$ are known exactly and have analytical forms for electron spectral density (3.69), for spin spectral density (3.88) and for conductivity (3.78).

We note that the analytical solution has unfixed parameters α_h. In the series we consider, there are three parameters the values of which can be obtained by fitting an analytical expression into to a numerical curve at corresponding parameters. For a range of parameters we discuss in this section, the values of coefficients α_h as well as exponents h are presented in Fig. 3.8.

Using the values of the coefficients α_h we obtain analytical solutions with all parameters fixed. The

θ_f, θ_b	$\rho_Q^{\rm fit}/\rho_Q^{\rm c} - 1, \quad T = 0$	$\rho_e^{\rm fit}/\rho_e^{\rm c} - 1, \quad T = 0, \quad \omega > 0$
$0.03\pi, 0.26\pi$	$-0.50\left\|\frac{\omega}{J}\right\| - 0.06\left\|\frac{\omega}{J}\right\|^{0.94} + 0.01\left\|\frac{\omega}{J}\right\|^{0.47}$	$-0.81\left\|\frac{\omega}{J}\right\| + 1.41\left\|\frac{\omega}{J}\right\|^{0.94} - 1.43\left\|\frac{\omega}{J}\right\|^{0.47}$
$0.08\pi, 0.26\pi$	$-0.62\left\|\frac{\omega}{J}\right\| - 0.06\left\|\frac{\omega}{J}\right\|^{0.94} + 0.01\left\|\frac{\omega}{J}\right\|^{0.47}$	$-0.87\left\|\frac{\omega}{J}\right\| + 1.36\left\|\frac{\omega}{J}\right\|^{0.94} - 1.41\left\|\frac{\omega}{J}\right\|^{0.47}$
$0.13\pi, 0.26\pi$	$-0.97\left\|\frac{\omega}{J}\right\| - 0.09\left\|\frac{\omega}{J}\right\|^{0.93} + 0.02\left\|\frac{\omega}{J}\right\|^{0.47}$	$-1.16\left\|\frac{\omega}{J}\right\| + 1.22\left\|\frac{\omega}{J}\right\|^{0.93} - 1.35\left\|\frac{\omega}{J}\right\|^{0.47}$
$0.14\pi, 0.26\pi$	$-1.09\left\|\frac{\omega}{J}\right\| - 0.09\left\|\frac{\omega}{J}\right\|^{0.93} + 0.02\left\|\frac{\omega}{J}\right\|^{0.47}$	$-1.28\left\|\frac{\omega}{J}\right\| + 1.17\left\|\frac{\omega}{J}\right\|^{0.93} - 1.32\left\|\frac{\omega}{J}\right\|^{0.47}$
$0.15\pi, 0.26\pi$	$-1.24\left\|\frac{\omega}{J}\right\| - 0.10\left\|\frac{\omega}{J}\right\|^{0.93} + 0.02\left\|\frac{\omega}{J}\right\|^{0.47}$	$-1.42\left\|\frac{\omega}{J}\right\| + 1.11\left\|\frac{\omega}{J}\right\|^{0.93} - 1.30\left\|\frac{\omega}{J}\right\|^{0.47}$
$0.03\pi, 0.32\pi$	$-0.54\left\|\frac{\omega}{J}\right\| - 0.03\left\|\frac{\omega}{J}\right\|^{0.91} - 0.02\left\|\frac{\omega}{J}\right\|^{0.69} + 0.01\left\|\frac{\omega}{J}\right\|^{0.46} + 0.05\left\|\frac{\omega}{J}\right\|^{0.23}$	$-0.82\left\|\frac{\omega}{J}\right\| + 0.12\left\|\frac{\omega}{J}\right\|^{0.91} + 0.30\left\|\frac{\omega}{J}\right\|^{0.69} - 0.12\left\|\frac{\omega}{J}\right\|^{0.46} - 0.93\left\|\frac{\omega}{J}\right\|^{0.23}$
$0.08\pi, 0.32\pi$	$-0.67\left\|\frac{\omega}{J}\right\| - 0.03\left\|\frac{\omega}{J}\right\|^{0.91} - 0.03\left\|\frac{\omega}{J}\right\|^{0.68} + 0.01\left\|\frac{\omega}{J}\right\|^{0.45} + 0.05\left\|\frac{\omega}{J}\right\|^{0.23}$	$-0.88\left\|\frac{\omega}{J}\right\| + 0.13\left\|\frac{\omega}{J}\right\|^{0.91} + 0.29\left\|\frac{\omega}{J}\right\|^{0.68} - 0.13\left\|\frac{\omega}{J}\right\|^{0.45} - 0.92\left\|\frac{\omega}{J}\right\|^{0.23}$
$0.13\pi, 0.32\pi$	$-1.04\left\|\frac{\omega}{J}\right\| - 0.04\left\|\frac{\omega}{J}\right\|^{0.89} - 0.03\left\|\frac{\omega}{J}\right\|^{0.67} + 0.02\left\|\frac{\omega}{J}\right\|^{0.44} + 0.07\left\|\frac{\omega}{J}\right\|^{0.22}$	$-1.18\left\|\frac{\omega}{J}\right\| + 0.14\left\|\frac{\omega}{J}\right\|^{0.89} + 0.26\left\|\frac{\omega}{J}\right\|^{0.67} - 0.14\left\|\frac{\omega}{J}\right\|^{0.44} - 0.90\left\|\frac{\omega}{J}\right\|^{0.22}$
$0.14\pi, 0.32\pi$	$-1.18\left\|\frac{\omega}{J}\right\| - 0.05\left\|\frac{\omega}{J}\right\|^{0.88} - 0.03\left\|\frac{\omega}{J}\right\|^{0.66} + 0.02\left\|\frac{\omega}{J}\right\|^{0.44} + 0.07\left\|\frac{\omega}{J}\right\|^{0.22}$	$-1.30\left\|\frac{\omega}{J}\right\| + 0.14\left\|\frac{\omega}{J}\right\|^{0.88} + 0.25\left\|\frac{\omega}{J}\right\|^{0.66} - 0.15\left\|\frac{\omega}{J}\right\|^{0.44} - 0.89\left\|\frac{\omega}{J}\right\|^{0.22}$
$0.15\pi, 0.32\pi$	$-1.35\left\|\frac{\omega}{J}\right\| - 0.05\left\|\frac{\omega}{J}\right\|^{0.87} - 0.04\left\|\frac{\omega}{J}\right\|^{0.65} + 0.02\left\|\frac{\omega}{J}\right\|^{0.44} + 0.08\left\|\frac{\omega}{J}\right\|^{0.22}$	$-1.44\left\|\frac{\omega}{J}\right\| + 0.14\left\|\frac{\omega}{J}\right\|^{0.87} + 0.23\left\|\frac{\omega}{J}\right\|^{0.65} - 0.15\left\|\frac{\omega}{J}\right\|^{0.44} - 0.88\left\|\frac{\omega}{J}\right\|^{0.22}$

Figure 3.9: Table of computed analytical expressions of spin and electron spectral densities (3.94) with all parameters fixed for a range of asymmetry angles (θ_f, θ_b). The polynomials approximate a corresponding numerical solution at small frequencies. The exponents are given by $h - 1$ where h are presented in the Fig. 3.8.

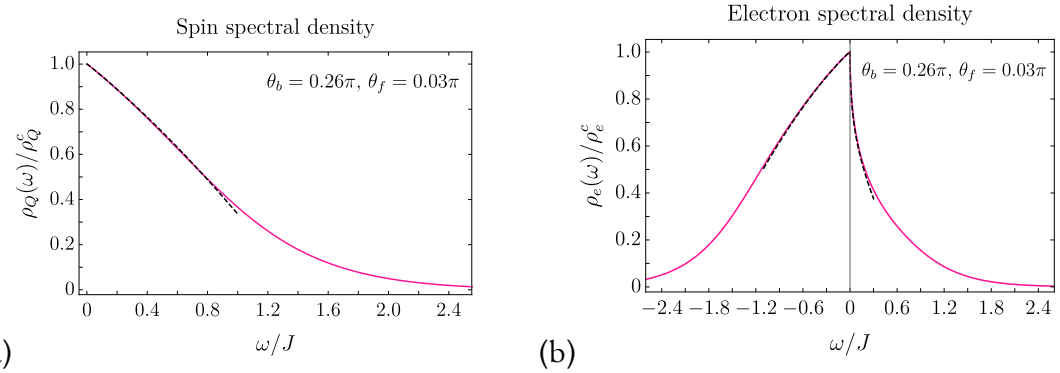

Figure 3.10: Spin (a) and electron (b) spectral densities. Solid magenta lines are numerical solutions. Black dashed lines are given by analytical solution (3.94). Here $\theta_b = 0.26\pi$ and $\theta_f = 0.03\pi$. The exponents and fitting functions are given in Figs. 3.8, 3.9 respectively.

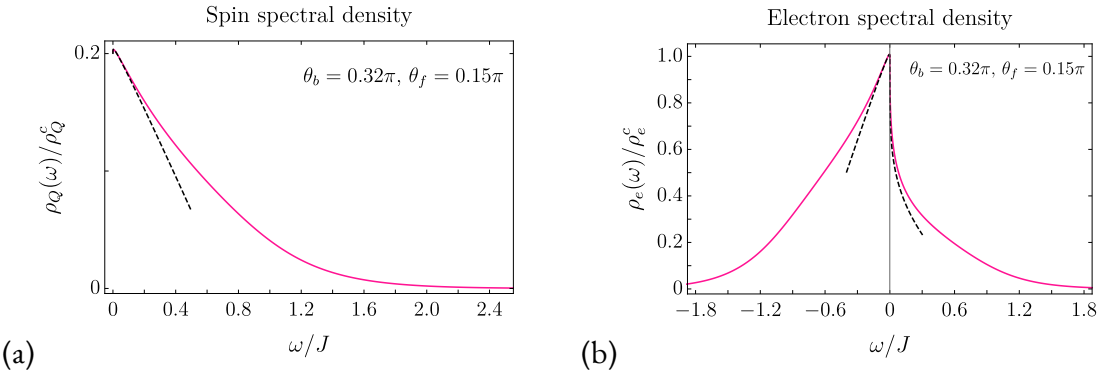

Figure 3.11: Spin (a) and electron (b) spectral densities. Same as in the Fig.3.10 except the parameters $\theta_b = 0.32\pi$ and $\theta_f = 0.15\pi$.

analytical formulas for spin and electron spectral densities are presented in the Figs. 3.9, 3.12. From the polynomials in the tables we notice that increasing the asymmetry angles leads to an increasing a linear coefficient compared to the coefficient of the $h_1 - 1$ exponent and coefficients of its non-linear corrections. Increasing the asymmetry angles up to the maximally allowed values, we observe that the linear coefficient is still comparable with all other terms. We show two examples of fitting the corresponding analytical expressions of the spin and electron spectral densities in the Figs. 3.10,3.11 for different asymmetry angles.

We conclude this section by discussing the optical and d.c. conductivity. In the Table 3.12 we present the analytical expressions for optical conductivity at zero temperature and finite temperature d.c. conductivity with all parameters fixed. We note that even though we do not discuss the finite temperature exact numerical solution in this paper, the coefficients α_b are fixed to their zero temperature values, and therefore, we can write down the analytical formulas at finite temperature as well. We again notice increasing the asymmetry angles leads to increasing the linear coefficient. Within the allowed range of asymmetry angles ($\theta_f \leq 0.15\pi$, as discussed in the Appendix B.1) the linear coefficient becomes larger but not large enough to neglect other terms. We explicitly show a behavior of optical conductivity at zero temperature in Fig. 3.13 for different asymmetry angles.

θ_f, θ_b	$\sigma^{\rm opt}/\sigma_0 - 1, \quad T = 0$	$\sigma^{\rm DC}/\sigma_0 - 1, \quad T \neq 0$
$0.03\pi, 0.26\pi$	$-0.50\left\|\frac{\omega}{J}\right\| + 0.65\left\|\frac{\omega}{J}\right\|^{0.94} - 0.96\left\|\frac{\omega}{J}\right\|^{0.47}$	$-0.50\left\|\frac{T}{J}\right\| - 1.48\left\|\frac{T}{J}\right\|^{0.47}$
$0.08\pi, 0.26\pi$	$-0.62\left\|\frac{\omega}{J}\right\| + 0.62\left\|\frac{\omega}{J}\right\|^{0.94} - 0.95\left\|\frac{\omega}{J}\right\|^{0.47}$	$-0.62\left\|\frac{T}{J}\right\| - 1.46\left\|\frac{T}{J}\right\|^{0.47}$
$0.13\pi, 0.26\pi$	$-0.97\left\|\frac{\omega}{J}\right\| + 0.53\left\|\frac{\omega}{J}\right\|^{0.93} - 0.91\left\|\frac{\omega}{J}\right\|^{0.47}$	$-0.97\left\|\frac{T}{J}\right\| - 1.39\left\|\frac{T}{J}\right\|^{0.47}$
$0.14\pi, 0.26\pi$	$-1.09\left\|\frac{\omega}{J}\right\| + 0.51\left\|\frac{\omega}{J}\right\|^{0.93} - 0.89\left\|\frac{\omega}{J}\right\|^{0.47}$	$-1.09\left\|\frac{T}{J}\right\| - 1.37\left\|\frac{T}{J}\right\|^{0.47}$
$0.15\pi, 0.26\pi$	$-1.24\left\|\frac{\omega}{J}\right\| + 0.47\left\|\frac{\omega}{J}\right\|^{0.93} - 0.87\left\|\frac{\omega}{J}\right\|^{0.47}$	$-1.24\left\|\frac{T}{J}\right\| - 1.34\left\|\frac{T}{J}\right\|^{0.47}$
$0.03\pi, 0.32\pi$	$-0.54\left\|\frac{\omega}{J}\right\| + 0.06\left\|\frac{\omega}{J}\right\|^{0.91} + 0.15\left\|\frac{\omega}{J}\right\|^{0.69} - 0.12\left\|\frac{\omega}{J}\right\|^{0.46} - 0.70\left\|\frac{\omega}{J}\right\|^{0.23}$	$-0.54\left\|\frac{T}{J}\right\| - 0.90\left\|\frac{T}{J}\right\|^{0.23}$
$0.08\pi, 0.32\pi$	$-0.67\left\|\frac{\omega}{J}\right\| + 0.06\left\|\frac{\omega}{J}\right\|^{0.91} + 0.14\left\|\frac{\omega}{J}\right\|^{0.68} - 0.12\left\|\frac{\omega}{J}\right\|^{0.45} - 0.70\left\|\frac{\omega}{J}\right\|^{0.23}$	$-0.67\left\|\frac{T}{J}\right\| - 0.88\left\|\frac{T}{J}\right\|^{0.23}$
$0.13\pi, 0.32\pi$	$-1.04\left\|\frac{\omega}{J}\right\| + 0.06\left\|\frac{\omega}{J}\right\|^{0.89} + 0.11\left\|\frac{\omega}{J}\right\|^{0.67} - 0.13\left\|\frac{\omega}{J}\right\|^{0.44} - 0.67\left\|\frac{\omega}{J}\right\|^{0.22}$	$-1.04\left\|\frac{T}{J}\right\| - 0.85\left\|\frac{T}{J}\right\|^{0.22}$
$0.14\pi, 0.32\pi$	$-1.18\left\|\frac{\omega}{J}\right\| + 0.06\left\|\frac{\omega}{J}\right\|^{0.88} + 0.11\left\|\frac{\omega}{J}\right\|^{0.66} - 0.14\left\|\frac{\omega}{J}\right\|^{0.44} - 0.67\left\|\frac{\omega}{J}\right\|^{0.22}$	$-1.18\left\|\frac{T}{J}\right\| - 0.84\left\|\frac{T}{J}\right\|^{0.22}$
$0.15\pi, 0.32\pi$	$-1.35\left\|\frac{\omega}{J}\right\| + 0.06\left\|\frac{\omega}{J}\right\|^{0.87} + 0.10\left\|\frac{\omega}{J}\right\|^{0.65} - 0.14\left\|\frac{\omega}{J}\right\|^{0.44} - 0.66\left\|\frac{\omega}{J}\right\|^{0.22}$	$-1.35\left\|\frac{T}{J}\right\| - 0.83\left\|\frac{T}{J}\right\|^{0.22}$

Figure 3.12: Table of computed analytical expressions of optical conductivity (3.95) at zero temperature (second column) and DC conductivity (3.83) at finite temperature with all parameters fixed for a range of asymmetry angles (θ_f, θ_b). The polynomials approximate a corresponding numerical solution at small frequencies. The exponents are given by $h - 1$ where the values of h are presented in the Fig. 3.8.

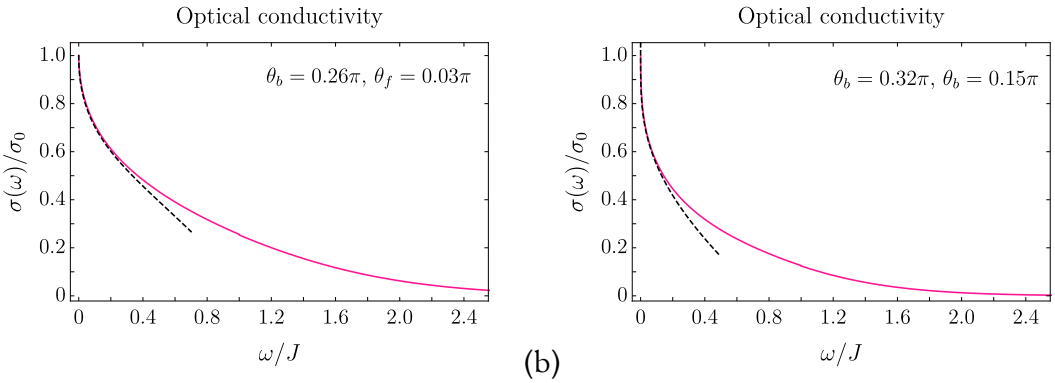

Figure 3.13: Optical conductivity for (a) $\theta_b = 0.26\pi$ and $\theta_f = 0.03\pi$ and (b) $\theta_b = 0.32\pi$ and $\theta_f = 0.15\pi$. Numerical solutions in both plots are given by the solid magenta lines and the black dashed lines are the analytical solutions presented in Fig. 3.12.

3.6 Conclusions

We have presented detailed numerical and analytic solutions of a critical non-Fermi liquid phase of random *t-J* models without quasiparticle excitations. This non-Fermi liquid phase of the *t-J* model has been proposed as a model for optimal doping criticality in the cuprates[92]. In this phase, fractionalized holons and spinons realize a deconfined critical state between two conventional states. At large doping, we use bosonic chargons which condense to realize a conventional Fermi liquid. At small doping, the pseudogap phase is realized by condensing bosonic spinons to form a metallic spin glass. In between these phases, lies the critical non-Fermi liquid studied in the present paper.

The solutions were obtained the large M limit of a model with SU(M) spin symmetry, and follow our previous analyses of the undoped insulator in Ref. [174]. The theory has the structure of the SYK model for fractionalized spinons and holons carrying gauge charges, which have random $q = 4$ body interaction terms between them. Note, however, that expressed in terms of the underlying gauge-invariant electrons, the interactions are not of the $q = 4$ SYK form. We found good agreement between the numerical and analytic approaches.

Section 3.2 derived the saddle point of a large dimension *t-J* models with random nearest-neighbor exchange and global SU(M) spin rotation symmetry. This approach helps define transport observables, including the conductivity, whose properties we have examined here. However, the same saddle point equations also apply to the model with all-to-all and random hopping and exchange for which the connection to SYK models is more direct.

Our attention focused on the leading and sub-leading singularities of several gauge-invariant physical observables at low frequencies and temperatures. These are controlled by operators with scaling dimension h which perturb the leading conformally invariant solution. As the theory is in $0+1$ space-time dimensions, we require $h > 1$ for the operator to be irrelevant in the infrared, and contribute to the sub-leading singularities.

An important operator that appears in all the subleading corrections is the time-reparameterization mode, or the boundary graviton of the holographic dual. This operator is universal in SYK criticality, and has $h_0 = 2$ exactly; no corrections are expected to this scaling dimension at all orders in $1/M$. It was also present in the previous analysis of the insulating model [174]. This operator leads to relative corrections in observables which scale ω^{h_0-1} or T^{h_0-1} in the IR. In particular, as the leading contribution to the resistivity is T-independent in the *t-J*, the first contribution from the graviton mode is a linear-in-T resistivity [81].

We also found that the *t-J* model has an irrelevant operator with scaling dimension $1 < h_1 < 2$ over the regime where scaling solutions were found numerically (see Fig. 3.8). No such operator appears in the insulating *J* model examined in the earlier paper [174]. This new operator will therefore lead to corrections which scale as ω^{h_1-1} or T^{h_1-1} in the IR, which are more singular than those from the graviton mode. However, it should be noted that this operator is not protected, and we do expect $1/M$ corrections to the value of h_1. We have not studied these corrections, and the possibility remains that such corrections will increase the value of h_1 above 2, and return the graviton mode as the dominant correction. Moreover, we found that the numerical co-efficient of the h_1 correction was quite small in the spin spectral density, and significantly smaller than that of the h_0 correction (see Fig. 3.9).

We note from Figs. 3.9 and 3.12 that the contributions of h_1 mode are more significant for the other observables, including the d.c. resistivity, and can be comparable to the $h_0 = 2$ contribution. It would be interesting to study the relative contributions of these modes at higher order in $1/M$ to understand the situation for SU(2) better.

A recent exact-diagonalization study of the random *t-J* model with SU(2) spin symmetry [160] computed the spin spectral density and found that it matched the spectral density similar to Fig. 3.10a over a wide range of frequencies near the critical doping where the spin-glass order vanished (spin-glass order is present at $M = 2$ for low doping). The numerics show $\rho_Q(\omega) \sim \mathrm{sgn}(\omega)\,[c_0 - c_1|\omega| + \ldots]$ at small ω, consistent with the numerical results in Table 3.9 where the h_1 contribution is small. It is

quite remarkable and encouraging that this numerical result at the physical values $M = 2$ and $M' = 1$ matches well with the large M, M' (with $k = M'/M$ fixed) theory considered in the present paper.

4

Maximal quantum chaos of the critical Fermi surface

The study of relaxational and thermalization phenomena in quantum many body systems has long relied on the quasiparticle decomposition of many body states, and the collisions of quasiparticles described by the Boltzmann equation and its generalizations. However, this powerful method is not reliable when we address similar phenomena in non-Fermi liquids without any quasiparticle excita-

tions. General arguments have been presented that such dissipative phenomena cannot occur at a rate which is parametrically larger than $k_B T/\hbar$ as the absolute temperature $T \to 0$ (so such a rate cannot vanish as T^a, with an exponent $a < 1$), and systems without quasiparticles have a rate of order $k_B T/\hbar$[84,29,152,20,185,71].

New insights into such issues have emerged from recent advances in the study of many-body quantum chaos and out-of-time-order correlators (OTOCs), for which the bounds on dissipative rates can be made precise. Inspired by holographic connections to the quantum dynamics of black holes, Maldacena, Shenker and Stanford[120] established that the Lyapunov exponent, λ_L, characterizing the temporal growth of the OTOC must be smaller than $2\pi k_B T/\hbar$. We can expect that any system which is close to this bound as $T \to 0$ cannot have a quasiparticle description, and this conclusion is supported by computations on the Sachdev-Ye-Kitaev (SYK) model[121,104]. Although difficult to measure in experiments, OTOCs have therefore emerged as an alternative to the Boltzmann equation, and are a valuable diagnostic of the physics of non-quasiparticle systems.

In this paper, we address the OTOC of a class of non-Fermi liquids most relevant to correlated electron systems[115]. We consider a Fermi surface coupled to a U(1) gauge field in two spatial dimensions, but our theory also applies to Fermi surfaces coupled to other critical bosons, as are realized near symmetry-breaking quantum phase transitions in metals with a zero momentum order parameter. The OTOC of such a system was addressed in previous work[145] in an uncontrolled analysis: it was found that $\lambda_L = \alpha k_B T/\hbar$ as $T \to 0$ with the constant $\alpha < 2\pi$. The present paper will present new results on this model which build on two recent developments:

(*i*) Gu and Kitaev (GK)[77] have shed new light on the structure of OTOCs in spatially extended systems. They established a ladder identity which shows that there is an additional contribution to the OTOC that arises from a pole at imaginary momentum, in the complex momentum plane. Provided the chaos butterfly velocity, v_B, is large enough, the pole contribution dominates at large spatial distances, and the resulting growth of the OTOC with time has exponent λ_L exactly equal to $2\pi k_B T/\hbar$.

(*ii*) A systematic approach to the study of the two-dimensional non-Fermi liquid state has been proposed[49,4]. This approach obtains the non-Fermi liquid as the large N saddle-point of a path integral over bilocal Green's functions and self energies. The new idea here is to study an ensemble of theories with different random couplings (but without spatial randomness), under the hypothesis that all of them flow to the same universal fixed point theory at low energies. Such a large N saddle-point is ideally suited to develop a systematic computation of the OTOC, along the lines of computations on the SYK model.

In our large N analysis of the two-dimensional non-Fermi liquid, we find that the butterfly velocity does indeed satisfy the needed inequality of GK. This leads to our main result: that the Lyapunov exponent of this system equals the maximal value of $2\pi T$ ($\hbar = k_B = 1$ henceforth).

4.1 The model

Our results are obtained within the 'patch' theory of the two-dimensional non-Fermi liquid[114,128], which describes the low energy properties of the Fermi surface without quasiparticles. Each point on the Fermi surface is characterized by a Fermi velocity v_F, and Fermi surface curvature κ/v_F. We introduce fermion fields $\psi_{\pm,j}$ ($j = 1 \ldots N$) defined in patches ($\pm$) near antipodal points, using the coordinate system shown in Fig. 4.1. The dispersion of the fermions in this co-ordinate system is $\varepsilon_k = \pm v_F k_x + (\kappa/2) k_y^2$, and we will henceforth use length scales in which $v_F = 1$ and $\kappa = 2$. These fermions are coupled to bosons φ_l ($l = 1 \ldots M$), which is the transverse component of the gauge field, or a symmetry breaking order parameter. The universal properties of the critical Fermi surface

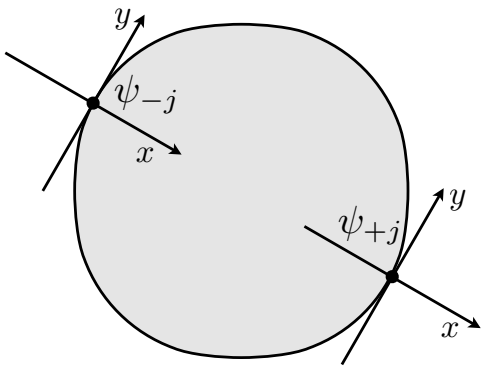

Figure 4.1: Antipodal patches $\pm$ on the Fermi surface.

in this patch theory are then described by the Lagrangian density

$$\begin{aligned}\mathcal{L} = &\sum_{r=\pm}\sum_{j=1}^{N}\psi^{\dagger}_{r,j}(\partial_\tau - ir\partial_x - \partial_y^2)\psi_{r,j} \\ &+ \sum_{r=\pm}\sum_{l=1}^{M}\sum_{ij=1}^{N}\frac{g_{ijl}}{N}r^s\psi^{\dagger}_{r,i}\psi_{r,j}\varphi_l + \frac{1}{2}\sum_{i=1}^{M}(\partial_y\varphi_i)^2\,. \end{aligned} \tag{4.1}$$

Here $s = 0$ for the nematic order parameter, and $s = 1$ for the gauge field; the value of s will not be important for any results here. The large N limit[49] is taken at fixed M/N, and for an ensemble of theories with spatially uniform (but flavor random) Yukawa couplings g_{ijl} which have zero mean and root mean square value g ($\overline{|g_{ijl}|^2} = g^2$). The scaling limit of the boson ($D(k)$) and fermion ($G_r(k)$) Green's functions can be computed exactly in the large N limit ($k = (\mathbf{k}, k_0) = (k_x, k_y, k_0)$, where k_0 is an imaginary Matsubara frequency)

$$\begin{aligned} D(k) &= \frac{|k_y|}{|k_y|^3 + c_b|k_0| + m^2}, \\ [G_r(k)]^{-1} &= rk_x + k_y^2 - i\mu(T)\mathrm{sgn}(k_0) \\ &\quad - ic_f\mathrm{sgn}(k_0)T^{2/3}H_{1/3}\left(\frac{|k_0| - \pi T\mathrm{sgn}(k_0)}{2\pi T}\right), \end{aligned} \tag{4.2}$$

where $H_{1/3}(z) = \zeta(1/3) - \zeta(1/3, z+1)$ the analytically continued harmonic number function of order $1/3$, and c_f and c_b are coupling dependent constants:

$$c_f = \frac{M}{N}\frac{2^{4/3}g^{4/3}}{3^{3/2}}\,, \quad c_b = \frac{g^2}{4\pi}\,. \tag{4.3}$$

We have also introduced a finite but small mass m^2 in the boson Green's function as an infrared regulator, and $\mu(T) = g^2 T/(3\sqrt{3}m^{2/3})$. We will eventually take the $m \to 0$ limit, and obtain a finite answer for the OTOC. To solve for the OTOC we use retarded and Wightman Green's functions, the forms of which we discuss in the Supplementary Information. For simplicity, we will also henceforth consider only the $+$ patch on the Fermi surface and drop the patch indices [*]: in the Supplementary Information, we show that the interactions between antipodal patches do not change the behavior of the OTOC.

4.2 The OTOC

We will be interested in the OTOC contianed within the squared anticommutator of fermionic operators

$$\mathcal{C}_x(t,0) = \frac{1}{N^2}\theta(t)\sum_{i,j=1}^{N}\mathrm{Tr}\Big[e^{-\beta H/2}\{\psi_i(x,t),\psi_j^\dagger(0)\}\,e^{-\beta H/2}\{\psi_i(x,t),\psi_j^\dagger(0)\}^\dagger\Big], \tag{4.4}$$

The function in (4.4) contains the OTOC $\langle\psi_i(x,t)\psi_j^\dagger(0)\psi_i^\dagger(x,t)\psi_j(0)\rangle$ (up to insertions of $e^{-\beta H/2}$), which describes chaos in the system and grows exponentially as $\sim e^{\lambda_L t} + \ldots$. We are interested in the spatial structure of (4.4) in the long time limit at large $|x|$. After Fourier transforming the spatial arguments to momentum space, and considering 4 distinct times for the fermion operators (see Fig. C.1 in

[*]For the theory with only one patch, the values of c_f, c_b are given by $c_f = (M/N)2^{5/3}g^{4/3}/3^{3/2}$ and $c_b = g^2/(8\pi)$.

the Supplementary Information), we generalize the construction of Kitaev and Suh [104] to argue that the early time OTOC can be written using a single mode ansatz

$$\mathrm{OTOC}_p(t_1,t_2,t_3,t_4;k,k') \simeq \frac{e^{\lambda_L(p)(t_1+t_2-t_3-t_4)/2}}{C(p)} \Upsilon_p^R(t_{12},k)\Upsilon_p^A(t_{34},k'). \tag{4.5}$$

Here the Υ's are vertex functions which only modify the overall magnitude of the OTOC. It was later shown by GK that the behavior of $C(p)$ is important for determining λ_L. As we review in the Supplementary Information, $C(p)$ has the important factor

$$C(p) \sim \cos\frac{\lambda_L(p)}{4T}. \tag{4.6}$$

which vanishes at the maximal value of $\lambda_L(p) = 2\pi T$. The resulting pole in (4.5) will ultimately be responsible for the maximal chaos in the non-Fermi liquid.

Now we can transform back to position space and obtain

$$\mathrm{OTOC}_x(t_1,t_2,t_3,t_4) \sim \frac{u(x,t)}{N}\int_{k,k'} \Upsilon_p^R(t_{12},k)\Upsilon_p^A(t_{34},k')\,,$$

where $t = (t_1+t_2-t_3-t_4)/2$ and

$$u(x,t) \sim \int_p \frac{e^{\lambda_L(p)t+ip\cdot x}}{\cos(\lambda_L(p)/(4T))}. \tag{4.7}$$

In the previous work [145], the chaos exponent was identified with $\lambda_L(0)$. GK performed a careful evaluation of the integral in (4.7) in one spatial dimension, and gave conditions under which it was dominated by the saddle point ($\lambda_L'(p=p_s)t + ix = 0$) or the pole ($\lambda_L(p=p_1) = 2\pi T$). Both the saddle point and the pole appear for purely imaginary values of momenta, with $p = i|p|$. When $|p_s| > |p_1|$, GK showed that the pole dominates, leading to a region of spacetime in which maximal chaos occurs.

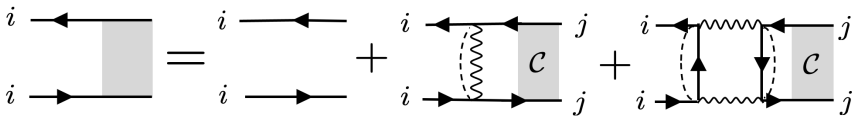

Figure 4.2: The Bethe-Salpeter equation for $\mathcal{C}(k_0, \omega, i|p_x|)$, which is exact at large N. Solid lines are fermion propagators, wavy lines are boson propagators and dashed lines are averaging over the flavor random couplings. The horizontal lines represent the retarded Green's functions and vertical lines are Wightman propagators.

Conversely, when $|p_s| < |p_1|$, the saddle point dominates, and there is no maximal chaos.

At first sight, it is not clear whether this one-dimensional analysis can be extended to the anisotropic two-dimensional non-Fermi liquid theory in (4.1). However, the theory in (4.1) has a 'sliding symmetry'[128], which implies that λ_L is a function only of $p_x + p_y^2$. This reduces the momentum integral in (4.7) to effectively a one-dimensional integral, and we can replace $p \cdot r$ by $p_x x$ and directly apply the results of GK.

4.3 The Lyapunov exponent

The remaining missing ingredient in determining whether the saddle point or the pole dominates for the critical Fermi surface is a knowledge of $\lambda_L(p)$ for imaginary p. For this we need to solve the Bethe-Salpeter equation for the squared anticommutator $\mathcal{C}$ in Fig. 4.2, with an imaginary external momentum. This leads to the following eigenvalue equation, extending the previously obtained equation[145] to an imaginary external momentum $p_x = i|p_x|$

$$\begin{aligned}
&\left[c_f T^{2/3}\left(H_{1/3}\left(\frac{-ik_0-\pi T}{2\pi T}\right)+H_{1/3}\left(\frac{-i(\omega-k_0)-\pi T}{2\pi T}\right)\right)-|p_x|+2\mu(T)\right]\mathcal{C}(k_0,\omega,i|p_x|)\\
&=g^2\frac{M}{N}\int\frac{dk_0'dk_y'}{(2\pi)^2}\frac{c_b(k_0-k_0')|k_y'|}{(|k_y'|^3+m^2)^2+c_b^2(k_0-k_0')^2}\frac{\mathcal{C}(k_0',\omega,i|p_x|)}{\sinh\frac{k_0-k_0'}{2T}}\\
&+\frac{g^{4/3}4\pi^{4/3}}{3\sqrt{3}}\frac{M}{N}\int\frac{dk_0'dk_{01}}{(2\pi)^2}\frac{(ik_{01}+(-ik_{01})^{2/3}(i(k_{01}-\omega)))}{k_{01}(i(k_{01}-\omega))^{1/3}(2k_{01}-\omega)}\frac{\mathcal{C}(k_0',\omega,i|p_x|)}{\cosh\frac{k_0-k_{01}}{2T}\cosh\frac{k_0'-k_{01}}{2T}}.
\end{aligned}\tag{4.8}$$

We note that the factors of M/N on the RHS of (4.8) cancel with those in the definition of c_f in

the $m \to 0$ limit, up to a rescaling of $p_x \to (N/M)p_x$. Therefore, considering $M \neq N$ will not affect any of our conclusions, and we will henceforth consider $M = N$ for simplicity.

4.4 Maximal chaos

Upon solving the eigenvalue equation (4.8), we obtain the Lyapunov exponent as a function of the external imaginary momentum $p_x = i|p_x|$. From Fig. 4.3, the values of the pole ($p_1 = i|p_1|$) and saddle point ($p_s = i|p_s|$) momenta can be obtained. The pole follows from $\lambda_L(p = p_1) = 2\pi T$, whereas for the saddle point, one needs to consider an additional condition, since the saddle point equation $\lambda_L'(p = p_s)t + ix = 0$ does not define the value of $|p_s|$. This condition follows from the fact that the ansatz (4.7) is valid only in the regime where initial correlations and non-linear effects can be ignored, which is when $\mathrm{OTOC}_x(t_1, t_2, t_3, t_4) \gg 1/N$, and therefore $u(x, t) \sim 1$. This gives the condition on the saddle point value $\lambda_L(p = p_s)t + ip_s x = 0$[77]. Combining this equation with the saddle point equation, we can then obtain $|p_s|$ from the graphical solution of $\lambda_L'(p = p_s) = \lambda_L(p = p_s)/|p_s|$.

As shown in Fig. 4.3, $|p_1|$ is significantly smaller than $|p_s|$. Specifically, we find $|p_1| \simeq 0.65\, g^{4/3} T^{2/3}$ and $|p_s| \simeq 1.04\, g^{4/3} T^{2/3} > |p_1|$, which confirms the dominance of the pole contribution according to GK. The chaos wavefront therefore travels with a butterfly velocity $v_B = 2\pi T/|p_1|$ set by the pole contribution. We note that $\lambda_L(p_x)$ does not depend upon the coupling g, as g can be removed by rescaling the external momentum $p_x \to p_x/g^{4/3}$. With no other dimensionful parameters in (4.8), this also implies that λ_L is proportional to temperature.

4.5 Phenomenological models

We extend our analysis to non-Fermi liquids with dynamical critical exponent $2 < z \leq 3$, in which quasiparticle excitations are still absent, and compute the Lyapunov exponents. For those theories,

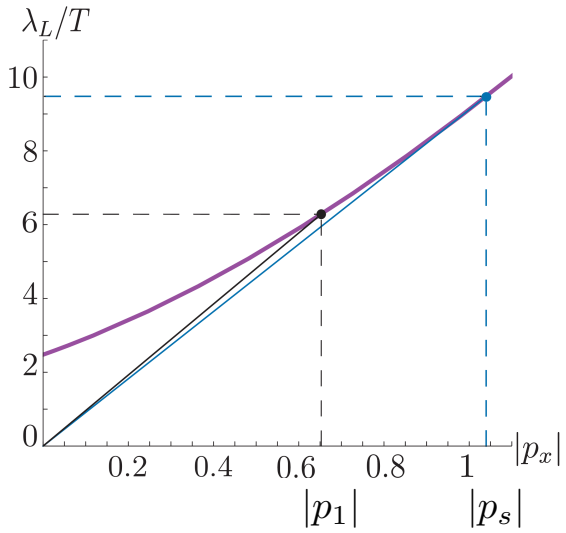

Figure 4.3: Plot of the Lyapunov exponent λ_L/T as a function of $|p_x|$. $|p_x|$ is presented in units of $g^{4/3}T^{2/3}$. We find $|p_1| \simeq 0.65\, g^{4/3}T^{2/3}$ and $|p_s| \simeq 1.04\, g^{4/3}T^{2/3}$. Since $|p_s| > |p_1|$, the butterfly velocity is given by $v_B = 2\pi T/|p_1| \simeq 9.67 g^{-4/3}T^{1/3}$ (slope of the black solid line). We also find the value of the velocity at the saddle point $v_s = 9.01\, g^{-4/3}T^{1/3}$ (slope of the blue solid line). As expected from previous work[145], we find $\lambda_L(0) = 2.48\ T$.

the boson Green's function has the form[49]

$$D(k) = \frac{|k_y|}{|k_y|^z + c_b|k_0| + m^2},$$

and the fermion self energy scales as $\Sigma \sim i\mathrm{sgn}(k_0)|k_0|^{2/z}$ ($z = 3$ for the original theory discussed earlier). Since $|\Sigma| \gg |k_0|$, quasiparticle excitations are not well defined in terms of the fermion spectral function.

The form of the eigenvalue equation for the OTOC changes slightly, and is discussed in the Supplementary Information. As we show in the Fig. 4.4, for each of these theories the butterfly velocity is also given by $v_B = 2\pi T/|p_1|$, and the Lyapunov exponent is maximal. To show this, we first solve the eigenvalue equations up to the pole momentum p_1. We then compare the instantaneous slope at p_1, which we call v_*, and the velocity $v_1 = 2\pi T/|p_1|$. For each plot we obtain $v_1 > v_*$. Since each of the curves in Fig. 4.4 is a positive, monotonically increasing, and convex function, this implies that

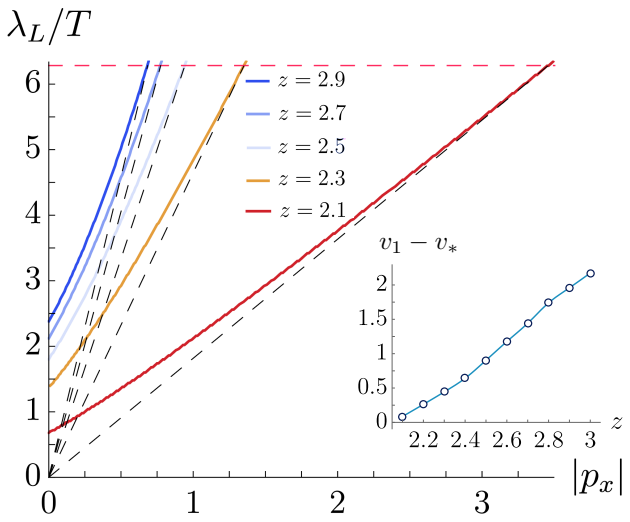

Figure 4.4: Main plot: resulting plots of the Lyapunov exponent λ_L/T as a function of $|p_x|$, for different values of the dynamical critical exponent $2 < z \leq 3$. The slopes of the black dashed lines are the butterfly velocities v_B. Inset: difference between $v_1 = v_B$ and the instantaneous slopes at $p_x = p_1$ (*i.e.* v_*). The difference is always positive, *i.e.* $\lambda_L(i|p_1|)/|p_1| > \lambda_L'(i|p_1|)$, which shows that the value of $|p_s|$, where $\lambda_L(i|p_s|)/|p_s| = \lambda_L'(i|p_s|)$, must be larger than $|p_1|$, leading to maximal chaos according to GK.

$|p_s| > |p_1|$, and the pole contribution therefore dominates with maximal chaos just like in the $z = 3$ case. We can further find the behavior of the exponent in the Fermi liquid case of $1 < z < 2$, in which quasiparticles are present. In this regime, $|\Sigma| \sim |k_0|^{2/z} \ll |k_0|$, and therefore the quasiparticle peak in the fermion spectral function is well defined. Similar to the discussion above, we can compute the Lyapunov exponent as a function of external momentum on imaginary axis and explicitly find $|p_s|$ and $|p_1|$. For a particular case of $z = 3/2$ [†], we find that the saddle point dominates as $|p_s| \simeq 4.32$, which is smaller than $|p_1| \simeq 7.84$. The resulting butterfly velocity in this case is $v_B \simeq 0.8\, v_F$, where $v_F = 1$ is the Fermi velocity. This result is expected from a general point of view: for a free fermion theory the exponent is a simply linear function of the external momentum $\lambda_L(i|p_x|) = |p_x|$ leading to the saddle point contribution at $|p_s| = 0$. We therefore expect that for any theory with quasiparticles, the pole contribution is negligible compared to a saddle point contribution, and the maximal chaos is

[†]The numerical values of $|p_s|$ and $|p_1|$ are provided for chosen parameters $g = 0.5$, $\Lambda = 50$, $T = 1$, and $z = 3/2$. See Supplementary Information for more details.

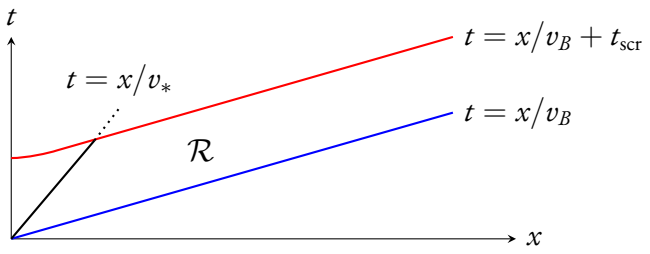

Figure 4.5: (Adapted from GK) Maximal chaos is present in the spacetime region denoted by $\mathcal{R}$, which is bounded by the three solid lines. Here $v_* = \lambda_L'(i|p_1|)$, and $t_{\rm scr} \sim \ln N$. As z is reduced from 3 to 2, v_* approaches $v_B = v_1$ from below (Fig. 4.4), and the size of the maximally chaotic region $\mathcal{R}$ is therefore squeezed to zero by the falling slope of the black line as $z \to 2$. For $z < 2$, there is consequently no maximally chaotic region.

no longer present (Supplementary Information).

4.6 Discussion

It is quite remarkable that the generic low energy theory of Fermi surfaces without quasiparticles in two spatial dimensions displays maximal chaos in the large N limit. Other spatially extended models connected to the SYK model (*e.g.* [80,98]), and certain conformal field theories [177,83,82], have been shown to display maximal chaos, but none of them have spatially dependent Green's functions *and* live in more than one spatial dimension. It is also remarkable that the critical Fermi surface displays maximal chaos without the presence of conformal symmetry, which also sets it apart from the previously mentioned examples that have conformal symmetry.

We believe that the maximal chaos of the Fermi surface is linked to the local nature of the singular self energy of the fermion at large N *i.e.* the self energy is frequency dependent, but independent of momentum, a feature the Fermi surface theory shares with the SYK model (along with the local frequency-only dependence of the fermion pairing vertex [49]). There are small contributions to the fermion anomalous dimension at 3-loop order [128], which are expected to make the self energy nonlocal, and it remains to be seen if such effects could reduce the maximal Lyapunov exponent. However, since $|p_s| - |p_1|$ is $\mathcal{O}(1)$ at large N (Fig. 4.3), we expect that the small $\mathcal{O}(1/N)$ corrections to

this quantity will not immediately be able to change its sign and thus reduce the maximal Lyapunov exponent.

We also examined a phenomenological model of a critical Fermi surface with dynamic critical exponent $z \leq 3$; quasiparticles re-emerge in such a model for $z < 2$. We found that the maximal chaos was retained for precisely the regime where quasiparticles are absent, $2 < z \leq 3$, although the size of the spacetime region for which it occurs shrinks to zero as $z \to 2$ (Fig. 4.5). It is also remarkable that the acceleration of chaos to the maximal rate by the butterfly effect is tied to the destruction of quasiparticles in this model. When quasiparticles are present, we found that the saddle-point contribution dominated with $\lambda_L \sim T^{2/z} \ll T$, which is parametrically smaller than the maximal rate (Appendix C).

5

Critical metallic phase in the overdoped random $t - J$ model

5.1 Introduction

Recent experimental works have highlighted certain fundamental properties of cuprate superconductors and their complex and rich phase diagrams. One of the key aspects is a transformation in the

normal state near an optimal doping $p = p_c$ [148,130,13,28] indicated most recently by thermal-Hall transport measurements [148,13] and by photoemission experiments [28]. While much attention has focused on the anomalous properties of the underdoped regime ($p < p_c$), it is often assumed that the overdoped regime ($p > p_c$) is a conventional Fermi liquid, and thus the latter has not attracted as much attention. However, careful experimental studies have reported significant strange-metal anomalies in transport properties also on the overdoped side [34,70,11]. These observations indicate the presence of a non-Fermi-liquid metal in an extended doping region above optimal doping. On the underdoped side, recent experiments have established that there is a spin glass phase [138,55] in the La-based compounds.

Concordant with these observations, we present here a theoretical model with an extended non-Fermi-liquid phase at large dopings, and a spin-glass phase at low doping.

Models with random interactions on a fully connected lattice in the Sachdev-Ye-Kitaev class [156,105] yield a systematic route to studying non-Fermi liquids: the exact solutions of such models serve as dynamic mean-field theories of more realistic microscopic models [85,86,29]. In this paper we report numerical and analytic solutions of a *t-J* model (Eq. (5.1)) with random and all-to-all hopping and exchange interactions across a wide range of doping. The model has a global SU(M) spin rotation symmetry, and we study a particular SYK-like large M limit with fermionic spinons. A previous study [92] found possible critical solutions of non-Fermi liquid metals by an analytic study of the low energy limit of the saddle point equations of this large M limit. From renormalization group arguments it appeared that these possible critical solutions only described a critical point or a small range of intermediate doping, and that a Fermi liquid solution would appear in the overdoped regime.

The present paper will present a full numerical solution of these large M saddle point equations for a wide range of doping. The solutions are obtained on both the real and imaginary frequency axes, with mutually consistent results. We also supplement the numerical results with asymptotic analytic analyses. Our main results are that the Fermi liquid is never the solution of the large-M saddle-point equations, and that one of the low energy critical solutions obtained earlier [92] extends to an all-energy

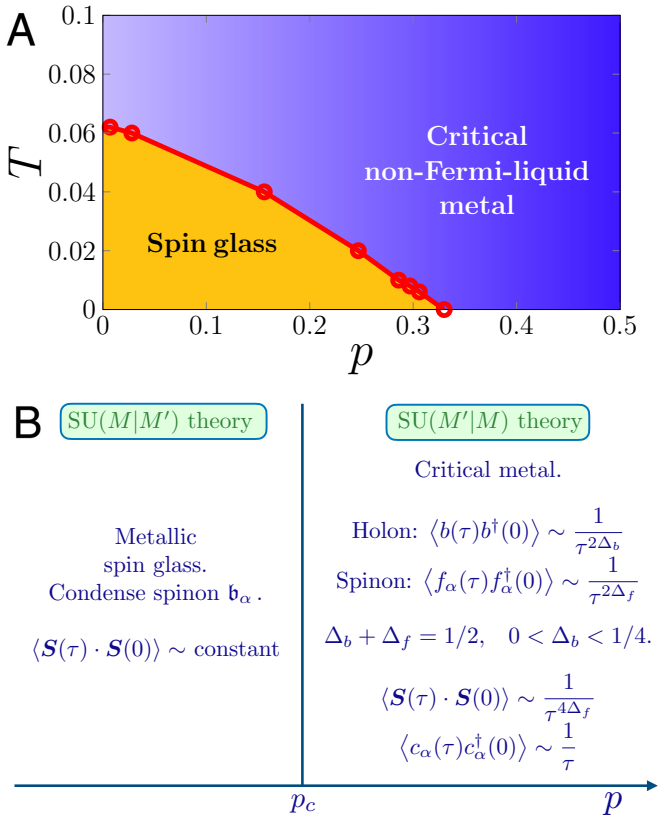

Figure 5.1: (A) Phase diagram as a function of doping p and temperture T obtained from numerically solving the fermionic spinon large M saddle-point equations of the random t-J model in Eq. (5.1) for $t = J = 1$. The red circles are critical doping value ($p_c(T)$) at a given temperature, obtained by looking at the spin-glass instability in the non-Fermi-liquid solution. The uncertainty for each p_c is within 0.003. The critical doping at $T = 0$ is obtained by directly solving the saddle-point equations on the real-frequency axis. (B) Properties of the $T = 0$ states. The low-doping spin-glass phase and large-doping critical-metal phase are separated by a quantum critical point at p_c. The critical metal has doping-dependent exponents $\Delta_{f,b}$, and a linear-T resistivity.

solution of the large-M equations in the entire overdoped regime. We further show that there is a phase transition to a low-doping spin-glass phase and construct a phase diagram (see Fig. 5.1).

Notable features of the novel critical non-Fermi liquid phase in Fig. 5.1 are

(*i*) spin correlations decay with an exponent which varies continuously with doping (unlike a Fermi liquid),

(*ii*) the electron correlators have the $\sim 1/\tau$ decay with imaginary time (as in a Fermi liquid), but with a pronounced particle-hole asymmetry (which is weak in a Fermi liquid), and

(*iii*) the mechanism of Ref.[81] applies across the entire overdoped critical phase, and the resistivity has a linear-T contribution as $T \to 0$ at all dopings in this phase (unlike the T^2 resistivity in a Fermi liquid).

We also note here that there is a distinct large M limit of the random *t-J* model[139] which yields a Fermi liquid ground state at all non-zero doping. We will discuss the relation to this limit in Section 5.5.

The plan of the paper is as follows. In Section 5.2 we introduce the model and discuss its general properties. In Section 5.3 we consider the critical solutions of the model introduced in Eq. (5.1), and show that there is a critical solution with doping-dependent exponents in the overdoped region. We then solve this model at zero temperature (Section 2.5.3.1), as well as finite temperature (Section 2.5.3.2), and show that it has an instability to a spin-glass phase. The results for spectral functions in the spin-glass phase are presented in Section 5.4 using an alternative bosonic spinon large M limit. In both phases we report physical observables such as electron and spin spectral densities at both zero and finite temperatures. We conclude with a discussion and implication of our results in Section 5.5. Technical details and additional results are presented in the appendices.

5.2 Model

We consider a model of electrons with random and all-to-all hopping and exchange interaction with double occupancy being prohibited. This is the random *t-J* model which considers doping a random Heisenberg magnet[156]. It is in the class of SYK models[156,105] and is suitable for studying metallic phases obtained upon doping a Mott insulator. The Hamiltonian is

$$H = \frac{1}{\sqrt{N}} \sum_{i \neq j=1}^{N} t_{ij} c_{i\alpha}^{\dagger} c_{j\alpha} + \frac{1}{\sqrt{N}} \sum_{i<j=1}^{N} J_{ij} \vec{S}_i \cdot \vec{S}_j - \mu \sum_i c_{i\alpha}^{\dagger} c_{i\alpha} \,, \tag{5.1}$$

with the constraint, $\sum_\alpha c_{i\alpha}^{\dagger} c_{i\alpha} \leq 1$, since double occupancy is not allowed. In the above Hamiltonian, c_α is the electron annihilation operator with $\alpha = \uparrow, \downarrow$, the spin operator is $S_i^a = c_{i\alpha}^{\dagger} \sigma_{\alpha\beta}^a c_{i\beta}/2$, and μ is the chemical potential. The complex hoppings t_{ij} and real exchange interactions J_{ij} are independent random numbers with zero mean and mean-square values t^2 and J^2 respectively.

Note that one could also consider a *t-J* model with non-random nearest-neighbor hopping and nearest-neighbor random exchange interactions on a large dimensional lattice. The on-site dynamical mean-field equations for such a model are the same as those obtained for the model in Eq. (5.1). It also allows for a definition of transport quantities such as resistivity.

We will consider the problem at finite hole doping (p). This was recently studied both analytically[92,175] and numerically[160,46]. In particular, a deconfined critical point scenario was proposed in Ref.[92] to describe a quantum phase transition between a spin-glass phase at low doping with carrier density p and a Fermi-liquid phase at large doping with carrier density $1 + p$. The deconfined critical point proposed therein had the property that the local spin susceptibility was marginal as in the SYK models[156,105]. This was based on renormalization group arguments. However, a large-M analysis[92] led to two types of critical metallic solutions. One of the critical solutions corresponds to the deconfined critical point (although it is a phase in large-M limit), while the other was believed to be

suppressed in favor of a Fermi-liquid phase.

In this work we find that, in fact, the second critical solution is stable, and a Fermi-liquid phase is never achieved within a large-$\mathcal{M}$ approach at the saddle-point level. This critical phase has the property that while the exponent of the spin correlation continuously varies with doping, the linear-T resistivity is present over the entire overdoped phase. This makes it an attractive candidate for the overdoped phase of cuprate in the light of recent experiments[34,11]. In the underdoped region, below a critical doping p_c, we find a spin-glass phase. Thus, the critical metal at large doping and spin-glass phase at small doping are separated by a quantum critical point at a finite doping p_c, as shown in Fig. 5.1.

As a result of the double-occupancy constraint each site has three states, namely empty ($|0\rangle$) and singly-occupied ($|\uparrow\rangle$ and $|\downarrow\rangle$) states. These can be conveniently described using holon and spinon operators. The electron is thus fractionalized into holon and spinons. The critical metallic solutions in the overdoped region has gapless and critical fermionic spinons and bosonic holons (Section 5.3), while the underdoped spin-glass phase will be described by a fermionic holon and bosonic spinons (Section 5.4).

5.3 Critical non-Fermi-liquid metal phase

In this section, we show that our model in Eq. (5.1) admits a critical metallic solution. This phase is described by fermionic spinon (f_α) and bosonic holon (b) operators. The electron and spin operators can be then written in terms of these fractional particles as

$$c_{i\alpha} = b^\dagger f_{i\alpha}\,,\;\; S_i^a = f_{i\alpha}^\dagger \frac{\sigma^a_{\alpha\beta}}{2} f_{i\beta}\,, \tag{5.2}$$

with the constraint, $f_{i\alpha}^\dagger f_{i\alpha} + b_i^\dagger b_i = 1$. This theory realizes a SU(1|2) superalgebra. The strategy to solve the model in Eq. (5.1) is to generalize to a larger symmetry. The spin index on the spinon operator (f_α) is generalized to $\alpha = 1, \ldots, \mathcal{M}$ and there is an additional orbital index for holon (b_ℓ)

such that $\ell = 1, \ldots, \mathcal{M}'$. This theory realizes a SU($\mathcal{M}'|\mathcal{M}$) superalgebra. In this larger symmetry the electron and spin operators take the form,

$$c_{\ell\alpha} = b_\ell^\dagger f_{i\alpha}\,, \;\; S^a = f_\alpha^\dagger T^a_{\alpha\beta} f_\beta\,, \tag{5.3}$$

where the matrices T^a obey SU($\mathcal{M}$) algebra. The constraint now takes the general form,

$$f_\alpha^\dagger f_\alpha + b_\ell^\dagger b_\ell = \kappa \mathcal{M}\,. \tag{5.4}$$

The idea is to take a large-$\mathcal{M}'$, $\mathcal{M}$ limit such that $k = \mathcal{M}'/\mathcal{M}$ is finite. This large $\mathcal{M}$ limit is taken *after* we have performed a disorder average, and taken the large-volume limit. Note that this large $\mathcal{M}$ limit is distinct from the large $\mathcal{M}$ limit in Ref. [139], which had $\mathcal{M}' = 1$; the latter limit leads to a Fermi liquid phase at $T = 0$ at all non-zero doping.

A detailed analysis of our large $\mathcal{M}$ limit can be found in Refs. [92,175] and here we simply recall the saddle-point equations derived therein, which are

$$G_b(i\omega_n) = \frac{1}{i\omega_n + \mu_b - \Sigma_b(i\omega_n)}, \tag{5.5}$$

$$\Sigma_b(\tau) = -t^2 G_f(\tau) G_f(-\tau) G_b(\tau), \tag{5.6}$$

$$G_f(i\omega_n) = \frac{1}{i\omega_n + \mu_f - \Sigma_f(i\omega_n)}, \tag{5.7}$$

$$\Sigma_f(\tau) = -J^2 G_f(\tau)^2 G_f(-\tau) + kt^2 G_f(\tau) G_b(\tau) G_b(-\tau), \tag{5.8}$$

where G_b and G_f are the boson and fermion Green's function respectively, while Σ_b and Σ_f are the boson and fermion self energies respectively. Here τ is the imaginary time and ω_n are the Matsubara

frequencies. The chemical potentials μ_f and μ_b are chosen to satisfy

$$\left\langle f^\dagger f \right\rangle = \kappa - kp \quad , \quad \left\langle b^\dagger b \right\rangle = p \, .$$

We will restrict our attention to the physical case, $\kappa = 1/2$ and $k = 1/2$. In terms of the holon and spinon Green's functions, the electron Green's functions and the spin correlator are,

$$G_c(\tau) = -\langle T_\tau c_\alpha(\tau) c^\dagger(0) \rangle = -G_f(\tau) G_b(-\tau) \tag{5.9}$$

$$\chi(\tau) = \langle \vec{S}(\tau) \cdot \vec{S}(0) \rangle = -G_f(\tau) G_f(-\tau) \, . \tag{5.10}$$

Similar equations have been obtained by a dynamic mean field theory of a non-random *t-J* model on the square lattice using a 'non-crossing' approximation, and studied numerically[85,86].

To solve the saddle-point equations on the imaginary-frequency axis, it is convenient to define

$$\beta \bar{r} = -G_b(i\omega_n = 0) \, . \tag{5.11}$$

Then we can eliminate μ_b and obtain the following set of equations to solve

$$G_b(i\omega_n) = \frac{1}{i\omega_n - 1/(\beta \bar{r}) - \Sigma_b(i\omega_n) + \Sigma_b(i\omega_n = 0)} \tag{5.12}$$

$$\Sigma_b(\tau) = -t^2 G_f(\tau) G_f(-\tau) G_b(\tau) \tag{5.13}$$

$$G_f(i\omega_n) = \frac{1}{i\omega_n + \mu_f - \Sigma_f(i\omega_n)} \tag{5.14}$$

$$\Sigma_f(\tau) = -J^2 G_f(\tau)^2 G_f(-\tau) + kt^2 G_f(\tau) G_b(\tau) G_b(-\tau) \tag{5.15}$$

$$- G_b(\tau = 0^-) = p \tag{5.16}$$

$$G_f(\tau = 0^-) = \kappa - kp \tag{5.17}$$

Thus we have 6 equations to solve for the 6 variables $\bar{r}$, μ_f, G_f, G_b, Σ_f, Σ_b. Note that Eq. (5.12) holds for all ω_n.

5.3.1 Real-frequency solution at zero temperature

In this section we discuss the solutions of the saddle-point equations on the real-frequency axis at $T = 0$. The details of real-frequency equations corresponding to Eqs. (5.12)-(5.17) can be found in SI Appendix D.1. We look for a low-frequency conformal solution for the fermion and boson Green's functions with the following form:

$$G_a(i\omega_n) = -iC_a \begin{pmatrix} e^{-i\theta_a} \\ -e^{i\theta_a} \end{pmatrix} \frac{1}{|\omega|^{1-2\Delta_a}}\,, \tag{5.18}$$

where the subscript $a = f, b$ corresponds to the fermion and boson Green's function respectively. In the above ansatz, C_a is a constant, θ_a is an asymmetry parameter, and Δ_a is the exponent determining the critical solution. Below we shall discuss the relation between these parameters and different possible solutions. The vector notation is introduced to denote the positive and negative frequency parts of the solution. Using this form of the Green's function it is then straightforward to write the corresponding spectral densities,

$$\begin{aligned} \rho_a(\omega) &= -\frac{1}{\pi}\mathrm{Im}[G_a(i\omega_n = \omega + i0^+)] \\ &= \frac{C_a}{\pi} \begin{pmatrix} \sin(\pi\Delta_a + \theta_a) \\ \sin(\pi\Delta_a - \theta_a) \end{pmatrix} \frac{1}{|\omega|^{1-2\Delta_a}}\,. \end{aligned} \tag{5.19}$$

The exponents of the fermion and boson Green's functions satisfy the constraint $\Delta_f + \Delta_b = 1/2$. The ansataz considered in Eq. (5.18) admits three types of solutions[92]:

(i) $\Delta_f = \Delta_b = 1/4$: This is the solution that leads to a marginal spin correlation, i.e., a $1/\tau$ decay as in the SY spin liquid [156] found in the insulating case. In Ref. [175] it was shown that such a solution exists only in a very small doping range near $p = 0$. This is also the solution that corresponds to the deconfined critical point discussed in Ref. [92]. We will not discuss this solution any further here, because we believe the actual ground state at very low doping is a spin glass.

(ii) $\Delta_b = 0\,, \Delta_f = 1/2$: Such a solution would be the analog of the Fermi liquid solution found in the large M limit of Ref. [139]. However, it turns out that such a solution is not a valid solution of the saddle-point equations of the large M limit considered here. We provide more details in SI Appendix D.1.2 in this regard.

(iii) $1/4 < \Delta_f < 1/2$: Here the J term in the fermion self-energy in Eq. (5.15) is sub-dominant at low energies, although it does have contributions at higher energies. This solution results in doping-dependent exponents. As we shall see below, we find this solution to be present for all values of doping, and it will be a valid solution in the overdoped region. Our subsequent analyses in this section will focus on this solution.

We now briefly discuss our strategy to find the solution (iii) and more details can be found in SI Appendix D.1. The conformal solution ansataz introduced in Eq. (5.18) satisfies two Luttinger constraints [92,175],

$$\begin{aligned} \frac{\theta_f}{\pi} + \left(\frac{1}{2} - \Delta_f\right) \frac{\sin\left(2\theta_f\right)}{\sin\left(2\pi\Delta_f\right)} &= \frac{1}{2} - \kappa + kp\,, \\ \frac{\theta_b}{\pi} + \left(\frac{1}{2} - \Delta_b\right) \frac{\sin(2\theta_b)}{\sin(2\pi\Delta_b)} &= \frac{1}{2} + p\,. \end{aligned} \tag{5.20}$$

For solution (iii) the constants C_f and C_b can not be determined individually but their product is a constant. This leads to another constraint involving $\theta's$ and $\Delta's$ as shown in Ref.[92],

$$k = -\frac{\Gamma(2-2\Delta_f)\Gamma(2\Delta_f)\sin\big(\pi\Delta_f+\theta_f\big)\sin\big(\pi\Delta_f-\theta_f\big)}{\Gamma(2-2\Delta_b)\Gamma(2\Delta_b)\sin(\pi\Delta_b+\theta_b)\sin(\pi\Delta_b-\theta_b)}\,, \tag{5.21}$$

where $k = 1/2$ in our case. Together with the constraint $\Delta_f + \Delta_b = 1/2$ and Eqs. (5.20)-(5.21), there are four equations to solve for four variables, namely Δ_f, Δ_b, θ_f, and θ_b, at a fixed doping p. Solving these equations gives us these parameters as a function of doping, as shown in Fig. 5.2 and Fig. D.3. Determination of the constants C_f and C_b requires full solution of the saddle point equation at all frequencies, and the resulting values are shown in Fig. D.3. Of particular interest is the doping dependence of Δ_b, shown in Fig. 5.2.

In the large-M limit, from Eq. (5.10) it is clear that the anomalous dimension of the electron operator is $\eta_c = 2(\Delta_f + \Delta_b) = 1$ and that of the spin operator is $\eta_S = 4\Delta_f = 2 - 4\Delta_b$. Therefore, from Eq. (5.10), as a function of the imaginary time the electron Green's function and the local spin correlation have the form,

$$G_c(\tau) \sim \frac{1}{\tau}\,, \quad \chi(\tau) \sim \frac{1}{\tau^{2-4\Delta_b}}\,. \tag{5.22}$$

Thus we find that although the electron Green's function is Fermi-liquid like the spin correlation is not. Therefore the solution we have found is a critical metallic phase with a doping-dependent exponent of the spin correlation. Only in the limit $p \to 1$ we have $\Delta_b \to 0$, leading to a Fermi-liquid like spin correction with a $1/\tau^2$ decay.

Having established the presence of solution (iii), we now solve the saddle-point equations on the real-frequency axis numerically to obtain the full ω dependence of the boson and fermion spectral densities. Using these we can also obtain the electron and spin spectral densities. Fig. D.1 shows the full ω-dependent solution for the fermion and boson spectral densities, while in Fig. 5.3 we plot the electron and spin spectral densities. The boson and fermion spectral densities have the form $\rho_a(\omega) \sim$

$\omega^{2\Delta_a-1}$ with $a = f, b$. Since $\Delta_a < 1/2$, we plot the rescaled spectral densities in Fig. D.1. Note that the fermion and boson spectral densities are not observable quantities. However, the electron and spin spectral densities are observable in photoemission and neutron scattering experiments. These are defined as follows:

$$\rho_c = -\frac{1}{\pi}\mathrm{Im}[G_c(i\omega \to \omega + i0^+)] \tag{5.23}$$

$$\rho_s = \frac{1}{\pi}\mathrm{Im}[\chi(i\omega \to \omega + i0^+)] = \frac{1}{\pi}\chi''(\omega)\,. \tag{5.24}$$

In SI Appendix D.1 we present more details on evaluating these spectral densities.

As noted above, the most striking feature of our solution is a continuously varying spin-correlation exponent. This is clearly seen in Fig. 5.2*A* which shows the exponent of the spin correlator $\chi(\tau) \sim 1/|\tau|^{\eta_s}$ where $\eta_s = 4\Delta_f$, and in Fig. 5.3*B*, where $\chi''(\omega) \sim \mathrm{sgn}(\omega)|\omega|^{4\Delta_f-1}$ at low frequencies. Only in the limit $p \to 1$, we see a Fermi-liquid like behavior, $\chi''(\omega) \sim \omega$, as $\Delta_f \to 1/2$. The electron spectral density is a constant in the low-frequency limit with different values for $\omega \to 0^+$ and $\omega \to 0^-$ (see Fig. 5.3*A*), thus resulting in a discontinuity at $\omega = 0$. It clearly displays a particle-hole asymmetry throughout this phase, which is relevant in the context of understanding the measurement of Seebeck coefficient in recent experiments[69,61].

As for the SYK model[29], the conformal solutions to Eqs. (5.5)-(5.8) have time reparameterization symmetry when the self-energies are singular so that $G_{f,b}(i\omega_n)\Sigma_{f,b}(i\omega_n) \simeq -1$. Ref.[81] discussed a mechanism relating the time reparameterization symmetry to a linear-T contribution to the resistivity, and the same mechanism applies to the cases (i) and (iii) above. Briefly, to obtain a model with spatial structure, we consider the *t-J* model on a large dimension lattice with non-random t_{ij} but random nearest-neighbor J_{ij}. In the limit of large dimension, the self-energies become local, and the Green's functions and self-energies obey equations closely related to Eqs. (5.5)-(5.8). The conductivity in this large dimension model is given by the Kubo formula applied at one loop to the electron Green's

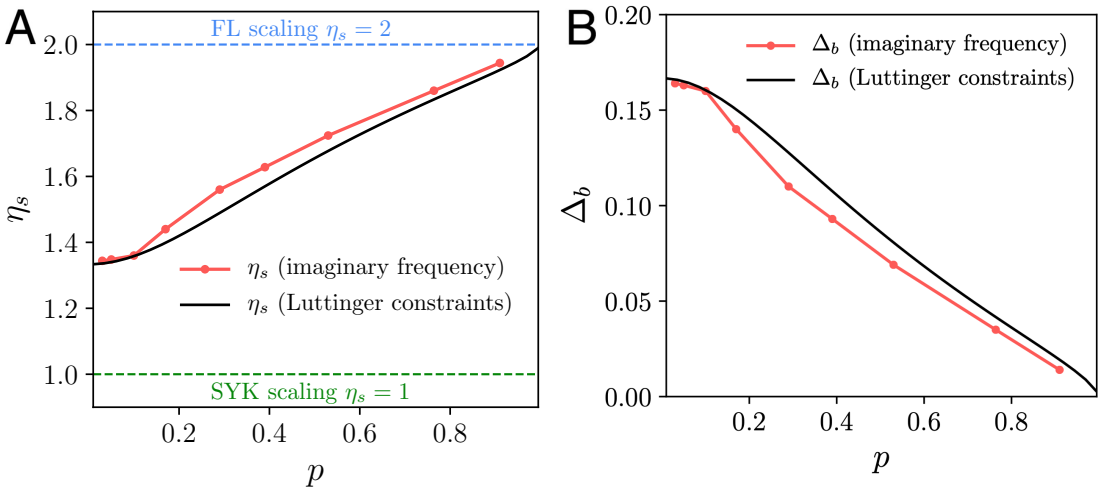

Figure 5.2: (A) We plot the doping dependence of the exponent η_s of the spin correlation $\chi(\tau) \sim 1/|\tau|^{\eta_s}$. We compute $\eta_s = 2 - 4\Delta_b$ in two independent ways, one by solving the Luttinger relations and the zero-frequency saddle point equations at $T = 0$ as explained in the text (black curve) and by computing η_s from the value of Δ_b obtained from the imaginary-frequency numerics (red curve), as discussed in Section 2.5.3.2. We find the two results in good agreement. At $p = 0$ we obtain $\eta_s = 4/3$, with η_s increasing monotonically with increasing doping such that $\eta_s \to 2$ as $p \to 1$. (B) We plot the doping dependence of Δ_b as obtained independently from the luttinger relations and $T = 0$ zero-frequency saddle point equations and from solving the imaginary frequency saddle point equations. We find at $p = 0$ $\Delta_b = 1/6$ and $\Delta_b \to 0$ as $p \to 1$. Consequently, this means $\Delta_f = 1/3$ at $p = 0$ and $\Delta_f \to 1/2$ as $p \to 1$.

function. The identity $\Delta_f + \Delta_b = 1/2$ implies that $G_c \sim 1/\tau$, and inserting this leading scaling behavior into the Kubo formula leads to a T-independent residual resistivity. To obtain temperature dependence, we consider the corrections to scaling from the time reparameterization operator, whose scaling dimension $h = 2$ leads to corrections which depend linearly on T or ω. Applying such a correction to the residual resistivity, we obtain a linear-in-T resistivity. The critical metal phase found here is therefore an attractive candidate for the overdoped cuprates. We also note that our solution is consistent with the findings of recent numerical work on a similar model[46], as we will discuss further in Section 5.5.

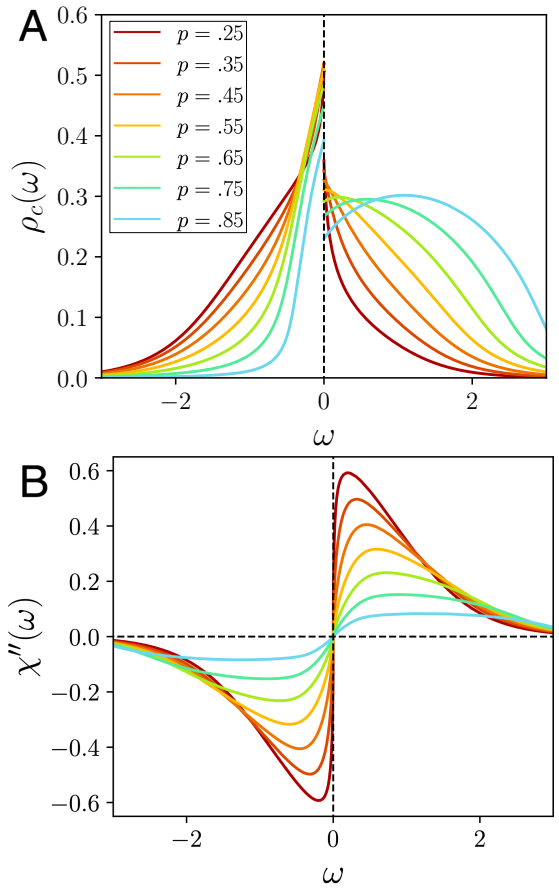

Figure 5.3: Plot of the electron spectral density (left) and spin spectral density (right) obtained at $t = J = 1$. The electron spectral density which discontinuously approaches two different constants $\omega = 0$, leading to $1/\tau$ decay of the electron density in imaginary time. The spin spectral density goes as $\text{sgn}(\omega)|\omega|^{4\Delta_f - 1}$ as $\omega \to 0$. Only for large p do we have Δ_f approach 1/4, which implies a linear frequency dependence and $1/\tau^2$ decay behavior in imaginary time characteristic of a Fermi liquid.

5.3.2 Imaginary-frequency solution

We also numerically solve Eqs. (5.12)-(5.17) on the imaginary-frequency axis at finite temperatures and for different doping values. A critical metallic solution is found for all values of doping. We calculate the parton Green's functions as well as gauge-invariant observables, namely, electron Green's function and spin correlation. These are shown in Fig. 5.4. The exponent of the bosonic Green's function, Δ_b, introduced in Eq. (5.18) can be determined from the temperature dependence of $G_b(i\omega = 0)$. In the low-temperature limit, the bosonic Green's function of the critical metallic solution has a conformal form at low frequencies, which follows the relation

$$G_b(i\omega = 0) = C_0 T^{-1+2\Delta_b}, \tag{5.25}$$

where C_0 is some constant and T is the temperature. In order to extract Δ_b from the data, we plot $\log(G_b(i\omega = 0))$ as a function of $\log(T)$ and perform a linear fit. The slope of this linear fit then determines Δ_b. In Fig. 5.2 we plot Δ_b determined from this procedure as a function of doping. It is in good agreement with the result obtained from analytic solution (shown as black curve in Fig. 5.2) discussed in Section 2.5.3.1. The lowest temperature that we used for the procedure is $T = 0.01$.

In the SI Appendix D.2 we present additional results obtained from solving the saddle-point equations on the imaginary-frequency axis. In particular, we calculate the electron Green's function and the spin correlation, which are physical observables. We find that the spin correlation $\chi(\tau)$ fits the conformal form to a very high accuracy and this allows us to extract the corresponding exponent. Moreover, using Pade approximation, we also perform a numerical analytic continuation to the real-frequency axis to obtain the electron and spin spectral densities. These are discussed in SI Appendix D.2.3, and are in remarkable agreement with those obtained from real-frequency analysis at zero temperature.

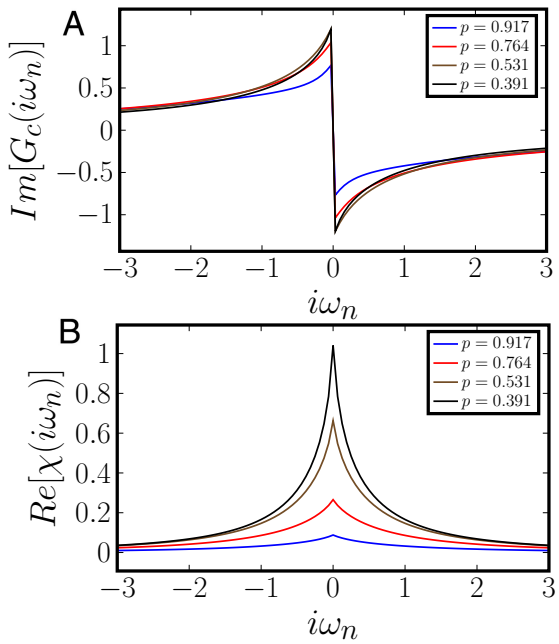

Figure 5.4: (A) Imaginary part of the electron Green's function on the Matsubara-frequency axis at $T = 0.01$ for different dopings. (B) Real part of the spin correlation on the Matsubara-frequency axis at $T = 0.01$ for different dopings. We have used $t = J = 1$.

5.3.3 Instability to spin-glass phase/quantum critical point

The critical metallic solution discussed above is expected to be stable at large doping values. In the low doping region we expect a spin-glass phase, which is connected to the spin-glass phase found in the insulating case [32]. The critical metallic phase and the spin-glass phase are separated by a quantum critical point at a finite doping. The critical value of doping can be estimated using a Ginzburg-Landau type free energy considered in Ref. [32]. It was derived by considering fluctuations over the saddle point leading to a $1/M$ correction and it has a form,

$$\mathcal{F} = \left[1 - \frac{J^2}{M}\chi^2(i\omega = 0)\right] \Psi^2 + \dots , \tag{5.26}$$

where $\chi(i\omega = 0) = \int_0^\beta \chi(\tau) d\tau$ is the local spin susceptiblity and Ψ is the spin-glass order parameter. In the insulating $p = 0$ phase studied in Ref. [32], it was found that $\chi(i\omega = 0)$ diverged logarithmically at $T = 0$ because the spin exponent has the 'marginal' value $\eta_s = 1$. Consequently the co-efficient of Ψ^2 is always negative as $T \to 0$, and spin glass order is present at $T = 0$. In our non-Fermi liquid solution, $\eta_s < 1$, and so $\chi(i\omega = 0)$ is finite at $T = 0$: this allows the possibility of $\Psi = 0$ and no spin glass order at $T = 0$. We find in the overdoped region the coefficient of the quadratic term is positive and the free energy is thus minimized by $\Psi = 0$. On the other hand, in the underdoped region this coefficient is negative leading to a non-zero spin-glass order parameter. A change in the sign of the coefficient of Ψ^2 at $T = 0$ thus indicates a quantum phase transition to a spin-glass phase and can be used to estimate the critical value of doping. We plot this coefficient at zero temperature in Fig. 5.5*A* as a function of doping for different values of J at $M = 2$. We clearly see that for larger values of J there is a quantum phase transition at a finite doping. In particular, for $J = 1$ we find $p_c \simeq 0.33$ and for $J = 0.5$ we get $p_c \simeq 0.25$. Similarly, in Fig. 5.5*B* we plot the coefficient in Eq. (5.26) as a function of doping for different values of M at a fixed $J = 1$ at zero temperature. It is clear that for large values of M there is no phase transition. We also plot the critical value of M as a function of

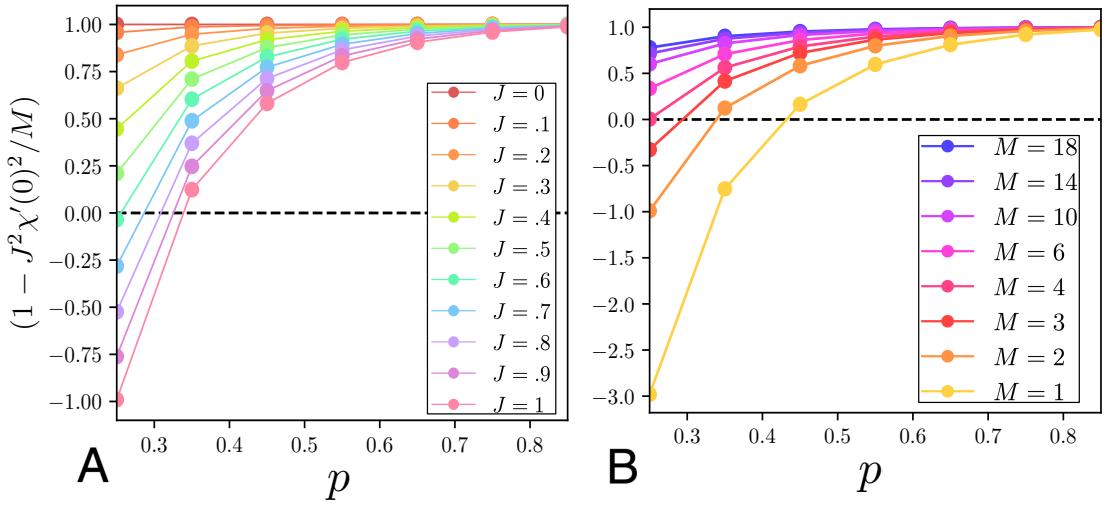

Figure 5.5: Plots of the coefficient of the quadratic term in the free energy in Eq. (5.26) as a function of doping for (A) different values of J with $t = 1$ and $M = 2$; (B) different values of M with $t = J = 1$. In both plots, $T = 0$.

doping in Fig. 5.6 at zero temperature. We perform a similar analysis at finite temperature to obtain the critical doping as a function of temperature (see Fig. D.8). The resulting phase diagram is shown in Fig. 5.1*A*. The spin-glass susceptibility increases with decreasing temperature and thus the spin-glass phase is found upon *cooling* the non-Fermi liquid at low doping. However, note that unlike in the case of the random Heisenberg model [156,63] (where the solution (i) with $\Delta_f = \Delta_b = 1/4$ is present) the spin-glass susceptibility does not diverge at low temperature in the present case. This is one of the important reasons for a stable critical solution at zero temperature in a broad doping region. We also note that while $1/M$ corrections are used in deriving the form of Eq. (5.26), we have used the $M \to \infty$ solution for the critical metal to compute $\chi'(0)$ as it appears in Eq. (5.26). While a more accurate estimate of p_c may be obtained by adding $1/M$ corrections to the critical metal solution, we emphasize that the $M \to \infty$ solution is sufficient to capture existence of a finite doping phase transition between the spin glass and critical metal.

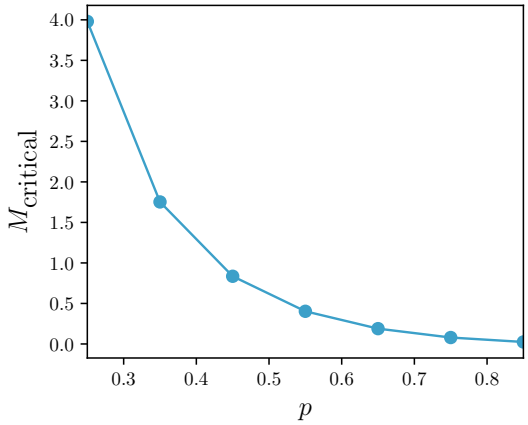

Figure 5.6: Plot showing critical value of M for which coefficient of quadratic term in free energy Eq. (5.26) changes sign at zero temperature.

5.4 Spin-glass phase

In this section we discuss the spin-glass phase present at lower dopings. In this case, we shall use the representation where spinons are bosonic (s) and holon is a fermion operator ($\mathfrak{f}$). In terms of these operators,

$$c_\alpha = \mathfrak{f}^\dagger s_\alpha \,, \quad \vec{S} = s_\alpha^\dagger \frac{\vec{\sigma}_{\alpha\beta}}{2} s_\beta \,, \tag{5.27}$$

and we realize a SU(2|1) superalgebra. Just as before, we shall now enlarge the symmetry here to SU($M|M'$), which means $\alpha = 1, \ldots, M$ and the holon operator acquires an index $\ell = 1, \ldots, M'$. Note that this bosonic spinon large M limit is *distinct* from the fermionic spinon large M limit followed in Section 5.3, and the two models are the same *only* for $M = 2$; so there is no reason to expect quantitive agreement between the results of the present section and those of Section 5.4.

The strategy to obtain the saddle-point equations is similar to that discussed earlier in Section 5.3.

From Refs. [92,175], we have

$$
\begin{aligned}
G_s(i\omega_n) &= \frac{1}{i\omega_n + \mu_s - \Sigma_s(i\omega_n)}\,, \\
G_{\mathfrak{f}}(i\omega_n) &= \frac{1}{i\omega_n + \mu_{\mathfrak{f}} - \Sigma_{\mathfrak{f}}(i\omega_n)}\,, \\
\Sigma_s(\tau) &= -kt^2 G_{\mathfrak{f}}(\tau) G_{\mathfrak{f}}(-\tau) G_s(\tau) + J^2 G_s(\tau)^2 G_s(-\tau)\,, \\
\Sigma_{\mathfrak{f}}(\tau) &= t^2 G_{\mathfrak{f}}(\tau) G_s(-\tau) G_s(\tau)\,, \\
G_s(\tau = 0^-) &= -\kappa + kp\,, \\
G_{\mathfrak{f}}(\tau = 0^-) &= p\,.
\end{aligned}
$$

Physically, the spin-glass phase can be understood as a condensation of bosonic spinons. Contrary to the earlier case, since we are interested in the spin-glass phase we need to retain the replica off-diagonal terms in the action upon disorder averaging. There is however some simplification and only replica off-diagonal components of the bosonic Green's function at $i\omega_n = 0$ are relevant. These are captured via the parameter g which is related to the spin-glass order parameter, as discussed in detail in SI Appendix D.3. After incorporating the spin-glass order in $G_s(\tau) = G_r(\tau) - g$, we obtain the

following saddle-point equations:

$$[G_r(i\omega_n)]^{-1} = i\omega_n - \frac{Jg}{\Theta} - [\Sigma_r(i\omega_n) - \Sigma_r(i\omega_n = 0)] \tag{5.28}$$

$$G_f(i\omega_n) = \frac{1}{i\omega_n + \mu_f - \Sigma_f(i\omega_n)}\,, \tag{5.29}$$

$$\Sigma_r(\tau) = J^2\Big([G_r(\tau)]^2\, G_r(-\tau) - 2gG_r(\tau)G_r(-\tau) - g\,[G_r(\tau)]^2 + 2g^2 G_r(\tau) + g^2 G_r(-\tau)\Big) - kt^2 G_f(\tau)G_f(-\tau)\Big(-g + G_r(\tau)\Big), \tag{5.30}$$

$$\Sigma_f(\tau) = t^2 G_f(\tau)\Big(g^2 - gG_r(\tau) - gG_r(-\tau) + G_r(-\tau)G_r(\tau)\Big)\,, \tag{5.31}$$

$$g - G_r(\tau = 0^-) = \kappa - kp \tag{5.32}$$

$$G_f(\tau = 0^-) = p\,. \tag{5.33}$$

The dimensionless parameter $\Theta = 1/\sqrt{3}$, as detailed in SI Appendix D.3. We solve the above equations on real and imaginary-frequency axes. The main observable in this phase is the spin-glass order parameter, which we plot as a function of doping in Fig. 5.7 at zero temperature. The spin-glass order parameter is finite at lower dopings and decreases upon increasing doping. We show results for the order parameter computed for small but finite temperature obtained using the imaginary frequency analysis in SI Appendix D.4. We also calculate the holon and spinon Green's functions as well as the electron Green's function and spin correlation at finite temperature. These quantities are detailed in the same SI Appendix D.4.

We solve the saddle-point equations Eqs. (5.28)-(5.33) at zero temperature to obtain the fermion and boson spectral functions, as well as the electron and spin spectral functions for a range of doping. In terms of the spinon and holon spectral functions the electron spectral function has the following form:

$$\rho_c(\omega) = \int_0^\omega d\omega_1 \rho_r(\omega_1)\rho_f(\omega_1 - \omega) + g\rho_f(-\omega)\,. \tag{5.34}$$

Similarly, we obtain the expression for the spin spectral function,

$$\rho_s(\omega) = g^2 \beta\omega\delta(\omega) + g\left[\rho_r(\omega) - \rho_r(-\omega)\right] - \int_0^\omega d\omega_1 \rho_r(\omega_1)\rho_r(\omega-\omega_1)\,, \tag{5.35}$$

as in Ref.[63]. The spectral functions at zero temperature for different values of doping are shown in Fig. 5.8. We note that the boson spectral function behaves linearly with frequency at small frequencies. Consequently, the spin spectral function also depends linearly on ω at small frequencies. We also note the double peak structure in the electron spectral function $\rho_c(\omega)$ in Fig. 5.8*B*. Recall that the electron spectral function is a convolution of the spinon and holon spectral functions, as well as a term proportional to $g\rho_{\mathrm{f}}(-\omega)$. At small dopings the value of g is larger and hence there is a dominant peak coming from fermion spectral function. As g decreases with increasing doping the contribution from the boson spectral function increases leading to the second peak at positive frequencies. All the spectral functions satisfy the respective sum rules, which are detailed in SI Appendix D.4.2.

Apart from the numerical analysis at zero temperature, we also perform a Pade-approximation based numerical analytic continuation of the imaginary-axis solution obtained at finite temperature. We evaluate the holon, spinon, electron, and spin spectral densities at finite temperature. These are discussed in SI Appendix D.2.3, and are consistent with those obtained from real-frequency calculation at zero temperature for some range of doping.

5.5 Discussion

We have presented a large-M solution for the random *t-J* model for the entire doping range. Our main finding is a critical non-Fermi-liquid metal phase at large dopings. This phase is characterized by a spin correlation exponent which varies continuously with doping, a linear in temperature contribution to the resistivity as $T \to 0$, and an electron spectral function with a Fermi-liquid-like decay at long time,

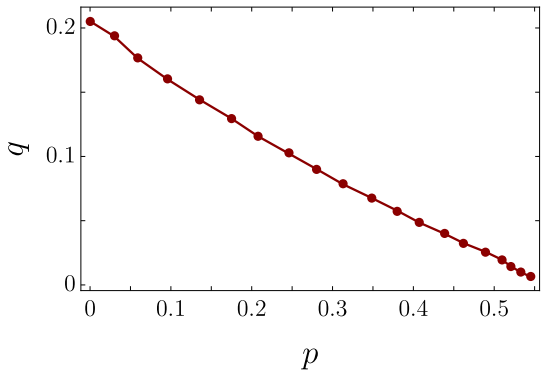

Figure 5.7: Plot of spin-glass order parameter, $q = g^2$, as a function of doping obtained by solving the bosonic spinon saddle-point Eqs. (5.28)-(5.33) on the real-frequency axis at $T = 0$. The point at $p = 0$ is obtained by solving Eqs. (D.66)-(D.68) at zero temperature on the real frequency axis. The parameters of the model are $J = t = 1$. The critical doping p_c at which the spin glass order vanishes in the present bosonic spinon computation need not be the same as that in the fermionic spinon computation in Section 2.5.3.3 because the models are identical only for $M = 2$.

but with a pronounced particle-hole asymmetry. This critical phase captures many aspects of experimental observations in the overdoped cuprates. It has been observed that in the overdoped region of cuprate materials there is a broad range of doping where the resistivity display a linear-T behavior [34,11]. Our findings propose a possible mechanism for this observation. Also, recent Seebeck coefficient measurements [69,61] hint towards a particle-hole asymmetric electron spectral density, which our solution also displays. It turns out that in our solution the electron Green's function appears Fermi-liquid like although the spin correlation does not. This may also explain the fact that experiments on overdoped cuprates probing electron Green's function directly, such as photoemission [28], may observe a Fermi-liquid behavior and can not access the critical phase. However, transport measurements obtain properties such as linear-T resistivity which is starkly in contrast to a Fermi liquid.

We also show that the overdoped critical phase has an instability towards a spin-glass phase at lower dopings. The spin-glass phase is characterized by a spin-glass order parameter, which we calculate using bosonic spinons. We show that this order parameter decreases upon increasing doping. In the context of cuprates, recent experiments have reported the presence of spin-glass phase at low doping [55].

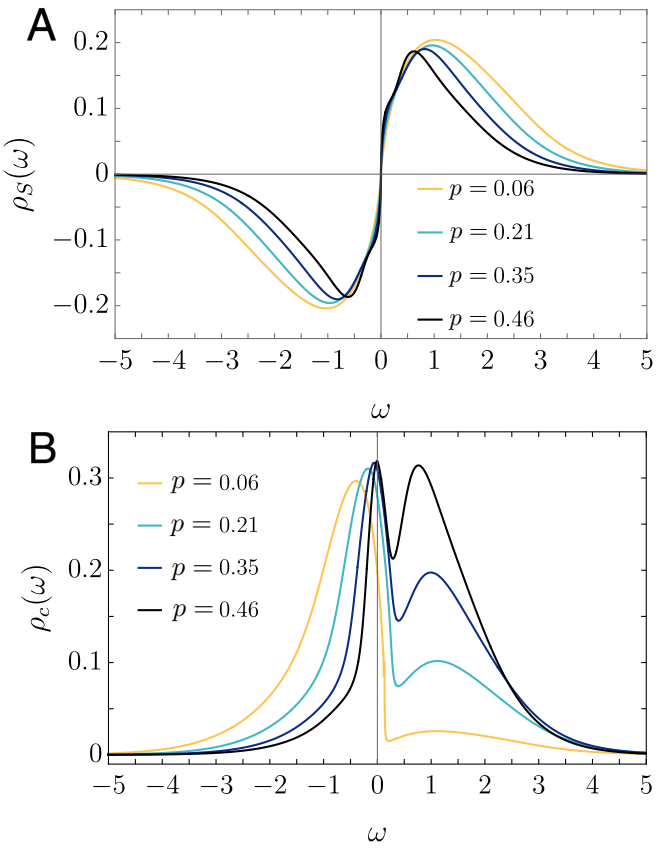

Figure 5.8: (A) Spin spectral function and (B) electron spectral function obtained at zero temperature via real frequency analysis for several values of doping. Note the linear in frequency behavior at small frequencies for $\rho_S(\omega)$. Parameters are $J = t = 1$.

Our work therefore presents a comprehensive analysis of model in Eq. (5.1) at variable doping and captures the quantum phase transition between the spin-glass phase and a critical non-Fermi-liquid metal. We also note that our results are consistent with recent numerical work on a related model[46].

A notable feature of our results is that we never find a Fermi-liquid phase in our large M limit of the t-J model, as discussed in SI Appendix D.1.2. This is in contrast to the distinct large M limit of Ref. [139], in which the boson b condenses at all non-zero p, leading to a Fermi-liquid phase at all doping. The two large M limits co-incide only for the physical value $M = 2$, and it is an open question which large M limit yields the correct picture at $M = 2$ for the random t-J model. However, we will note that the

numerical study of the $M = 2$ case in Ref.[46] does show indications of non-Fermi liquid behavior in the overdoped regime over the T range studied, as their measured spin exponent η_s varies with doping in a manner consistent with Fig. 5.2A. Thus, although a Fermi liquid phase may eventually appear at very low T in the overdoped regime for $M = 2$, it does appear that our non-Fermi liquid solution is an attractive description of the physics over a wide range of temperatures and dopings accessible in numerics and experiments.

In conclusion, our work presents a critical metallic phase as an attractive candidate for the overdoped cuprates which matches observations over a significant temperature range. This phase is obtained for a model with random and all-to-all interactions. Although such a model is far from the microscopic Hamiltonian of the cuprates, the saddle point equations solved are closely related to dynamic mean field equations of more realistic models in finite dimensions[85,86], as has been extensively discussed in a recent review[29]. At very low temperatures, we ultimately expect a crossover to behavior characteristic of finite-dimensional systems, and describing this crossover remains an important topic for future research.

6

Equilibrium dynamics of infinite-range quantum spin glasses in a field

6.1 Introduction

Modern advances in the development and control of programmable quantum simulators[48,101,119,47] have led to remarkable implementations of the idea of solving classical optimization problems by

quantum tunnelling[19,50]. In a recent experiment, for instance,[48] used a two-dimensional Rydberg atom array to investigate quantum optimization algorithms and demonstrated a superlinear quantum speedup in finding exact solutions.

In such a setup, each atom can be either in the atomic ground state or in a highly excited Rydberg state (with a large principal quantum number), thus realizing a quantum two-level system, which can be represented by the eigenstates of the Pauli operator Z_i on atom i. The laser-induced Rabi flipping is then described by the operator $g\sum_i X_i$, while the laser detuning is given by $\Delta\sum_i Z_i$. The long-ranged van der Waals interactions between two atoms are active only when both are in the Rydberg state, so an interaction J_{ij} between atoms i and j, $J_{ij}(1+Z_i)(1+Z_j)/4$, provides a route to implementing pairwise constraints on the optimization problems[48,100,22,136,91]. The atoms, which are trapped in optical tweezers, can be arranged in arbitrary geometries, and positioning them on randomly site-diluted lattices—as in Ref.[48]—introduces an element of spatial disorder in the Hamiltonian.

Inspired by the success of random, infinite-range models in understanding classical optimization problems[129], we will examine here the equilibrium dynamics of the infinite-range Ising spin glass in a field, h, with the Hamiltonian

$$H=\sum_{i<j}J_{ij}Z_iZ_j-g\sum_i X_i-h\sum_i Z_i \tag{6.1}$$

where $i,j=1\ldots N$ denote the lattice sites, and the interactions between them, J_{ij}, are taken as independent random numbers drawn from the probability distribution

$$P(J_{ij})\propto\exp\left[-\frac{NJ_{ij}^2}{2J^2}\right]. \tag{6.2}$$

This model has been much studied in the quantum spin glass literature[182,110,149,21,131,183,150,151], as well as[97,9,168,6,133,134,184,116,102], but only a few results have been obtained for the model with a nonzero

field, $h \neq 0$ [150,184,123,158,102], which is an essential ingredient in the optimization toolbox of Rydberg quantum simulators. Here, we shall provide exact results for the equilibrium long-time dynamics of the $N = \infty$ model with h nonzero. Our results here are a prelude to the study of the experimental case where the couplings are time-dependent, but nonequilibrium results will not be presented here.

The equilibrium solution for the $N = \infty$ quantum Ising model with independent random interactions requires the self-consistent solution of a (0+1)-dimensional replicated Ising model with long-range interactions [184,102]. Such a model is not exactly solvable, so a full solution at all times requires Monte Carlo simulations. However, it was argued in Ref. [150] that a Landau-theory-like strategy of expanding the quantum action functional in powers of an appropriately subtracted Z autocorrelation function (which is also a matrix in replica space) can provide the exact form of the long-time correlations in the $N = \infty$ model. Here, we shall implement this strategy for the $h \neq 0$ model, and obtain the low-frequency dynamic spin spectrum, along with the Parisi spin glass order parameter with full replica symmetry breaking.

Given the difficulty in obtaining the exact solution of the $N = \infty$ quantum Ising model at all times, we will also study a cousin of the quantum Ising model which has been the focus of some attention in the literature, but only at zero field: this is the 'spherical quantum p-rotor model' [38,41,97,7,172,181]. Modern quantum simulation experiments have begun to examine multiple-qubit interactions [126], and so it is of interest to also study these models with $p > 2$. Moreover, it is for $p > 2$ that there are no efficient classical algorithms for low energy states of p-spin classical models, and so there is greater scope for impact from quantum simulation [15].

In the literature, this model has been referred to as a 'p-spin' model rather than a 'p-rotor' model. While the distinction between spins and rotors is not important for classical systems, it is crucial for quantum systems. 'Spin' usually refers to a quantum degree of freedom whose components do not commute with each other, while the components of a rotor all commute. Accordingly, we will use the 'p-rotor' terminology in this paper.

As an aside, we also note studies of the Heisenberg spin glass model[29,156,139,62,63,17,10,24,160,46,32], which will not be considered in the present paper. In the Heisenberg model, the states on each site i have a twofold degeneracy, unlike both the Ising and rotor models considered here. An important consequence is that there is no trivial paramagnetic state in the Heisenberg model. In contrast, the Ising and rotor models have a gapped paramagnet with a nondegenerate ground state at large g.

We define the spherical quantum p-rotor model here by an imaginary time (τ) path integral over continuous real rotor/spin coordinates σ_i, which are the analogs of the discrete $Z_i = \pm 1$ Ising spins. The partition function of this model at an inverse temperature $\beta = 1/T$, and in a field h is

$$Z[J_{i_1\ldots i_p}] = \int \mathcal{D}\sigma_i(\tau)\ \exp\left[-\int_0^\beta d\tau \left(\frac{1}{2g}\dot{\sigma}_i(\tau)\dot{\sigma}_i(\tau) + \sum_{i_1<\ldots<i_p} J_{i_1\ldots i_p}\sigma_{i_1}(\tau)\ldots\sigma_{i_p}(\tau) - h\sum_i \sigma_i(\tau)\right)\right], \tag{6.3}$$

with repeated indices summed over, and $\dot{\sigma}_i(\tau) \equiv d\sigma_i/d\tau$. Importantly, in order to keep the energy finite, we equip the rotors with a spherical constraint

$$\sum_{i=1}^{N} \sigma_i(\tau)\,\sigma_i(\tau) = N, \tag{6.4}$$

i.e., the rotor degrees of freedom lie on an N-dimensional sphere of radius $\sqrt{N}$. These rotors interact with p-rotor couplings $J_{i_1\ldots i_p}$, and all of these couplings are taken to be independent random variables with distribution

$$P(J_{i_1\ldots i_p}) \propto \exp\left[-\frac{N^{p-1}}{p!}\frac{J_{i_1\ldots i_p}^2}{J^2}\right], \tag{6.5}$$

where the width of the distribution over couplings is set by the scale J. The factor of N^{p-1} ensures that the Hamiltonian is of order N, and accordingly, enforces an extensive scaling of the energy and free energy.

Owing to the global nature of the constraint in (6.4), the solution of the spherical p-rotor model is simpler than that of the Ising model with a local constraint $Z_i = \pm 1$ on every site i. On the other hand, the global constraint also makes the p-rotor model a less physical generalization of the Rydberg experiments. The solution of the p-rotor model requires analysis of a closed set of self-consistent Schwinger-Dyson equations, in which the self-energies are written as polynomials of the Green's functions. Such Schwinger-Dyson equations have been numerically studied earlier at $h = 0$ and in imaginary time and frequency [38,7]; here, we will extend the numerical solution to $h \neq 0$ and obtain the full dynamic rotor spectrum by direct solution in real-frequency space. We will also compute the Parisi spin glass order parameter and find that as in the spherical classical p-rotor model [72,60,36,26,169] (obtained by taking the $g = 0$ limit of (6.3)), there is only one-step replica symmetry breaking.

6.1.1 Main results

Our results are expressed in terms of a field $Q_{ab}(\tau_1, \tau_2)$ which is bilocal in imaginary time and a matrix in replica space with indices $a, b = 1, \ldots, n$. This field is related to the spin/rotor autocorrelation functions via

$$Q_{ab}(\tau_1, \tau_2) \sim \begin{cases} \frac{1}{N} \sum_i Z_{ia}(\tau_1) Z_{ib}(\tau_2) & , \quad \text{Ising model} \\ \frac{1}{N} \sum_i \sigma_{ia}(\tau_1) \sigma_{ib}(\tau_2) & , \quad p\text{-rotor model} \end{cases} , \tag{6.6}$$

where a, b are replica indices. Time-translational symmetry requires that the $N = \infty$ solution take the form

$$Q_{ab}(\tau_1, \tau_2) = \frac{1}{\beta} \sum_{\nu_n} Q_{ab}(i\nu_n) e^{i\nu_n(\tau_1 - \tau_2)} , \tag{6.7}$$

where ν_n is a bosonic Matsubara frequency. We choose the following ansatz for Q_{ab}:

$$Q_{ab}(i\nu_n) = \begin{cases} Q_r(i\nu_n) + \beta q_{EA}\delta_{\nu_n,0}, & a = b \\ \beta q_{ab}\delta_{\nu_n,0}, & a \neq b \end{cases}. \tag{6.8}$$

The replica off-diagonal terms in Q_{ab} are chosen to be time-independent, because there is no correlation between the time evolution of the spins in distinct replicas[150]. We have parameterized these off-diagonal terms in terms of a Parisi matrix q_{ab}; as in the classical spin glass theory[53], this matrix has an ultrametric structure which is characterized by the Parisi function $q(u)$, with $q(1) \equiv q_{EA}$, the Edwards-Anderson order parameter at $T = 0$. We have included an additive factor of βq_{EA} in the replica diagonal term of (6.8) for convenience. We will find that this ensures the solution for $Q_r(\tau)$ vanishes as $\tau \to \infty$ at $T = 0$. Also, the diagonal components q_{aa} do not appear in the above, and we use this freedom to choose $q_{aa} = 0$.

For the Ising model studied in Sec. 6.2, we find that low-frequency (ω) spectrum in the replica-symmetry-breaking phase with $h \neq 0$ is the same as that obtained earlier[150,6,102] at $h = 0$:

$$\mathrm{Im}\, Q_r(\omega) \sim \omega. \tag{6.9}$$

Note that a gapless spectrum for $h \neq 0$ is more surprising than at $h = 0$ because there is no $Z_i \to -Z_i$ symmetry that can be broken in the spin glass phase. The replica symmetry breaking is characterized by the Parisi function $q(u)$ shown in Fig. 6.1. This function has the same form as that found for the classical Ising model with $g = 0$[173]. The function $q(u)$ is nonanalytic at $u = x$, and the value of x vanishes linearly with T as $T \to 0$ as (see Eq. (6.38))

$$x = \frac{2y}{\kappa} T q_{EA}, \tag{6.10}$$

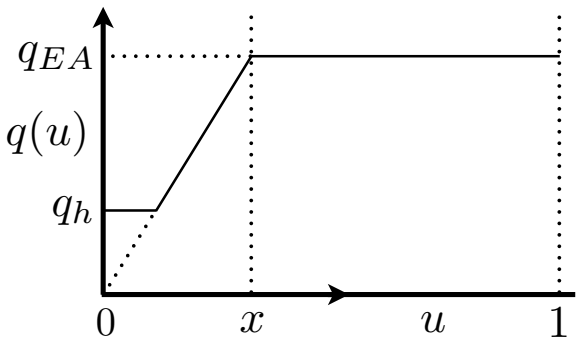

Figure 6.1: The Parisi spin glass order parameter for the Ising model at $h \neq 0$.

where y and κ are couplings of order unity in the Landau action (see Eq. (6.19)). Thus, although the breakpoint of the replica symmetry breaking vanishes as $T \to 0$, it is nevertheless important that the T- and h-dependent structure in Fig. 6.1 be included to obtain the gapless spectrum at $T = 0$ in (6.9). The smaller u plateau in Fig. 6.1 is at [173,150]

$$q_h = \left(\frac{3h^2}{8y}\right)^{1/3} . \tag{6.11}$$

The h-dependence of (6.11) is the only h-dependence in the solution for the spin glass state; the dynamic spectrum in (6.9) is h-independent. This happens because there is a decoupling between the saddle point equations for static and dynamic components of the spin glass order parameter, and only the value of q_{EA} is present in both the static and dynamic equations. The replica-symmetric paramagnetic solution does have an energy gap, and all aspects of its spectrum are h-dependent.

The results for the spherical quantum p-rotor model, $p \geq 3$, studied in Sec. 6.3, do have differences from the Ising model tied to the one-step replica symmetry breaking in the former, shown in Fig. 6.2, which is in turn tied to the nonlocal rotor constraint in (6.4). This $q(u)$ is characterized by a break-point at $u = x$, and the large-N saddle-point equations leave the value of x undetermined. The mathematical solution of the classical problem at $g = 0$ [169] implies we should compute the free energy $\mathcal{F}$, and then use the solution of $\partial\mathcal{F}/\partial x = 0$ to determine x. At such an x, and indeed at all

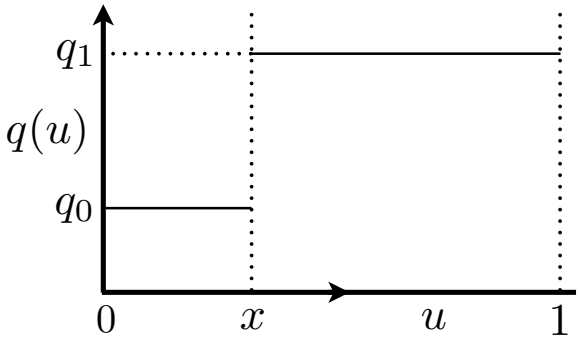

Figure 6.2: The Parisi spin glass order parameter for the spherical quantum p-rotor model for $p \geq 3$.

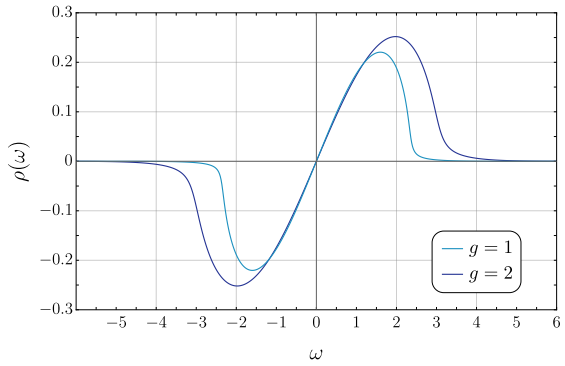

Figure 6.3: Behavior of the zero-temperature spectral function $\rho(\omega) = \mathrm{Im} Q_r(\omega)/\pi$, as determined by Eqs. (6.113)-(6.120), for the one-step replica-symmetry-breaking solution of the $p = 3$ spherical quantum p-rotor model at different values of the transverse field g (with $J = 1$). The marginal stability condition (6.109) is imposed. The spectrum is independent of h as long as we are in the replica-symmetry-breaking phase in Fig. 6.10.

generic values of x, the spectrum of $Q_r(\omega)$ turns out to have a gap. Earlier work [39,41,38] has advocated use of a 'marginal stability' condition, which leads to precisely the value of x for which the spectrum is gapless. We find that such a gapless spectrum obeys (6.9) as in the Ising model, and we show a plot of Im $Q_r(\omega)$ for all frequencies in Fig. 6.3. Also, as in the Ising model, the spectrum in the spin glass phase is h-independent, and for similar reasons. The lower plateau at q_0 in Fig. 6.2 vanishes as $h \to 0$ as $q_0 \sim h^2$, unlike (6.11) for the Ising model. The value of x still vanishes linearly with T, as in the Ising model. We note that the $p = 2$ spherical model has no replica symmetry breaking, and the rotor spectrum is always gapped for $h \neq 0$.

6.2 Ising model

6.2.1 Landau action

We motivate the structure of the Landau action for the Ising model by recalling the solution of the spherical model for the $p = 2$ case[183], in which the interactions have the same form as in the Ising model, but the local Ising constraint has been replaced by the global constraint in (6.4). At $h = 0$, the large-N solution in the paramagnetic phase is of the form (see Appendix E.3, and Chapter 33 in Ref.[155])

$$Q_{ab}(i\nu_n) = \frac{2g\delta_{ab}}{\nu_n^2 + (\Delta^2 + \Lambda^2)/2 + \left[(\nu_n^2 + \Delta^2)(\nu_n^2 + \Lambda^2)\right]^{1/2}}, \tag{6.12}$$

where ν_n is a Matsubara frequency, Δ is a small energy gap, and Λ is a high cutoff frequency. In the spin glass phase of the spherical model, the solution is gapless and replica symmetric:

$$Q_{ab}(i\nu_n) = \beta q_{EA}\delta_{\nu_n,0} + \frac{2g\delta_{ab}}{\nu_n^2 + \Lambda^2/2 + |\nu_n|\left[\nu_n^2 + \Lambda^2\right]^{1/2}}, \tag{6.13}$$

where q_{EA} is the Edwards-Anderson order parameter.

We shall be interested in extending this solution beyond the spherical limit to the Ising model—at low frequency scales in the vicinity of the quantum critical point, where $|\nu_n|$, Δ, $T \ll \Lambda$, q_{EA} is small—and allow for replica symmetry breaking. In this regime, we can approximate the paramagnetic solution of the spherical model by

$$Q_{ab}(i\nu_n) = \delta_{ab}\left[A - B\sqrt{\nu_n^2 + \Delta^2} + \dots\right], \tag{6.14}$$

where A, B are positive constants, while the spin glass solution is

$$Q_{ab}(i\nu_n) = \beta q_{EA}\delta_{\nu_n,0} + \delta_{ab}\left[A - B|\nu_n|\right] + \ldots \quad . \tag{6.15}$$

We now notice that if we shift Q by a frequency-independent and replica-diagonal constant,

$$Q_{ab}(i\nu_n) \to Q_{ab}(i\nu_n) - A\delta_{ab}, \tag{6.16}$$

then the shifted $Q_{ab}(i\nu_n)$ becomes small at the relevant low-frequency scales on both sides of the quantum critical point. This makes the shifted $Q_{ab}(i\nu_n)$ a suitable field in which to carry out the Landau expansion of the Ising model. In terms of the original bilocal field, the shift is

$$Q_{ab}(\tau_1,\tau_2) \to Q_{ab}(\tau_1,\tau_2) - A\,\delta_{ab}\,\delta(\tau_1-\tau_2), \tag{6.17}$$

and the constant A characterizes nonuniversal, short-time physics not of interest to us.

Working with this shifted field, the important low-order terms in the Landau expansion for the action of the Ising model are [150]

$$\mathcal{A}_h = \mathcal{A} - \frac{h^2}{2}\sum_{ab}\int d\tau_1 d\tau_2 Q_{ab}(\tau_1,\tau_2) - \frac{\beta}{2}\chi_{hb}h^2, \tag{6.18}$$

where h is the longitudinal field, χ_{hb} is a background contribution to the linear spin susceptibility, and

the $h = 0$ Landau action is

$$\begin{aligned}\mathcal{A} &= \frac{1}{\kappa}\int d\tau \sum_a \left[\frac{\partial}{\partial\tau_1}\frac{\partial}{\partial\tau_2} + r\right] Q_{aa}(\tau_1,\tau_2)\Big|_{\tau_1=\tau_2=\tau} \\ &- \frac{\kappa}{3}\int d\tau_1 d\tau_2 d\tau_3 \sum_{abc} Q_{ab}(\tau_1,\tau_2)Q_{bc}(\tau_2,\tau_3)Q_{ca}(\tau_3,\tau_1) \\ &+ \frac{U}{2}\int d\tau \sum_a Q_{aa}(\tau,\tau)Q_{aa}(\tau,\tau) - \frac{y}{6}\int d\tau_1 d\tau_2 \sum_{ab}\left[Q_{ab}(\tau_1,\tau_2)\right]^4 ; \end{aligned} \tag{6.19}$$

see Appendix A of Ref.[150] for a derivation of Eq. (6.19) from (6.1). Here, r is the parameter which tunes across the spin glass transition at $h = 0$: it is analogous to the coupling g in the Ising Hamiltonian in (6.1) with $r \sim g - g_c$, and $r = 0$ at the $g = g_c$ quantum critical point. The cubic term κ is analogous to the cubic term in Parisi's original theory of classical spin glasses[53,140]. The U term only involves a single replica, and is a quantum self-interaction of the soft Ising order parameter. The y term is analogous to a quartic term in the classical case[53], where it is the term responsible for full replica symmetry breaking in the spin glass phase; however, the dynamic quantum effects of y are weak, and can be treated perturbatively.

Note that (6.19) does not contain the allowed quadratic term $\int d\tau_1 d\tau_2 [Q_{ab}(\tau_1,\tau_2)]^2$. We have removed such a term by exploiting the shift in (6.17). We will see below that such a choice is equivalent to the requirement for the validity of the Landau theory that the full function $Q_{ab}(i\nu_n)$ is small near the quantum critical point. This shift strategy is analogous to that followed for the critical theory of the Yang-Lee edge singularity[54,25].

Our analysis of the physics of the action $\mathcal{A}_h$ will examine the behavior as a function of the tuning parameter across the spin glass transition r, the longitudinal field h, and the temperature T. We will keep the couplings κ and U of order unity and obtain results for small y. We find that for $h > 0$ there are contributions nonanalytic in y that are important to include; however, analytic corrections in integer powers of y are not crucial, and these are relegated to Appendix E.1.

The analysis of thermodynamic properties in the spin glass phase in Ref. [150] was carried out with a vanishing coefficient of the quartic term, $y = 0$: in this case the order parameter has replica symmetry. Here, we will extend the solution to small $y \neq 0$, and show that the solution has broken replica symmetry. We also show that the spin fluctuation spectrum remains gapless both at $y = 0$ and $y \neq 0$.

6.2.2 Free energy

Inserting the time-translational symmetric ansatz of (6.7) into (6.18) and (6.19), we obtain the free energy

$$\mathcal{F}_h = \mathcal{F} - \frac{h^2}{2} \sum_{ab} Q_{ab}(i\nu_n = 0) - \frac{1}{2}\chi_{bb} h^2 \,, \tag{6.20}$$

where the h-independent free energy is

$$\begin{aligned} \mathcal{F} = & \frac{1}{\beta\kappa} \sum_a \sum_{\nu_n} (\nu_n^2 + r) Q_{aa}(i\nu_n) - \frac{\kappa}{3\beta} \sum_{abc} \sum_{\nu_n} Q_{ab}(i\nu_n) Q_{bc}(i\nu_n) Q_{ca}(i\nu_n) \\ & + \frac{U}{2} \sum_a \left[\frac{1}{\beta} \sum_{\nu_n} Q_{aa}(i\nu_n) \right]^2 \\ & - \frac{y}{6\beta^3} \sum_{ab} \sum_{\nu_n, \nu_n', \nu_n''} Q_{ab}(i\nu_n) Q_{ab}(i\nu_n') Q_{ab}(i\nu_n'') Q_{ab}(-i\nu_n - i\nu_n' - i\nu_n''). \end{aligned} \tag{6.21}$$

We now insert (6.8) into (6.21) and obtain the free energy

$$\frac{\mathcal{F}_h}{n} = \mathcal{F}_{sg,h} + \mathcal{F}_Q, \tag{6.22}$$

which consists of two pieces: a 'spin glass' and a 'quantum' component.

The first 'spin glass' component in (6.22) is given by

$$\mathcal{F}_{sg,h} = \mathcal{F}_{sg} - \frac{\beta h^2}{2n}\sum_{ab} q_{ab} - \frac{h^2}{2}Q_r(0) - \frac{\beta h^2}{2}q_{EA} - \frac{1}{2}\chi_{hh}h^2\,, \tag{6.23}$$

where the h-independent terms are

$$\begin{aligned}\mathcal{F}_{sg} =& -R_1\frac{1}{n}\mathrm{Tr}q^2 - \frac{R_2}{3}\frac{1}{n}\mathrm{Tr}q^3 - \frac{R_3}{6}\frac{1}{n}\sum_{ab}q_{ab}^4 \\ &+ r\frac{q_{EA}}{\kappa} - \frac{\kappa}{3\beta}\left[(Q_r(0)+\beta q_{EA})^3 - Q_r(0)^3\right] - \frac{\beta y}{6}q_{EA}^4 - \frac{2y}{3}q_{EA}^3 Q_r(0)\,,\end{aligned} \tag{6.24}$$

with

$$R_1 \;=\; \beta\kappa(Q_r(0)+\beta q_{EA}), \quad R_2 = \kappa\beta^2, \quad R_3 = \beta y. \tag{6.25}$$

The terms involving q_{ab} in (6.24) are identical to those of the Landau theory of the classical spin glass in Section 3.4 of Ref. [53].

The second 'quantum' component in (6.22) is h-independent

$$\begin{aligned}\mathcal{F}_Q \;=\;& \frac{1}{\beta\kappa}\sum_{\nu_n}(\nu_n^2+r)Q_r(i\nu_n) - \frac{\kappa}{3\beta}\sum_{\nu_n}Q_r^3(i\nu_n) + \frac{U}{2}\left[\frac{1}{\beta}\sum_{\nu_n}Q_r(i\nu_n)+q_{EA}\right]^2 \\ &- \frac{yq_{EA}^2}{\beta}\sum_{\nu_n}Q_r(i\nu_n)Q_r(-i\nu_n) - \frac{2yq_{EA}}{3\beta^2}\sum_{\nu_n,\nu_n'}Q_r(i\nu_n)Q_r(i\nu_n')Q_r(-i\nu_n-i\nu_n') \\ &- \frac{y}{6\beta^3}\sum_{\nu_n,\nu_n',\nu_n''}Q_r(i\nu_n)Q_r(i\nu_n')Q_r(i\nu_n'')Q_r(-i\nu_n-i\nu_n'-i\nu_n'').\end{aligned} \tag{6.26}$$

We will solve the saddle-point equations for $\mathcal{F}_{sg}$ exactly, while those for $\mathcal{F}_Q$ can be solved order-by-order in y. We will present the y^0 solution below, while the y^1 solution is presented in Appendix E.1. It turns out that the solution of $\mathcal{F}_{sg}$ contains terms nonperturbative in y for $h \neq 0$, so it is important

to treat the spin glass terms exactly.

6.2.3 Saddle-point equations

The saddle-point equations are most easily determined by taking the derivative of (6.21) with respect to $Q_{ab}(i\nu_n)$:

$$\frac{\beta h^2}{2}\delta_{\nu_n,0} = \frac{1}{\kappa}(\nu_n^2 + r)\delta_{ab} - \kappa \sum_c Q_{ac}(i\nu_n)Q_{cb}(i\nu_n) + U\delta_{ab}\frac{1}{\beta}\sum_{\nu_n'} Q_{aa}(i\nu_n') \\ - \frac{2y}{3\beta^2}\sum_{\nu_n',\nu_n''} Q_{ab}(i\nu_n')Q_{ab}(i\nu_n'')Q_{ab}(-i\nu_n - i\nu_n' - i\nu_n''). \tag{6.27}$$

The replica off-diagonal equation of (6.27) is

$$\frac{\beta h^2}{2} = -2R_1 q_{ab} - R_2 \sum_c q_{ac}q_{cb} - \frac{2R_3}{3}q_{ab}^3\,, \tag{6.28}$$

while the replica diagonal part gives

$$0 = \frac{1}{\kappa}(\nu_n^2 + r) - \kappa\left[Q_r(i\nu_n)\right]^2 + \frac{U}{\beta}\sum_{\nu_n'} Q_r(i\nu_n') + uq_{EA} \\ - \frac{2y}{3\beta^2}\sum_{\nu_n',\nu_n''} Q_r(i\nu_n')Q_r(i\nu_n'')Q_r(-i\nu_n - i\nu_n' - i\nu_n'') \\ - \frac{2y}{\beta}q_{EA}\sum_{\nu_n'} Q_r(i\nu_n')Q_r(i\nu_n - i\nu_n') - 2yq_{EA}^2 Q_r(i\nu_n) \\ + \delta_{\nu_n,0}\left[-\kappa\beta^2\sum_c q_{ac}q_{ca} - \kappa\beta^2 q_{EA}^2 - 2\kappa\beta q_{EA}Q_r(0) - \frac{2\beta y}{3}q_{EA}^3 - \frac{\beta h^2}{2}\right]. \tag{6.29}$$

6.2.4 Zero-field limit

In this section, we first rederive the results obtained earlier [150,63] at $h = 0$, which we will then contrast with the case for a nonzero field later in Sec. 6.2.5.

Quantum paramagnet

In the paramagnetic phase, with $q_{EA} = 0$ and $q_{ab} = 0$, the spin glass free energy is $\mathcal{F}_{sg} = 0$. At $h = 0$, $\mathcal{F}_{sg,h} = 0$ wherefore only the quantum component survives, and Eq. (6.29) simplifies to an equation for $Q_r(i\nu_n)$ alone:

$$0 = \frac{1}{\kappa}(\nu_n^2 + r) - \kappa\left[Q_r(i\nu_n)\right]^2 + \frac{U}{\beta}\sum_{\nu_n'} Q_r(i\nu_n') - \frac{2y}{3\beta^2}\sum_{\nu_n',\nu_n''} Q_r(i\nu_n')Q_r(i\nu_n'')Q_r(-i\nu_n - i\nu_n' - i\nu_n'')\,. \tag{6.30}$$

This can be solved iteratively in powers of y. At order y^0, the solution agrees with the form in (6.14)

$$Q_{r0}(i\nu_n) = -\frac{\sqrt{\nu_n^2 + \Delta^2}}{\kappa}\,, \tag{6.31}$$

where the gap Δ is given by the solution of

$$\Delta^2 = r - \frac{U}{\beta}\sum_{|\nu_n|<\Lambda}\sqrt{\nu_n^2 + \Delta^2}, \tag{6.32}$$

and we have introduced a frequency cutoff to make the frequency summation finite. This cutoff dependence is inherent to the low frequency expansion in the Landau theory. We will also need the cutoff at higher orders in y, but the form of the low-frequency dynamics remain cutoff-independent: we will verify this in Section 6.3 where no cutoff dependence is needed, because the theory is solved exactly without Landau expansion, and similar low-frequency behavior appears. The cutoff-dependent

critical point $r = r_{c0}$ is obtained by setting $\Delta = 0$, and is given by

$$r_{c0} = \frac{U}{\beta} \sum_{|\nu_n|<\Lambda} |\nu_n| \,. \tag{6.33}$$

The order y^1 corrections to the saddle point appear in Appendix E.1.1.

Free energy: As mentioned above, for the case of the paramagnet, we have $\mathcal{F}_{sg} = 0$ for the spin glass component of the free energy in (6.22). The free energy $\mathcal{F}_Q$ in (6.22) at order y^0 is

$$\mathcal{F}_Q^0 = -\frac{2}{3\kappa^2\beta} \sum_{\nu_n} (\nu_n^2 + \Delta^2)^{3/2} - \frac{\left[\Delta^2 - r\right]^2}{2\kappa^2 u} \,, \tag{6.34}$$

where Δ is the solution of (6.32). The order y^1 correction to $\mathcal{F}_Q$ appears in Appendix E.1.1.

Spin glass

We begin by solving (6.28) at $h = 0$, which is the same equation of state as that obtained for the classical spin glass. In terms of the Parisi function $q(u)$ characterizing the $n \to 0$ limit of the replica matrix q_{ab}, we can write (6.28) at $h = 0$ as (see Appendix E.5)

$$2R_1 q(u) + \frac{2R_3}{3} q^3(u) = R_2 \left[2q(u) \int_0^1 q(v)dv + \int_0^u dv (q(u) - q(v))^2 \right] . \tag{6.35}$$

This is the same as Eq. (3.74) in Ref. [53] for the classical case. A replica-symmetric solution with $q(u) =$ constant is possible, but this is not the preferred solution at $h = 0$ (as in the classical case, and, as we will see in Sec. 6.2.5, for the quantum $h \neq 0$ case). So, we only consider the replica-symmetry-breaking

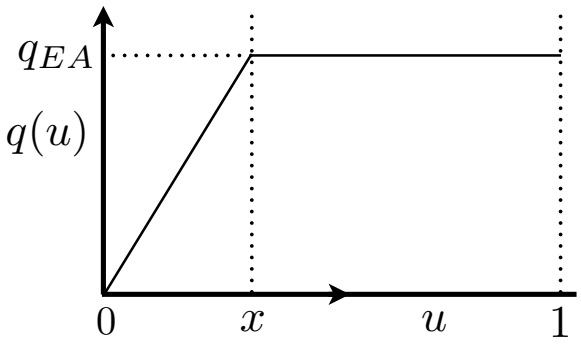

Figure 6.4: The Parisi spin glass order parameter for the Ising model at $h = 0$.

solution here, as shown in Fig. 6.4:

$$q(u) = \begin{cases} q_{EA}u/x & , \quad 0 < u < x \\ q_{EA} & , \quad x < u < 1 \end{cases} , \tag{6.36}$$

with

$$\begin{aligned} q_{EA} &= \frac{R_2 - (R_2^2 - 4R_1R_3)^{1/2}}{2R_3}, \\ x &= \frac{2R_3 q_{EA}}{R_2} . \end{aligned} \tag{6.37}$$

Using (6.25), we can exactly simplify (6.37) to

$$Q_r(0) = -\frac{y}{\kappa} q_{EA}^2, \quad x = 2yq_{EA}/(\beta\kappa) . \tag{6.38}$$

It can now be verified that the term proportional to $\delta_{\nu_n,0}$ in (6.29) vanishes

$$\kappa\beta^2 \int_0^1 du[q(u)]^2 - \kappa\beta^2 q_{EA}^2 - 2\kappa\beta q_{EA} Q_r(0) - \frac{2\beta y}{3} q_{EA}^3 = 0 . \tag{6.39}$$

We can therefore conclude that the complete saddle-point equations for $Q_r(i\nu_n)$ and $q(u)$ reduce to the following three equations for $Q_r(i\nu_n)$, q_{EA} and x:

$$\begin{aligned} 0 = &\frac{1}{\kappa}(\nu_n^2 + r) - \kappa\left[Q_r(i\nu_n)\right]^2 + \frac{U}{\beta}\sum_{\nu_n'} Q_r(i\nu_n') + uq_{EA} \\ &- \frac{2y}{3\beta^2}\sum_{\nu_n',\nu_n''} Q_r(i\nu_n')Q_r(i\nu_n'')Q_r(-i\nu_n - i\nu_n' - i\nu_n'') \\ &- \frac{2y}{\beta}q_{EA}\sum_{\nu_n'} Q_r(i\nu_n')Q_r(i\nu_n - i\nu_n') - 2yq_{EA}^2 Q_r(i\nu_n), \end{aligned} \tag{6.40}$$

$$yq_{EA}^2 = -\kappa Q_r(0), \tag{6.41}$$

$$\beta\kappa x = 2yq_{EA}. \tag{6.42}$$

Note that only the value of q_{EA} is needed from the spin glass solution for the solution of the quantum equation for $Q_r(i\nu_n)$ in (6.40).

Gapless condition: Now, let us analytically continue (6.40) to real frequency, and assume that

$$Q_r(\omega \to 0) = Q_r(0) + |\omega|^\alpha\left[a + ib\,\mathrm{sgn}(\omega)\right] \tag{6.43}$$

with $\alpha > 0$. Then, at $T = 0$, the terms of order Q_r^2 and Q_r^3 in (6.40) will have imaginary parts which vanish faster than $|\omega|^\alpha$ as $|\omega| \to 0$. Collecting all terms of order $|\omega|^\alpha$ in the imaginary part of (6.40), we obtain the condition

$$-2\kappa Q_r(0) - 2yq_{EA}^2 = 0, \tag{6.44}$$

which is automatically satisfied from (6.41). So, the spin dynamics are gapless at all values of y in the spin glass phase with $h = 0$. We will see in the explicit solution below that the exponent $\alpha = 1$, so

that $\mathrm{Im}Q_r(\omega \to 0) \sim \omega$.

SOLUTION: The equations (6.40–6.42) can be solved iteratively in powers of y. At order y^0, we have

$$\begin{aligned} q_{EA0} &= \frac{1}{\beta\kappa}\sum_{\nu_n}|\nu_n| - \frac{r}{\kappa U} \equiv \frac{1}{\kappa U}(r_{c0} - r), \\ Q_{r0}(i\nu_n) &= -\frac{|\nu_n|}{\kappa}, \\ x &= 0\,. \end{aligned} \tag{6.45}$$

The order y^1 corrections to the saddle point appear in Appendix E.1.1.

FREE ENERGY: Inserting the solution (6.36)–(6.38) back into (6.24), and using the relation (see Appendix E.5)

$$\begin{aligned} &-R_1\frac{1}{n}\mathrm{Tr}q^2 - \frac{R_2}{3}\frac{1}{n}\mathrm{Tr}q^3 - \frac{R_3}{6}\frac{1}{n}\sum_{ab}q_{ab}^4 \\ &= R_1\int_0^1 du[q(u)]^2 - \frac{R_2}{3}\int_0^1 du\left[u[q(u)]^3 + 3q(u)\int_0^u dv[q(v)]^2\right] + \frac{R_3}{6}\int_0^1 du[q(u)]^4, \end{aligned} \tag{6.46}$$

we obtain

$$\mathcal{F}_{sg} = \frac{rq_{EA}}{\kappa} + \frac{y^2 q_{EA}^5}{5\kappa}\,. \tag{6.47}$$

This is the full expression for $\mathcal{F}_{sg}$ in (6.22), valid to all orders in y in terms of the exact q_{EA}. However, q_{EA} is known only to order y^1 in (E.8).

As in the paramagnet, we will only determine $\mathcal{F}_Q$ in (6.22) order-by-order in y. At order y^0, the

value of $\mathcal{F}_Q$ is

$$\mathcal{F}_Q^0 = -\frac{rq_{EA0}}{\kappa} - \frac{2}{3\kappa^2\beta}\sum_{\nu_n}|\nu_n|^3 - \frac{r^2}{2U\kappa^2}. \tag{6.48}$$

The order y^1 correction to $\mathcal{F}_Q$ appears in Appendix E.1.1.

Phase diagram

At order y^0, the system is the spin glass phase for $r < r_{0c}$, where r_{c0} is given by Eq. (6.33). In the classical limit, $T \gg \Lambda$, we need only consider the $\nu_n = 0$ term, so the phase boundary is at $r = 0$. In the quantum limit $T \ll \Lambda$, we can evaluate the summation over Matsubara frequencies using the identity

$$\frac{1}{\beta}\sum_{\nu_n} D(i\nu_n) = \int_0^\infty \frac{d\nu}{\pi} D(i\nu) + 2\int_0^\infty \frac{d\Omega}{\pi}\frac{\mathrm{Im}D(\Omega)}{e^{\Omega/T}-1} \tag{6.49}$$

for odd spectral functions $\mathrm{Im}D(\Omega) = -\mathrm{Im}D(-\Omega)$. Then, we obtain the phase boundary at

$$r = U\frac{\Lambda^2}{2\pi} - U\frac{\pi T^2}{3}\,. \tag{6.50}$$

The phase boundary depends on the value of cutoff. However, the temperature dependent part is cutoff-independent.

6.2.5 Nonzero field

Having reviewed the results in the absence of a longitudinal field above, we now address the $h \neq 0$ case and determine its phase diagram.

Replica-symmetric solution

Due to the longitudinal magnetic field, there is an average moment on each site, so q_{EA} is always nonzero; therefore, the replica-symmetric solution is nothing but the paramagnet. Thus q_{EA} is no longer an order parameter, and we will rely on replica symmetry breaking to identify the spin glass phase in Section 6.2.5. For $q_{ab} = q_{EA}(1 - \delta_{ab})$, Eq. (6.28), together with (6.25), reads

$$3h^2 + 12\kappa q_{EA} Q_r(0) + 4y q_{EA}^3 = 0\,. \tag{6.51}$$

Resultantly, the term proportional to $\delta_{\nu_n,0}$ in (6.29) vanishes so that the equation for $Q_r(i\nu_n)$ remains unchanged from that in (6.40). The gapless condition in (6.44) *is not* satisfied by (6.51), even though $q_{EA} \neq 0$. Thus, the solution for $Q_r(i\nu)$ will have a gap.

At order y^0, the solution for $Q_{r0}(i\nu_n)$ from (6.29) has the same form as (6.31), but the equation for the gap Δ in (6.32) is now modified to [150]

$$\Delta^2 = r + \frac{U\kappa h^2}{4\Delta} - \frac{U}{\beta}\sum_{|\nu_n|<\Lambda}\sqrt{\nu_n^2 + \Delta^2} \tag{6.52}$$

while

$$q_{EA0} = \frac{h^2}{4\Delta}\,. \tag{6.53}$$

The solutions to Eq. (6.52) are shown in Fig. 6.5. Note that the gap Δ is h-dependent. The order y^1 corrections to the saddle point appear in Appendix E.1.2.

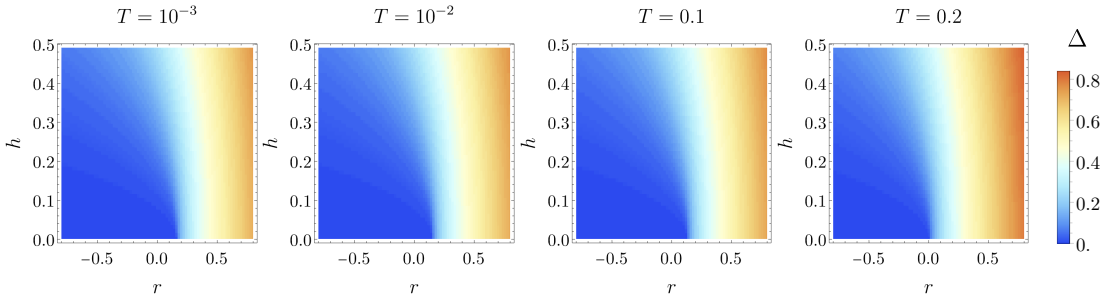

Figure 6.5: The gap Δ of the replica-symmetric solution of the Ising model as a function of r and h for various temperatures, as determined from (6.52). The parameters U, κ, and Λ have all been set to unity in these calculations.

FREE ENERGY: Inserting the solution for $Q_r(0)$ in (6.51) into (6.23) we obtain the spin glass component of the free energy

$$\mathcal{F}_{sg,h} = \frac{q_{EA} r}{\kappa} + \frac{y^2 q_{EA}^5}{9\kappa} + \frac{h^2 q_{EA}^2 y}{6\kappa} + \frac{h^4}{16 q_{EA} \kappa} - \frac{1}{2}\chi_{bb} h^2. \tag{6.54}$$

Note that we need to insert the solution for q_{EA} in (E.15) into (6.54).

For the quantum component, the order y^0 contribution to the free energy in (6.26) is

$$\mathcal{F}_Q^0 = -\frac{2}{3\kappa^2\beta}\sum_{\nu_n}(\nu_n^2 + \Delta^2)^{3/2} - \frac{\left[\Delta^2 - r\right]^2}{2\kappa^2 U} - \frac{h^2(r - \Delta^2)}{4\kappa\Delta}\,, \tag{6.55}$$

which reduces to (6.34) at $h = 0$. The order y^1 correction to $\mathcal{F}_Q$ appears in Appendix E.1.2.

REPLICA SYMMETRY BREAKING

From (6.28), the equation (6.35) for the Parisi function is modified to

$$\frac{\beta h^2}{2} + 2R_1 q(u) + \frac{2R_3}{3} q^3(u) = R_2\left[2q(u)\int_0^1 q(v)dv + \int_0^u dv(q(u) - q(v))^2\right]. \tag{6.56}$$

The solution of (6.56) is modified from (6.36) to that shown in Fig. 6.1

$$q(u) = \begin{cases} q_b, & 0 < u < (q_b/q_{EA})x \\ q_{EA}u/x, & (q_b/q_{EA})x < u < x \\ q_{EA}, & x < u < 1 \end{cases} . \tag{6.57}$$

The function $q(u)$ is nonanalytic at $u = (q_b/q_{EA})x$ and $u = x$, but has no discontinuities. The values of q_{EA} and x are unchanged from those in (6.38), and the value of q_b is in (6.11). The result in (6.11) is the origin of the nonanalytic dependence on y.

It can now be verified that the term proportional to $\delta_{\nu_n,0}$ in (6.29) vanishes, and the equations for $Q_r(i\nu_n)$, x, q_{EA} remain unchanged from those in (6.40)–(6.42). Indeed, the *only* change from the $h = 0$ solution in Sec. 6.2.4 is in the form of $q(u)$ for $x < (q_b/q_{EA})x$ in (6.57).

Hence, the gapless condition in (6.44) *is* now satisfied, and the solutions for $Q_r(i\nu_n)$ and q_{EA} remain unchanged from that for the $h = 0$ gapless spectrum in Sec. 6.2.4.

FREE ENERGY: Inserting the solution (6.57), (6.11) into (6.23), we obtain the extension of (6.47) to nonzero h

$$\mathcal{F}_{sg,h} = \frac{q_{EA}r}{\kappa} + \frac{y^2 q_{EA}^5}{5\kappa} + \frac{3(9h^{10}y)^{1/3}}{40\kappa} - \frac{1}{2}\chi_{hh}h^2, \tag{6.58}$$

which agrees with (6.47) at $h = 0$.

As the introduction of h does not modify the values of $Q_r(i\nu_n)$ and q_{EA}, the free energy $\mathcal{F}_Q$ remains the same as that in Sec. 6.2.4.

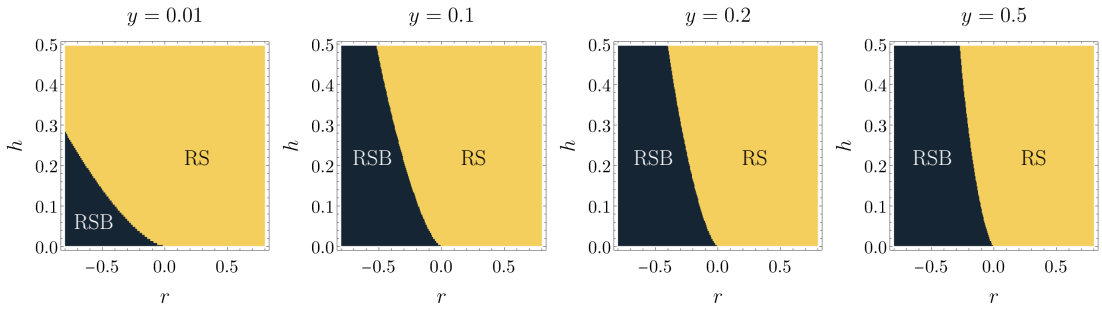

Figure 6.6: Phase diagram of the Ising model in the (r, h) plane for various values of y at $T = 0.2$, illustrating the replica-symmetric (RS) and replica-symmetry-breaking (RSB) phases. Here, the Landau parameter r is interpreted as proportional to $g - g_c$, where g is the transverse field, and g_c is the critical transverse field at $T = 0, h = 0$. The value of Δ at each point in parameter space is obtained from Fig. 6.5, and U, κ, Λ have been set to unity, as previously.

Phase diagram

To obtain the phase boundary between the replica-symmetric and replica-symmetry-breaking phases, we compare their free energies at leading nontrivial order in y.

For the gapped replica-symmetric phase we have the free energy given by (6.53)–(6.55)

$$\mathcal{F}_{rs} = \mathcal{F}_{sg,h} + \mathcal{F}_Q^0 = \frac{h^2\Delta}{2\kappa} - \frac{2}{3\kappa^2\beta}\sum_{|\nu_n|<\Lambda}(\nu_n^2 + \Delta^2)^{3/2} - \frac{\left[\Delta^2 - r\right]^2}{2\kappa^2 U} - \frac{1}{2}\chi_{hh}h^2\,, \tag{6.59}$$

where the gap Δ is given by the solution of (6.52),

For the gapless replica-symmetry-breaking phase we have from (6.48) and (6.58)

$$\mathcal{F}_{rsb} = \mathcal{F}_{sg,h} + \mathcal{F}_Q^0 = \frac{3(9h^{10}y)^{1/3}}{40\kappa} - \frac{2}{3\kappa^2\beta}\sum_{|\nu_n|<\Lambda}|\nu_n|^{3/2} - \frac{r^2}{2\kappa^2 U} - \frac{1}{2}\chi_{hh}h^2\,. \tag{6.60}$$

The summations in (6.52), (6.59), and (6.60) can be evaluated for $T, \Delta \ll \Lambda$ using identities

obtained from (6.49):

$$\frac{1}{\beta}\sum_{|\nu_n|<\Lambda}(\nu_n^2+\Delta^2)^{1/2}=\frac{\Lambda^2}{2\pi}+\frac{\Delta^2}{4\pi}\left(1+\ln\left(4\Lambda^2/\Delta^2\right)\right)-2\int_\Delta^\infty\frac{d\Omega}{\pi}\frac{(\Omega^2-\Delta^2)^{1/2}}{e^{\Omega/T}-1},$$
$$\frac{1}{\beta}\sum_{|\nu_n|<\Lambda}(\nu_n^2+\Delta^2)^{3/2}=\frac{\Lambda^4}{4\pi}+\frac{3\Lambda^2\Delta^2}{4\pi}+\frac{3\Delta^4}{32\pi}\left(3+\ln\left(16\Lambda^4/\Delta^4\right)\right)+2\int_\Delta^\infty\frac{d\Omega}{\pi}\frac{(\Omega^2-\Delta^2)^{3/2}}{e^{\Omega/T}-1}.$$
(6.61)

The phase diagram so obtained is shown in Fig. 6.6; note that due to the $n\to 0$ limit, we have to choose the phase with the maximum free energy [173]. We observe that the extent of the RSB phase in parameter space, which occurs for $r<0$, shrinks with increasing h and as y is reduced. Note that Δ remains finite, albeit small, at the transition point for $h>0$ (it vanishes at the transition for $h=0$), indicating a first-order transition.

6.3 Quantum spherical p-rotor model

We now turn to the analysis of the p-rotor model described in Eq. (6.3). The classical infinite-range spin glass with p-spin interactions, but without any spherical constraints, was originally introduced by Derrida [44,45]. Gross & Mézard [72] first studied the generalization of this model to nonzero magnetic fields, obtaining an exact solution for $p\to\infty$. The classical spherical model [26] can also be solved for any finite p, including in the presence of an external field [36,27]. Quantum extensions of these models, by adding a noncommuting transverse field, have been investigated both with (for $p=3$) [38,7] and without (for $p\to\infty$) [67] the supplementary spherical constraint. However, the problem of the quantum model in a longitudinal field, which we examine next, has remained unexplored so far.

6.3.1 Effective action

To begin, we derive the effective action for the quantum spherical p-rotor model, which will then form the basis for our subsequent saddle-point calculations. In the path integral, the spherical constraint (6.4) can be enforced using the exponential representation of the Dirac delta function

$$\delta\left(\sum_{i=1}^{N}\sigma_i(\tau)\sigma_i(\tau)-N\right)=\int\mathcal{D}z\exp\left[i\int_0^\beta d\tau\, z(\tau)\left(\sum_{i=1}^{N}\sigma_i(\tau)\sigma_i(\tau)-N\right)\right], \tag{6.62}$$

which is then inserted into Eq. (6.3) at the expense of introducing an auxiliary field $z(\tau)$.

At this stage, since the disorder is quenched, we average the free energy $\log Z[J_{i_1\ldots i_p}]$ over disorder—using the replica trick—instead of the partition function $Z[J_{i_1\ldots i_p}]$ itself (which would correspond to the annealed average). The replicated partition function is given by

$$\begin{aligned}\overline{Z^n}=\int dJ_{i_1\ldots i_p}P(J_{i_1\ldots i_p})\int\mathcal{D}\sigma_i^a\,\mathcal{D}z^a\,\exp\Bigg[i\int_0^\beta d\tau\, z^a(\tau)\big(\sigma_i^a(\tau)\sigma_i^a(\tau)-N\big) \\ -\int_0^\beta d\tau\left(\frac{1}{2g}\dot\sigma_i^a(\tau)\dot\sigma_i^a(\tau)+\sum_{i_1<\ldots<i_p}J_{i_1\ldots i_p}\sigma_{i_1}^a(\tau)\ldots\sigma_{i_p}^a(\tau)+h\sum_i\sigma_i^a(\tau)\right)\Bigg],\end{aligned} \tag{6.63}$$

where $a=1,\ldots,n$ is the replica index. Now, we can perform the disorder average by evaluating simple Gaussian integrals to find

$$\begin{aligned}\overline{Z^n}=\int\mathcal{D}\sigma_i^a\,\mathcal{D}z^a\,\exp\Bigg[-\int_0^\beta d\tau\left(\frac{1}{2g}\dot\sigma_i^a(\tau)\dot\sigma_i^a(\tau)-iz^a(\tau)\big(\sigma_i^a(\tau)\sigma_i^a(\tau)-N\big)+h\sum_i\sigma_i^a(\tau)\right) \\ +\frac{J^2}{4N^{p-1}}\int_0^\beta\int_0^\beta d\tau\,d\tau'\sum_{a,b=1}^{n}\left(\sum_{i=1}^{N}\sigma_i^a(\tau)\sigma_i^b(\tau')\right)^p\Bigg].\end{aligned} \tag{6.64}$$

Note that the overlap between two different replicas of the system

$$Q_{ab}(\tau,\tau') \equiv \frac{1}{N}\sum_{i=1}^{N} \overline{\langle \sigma_i^a(\tau)\sigma_i^b(\tau')\rangle}, \tag{6.65}$$

where the overline denotes an average over disorder realizations, appears naturally in Eq. (6.64). We then insert the identity

$$\begin{aligned} 1 &= \int \mathcal{D}Q_{ab}\ \delta\left(NQ_{ab}(\tau,\tau') - \sum_{i=1}^{N}\sigma_i^a(\tau)\sigma_i^b(\tau')\right) \\ &= \int \mathcal{D}Q_{ab}\mathcal{D}\lambda_{ab}\ \exp\left[i\int_0^\beta\int_0^\beta d\tau d\tau'\ \lambda_{ab}(\tau,\tau')\left(NQ_{ab}(\tau,\tau') - \sum_{i=1}^{N}\sigma_i^a(\tau)\sigma_i^b(\tau')\right)\right] \end{aligned} \tag{6.66}$$

into the partition function, which, in terms of the collective variables Q_{ab}, λ_{ab}, reads

$$\begin{aligned} \overline{Z^n} = \int \mathcal{D}\sigma_i^a\,\mathcal{D}z^a\,\mathcal{D}Q_{ab}\,\mathcal{D}\lambda_{ab}\ \exp\Bigg[&-\int_0^\beta d\tau\left(\frac{1}{2g}\dot\sigma_i^a(\tau)\dot\sigma_i^a(\tau) - iz^a(\tau)\sigma_i^a(\tau)\sigma_i^a(\tau) + h\sum_i \sigma_i^a(\tau)\right) \\ &- i\int_0^\beta\int_0^\beta d\tau\, d\tau'\ \sigma_i^a(\tau)\lambda_{ab}(\tau,\tau')\sigma_i^b(\tau')\Bigg] \\ \times \exp\Bigg[&- Ni\sum_{a=1}^{n}\int_0^\beta d\tau z^a(\tau) \\ &+ N\int_0^\beta\int_0^\beta d\tau d\tau'\left(i\lambda_{ab}(\tau,\tau')Q_{ab}(\tau,\tau') + \frac{J^2}{4}\sum_{a,b=1}^{n}\left(Q_{ab}(\tau,\tau')\right)^p\right)\Bigg]. \end{aligned} \tag{6.67}$$

Here, we have replaced bilinears of σ_i with Q_{ab} wherever possible and collected in the first two lines all the remaining terms involving the σ_i fields, which we will integrate out in the next step. Using, for

concreteness, the convention

$$\int \mathcal{D}v(x) \exp\left[-\frac{1}{2}\int\int dx\,dx' v(x)\,\mathbf{M}(x,x')\,v(x') + \int dx j(x)\,v(x)\right] \tag{6.68}$$

$$= \sqrt{\frac{(2\pi)^n}{\det \mathbf{M}}} \exp\left[\frac{1}{2}\int\int dx\,dx' j(x)\,\mathbf{M}^{-1}(x,x')\,j(x')\right] \tag{6.69}$$

for n-dimensional vectors v, j and an $n \times n$ matrix $\mathbf{M}$, we obtain

$$\overline{Z^n} = \int \mathcal{D}z^a\,\mathcal{D}Q_{ab}\,\mathcal{D}\lambda_{ab} \det{}^{-N/2}\left[-\frac{1}{\pi}\delta_{ab}\delta(\tau-\tau')\left(\frac{1}{2g}\partial_{\tau'}^2 + i z^a(\tau)\right) + \frac{i}{\pi}\lambda_{ab}(\tau,\tau')\right] \tag{6.70}$$

$$\times \exp\left\{\frac{N\hbar^2}{2}\int_0^\beta\int_0^\beta d\tau\,d\tau' \sum_{ab}\left(2\mathcal{G}(\tau,\tau') + 2i\boldsymbol{\lambda}(\tau,\tau')\right)^{-1}_{ab}\right\}$$

$$\times \exp\left[-Ni\sum_{a=1}^n\int_0^\beta d\tau z^a(\tau) + N\int_0^\beta\int_0^\beta d\tau d\tau'\left(i\lambda_{ab}(\tau,\tau')Q_{ab}(\tau,\tau')\right.\right.$$

$$\left.\left. + \frac{J^2}{4}\sum_{a,b=1}^n \left(Q_{ab}(\tau,\tau')\right)^p\right)\right]$$

$$\equiv \int \mathcal{D}z^a\,\mathcal{D}Q_{ab}\,\mathcal{D}\lambda_{ab} \exp(-\mathcal{S}_{\text{eff}}), \tag{6.71}$$

with the matrix $\mathcal{G}$ defined in replica and imaginary-time space as

$$\mathcal{G}_{ab}(\tau,\tau') \equiv -\delta_{ab}\,\delta(\tau-\tau')\left(\frac{1}{2g}\partial_{\tau'}^2 + i z^a(\tau)\right). \tag{6.72}$$

The replicated effective action can thus be extracted as

$$\begin{aligned}\frac{S_{\text{eff}}}{N} = \frac{1}{2}\log\det\left[\frac{1}{\pi}\left(\mathcal{G}_{ab}(\tau,\tau') + i\lambda_{ab}(\tau,\tau')\right)\right] + i\sum_{a=1}^{n}\int_0^\beta d\tau\, z^a(\tau) \\ - \int_0^\beta\int_0^\beta d\tau\, d\tau'\left[i\lambda_{ab}(\tau,\tau')Q_{ab}(\tau,\tau') + \frac{J^2}{4}\sum_{a,b=1}^{n}\left(Q_{ab}(\tau,\tau')\right)^p \right. \\ \left. + \frac{h^2}{4}\sum_{a,b=1}^{n}\left(\mathcal{G}(\tau,\tau') + i\boldsymbol{\lambda}(\tau,\tau')\right)^{-1}_{ab}\right].\end{aligned} \tag{6.73}$$

One of the advantages of the replica approach we are now positioned to harness is that since the effective action (6.73) is proportional to N, the saddle-point approximation is exact in the limit $N \to \infty$.

6.3.2 Saddle-point equations

We will only be interested in the saddle point of the theory (6.73), in which case we can assume that all fields are time-translation invariant and transform to Matsubara frequency space, as in (6.7). Then, we have

$$\begin{aligned}\frac{S_{\text{eff}}}{N} = \frac{1}{2}\sum_{\omega_n}\log\det\left[\frac{1}{\pi}\left(\delta_{ab}\left(\frac{1}{2g}\omega_n^2 - iz^a\right) + i\lambda_{ab}(\omega_n)\right)\right] + i\beta\sum_{a=1}^{n} z^a \\ - \sum_{a,b=1}^{n}\sum_{\omega_n} i\lambda_{ab}(-\omega_n)Q_{ab}(\omega_n) - \frac{\beta h^2}{4}\Big[-i\delta_{ab}z^a + i\lambda_{ab}(\omega_n=0)\Big]^{-1}_{ab} \\ - \frac{J^2}{4}\int_0^\beta\int_0^\beta d\tau d\tau'\left(Q_{ab}(\tau-\tau')\right)^p\ .\end{aligned} \tag{6.74}$$

We now employ a slight change of notation to obtain expressions similar to those in Ref. [155], defining

$$-iz^a = \frac{\overline{\lambda}}{2g} \quad , \quad i\lambda_{ab}(\omega_n) = -\frac{\Sigma_{ab}(\omega_n)}{2g}, \tag{6.75}$$

in terms of which, the effective action is

$$\frac{S_{\text{eff}}}{N} = \frac{1}{2}\sum_{\omega_n} \log\det\left[\frac{1}{2\pi g}\left(\delta_{ab}\left(\omega_n^2+\overline{\lambda}\right)-\Sigma_{ab}(\omega_n)\right)\right] - \beta\sum_{a=1}^{n}\frac{\overline{\lambda}}{2g} \tag{6.76}$$

$$+\sum_{a,b=1}^{n}\left(\frac{1}{2g}\sum_{\omega_n}\Sigma_{ab}(-\omega_n)Q_{ab}(\omega_n) - \frac{\beta h^2 g}{2}\left[\overline{\lambda}\delta_{cd}-\Sigma_{cd}(\omega_n=0)\right]^{-1}_{ab}\right.$$

$$\left.-\frac{J^2}{4}\int_0^\beta\int_0^\beta d\tau d\tau'\left(Q_{ab}(\tau-\tau')\right)^p\right). \tag{6.77}$$

Now, we use the identity (E.96) to absorb the h^2 term into the log det as

$$\frac{S_{\text{eff}}}{N} = \frac{1}{2}\sum_{\omega_n} \log\det\left[\frac{1}{2\pi g}\left(\delta_{ab}\left(\omega_n^2+\overline{\lambda}\right)-\Sigma_{ab}(\omega_n)-\beta h^2 g\delta_{\omega_n,0}\right)\right] - \beta\sum_{a=1}^{n}\frac{\overline{\lambda}}{2g}$$

$$+\sum_{a,b=1}^{n}\left(\frac{1}{2g}\sum_{\omega_n}\Sigma_{ab}(-\omega_n)Q_{ab}(\omega_n) - \frac{J^2}{4}\int_0^\beta\int_0^\beta d\tau d\tau'\left(Q_{ab}(\tau-\tau')\right)^p\right). \tag{6.78}$$

Then, the saddle-point equation with respect to $\Sigma_{ab}(\omega_n)$ is

$$Q_{ab}(\omega_n) = g\left[\delta_{ab}\left(\omega_n^2+\overline{\lambda}\right)-\Sigma_{ab}(\omega_n)-\beta h^2 g\delta_{\omega_n,0}\right]^{-1}_{ab}. \tag{6.79}$$

Inserting this back into (6.78), we obtain an effective action just for Q_{ab} and $\overline{\lambda}$:

$$\frac{S_{\text{eff}}}{N} = -\frac{1}{2}\sum_{\omega_n}\log\det Q_{ab}(\omega_n) - \beta\sum_{a=1}^{n}\frac{\overline{\lambda}}{2g} \tag{6.80}$$

$$+\sum_{a,b=1}^{n}\left(\frac{1}{2g}\sum_{\omega_n}\left[(\omega_n^2+\overline{\lambda})\delta_{ab}-\beta h^2 g\delta_{\omega_n,0}\right]Q_{ab}(\omega_n)\right.$$

$$\left.-\frac{J^2}{4}\int_0^\beta\int_0^\beta d\tau d\tau'\left(Q_{ab}(\tau-\tau')\right)^p\right).$$

From this, the saddle-point equations for Q_{ab} and $\overline{\lambda}$ can be read off as

$$\begin{aligned} 1 &= \frac{1}{\beta}\sum_{\omega_n} Q_{aa}(\omega_n), \\ \Sigma_{ab}(\tau) &= \frac{pJ^2}{2}\left(Q_{ab}(\tau)\right)^{p-1}, \\ gQ^{-1}_{ab}(\omega_n) &= \delta_{ab}(\omega_n^2+\overline{\lambda}) - \Sigma_{ab}(\omega_n) - \beta h^2 g\delta_{\omega_n,0}, \end{aligned} \tag{6.81}$$

with the Fourier transform defined by

$$Q_{ab}(\omega_n) = \int_0^\beta d\tau\, Q_{ab}(\tau)e^{i\omega_n\tau}, \tag{6.82}$$

and similarly for $\Sigma_{ab}(\omega_n)$. We numerically study these equations for the replica-symmetric and one-step replica-symmetry-breaking cases for specific values of p. In the discussion below, we focus on the $p=3$ model since, as we show below, it exhibits an interesting and nontrivial phase diagram due to the competition between these solutions.

For completeness, the solution of the $p=2$ model is presented in Appendix E.3. Note that with $p=2$ and $h=0$, Eq. (6.81) reduce to (33.32) and (33.33) in [155]. Moreover, for $p=4$, $h=0$ the equations (6.81) are very similar to Eqs. (S50–S53) in Ref. [33], the main difference being that ω_n^2 is replaced by $i\omega_n$.

6.3.3 Replica-symmetric solution

In this section, we numerically determine the replica-symmetric (RS) solution of the $p=3$ model as a function of transverse and longitudinal fields (g and h, respectively), while choosing the temperature to be close to zero.

The ansatz (6.8) for the replica overlap functions in the RS case necessarily has a replica off-diagonal

component

$$Q_{ab}(\omega_n) = \beta q \delta_{\omega_n,0} + Q_r(\omega_n)\delta_{ab},$$
$$\Sigma_{ab}(\omega_n) = \beta \varrho \delta_{\omega_n,0} + \Sigma_r(\omega_n)\delta_{ab}, \tag{6.83}$$

since, for nonzero h, the static moment is always nonzero. Then, using the identities in Appendix E.5, the equations in (6.81) become (for $p = 3$)

$$1 = q + \frac{1}{\beta}\sum_{\omega_n} Q_r(\omega_n), \tag{6.84}$$
$$\Sigma_r(\tau) = \frac{3gJ^2}{2}(q + Q_r(\tau))^2 - \frac{3gJ^2}{2}q^2, \tag{6.85}$$
$$\varrho = \frac{3}{2}gJ^2q^2, \tag{6.86}$$
$$\frac{g}{Q_r(\omega_n)} = \omega_n^2 + \overline{\lambda} - \Sigma_r(\omega_n), \tag{6.87}$$
$$\frac{gq}{Q_r(\omega_n = 0)^2} = \varrho + gh^2. \tag{6.88}$$

We solve these equations self-consistently in the imaginary-frequency domain for the order parameter q as a function of the transverse field g at low temperatures for several values of the longitudinal field, as shown in Fig. 6.7. In this model, the phase transition between the RS phase ($q \neq 0$) and the paramagnet (PM, $q = 0$) occurs only at zero longitudinal field. With even a slight increase in h, the replica-symmetric solution becomes equivalent to the paramagnet for all values of g as q is always non-zero (see (6.88)), as in Sec. 6.2.5.

Regardless of the value of the longitudinal field, we can show that the spectrum of the RS solution is gapped. To do so, we compute the dynamic spin susceptibility of the system, which requires analytic continuation of the equations (6.84)–(6.88) to real frequencies. Taking the zero-temperature limit,

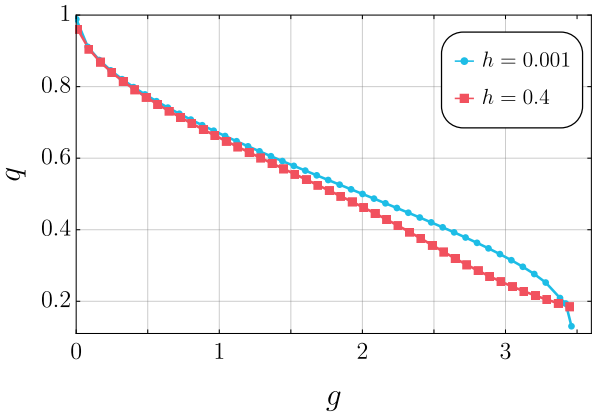

Figure 6.7: Behavior of the order parameter q for the replica-symmetric solution of the quantum spherical $p = 3$ model as a function of the transverse field g for different values of longitudinal fields h (with $J = 1$, $T = 0.005$). The phase transition between the replica-symmetric and paramagnetic solutions occurs only for $h = 0$.

we obtain equations of the form

$$\rho(\omega) = \frac{g}{\pi} \frac{\Sigma_r''(\omega)}{(\Sigma_r''(\omega))^2 + (-\omega^2 + \bar{\lambda} - \Sigma_r'(\omega))^2}, \tag{6.89}$$

$$\Sigma_r''(\omega) = 3\pi g J^2 \left(q\rho(\omega) + \frac{1}{2} \int_0^\omega d\omega_1 \rho(\omega_1)\rho(\omega - \omega_1) \right), \tag{6.90}$$

$$\Sigma_r'(\omega) = 2 \int_0^{+\infty} \frac{d\nu}{\pi} \frac{\nu\Sigma_r''(\nu) - \omega\Sigma_r''(\omega)}{\nu^2 - \omega^2}, \tag{6.91}$$

$$\varrho = \frac{3}{2} g J^2 q^2, \tag{6.92}$$

$$q = \frac{g\varrho + g^2 h^2}{[\bar{\lambda} - \Sigma_r'(\omega = 0)]^2}, \tag{6.93}$$

$$1 = q + \int_0^{+\infty} d\omega \rho(\omega), \tag{6.94}$$

where the spectral representation of the regular component of the replica overlap $Q_{ab}(i\omega_n)$ is

$$Q_r(z) = \int_{-\infty}^{\infty} d\omega \frac{\omega\rho(\omega)}{z^2 + \omega^2}, \tag{6.95}$$

and $\Sigma_r'(\omega)$ and $\Sigma_r''(\omega)$ are the real and imaginary parts of $\Sigma_r(i\omega_n)$, respectively. The spectral function

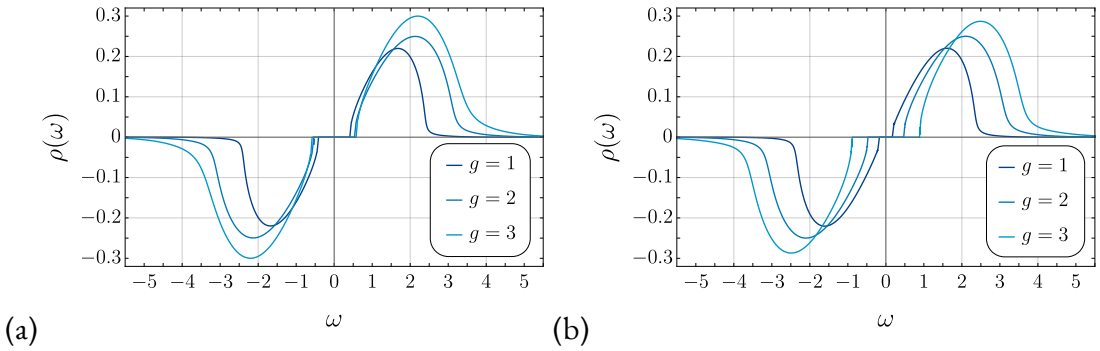

Figure 6.8: Spectral functions of the quantum spherical $p = 3$ model for (a) $h = 0$ and (b) $h = 1$ at zero temperature (with $J = 1$). (a) The phase transition between the RS phase and the quantum paramagnet occurs at a finite $g > 3$, and the gap thus eventually saturates upon increasing g. (b) The replica-symmetric solution persists for all values of g with a gap that grows with increasing g.

is related to the retarded Green's function as $\rho(\omega) = \text{Im}\, Q_r(\omega)/\pi$. Taking the $z \to \infty$ limit above, the associated sum rule becomes $\int_0^{+\infty} d\omega\, \omega\rho(\omega) = g/2$.

We note that the equations above, strictly speaking, permit several solutions, one of which has a discontinuity at zero frequency given by $\rho(\omega = 0) = 1/(2\pi J\sqrt{6q})$. To avoid this, we initialize the system with a simple step function with a small gap and let the equations converge (defined as when the error reaches 10^{-20}). As a final step, we also check that the sum rule is satisfied.

The spectral functions obtained in this fashion are presented in Fig. 6.8. For $h = 0$, we observe that as g increases, the gap saturates to a finite value and eventually, after the transition point, the system becomes a quantum-disordered paramagnet, as shown in Appendix E.4. However, at a finite field, the gap increases with increasing g without a visible saturation since the replica-symmetric solution and the paramagnet are one and the same.

6.3.4 One-step replica symmetry breaking

In this section, we now allow for nontrivial structure in the replica off-diagonal space. In general, replacing Eq. (6.83), we can write

$$\begin{aligned} Q_{ab}(\omega_n) &= \beta q_{ab}\delta_{\omega_n,0}; \quad a \neq b, \\ \Sigma_{ab}(\omega_n) &= \beta \varrho_{ab}\delta_{\omega_n,0}; \quad a \neq b. \end{aligned} \tag{6.96}$$

The matrices q_{ab} and ϱ_{ab} are characterized by Parisi functions $q(u)$ and $\varrho(u)$ with $u \in [0,1]$. For the diagonal components, we make the same ansatz as in (6.83)

$$\begin{aligned} Q_{aa}(\omega_n) &= \beta q_1\, \delta_{\omega_n,0} + Q_r(\omega_n), \\ \Sigma_{aa}(\omega_n) &= \beta \varrho_1\, \delta_{\omega_n,0} + \Sigma_r(\omega_n). \end{aligned} \tag{6.97}$$

We consider the one-step replica-symmetry-breaking (RSB) ansatz, for which (see Fig. 6.2)

$$q(u) = \begin{cases} q_1\,, & x < u < 1 \\ q_0\,, & 0 < u < x \end{cases}, \quad \text{and} \quad \varrho(u) = \begin{cases} \varrho_1\,, & x < u < 1 \\ \varrho_0\,, & 0 < u < x \end{cases}. \tag{6.98}$$

Using the identities in Appendix E.5, the equations in (6.81) now become

$$1 = q_1 + \frac{1}{\beta}\sum_{\omega_n} Q_r(\omega_n), \tag{6.99}$$

$$\varrho_1 + \Sigma_r(\tau) = \frac{pgJ^2}{2}(q_1 + Q_r(\tau))^{p-1}, \tag{6.100}$$

$$\varrho_1 = \frac{pgJ^2}{2}q_1^{p-1}, \tag{6.101}$$

$$\varrho_0 = \frac{pgJ^2}{2}q_0^{p-1}, \tag{6.102}$$

$$Q_r(\omega_n) = \frac{g}{\omega_n^2 + m^2 - \Sigma_r(\omega_n) + \Sigma_r(\omega_n = 0)}, \tag{6.103}$$

$$gh^2 + \varrho_1 = \frac{q_1 g + m^2\beta x(q_1 - q_0)^2}{[g/m^2 + \beta x(q_1 - q_0)]^2}, \tag{6.104}$$

$$gh^2 + \varrho_0 = \frac{gq_0}{[g/m^2 + \beta x(q_1 - q_0)]^2}, \tag{6.105}$$

where we have simplified the equations by changing variables and introducing $m^2 = \overline{\lambda} - \Sigma_r(\omega_n = 0)$.

There are eight unknowns, namely, m^2, Q_r, Σ_r, q_1, q_0, ϱ_1, ϱ_0, and βx, in the equations above. All but one of these variables can be determined by solving the seven equations (6.99)–(6.105). However, the value of the breakpoint βx is undetermined and can be fixed either by demanding a gapless solution, as in Appendix 3 of Ref.[33], or by requiring the free energy to be stationary with respect to x. The additional equation then makes the system complete and the solution can be obtained by solving the set of equations self-consistently. In the following, we derive this extra equation in both cases: by imposing the gapless constraint, and by using the free energy. In general the two methods lead to different solutions. It is known for the classical system that the gapless condition is chosen by dynamic preparation[41,16,17], while the free energy stationarity is chosen by the thermodynamic equilibrium state[169].

Gapless condition

Let us first determine the condition for a gapless spectrum in the RSB case; our approach here is similar to the analysis in Ref. [33]. For a gapless spectrum, we expect the low-frequency expansion of Q_r, for real ω, to have the form

$$Q_r(\omega + i\eta) = \frac{g}{m^2} + |\omega|^\alpha \left[a + ib\,\mathrm{sgn}(\omega)\right] + \ldots, \tag{6.106}$$

for some $\alpha > 0$, $b > 0$. From (6.100), we find that the leading singularity in $\Sigma_r(\omega)$ is given by the linear-in-$Q_r(\omega)$ term in (6.100), so

$$\begin{aligned} \mathrm{Im}\,\Sigma_r(\omega + i\eta) &= \frac{p(p-1)g\tilde{J}^2}{2} q_1^{p-2} \mathrm{Im}\, Q_r(\omega + i\eta), \\ &= \frac{p(p-1)g\tilde{J}^2}{2} q_1^{p-2} b\,|\omega|^\alpha\,\mathrm{sgn}(\omega)\,. \end{aligned} \tag{6.107}$$

However, from (6.103), for low frequencies, we also have

$$\mathrm{Im}\,\Sigma_r(\omega + i\eta) = -g\,\mathrm{Im}\left[Q_r(\omega + i\eta)\right]^{-1} = \frac{m^4}{g} b\,|\omega|^\alpha\,\mathrm{sgn}(\omega)\,. \tag{6.108}$$

Therefore, comparing equations (6.107) and (6.108), we arrive at the constraint on the variable m that has to be satisfied for the gapless solution to exist:

$$m^4 = \frac{p(p-1)g^2\tilde{J}^2}{2} q_1^{p-2}\,. \tag{6.109}$$

It is easy to check that for the special case of $p = 2$, this expression precisely agrees with Eq. (33.41) in Ref. [155] and is similar to Eq. (4.11) in Ref. [7].

It is important to note that upon solving the replica-symmetric equations self-consistently, we did not obtain a gapless solution. One way to understand this is to plug the gapless constraint (6.109) into the equations for the replica-symmetric case (6.84)–(6.88), which expressly demonstrates that the

constraint cannot be satisfied for any values of h. Therefore, the replica-symmetric solution always has a gap.

Free energy

Another way to fix x is to determine the saddle point of the free energy with respect to x. To do so, we rewrite the effective action of the p-rotor model (6.80) explicitly for the one-step replica-symmetry-breaking case

$$\begin{aligned}\frac{S_{\text{eff}}}{Nn} = &-\frac{1}{2}\sum_{\omega_n}\log[Q_r(\omega_n)] - \frac{1}{2}\frac{\beta q_0}{Q_r(\omega_n=0)+\beta x(q_1-q_0)} + \frac{1}{2x}\ln\frac{Q_r(\omega_n=0)}{Q_r(\omega_n=0)+\beta x(q_1-q_0)}\\ &-\frac{\beta\overline{\lambda}}{2g} + \frac{1}{2g}\sum_{\omega_n}(\omega_n^2+\overline{\lambda})Q_r(\omega_n) + \frac{\overline{\lambda}\beta q_1}{2g} - \frac{\beta h^2}{2}\left[Q_r(\omega_n=0)+\beta x(q_1-q_0)\right]\\ &-\frac{\beta J^2}{4}\int_0^\beta d\tau\left[(Q_r(\tau)+q_1)^p - q_1^p(1-x) - q_0^p x\right]. \end{aligned} \tag{6.110}$$

This action allows one to directly verify that the saddle-point equations are in fact correct: taking the derivative of (6.110) with respect to q_0 and $\overline{\lambda}$, we see that the equations (6.99) and (6.105) indeed hold after a change of variables to $m^2 = \overline{\lambda} - \Sigma_r(\omega_n = 0)$.

To obtain an equation for x, we differentiate the action with respect to the breakpoint and obtain

$$\begin{aligned}\frac{\partial S_{\text{eff}}}{\partial x} = 0 \quad \Rightarrow \quad &\frac{J^2\beta^2}{4}(q_1^p - q_0^p) - \frac{1}{2x^2}\log\left[1+\frac{\beta x(q_1-q_0)}{Q_r(\omega_n=0)}\right]\\ &+\frac{\beta^2 h^2}{2}(q_1-q_0) + \frac{\beta(q_1-q_0)(Q_r(\omega_n=0)+\beta q_1 x - 2\beta q_0 x)}{2x(Q_r(\omega_n=0)+\beta x(q_1-q_0))^2} = 0. \end{aligned} \tag{6.111}$$

Although such a saddle-point condition has been employed to obtain the equilibrium state for the classical model [169], we will not use (6.111) here. It what follows, we instead use the gapless constraint to determine the breakpoint x.

Spectral functions

As for the replica-symmetric case before, we are interested in the behavior of the spectral functions in the RSB case. To this end, we analytically continue the equations on the imaginary-frequency axis (6.99)–(6.102) and (6.103)–(6.105), focusing on the $p = 3$ case at zero temperature. After such analytic continuation, we obtain

$$1 = q_1 + \int_0^{+\infty} d\omega \rho(\omega), \tag{6.112}$$

$$\Sigma_r''(\omega) = 3\pi g J^2 \left(q_1 \rho(\omega) + \frac{1}{2} \int_0^{\omega} d\omega_1 \rho(\omega_1) \rho(\omega - \omega_1) \right), \tag{6.113}$$

$$\Sigma_r'(\omega) = 2 \int_0^{+\infty} \frac{d\nu}{\pi} \frac{\nu \Sigma_r''(\nu) - \omega \Sigma_r''(\omega)}{\nu^2 - \omega^2}, \tag{6.114}$$

$$\varrho_1 = \frac{3gJ^2}{2} q_1^2, \tag{6.115}$$

$$\varrho_0 = \frac{3gJ^2}{2} q_0^2, \tag{6.116}$$

$$\rho(\omega) = \frac{g}{\pi} \frac{\Sigma_r''(\omega) - \Sigma_r''(\omega = 0)}{(\Sigma_r''(\omega) - \Sigma_r''(\omega = 0))^2 + (\omega^2 - m^2 + \Sigma_r'(\omega) - \Sigma_r'(\omega = 0))^2}, \tag{6.117}$$

$$gh^2 + \varrho_1 = \frac{q_1 g + m^2 \beta x (q_1 - q_0)^2}{[g/m^2 + \beta x (q_1 - q_0)]^2}, \tag{6.118}$$

$$gh^2 + \varrho_0 = \frac{g q_0}{[g/m^2 + \beta x (q_1 - q_0)]^2}. \tag{6.119}$$

For the final equation, as mentioned, we use the gapless constraint

$$m^4 = 3g^2 J^2 q_1, \tag{6.120}$$

derived above in (6.109), and this gapless behavior should also be reflected in the spectral functions. Therefore, we are allowed to make a linear ansatz

$$\rho(\omega) = \omega f(\omega). \tag{6.121}$$

We insert this ansatz in Eqs. (6.113)–(6.119) and solve the equations self-consistently for $f(\omega)$. It is quite challenging to obtain the self-consistent solution to these equations for all unknowns. Instead, we simplify this task by solving the equations on the imaginary-frequency axis and self-consistently obtain the value of the order parameter q_1 at a temperature close to zero with a high precision. Then, we use this result to obtain the behavior of the spectral functions. To ensure that the converged solution is meaningful, we check the sum rule, which, in this case, is given by $\int_0^{+\infty} d\omega\, \omega^2 f(\omega) = g/2$.

We sketch the behavior of the spectral functions $\mathrm{Im}\, Q_r(\omega)$ in Fig. 6.3. From the equations above, it is clear that spectral functions are independent of h, βx and q_0. Only two parameters, namely, q_0 and βx, depend on h. This is similar to the behavior of the Ising model in Sec. 6.2.5, where the only change from the $h = 0$ solution in Sec. 6.2.4 was in the form of $q(u)$ for $u < (q_h/q_{EA})x$ in (6.57). It is also instructive to determine the dependence of q_0 and βx on h in the $h \to 0$ limit, which can be calculated from the equations (6.118) and (6.119). We find that, to the lowest order, the dependence is simply

$$q_0 = \frac{4g^2}{m^4} h^2; \;\; \beta x = \frac{g}{q_1 m^2} - \frac{4g^2}{3m^2 J^2 q_1^3} h^2, \tag{6.122}$$

which, as noted in Sec. 6.1.1, is in distinction to the $h^{2/3}$ scaling observed for the Ising spin glass.

6.3.5 Phase diagram

Finally, having assembled all the necessary ingredients, we now compute the phase diagram of the quantum spherical $p = 3$-rotor model in a longitudinal field at low temperatures. To do so, we first determine the boundary of stability of the RSB solution by self-consistently computing the spin glass order parameter from equations (6.99)–(6.105) and comparing q_0 and q_1. For the stability of the RSB solution, one has to require $q_0 \leq q_1$ [26], and the solution ceases to be physical when $q_0 > q_1$. Our numerical results in this regard are displayed in Fig. 6.9. In particular, Fig. 6.9(a) presents q_0 and q_1 as

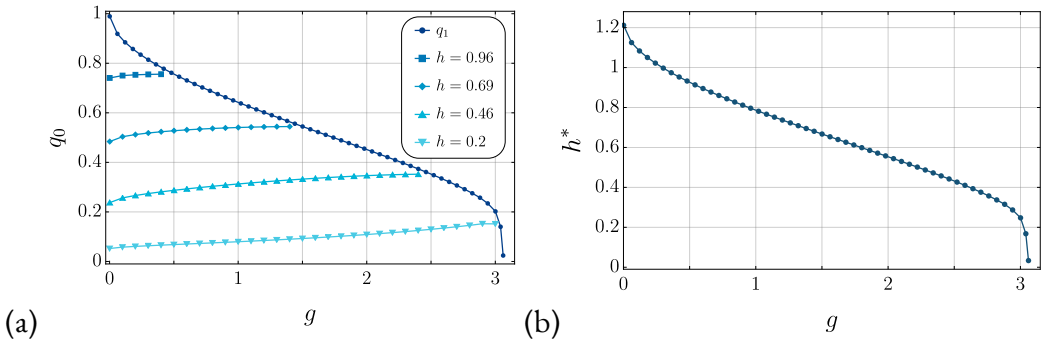

Figure 6.9: (a) Behavior of q_0 and q_1 as a function of g for the spherical quantum $p = 3$-rotor model in a longitudinal field with $T = 0.005$ and $J = 1$. Note that q_1 is independent of h but q_0 is not. (b) Boundary of stability of the RSB phase as determined by setting $q_0(g, h^*) = q_1(g)$. For $h > h^*(g)$, the necessary condition $q_0 \leq q_1$ required for the RSB solution no longer holds. Note that both plots are extrapolated around $q_0 \simeq 0$ and $h^* \simeq 0$.

a function of g for various values of h; the RSB solution exists only for q_0 that lie below the line $q_1(g)$. Based on this information, Fig. 6.9(b) traces, in g-h space, the line $h^*(g)$ along which $q_0(g, h^*) = q_1(g)$. Since this marks the boundary of stability of the RSB solution, the phase transition between the RSB and RS phases may occur at this line.

To check whether this is indeed the case, we compute the free energies of both the RS and RSB solutions. The free energy in the RS case can be written using (6.80) and we obtain

$$\begin{aligned}\frac{F_{\text{eff}}^{\text{RS}}}{Nn} = &-\frac{1}{2\beta}\sum_{\omega_n}\log[(\omega_n^2+\Gamma^2)Q_r(\omega_n)/g] - \frac{1}{2}\frac{q}{Q_r(\omega_n=0)} \\ &-\frac{\overline{\lambda}}{2g}+\frac{\overline{\lambda}q}{2g}+\frac{1}{2g\beta}\sum_{\omega_n}\left[(\omega_n^2+\overline{\lambda})Q_r(\omega_n)-g\right] \\ &-\frac{h^2}{2}Q_r(\omega_n=0) - \frac{J^2}{4}\int_0^\beta d\tau\left[(q+Q_r(\tau))^3-q^3\right]+\frac{\Gamma}{2}+\frac{1}{\beta}\ln\left[1-e^{-\beta\Gamma}\right], \qquad (6.123)\end{aligned}$$

where we inserted a factor of $(\omega_n^2+\Gamma^2)/g$ into the argument of the logarithm to regularize the behavior at large $|\omega_n|$, and subtracted a constant to regulate the frequency summation in the term linear in Q_r. This is equivalent to normalizing the path integral with an oscillator of frequency Γ. In order to make the resulting expression independent of Γ, we subtracted the free energy of this oscillator. For the RSB

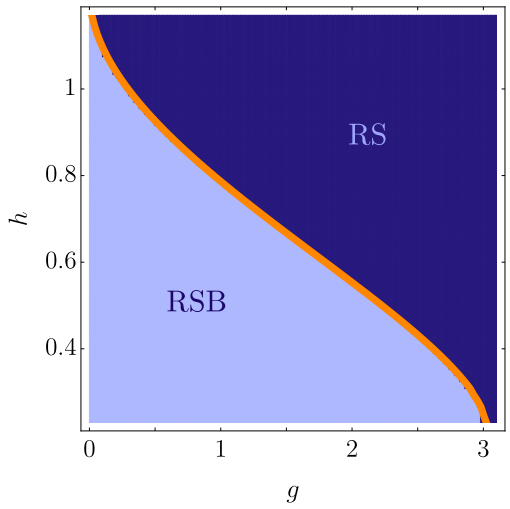

Figure 6.10: Phase diagram of the spherical quantum $p = 3$-rotor model in a longitudinal field with $T = 0.005$ and $J = 1$. The phase diagram is evaluated by calculating the difference between the free energies of the replica-symmetric (RS, 6.123) and replica-symmetry-breaking (RSB, 6.124) solutions. The orange line on the phase boundary traces the function $h^*(g)$ plotted in Fig. 6.9(b).

case, we use the expression for the free energy computed above, focusing on $p = 3$,

$$\begin{aligned}\frac{F_{\text{eff}}^{\text{RSB}}}{Nn} = &-\frac{1}{2\beta}\sum_{\omega_n}\log[(\omega_n^2+\Gamma^2)Q_r(\omega_n)/g] - \frac{1}{2}\frac{q_0}{Q_r(\omega_n=0)+\beta x(q_1-q_0)} \\ &+\frac{1}{2\beta x}\ln\frac{Q_r(\omega_n=0)}{Q_r(\omega_n=0)+\beta x(q_1-q_0)} - \frac{\overline{\lambda}}{2g} + \frac{1}{2g\beta}\sum_{\omega_n}\left[(\omega_n^2+\overline{\lambda})Q_r(\omega_n) - g\right] \\ &+\frac{\overline{\lambda}q_1}{2g} - \frac{h^2}{2}\left[Q_r(\omega_n=0)+\beta x(q_1-q_0)\right] \\ &-\frac{J^2}{4}\int_0^\beta d\tau\left[(q_1+Q_r(\tau))^3 - q_1^3(1-x) - q_0^3 x\right] + \frac{\Gamma}{2} + \frac{1}{\beta}\ln\left[1-e^{-\beta\Gamma}\right]. \end{aligned} \tag{6.124}$$

Here, we use the same regularization as for the free energy of the replica-symmetric solution. In both cases, Γ has to be much smaller than the Matsubara frequency cutoff.

We evaluate the difference in free energies between the RSB and RS solutions to find the parameter regions where each phase is dominant. Following the discussion in Ref. [173], we pick the ground state as the one that has a larger free energy. The resulting phase diagram is shown in Fig. 6.10; we find

that the phase boundary obtained by comparing the free energies coincides (to a precision of $|F_{\rm eff}^{\rm RSB} - F_{\rm eff}^{\rm RS}|/(Nn) < 10^{-5}$) with the line $h^*(g)$ demarcating the stability of the RSB solution in Fig. 6.9(b).

6.4 Conclusions

Motivated by the quantum simulation of spatially disordered long-ranged interacting systems for solving combinatorial optimization problems[48,171], we have studied the equilibrium dynamic properties of two quantum spin glass models with infinite-range interactions: the Ising model in (6.1), and the spherical p-rotor model in (6.3) and (6.4). In addition to random couplings between spins/rotors, both models have an applied longitudinal field h, and do not break any global symmetry in any phase. A coupling g tunes the strength of the quantum fluctuations, and at large g, we obtain a gapped paramagnetic phase. Our primary interest was in the small-g regime, where replica symmetry breaking leads to a quantum spin glass phase.

For the Ising model, we employed the Landau theory approach of Ref. [150] to show that the spin glass phase has full replica symmetry breaking, with the Parisi function sketched in Fig. 6.1. We computed the spin autocorrelation function in this spin glass phase, and showed that it is generically gapless, with a spectral density which vanishes linearly with frequency (see (6.9) and Secs. 6.2.4 and 6.2.5).

In contrast, the spherical p-rotor model ($p \geq 3$) has a different behavior in the spin glass phase. There is only one-step replica symmetry breaking (see Fig. 6.2), and the breakpoint x remains undetermined by the saddle-point equations for the matrix spin glass order parameter. Rigorous mathematical work on the classical $g = 0$ model [169] has shown that the equilibrium value of x is determined by the stationarity of the free energy with respect to x. For this x, we showed that the spin glass state has an energy gap. In contrast, if a marginal stability condition [39,41,38] is used to determine x, we found a gapless spectrum with a linear frequency dependence at small frequency (see Fig. 6.3), similar to that of the Ising model.

Our results on the nature of the spin glass phase also find relevance in the context of quantum optimization problems since the properties of the gap—or lack thereof—directly inform the feasibility of preparing low-energy states via adiabatic algorithms [3,23,157].

Looking ahead, it would be useful to obtain the results described here without the replica method, using a path integral on the Schwinger-Keldysh contour. This has already been studied for the spherical p-rotor model [41,16,17], where the breakpoint of one-step replica symmetry breaking, x, has been connected to an effective temperature of the aging dynamics. Moreover, the equation for a gapless spectrum in (6.109) is the same as Eq. (6.24) obtained in Ref. [41] from aging dynamics. However, the aging dynamics of the quantum Ising model [97] with the crucial y quartic term have not been studied so far, and it would be interesting to relate that to the full replica symmetry breaking characterized by Fig. 6.1. Such a computation would be the analog of earlier studies [163,162,164,40,5] of aging dynamics in classical spin glasses described by Langevin equations, and we expect that there would be significant differences [56,5] between the Ising model and the spherical model in the quantum problem too.

A

Supplementary Information for Chapter 2

A.1 Free energy from conformal perturbations

We can also use the conformal perturbation methods of Section 2.3 to compute the low temperature expansion for the free energy. We find [107,51,122]

$$\begin{aligned}\beta F_{\rm SYK} =& \beta F_{\rm CFT} + \sum_h g_h \int_0^\beta d\tau \langle O_h \rangle_\beta - \frac{1}{2}\sum_{h,h'} g_h g_{h'} \int_0^\beta d\tau_1 d\tau_2 \langle O_h(\tau_1) O_{h'}(\tau_2)\rangle_\beta \\ &+ \frac{1}{6}\sum_{h,h',h''} g_h g_{h'} g_{h''} \int_0^\beta d\tau_1 d\tau_2 d\tau_2 \langle O_h(\tau_1) O_{h'}(\tau_2) O_{h''}(\tau_3)\rangle_\beta + \dots . \end{aligned} \tag{A.1}$$

The one-point functions in thermal CFT are not necessarily zero and from the scale symmetry we have [95,90]

$$\langle O_h \rangle_\beta = N b_h / (\beta J)^h . \tag{A.2}$$

To find constants b_h we consider thermal conformal two point function

$$G_\beta(\tau) = -\frac{1}{N}\langle \chi_i(\tau)\chi_i(0)\rangle_\beta = -\frac{b^\Delta \operatorname{sgn}(\tau)}{|\frac{\beta J}{\pi}\sin\frac{\pi\tau}{\beta}|^{2\Delta}} . \tag{A.3}$$

Expanding it in series for $\tau \to 0$ we obtain

$$G_\beta(\tau) = -\frac{b^\Delta \operatorname{sgn}(\tau)}{|J\tau|^{2\Delta}}\left(1 + \frac{\pi^3}{3}\Delta\left|\frac{\tau}{\beta}\right|^2 + \frac{\pi^4}{90}\Delta(1+5\Delta)\left|\frac{\tau}{\beta}\right|^4 + \dots\right) . \tag{A.4}$$

On the other hand using OPE in (2.32) we find

$$G_\beta(\tau) = -\frac{b^\Delta \operatorname{sgn}(\tau)}{|J\tau|^{2\Delta}}\left(1+\sum_h c_h |J\tau|^h \langle O_h\rangle_\beta\right), \tag{A.5}$$

where we assumed that the two-point functions of O_h are normalized as in (2.32). Comparing (A.4) and (A.5) we find that only operators with $h = 2k$, where $k = 1, 2, 3, \ldots$ have non-zero one point function, but all operators with $h_1, h_2, h_3, \ldots$ should have zero one point function. As we already stressed before conformal symmetry is broken in the SYK model and the analysis above should be taken with caution. The role of higher expansion terms in (A.4) with $k > 1$ is unclear. Moreover in [35] it was conjectured that the free energy has a term $T^{3.77}$ in small T expansion and thus this would imply non-zero one point function $\langle O_{h_1}\rangle_\beta$. Whether this is correct or not remains an open question. For $h_0 = 2$ operator we find $b_0 c_0 = \frac{\pi^2}{3}\Delta$. Thus the contribution of the one-point function of $h_0 = 2$ operator to the free energy is

$$\beta\delta F_{h_0} = \beta g_0 \langle O_{h_0}\rangle_\beta = \frac{N\pi^2\Delta}{3(\beta J)^2}\frac{\beta g_0}{c_0} = -\frac{2\pi^2 N}{(\beta J)}\alpha_S, \tag{A.6}$$

where $\alpha_S = \frac{1}{6}(1-\Delta)b^\Delta |k'_{\rm A}(2)|\alpha_0$ is the Schwarzian action coupling and this result agrees with [121,104]. For the second order correction we find

$$\begin{aligned}\beta\delta^2 F_h &= -\frac{1}{2}\sum_h g_h^2 \int_0^\beta d\tau_1 d\tau_2 \langle O_h(\tau_1) O_h(\tau_2)\rangle = -\frac{1}{2}\sum_h N g_h^2 \beta \int_\varepsilon^{\beta-\varepsilon} d\tau \left(\frac{\pi}{\beta J \sin\frac{\pi\tau}{\beta}}\right)^{2h} \\ &= -\frac{1}{2}\sum_h \left(\frac{N(g_h^2/J^2)(\beta J)}{(h-1/2)(\varepsilon J)^{2h-1}} + \frac{N(g_h^2/J^2)}{(\beta J)^{2h-2}}\frac{\pi^{2h-\frac{1}{2}}\Gamma(\frac{1}{2}-h)}{\Gamma(1-h)}\right),\end{aligned} \tag{A.7}$$

where we regulated the integral in UV by a cutoff $\varepsilon \sim 1/J$. The first term is proportional to $N(\beta J)$ and represents correction to the ground energy, whereas the second term is finite and gives contribution

to the free energy of order $1/(\beta J)^{2h-2}$, so we find

$$\beta\partial^2 F_h = N(q-1)b^{\Delta}(-k'_{\rm A}(h))\frac{(\pi/2)^{2h-1}(\cos(\pi h)+1)\Gamma(h)^2}{(2h-1)\cos(\pi h)\Gamma\left(h-\frac{1}{2}\right)^2}\frac{\alpha_h^2}{(\beta J)^{2h-2}}\,. \tag{A.8}$$

For $h_0 = 2$ this result gives $\beta\partial^2 F_{h_0} = N2\pi^2 q\alpha_S\alpha_0/(\beta J)^2$, which exactly agrees with $N/(\beta J)^2$ correction computed in [104,35] using careful analysis of $h_0 = 2$ mode [*]. Moreover using the result for the large q free energy from [170] we find for $1/(\beta\mathcal{J})^2$ term

$$\beta F \supset \Big(\frac{\pi^2}{q^2} - \frac{\pi^2(24+5\pi^2)}{9q^3} + \dots\Big)\frac{N}{(\beta\mathcal{J})^2}\,. \tag{A.9}$$

On the other hand taking large q limit of (A.8) for h_0 operator and using that $\tilde{\alpha}_0 = \frac{2}{q} - \frac{12+7\pi^2}{9q^2} + \dots$ (see Appendix A.2) we obtain

$$\beta\partial^2 F_{h_0} = \Big(\frac{\pi^2}{q^2} - \frac{\pi^2\left(24+5\pi^2\right)}{9q^3} + \dots\Big)\frac{N}{(\beta\mathcal{J})^2}. \tag{A.10}$$

We see that $\beta\partial^2 F_{h_0}$ exactly coincides with $1/q^2$ and $1/q^3$ orders in the large q expansion. This implies that if the one point function $\langle O_{h_1}\rangle_\beta$ is not zero it should start contributing only at the $1/q^4$ order, which seems unlikely. The third order correction is given by

$$\begin{aligned}\beta\partial^3 F_{hh'h''} &= \frac{1}{6}g_h g_{h'} g_{h''}\int_0^\beta \frac{d\tau_1 d\tau_2 d\tau_3 N c_{hh'h''}}{(\frac{\beta J}{\pi}\sin\frac{\pi\tau_{12}}{\beta})^{h+h'-h''}(\frac{\beta J}{\pi}\sin\frac{\pi\tau_{13}}{\beta})^{h+h''-h'}(\frac{\beta J}{\pi}\sin\frac{\pi\tau_{23}}{\beta})^{h'+h''-h}}\\ &= \frac{N c_{hh'h''}g_h g_{h'}g_{h''}\Gamma(\frac{1-2(h+h'-h'')}{2})\Gamma(\frac{1-2(h+h''-h')}{2})\Gamma(\frac{1-2(h'+h''-h)}{2})\Gamma(1-h-h'-h'')}{6\pi^{\frac{3}{2}-h-h'-h''}(\beta J)^{h+h'+h''}\Gamma(1-2h)\Gamma(1-2h')\Gamma(1-2h'')}\,.\end{aligned} \tag{A.11}$$

[*] In [121] it was shown that $\langle O_{h_0}(\tau_1)O_{h_0}(\tau_2)\rangle = \frac{N4\pi^2\alpha_S}{\beta^3 J}$ rather than $\langle O_{h_0}(\tau_1)O_{h_0}(\tau_2)\rangle = \frac{N}{|\tau_{12}|^4}$. Nevertheless in our computation we assumed the later form of this correlation function and obtained the correct result.

Using general expression for $c_{hh'h''}$ [75] for the case when $h = h' = h'' = h_0 \to 2$ we find $c_{h_0h_0h_0} \propto 1/(h_0-2)^{3/2}$ and therefore the full result (A.11) is divergent in this case. This signals that the conformal perturbation theory developed above should be taken very cautiously for $h_0 = 2$ operator and in general may produce incorrect results.

A.2 Large q two point function in the fermionic SYK model

We consider the fermionic SYK$_q$ model with zero chemical potential $\mu_f = 0$. In this case there is a Particle-Hole symmetry and the Schwinger-Dyson equations are $G(i\omega_n)^{-1} = i\omega_n - \Sigma(i\omega_n)$ and $\Sigma(\tau) = J^2 G(\tau)^{q-1}$. At the limit $q \to \infty$ the two point function at finite temperature $T = 1/\beta$ admits $1/q$ decomposition [121]:

$$G(\tau) = -\frac{1}{2}\mathrm{sgn}(\tau)\Big(1 + \frac{1}{q}g(\tau) + \frac{1}{q^2}h(\tau) + \dots\Big)\,, \tag{A.12}$$

where $g(\tau) = 2\log\Big(\frac{\cos\frac{\pi v}{2}}{\cos x}\Big)$ and we defined $x \equiv \frac{\pi v}{2} - \frac{\pi v \tau}{\beta}$ and v is found from transendental equation $\beta\mathcal{J} = \frac{\pi v}{\cos\frac{\pi v}{2}}$ with rescaled coupling $\mathcal{J} = (2^{1-q}q)^{1/2}J$. The next order $h(\tau)$ was found in [170] and reads

$$h(\tau) = \frac{g^2(x)}{2} - 2\ell(x) - 4\Big(\tan x \int_0^x dy\ell(y) + 1\Big) + \frac{4(\tan\frac{\pi v}{2}\int_0^{\frac{\pi v}{2}} dy\ell(y) + 1)(1 + x\tan x)}{1 + \frac{\pi v}{2}\tan\frac{\pi v}{2}}\,, \tag{A.13}$$

where $\ell(x) = g(x) - e^{-g(x)}\mathrm{Li}_2(1 - e^{g(x)})$. Also the expression for the large q free energy of the Majorana SYK is

$$\beta F/N = -\frac{1}{2}\log 2 - \pi v\Big(\tan\frac{\pi v}{2} - \frac{\pi v}{4}\Big)\frac{1}{q^2} - \pi v\Big(\pi v - 2\tan\frac{\pi v}{2}\Big(1 - \frac{\pi^2 v^2}{12}\Big)\Big)\frac{1}{q^3} + \dots\,. \tag{A.14}$$

At large $\beta\mathcal{J}$ limit one finds

$$v = 1 - \frac{2}{\beta\mathcal{J}} + \frac{4}{(\beta\mathcal{J})^2} - \frac{24+\pi^2}{3(\beta\mathcal{J})^3} + \frac{8\left(6+\pi^2\right)}{3(\beta\mathcal{J})^4} + \dots \,. \tag{A.15}$$

Using this expansion and equations for $g(\tau)$ and $h(\tau)$ we can find at $\beta = \infty$ that $g(\tau) = \log u^2$ and

$$\begin{aligned} h(\tau) = &-\frac{4}{3}(1-u) - \frac{\pi^2}{9}u(3+u^{-3}) - \frac{2}{3}\log\left(u^2\right) + \frac{1}{6}(4u+3)\log^2(u^2) \\ &+ \frac{8}{3}u\log\left(u^2\right)\log\left(1+u^{-1}\right) - \frac{16}{3}u\mathrm{Li}_2(-u^{-1}) + \frac{2}{3}u(2+u^{-3})\mathrm{Li}_2(1-u^2)\,, \end{aligned} \tag{A.16}$$

where we denoted $u \equiv 1/(1+\mathcal{J}\tau)$. Conformal approximation to the two-point function at $\beta = \infty$ has the form

$$G^c(\tau) = -b^{1/q}\frac{\mathrm{sgn}(\tau)}{|J\tau|^{2/q}}, \quad b = \frac{q-2}{2\pi q}\tan\frac{\pi}{q}\,, \tag{A.17}$$

therefore we can write the two point function (A.12) as

$$\begin{aligned} G(\tau) &= G^c(\tau)(\mathcal{J}\tau)^{\frac{2}{q}}\left(\frac{q-2}{\pi}\tan\frac{\pi}{q}\right)^{-1/q}\left(1+\frac{1}{q}g(\tau)+\frac{1}{q^2}h(\tau)+\dots\right) \\ &= G^c(\tau)\left(1+\frac{2\log\mathcal{J}\tau}{q}+\frac{2(1+\log^2\mathcal{J}\tau)}{q^2}+\dots\right)\left(1-\frac{2\log(1+\mathcal{J}\tau)}{q}+\frac{1}{q^2}h(\tau)+\dots\right). \end{aligned} \tag{A.18}$$

Finally using result (A.16) and expanding everything in the limit $\mathcal{J}\tau \to \infty$ we find

$$\begin{aligned} G(\tau) =& G^c(\tau)\Bigg(1+\Big(-\frac{2}{\mathcal{J}\tau}+\frac{1}{(\mathcal{J}\tau)^2}-\frac{2}{3(\mathcal{J}\tau)^3}+\dots\Big)\frac{1}{q} \\ &+\Big(\frac{12+7\pi^2}{9}\left(\frac{1}{\mathcal{J}\tau}-\frac{1}{(\mathcal{J}\tau)^2}+\frac{1}{(\mathcal{J}\tau)^3}\right) \\ &-\frac{7}{2(\mathcal{J}\tau)^2}+\frac{3}{(\mathcal{J}\tau)^3}-\frac{6\log(\mathcal{J}\tau)}{(\mathcal{J}\tau)^2}+\frac{12\log(\mathcal{J}\tau)}{(\mathcal{J}\tau)^3}+\dots\Big)\frac{1}{q^2}+\dots\Bigg)\,. \end{aligned} \tag{A.19}$$

On the other hand from the resonance theory described in Section 2.4 we expect to have

$$G(\tau) = G^c(\tau)\left(1 - \sum_{k=0}^{\infty} \frac{\alpha_k}{|J\tau|^{b_k-1}} - \sum_{k,m=0}^{\infty} \frac{a_{km}\alpha_k\alpha_m}{|J\tau|^{b_k+b_m-2}} - \sum_{k,m,l=0}^{\infty} \frac{a_{kml}\alpha_k\alpha_m\alpha_l}{|J\tau|^{b_k+b_m+b_l-3}} - \dots\right), \quad \text{(A.20)}$$

where $\alpha_k, a_{km}, a_{kml}$ are all functions of q. In the large q limit solving $k_{\mathrm{A}}(h) = 1$, where

$$k_{\mathrm{A}}(h) = \frac{\Gamma(2\Delta - h)\Gamma(2\Delta + h - 1)}{\Gamma(2\Delta - 2)\Gamma(2\Delta + 1)}\left(1 - \frac{\sin(\pi h)}{\sin(2\pi\Delta)}\right) \quad \text{(A.21)}$$

we find that operators dimensions apart from $h_0 = 2$ admit $1/q$ decomposition and read

$$h_1 = 3 + \frac{4}{q} + \dots, \quad h_2 = 5 + \frac{22}{9q} + \dots, h_k = 2k + 1 + \frac{2(2k^2 + k + 1)}{(k+1)(2k-1)q} + \dots. \quad \text{(A.22)}$$

Using these anomalous dimensions in (A.20) we find

$$\begin{aligned} G(\tau) =& G^c(\tau)\left(1 - \frac{\tilde\alpha_0}{(\mathcal{J}\tau)} - \frac{a_{00}\tilde\alpha_0^2}{(\mathcal{J}\tau)^2} - \frac{\tilde\alpha_1}{(\mathcal{J}\tau)^{2+\frac{4}{q}+\dots}} - \frac{a_{000}\tilde\alpha_0^3}{(\mathcal{J}\tau)^3} - \frac{2a_{01}\tilde\alpha_0\tilde\alpha_1}{(\mathcal{J}\tau)^{3+\frac{4}{q}+\dots}} - \frac{\tilde\alpha_2}{(\mathcal{J}\tau)^{4+\frac{22}{9q}+\dots}} - \dots\right) \\ =& G^c(\tau)\left(1 - \frac{\tilde\alpha_{b_0}}{(\mathcal{J}\tau)} - \frac{a_{00}\tilde\alpha_0^2}{(\mathcal{J}\tau)^2} - \frac{\tilde\alpha_1}{(\mathcal{J}\tau)^2}\left(1 - \frac{4}{q}\log(\mathcal{J}\tau) + \dots\right)\right. \\ & \left. - \frac{\tilde\alpha_2}{(\mathcal{J}\tau)^4}\left(1 - \frac{22}{9q}\log(\mathcal{J}\tau) + \dots\right) - \dots\right), \end{aligned} \quad \text{(A.23)}$$

where we denoted $\tilde\alpha_k(q) = (2^{1-q}q)^{\frac{b_k-1}{2}}\alpha_k(q)$. Comparing (A.19) and (A.23) we find relations

$$\tilde\alpha_0(q) = \frac{2}{q} - \frac{12 + 7\pi^2}{9q^2} + \dots, \quad \tilde\alpha_1(q) = -\frac{3}{2q} + \frac{7\pi^2 + 33 - 24a_{00}^{(2)}}{6q^2} + \dots, \quad \text{(A.24)}$$

$$a_{00}(q) = \frac{q}{8} + a_{00}^{(2)} + \dots, \ a_{01}(q) = -\frac{q}{2} + a_{01}^{(2)} + \dots, \quad \text{(A.25)}$$

$$a_{000}(q) = -\frac{7}{24}q^2 + \frac{1}{8}(6a_{01}^{(2)} - 8a_{00}^{(2)} + 4)q + \dots \quad \text{(A.26)}$$

We notice that $\log(\mathcal{J}\tau)/(\mathcal{J}\tau)^2$ and $\log(\mathcal{J}\tau)/(\mathcal{J}\tau)^3$ terms in $1/q^2$ order arise due to h_1 operator. The large q results (A.26) for a_{00}, a_{01} and a_{000} match with an arbitrary q formulas (2.80) and (2.85) derived in the Section 2.4. This comparison also fixes $a_{00}^{(2)} = 0$ and $a_{01}^{(2)} = -3/2$.

A.3 Two point function for $q = 2$ in the fermionic SYK model

For $q = 2$ the exact result for the two point function for $\tau > 0$ at zero temperature is [121]:

$$G(\tau) = -\int_0^\pi \frac{d\theta}{\pi} \cos^2\theta e^{-2J\tau\sin\theta} = \frac{\boldsymbol{L}_1(2J\tau) - I_1(2J\tau)}{2J\tau} = -\frac{1}{\pi J\tau} + \frac{1}{4\pi(J\tau)^3} + \frac{3}{16\pi(J\tau)^5} + \dots , \tag{A.27}$$

where $I_1(x)$ and $\boldsymbol{L}_1(x)$ are modified Bessel and Struve functions. For $q = 2$ the conformal two point function is

$$G^c(\tau) = -\frac{1}{\pi J\tau}, \tag{A.28}$$

where we used that $b^{1/2} = 1/\pi$. Thus we find

$$G(\tau) = G^c(\tau)\left(1 - \frac{1}{4(J\tau)^2} - \frac{3}{16(J\tau)^4} - \frac{45}{64(J\tau)^6} - \dots\right). \tag{A.29}$$

On the other hand using formula (A.20) and that for $q = 2$ operators dimensions are simply $h_k = 2(k+1)$ we expect to have

$$G(\tau) = G^c(\tau)\left(1 - \sum_{k=0}^{\infty} \frac{\alpha_k}{(J\tau)^{2k+1}} - \sum_{k,m=0}^{\infty} \frac{a_{km}\alpha_k\alpha_m}{(J\tau)^{2(k+m+1)}} - \sum_{k,m,l=0}^{\infty} \frac{a_{kml}\alpha_k\alpha_m\alpha_l}{(J\tau)^{2(k+m+l)+3}} - \dots\right). \tag{A.30}$$

Comparing (A.29) and (A.30) we obtain relations between $\alpha_k(q)$ and $a_{km}(q)$, $a_{kml}(q)$, etc for $q=2$

$$\alpha_0(2)=0\,,\quad \alpha_1(2)=-a_{000}(2)\alpha_0^3(2)\,,\quad a_{00}(2)\alpha_0^2(2)=\frac{1}{4}\,,\quad 2a_{01}(2)\alpha_0(2)\alpha_1(2)=\frac{3}{16}\,. \tag{A.31}$$

Moreover using that $\alpha_0(q)=\frac{\pi}{8}(q-2)+\dots$ for $q\to 2$ [121] we obtain that $a_{00}(q)\to\frac{16}{\pi^2(q-2)^2}+\dots$, which agrees with the arbitrary q formula (2.80) for $a_{bb'}(q)$.

A.4 Finite Temperature Generalization for Spectral Densities

Consider retarded Green's function in real time

$$G_{fR}(t)=-i\theta(t)\langle\{f(t),f^\dagger(0)\}\rangle,\quad G_{\mathfrak{b}R}(t)=-i\theta(t)\langle[\mathfrak{b}(t),\mathfrak{b}^\dagger(0)]\rangle\,, \tag{A.32}$$

where $\theta(t)$ is the Heaviside step function and should not be confused with the asymmetry angle. Below we again suppress subscript $a=f,\mathfrak{b}$ and only retain ζ factor, where $\zeta_f=-1$ and $\zeta_\mathfrak{b}=1$. We can obtain retarded Green's function by analytically continuing imaginary time one:

$$G_R(t)=i\theta(t)\big(G(it+0)-G(it-0)\big)\,. \tag{A.33}$$

The full retarded Green's function can be written as a conformal part plus corrections $G_R(t)=G^c_R(t)+\delta G_R(t)$ and for the conformal retarded Green's function we find

$$G^c_R(t)=-i\theta(t)\frac{(e^{-i\pi(\Delta+i\mathcal{E})}-\zeta e^{i\pi(\Delta+i\mathcal{E})})b^\Delta e^{-\frac{2\pi i\mathcal{E}}{\beta}t}}{(\frac{\beta J}{\pi}\sinh\frac{\pi t}{\beta})^{2\Delta}}\,. \tag{A.34}$$

We split correction $\delta G_R(t)$ on two terms $\delta G_R(t) = \delta G_R^{\mathrm{A}}(t) + \delta G_R^{\mathrm{S}}(t)$ where

$$\delta_b G_R^{\mathrm{A/S}}(t) = -\frac{1}{2}(v_{b+} \pm v_{b-}) \frac{\alpha_b}{(\beta J)^{b-1}} f_{Rb}^{\mathrm{A/S}}(t) G_R^c(t)\,, \tag{A.35}$$

and for $f_{Rb}^{\mathrm{A/S}}(t)$ we have

$$f_{Rb}^{\mathrm{A/S}}(t) = \frac{e^{-i\pi(\Delta+i\mathcal{E})} f_b^{\mathrm{A/S}}(it+0) \mp \zeta e^{i\pi(\Delta+i\mathcal{E})} f_b^{\mathrm{A/S}}(it-0)}{e^{-i\pi(\Delta+i\mathcal{E})} - \zeta e^{i\pi(\Delta+i\mathcal{E})}}\,, \tag{A.36}$$

where functions $f_b^{\mathrm{A/S}}(\tau)$ are defined in (2.93) and (2.94). To find $f_b^{\mathrm{A/S}}(it \pm 0)$ we notice that function $A_b(u)$ is analytic in $\mathbf{C}$ and has a branch cut $[1, +\infty)$. Inside the unit circle $|u| \leq 1$ we can compute $A_b(u)$ using series expansion. Analytic continuation of $f_b^{\mathrm{A/S}}(\tau)$ will produce two terms $A_b(e^{-\frac{2\pi t}{\beta}})$ and $A_b(e^{\frac{2\pi t}{\beta}} \pm i0)$, where the last function is computed above or below the branch cut. Using formulas for linear transformations of the hypergeometric function we can represent $f_b^{\mathrm{A}}(it \pm 0)$ in the convenient form

$$\begin{aligned}
f_b^{\mathrm{A}}(it \pm 0) &= \frac{\pi (2\pi)^{b-1} \Gamma(b)^2}{2 \sin\frac{\pi b}{2} \sin(2\pi b) \Gamma(2b-1)} \left(\frac{(1 + e^{\pm i\pi b}) B_b(e^{-\frac{2\pi t}{\beta}})}{\Gamma(1-b)^2} - (b \to 1-b) \right)\,, \\
f_b^{\mathrm{S}}(it \pm 0) &= \pm \frac{i\pi (2\pi)^{b-1} \Gamma(b)^2}{2 \cos\frac{\pi b}{2} \sin(2\pi b) \Gamma(2b-1)} \left(\frac{(1 - e^{\pm i\pi b}) B_b(e^{-\frac{2\pi t}{\beta}})}{\Gamma(1-b)^2} - (b \to 1-b) \right)\,,
\end{aligned} \tag{A.37}$$

where $B_b(u) = (1-u)^b \mathbf{F}(b, b, 2b, 1-u)$ is unambiguous for $u = e^{-\frac{2\pi t}{\beta}}$ and can be computed using series expansion. We notice that B_b coincides with the function $B_{b,0}^+$ used in [104,103,81]. Using (A.36)

we obtain for the fermions

$$
\begin{aligned}
f^{\mathrm{A}}_{Rh}(t) =& \frac{(2\pi)^{h-2}\cos\frac{\pi h}{2}\Gamma(h)^2}{\cos(\pi h)\Gamma(2h-1)}\left(\Gamma(h)^2\Big(1+\frac{\cos(\pi(\Delta-h+i\mathcal{E}))}{\cos(\pi(\Delta+i\mathcal{E}))}\Big)B_h(e^{-\frac{2\pi t}{\beta}})-(h\to 1-h)\right),\\
f^{\mathrm{S}}_{Rh}(t) =& \frac{i(2\pi)^{h-2}\sin\frac{\pi h}{2}\Gamma(h)^2}{\cos(\pi h)\Gamma(2h-1)}\left(\Gamma(h)^2\Big(1-\frac{\cos(\pi(\Delta-h+i\mathcal{E}))}{\cos(\pi(\Delta+i\mathcal{E}))}\Big)B_h(e^{-\frac{2\pi t}{\beta}})-(h\to 1-h)\right)
\end{aligned}
\tag{A.38}
$$

and for bosons we need to change cos $\to$ sin inside the brackets. For $h^{\mathrm{A}}_0 = 2$ mode we find

$$
f^{\mathrm{A}}_{R0}(t) = 2-\frac{\pi\tan(\pi(\Delta+i\mathcal{E}))+\frac{2\pi t}{\beta}}{\tanh\Big(\frac{\pi t}{\beta}\Big)}\,,\quad f^{\mathrm{S}}_{R0}(t) = -\frac{i\pi}{\tanh\Big(\frac{\pi t}{\beta}\Big)} \tag{A.39}
$$

and for bosons we need to change tan $\to -\cot$. To compute expression for the spectral density we need to find retarded Green's function in frequency space $G_R(\omega) = G^c_R(\omega) + \delta G_R(\omega)$. For the conformal part we take the Fourier transform of (A.34) and find

$$
G^c_R(\omega) = -i\frac{C}{J}\Big(\frac{\beta J}{2\pi}\Big)^{1-2\Delta}e^{-i\theta}\frac{\Gamma(\Delta-i\omega')}{\Gamma(1-\Delta-i\omega')}\,, \tag{A.40}
$$

where $\omega' \equiv \frac{\beta\omega}{2\pi} - \mathcal{E}$ and the constant C is defined after (2.53). Formulas written with the use of asymmetry angle are the same for both fermions and bosons. Next for $\delta G_R(\omega) = \delta G^{\mathrm{A}}_R(\omega) + \delta G^{\mathrm{S}}_R(\omega)$ we introduce $f^{\mathrm{A/S}}_{Rh}(\omega)$ as

$$
\delta_h G^{\mathrm{A/S}}_R(\omega) = -\frac{1}{2}(v_{h+}\pm v_{h-})\frac{\alpha_h}{(\beta J)^{h-1}}f^{\mathrm{A/S}}_{Rh}(\omega)G^c_R(\omega)\,, \tag{A.41}
$$

and we stress that $f^{A/S}_{Rh}(\omega)$ are not Fourier transforms just of $f^{A/S}_{Rh}(t)$. After some computations we obtain

$$f^{A}_{Rh}(\omega) = \frac{(2\pi)^{h-2}\cos\frac{\pi h}{2}\Gamma(h)^2}{\cos(\pi h)\Gamma(2h-1)}\left(\frac{\Gamma(h)}{\Gamma(1-h)}\Big(e^{2i\theta}-\frac{\sin\big(\frac{\pi h}{2}-2\pi\Delta\big)}{\sin\big(\frac{\pi h}{2}\big)}\Big)J_h(\omega)-(h\to 1-h)\right),$$
$$f^{S}_{Rh}(\omega) = \frac{i(2\pi)^{h-2}\sin\frac{\pi h}{2}\Gamma(h)^2}{\cos(\pi h)\Gamma(2h-1)}\left(\frac{\Gamma(h)}{\Gamma(1-h)}\Big(\frac{\cos\big(\frac{\pi h}{2}-2\pi\Delta\big)}{\cos\big(\frac{\pi h}{2}\big)}-e^{2i\theta}\Big)J_h(\omega)-(h\to 1-h)\right), \tag{A.42}$$

where the function $J_h(\omega)$ is

$$J_h(\omega) = \Gamma(1-\Delta-i\omega')\Gamma(1+h-2\Delta)\Gamma(2\Delta)\,{}_3\mathbf{F}_2\left(\begin{matrix}h,h,1+h-2\Delta\\ 2h,1+h-\Delta-i\omega'\end{matrix};1\right) \tag{A.43}$$

and ${}_3\mathbf{F}_2$ is the regularized hypergeometric function. For $h^{A}_0 = 2$ we find $f^{S}_{R0}(\omega) = \pi\omega'/\Delta$ and

$$f^{A}_{R0}(\omega) = \frac{1}{\Delta}\Big(2\Delta-1-i\omega'\big(\pi\tan(\pi(\Delta+i\mathcal{E}))+\psi(1-\Delta-i\omega')-\psi(\Delta-i\omega')\big)\Big), \tag{A.44}$$

where $\psi(z)\equiv\Gamma'(z)/\Gamma(z)$ is the digamma function and we used that $\tan(\pi(\Delta+i\mathcal{E})) = \tan\pi\Delta + (e^{2i\theta}-1)/\sin(2\pi\Delta)$ for fermions. For bosons we need to change $\tan\to-\cot$.

For the spectral density we find $\rho(\omega) = \rho^{c}(\omega)+\delta\rho(\omega)$, where

$$\rho^{c}(\omega) = -\frac{1}{\pi}\mathrm{Im}G^{c}_{R}(\omega) = \frac{C}{\pi J}\Big(\frac{\beta J}{2\pi}\Big)^{1-2\Delta}\mathrm{Re}\Big(e^{-i\theta}\frac{\Gamma(\Delta-i\omega')}{\Gamma(1-\Delta-i\omega')}\Big) \tag{A.45}$$

and the correction is

$$\delta\rho(\omega) = \sum_h \frac{\alpha_h}{2\pi(\beta J)^{h-1}}\Big((v_{h+}+v_{h-})\mathrm{Im}(G^{c}_{R}(\omega)f^{A}_{Rh}(\omega))+(v_{h+}-v_{h-})\mathrm{Im}(G^{c}_{R}(\omega)f^{S}_{Rh}(\omega))\Big). \tag{A.46}$$

Finally we find formulas for the spin-spin correlator and spin-spin spectral density at non-zero temperature. The spin-spin correlator in imaginary time is $Q(\tau) = -\zeta G(\tau)G(-\tau)$ (note, $Q(\tau)$ is denoted $\chi_L(\tau)$ in Section 2.1). Retaining only leading linear corrections we obtain

$$Q(\tau) = Q^c(\tau)\left(1 - \sum_b (v_{b+} + v_{b-})\frac{\alpha_b}{(\beta J)^{b-1}} f_b^{\mathrm{A}}(\tau) - \dots\right), \tag{A.47}$$

where we notice that functions $f_b^{\mathrm{S}}(\tau)$ don't contribute at the leading order and the conformal part of the spin-spin correlator is

$$Q^c(\tau) = -\zeta G^c(\tau)G^c(-\tau) = -\frac{b^{2\Delta}}{|\frac{\beta J}{\pi}\sin\frac{\pi\tau}{\beta}|^{4\Delta}}. \tag{A.48}$$

We can find retarded spin-spin correlator in real time $Q_R(t) = -i\theta(t)\langle[S(t), S(0)]\rangle$ by analytic continuation of the imaginary time one:

$$Q_R(t) = i\theta(t)(Q(it+0) - Q(it-0)). \tag{A.49}$$

We notice that all formulas for $Q_R(t)$ are essentially the same as for bosonic $G_R(t)$ with replacement $\Delta \to 2\Delta$ and $\mathcal{E} = 0$ (or $\theta = \pi/2$). Below we still repeat some main steps.

As usual $Q_R(t)$ is split on two terms $Q_R(t) = Q_R^c(t) + \delta Q_R(t)$ where the conformal part and correction have the form

$$Q_R^c(t) = -\theta(t)\frac{2\sin(2\pi\Delta)b^{2\Delta}}{(\frac{\beta J}{\pi}\sinh\frac{\pi t}{\beta})^{4\Delta}}, \quad \delta_b Q_R(t) = -(v_{b+} + v_{b-})\frac{\alpha_b}{(\beta J)^{b-1}} f_{Rb}^{\mathrm{A}}(t) Q_R^c(t) \tag{A.50}$$

and here the bosonic function $f_{Rb}^{\mathrm{A}}(t)$ in (A.38) is for $\mathcal{E} = 0$ and $\Delta \to 2\Delta$. Now taking the Fourier

transform of $Q_R(t)$ we get $Q_R(\omega) = Q_R^c(\omega) + \delta Q_R(\omega)$, where the conformal part is

$$Q_R^c(\omega) = -\frac{\pi b^{2\Delta}}{J\Gamma(4\Delta)\cos(2\pi\Delta)}\Big(\frac{\beta J}{2\pi}\Big)^{1-4\Delta}\frac{\Gamma(2\Delta - i\frac{\beta\omega}{2\pi})}{\Gamma(1-2\Delta - i\frac{\beta\omega}{2\pi})}\,. \tag{A.51}$$

The correction has the form

$$\delta Q_R(\omega) = -\sum_h (v_{h+} + v_{h-})\frac{\alpha_h}{(\beta J)^{h-1}} f_{Rh}^{\mathrm{A}}(\omega) Q_R^c(\omega)\,, \tag{A.52}$$

where the function $f_{Rh}^{\mathrm{A}}(\omega)$ in (A.42) is computed here for $\Delta \to 2\Delta$, $\theta = \pi/2$ and $\omega' = \frac{\beta\omega}{2\pi}$. Therefore for $h_0^{\mathrm{A}} = 2$ mode we find

$$f_{R0}^{\mathrm{A}}(\omega) = \frac{1}{2\Delta}\Big(4\Delta - 1 - i\frac{\beta\omega}{2\pi}\big(\psi(1-2\Delta - i\frac{\beta\omega}{2\pi}) - \psi(2\Delta - i\frac{\beta\omega}{2\pi}) - \pi\cot(2\pi\Delta)\big)\Big)\,. \tag{A.53}$$

We are mainly interested in $\Delta = 1/4$ case. At $\Delta \to 1/4$ limit the conformal part $Q_R^c(\omega)$ is diverging and we get

$$Q_R^c(\omega) = \frac{2b^{1/2}}{J}\left(\frac{1}{4(\Delta - \frac{1}{4})} + \psi\Big(\frac{1}{2} - \frac{i\beta\omega}{2\pi}\Big) + \gamma - \log\Big(\frac{\beta J}{2\pi}\Big) + \dots\right)\,. \tag{A.54}$$

The diverging part is real and doesn't not contribute to the spectral density. On the other hand the function $f_{Rh}^{\mathrm{A}}(\omega)$ goes to zero as $(\Delta - 1/4)$ and we obtain

$$\begin{aligned} f_{Rh}^{\mathrm{A}}(\omega) Q_R^c(\omega) = &-\frac{b^{1/2}(2\pi)^{h-1}\cos\frac{\pi h}{2}\Gamma(h)^2}{J\cos(\pi h)\Gamma(2h-1)} \\ &\times\left[\frac{\Gamma(h)^2\Gamma(\frac{\pi - i\beta\omega}{2\pi})}{\tan\frac{\pi h}{2}\Gamma(1-h)}\,{}_3\mathbf{F}_2\left(\begin{matrix}h, h, h\\ 2h, \frac{\pi(2h+1) - i\beta\omega}{2\pi}\end{matrix}; 1\right) - (h \to 1-h)\right]\,, \end{aligned} \tag{A.55}$$

where ${}_3\mathbf{F}_2$ is the regularized hypergeometric function. The spin-spin spectral density $\rho_Q(\omega)$ can be

found as

$$\rho_Q(\omega) = -\frac{1}{\pi}\mathrm{Im}Q_R(\omega) \tag{A.56}$$

We write $\rho_Q(\omega) = \rho_Q^c(\omega) + \delta\rho_Q(\omega)$ and using (A.55) we obtain

$$\rho_Q(\omega) = \frac{b^{1/2}}{J}\tanh\left(\frac{\beta\omega}{2}\right)\left(1 - \sum_h (v_{h+} + v_{h-})\frac{\alpha_h}{(\beta J)^{h-1}}\mathcal{R}_h^{\mathrm{A}}\left(\frac{\beta\omega}{2\pi}\right) - \dots\right), \tag{A.57}$$

where the function $\mathcal{R}_h^{\mathrm{A}}(\omega)$ is

$$\mathcal{R}_h^{\mathrm{A}}(\omega) = \frac{2\left(\frac{\pi}{2}\right)^h \Gamma(h)}{\sqrt{\pi}\sin\left(\frac{\pi h}{2}\right)\Gamma\left(h-\frac{1}{2}\right)}\mathrm{Re}\,{}_3\mathbf{F}_2\left(\begin{matrix} h & 1-h & \frac{1}{2}+i\omega \\ & 1 & 1 \end{matrix}; 1\right). \tag{A.58}$$

To get this expression we used two identities for the regularized hypergeometric function

$$\begin{aligned} {}_3\mathbf{F}_2\left(\begin{matrix} 1-h, 1-h, 1-h \\ 2-2h, 1-h+a \end{matrix}; 1\right) =& \frac{\Gamma(h)^3}{\Gamma(1-h)^3}{}_3\mathbf{F}_2\left(\begin{matrix} h, h, h \\ 2h, h+a \end{matrix}; 1\right) \\ &+ \frac{\Gamma(h)^3}{\Gamma(a)\Gamma(2-2h)\Gamma(2h-1)}{}_3\mathbf{F}_2\left(\begin{matrix} 1-h, h, 1-a \\ 1, 1 \end{matrix}; 1\right), \end{aligned} \tag{A.59}$$

$$\begin{aligned} {}_3\mathbf{F}_2\left(\begin{matrix} h, h, h \\ 2h, h+a \end{matrix}; 1\right) =& \frac{\Gamma(1-a)\Gamma(1-h)^2}{\Gamma(h)\Gamma(h+a)\Gamma(1-h-a)}{}_3\mathbf{F}_2\left(\begin{matrix} h, 1-h, 1-a \\ 1, 1 \end{matrix}; 1\right) \\ &+ \frac{\Gamma(1-h)^2}{\Gamma(h)\Gamma(a)}{}_3\mathbf{F}_2\left(\begin{matrix} h, 1-h, a \\ 1, 1 \end{matrix}; 1\right). \end{aligned} \tag{A.60}$$

Retaining only $h_0^{\mathrm{A}} = 2$ mode we obtain

$$\rho_Q(\omega) = \frac{b^{1/2}}{J}\tanh\left(\frac{\beta\omega}{2}\right)\left(1 - \frac{2\alpha_0^{\mathrm{A}}\omega}{J}\tanh\left(\frac{\beta\omega}{2}\right) - \dots\right), \tag{A.61}$$

where we used that $v_{0+} + v_{0-} = 2$ and

$$ {}_3\mathbf{F}_2\left(\begin{matrix}1-h, h, \frac{1}{2}+i\omega \\ 1, 1\end{matrix}; 1\right) = -2i\omega - 2i\omega(\psi(1/2 - i\omega) + \gamma_E)(h-2) + O((h-2)^2)\,. \quad \text{(A.62)} $$

A.5 Zero temperature numerics for the Bosonic/Fermionic SYK and the Random Rotor models

We consider Dyson-Schwinger equations for the retarded Green's function for bosonic and fermionic SYK for $q = 4$ case, which is obtained by analytic continuation from the Matsubara frequency $i\omega_n \to \omega + i0$. The first Dyson-Schwinger equation reads

$$ G_R(\omega)^{-1} = \omega + i0 + \mu - \Sigma_R(\omega)\,. \quad \text{(A.63)} $$

Here for brevity we don't explicitly label Green's functions by index $a = f, \mathfrak{b}$ but we will use symbol ζ_a, which is $\zeta_f = -1$ and $\zeta_\mathfrak{b} = 1$. In general for the Green's function and self-energy we define analytic in the upper half plane functions $G(z)$ and $\Sigma(z)$, which are expressed through the spectral densities $\rho(\omega)$ and $\sigma(\omega)$ as

$$ G(z) = \int_{-\infty}^{+\infty} d\omega \frac{\rho(\omega)}{z-\omega}\,, \quad \Sigma(z) = \int_{-\infty}^{+\infty} d\omega \frac{\sigma(\omega)}{z-\omega}\,. \quad \text{(A.64)} $$

The Matsubara and retarded Green's functions can be obtained from these functions by taking $z = i\omega_n$ and $z = \omega + i0$. We can find the spectral density as $\rho(\omega) = -\frac{1}{\pi}\mathrm{Im}G_R(\omega)$. Also using the representation (A.64) we can obtain Green's function in imaginary time expressed through integral over the spectral density

$$ G(\tau) = \frac{1}{\beta}\sum_n G(i\omega_n)e^{-i\omega_n\tau} = -\int_{-\infty}^{+\infty} d\omega \frac{\rho(\omega)e^{-\omega\tau}}{1-\zeta e^{-\beta\omega}}, \quad \tau \in (0,\beta)\,. \quad \text{(A.65)} $$

We notice that $\zeta G(\beta^-) - G(0^+) = \int_{-\infty}^{+\infty} d\omega\rho(\omega) = 1$ for arbitrary temperature. To obtain the second Dyson-Schwinger equation for the retarded self-energy $\Sigma_R(\omega)$ we consider this equation in the Matsubara space $\Sigma(\tau) = J^2 G^2(\tau)G(\beta-\tau)$ and use (A.65) to write it through the spectral density

$$\Sigma(i\omega_n) = -J^2 \int_{-\infty}^{+\infty} \prod_{i=1}^{3} (d\omega_i \rho(\omega_i)) \frac{n(\omega_1)n(\omega_2)n(-\omega_3) + n(-\omega_1)n(-\omega_2)n(\omega_3)}{\omega_1 + \omega_2 - \omega_3 - i\omega_n}\,, \qquad \text{(A.66)}$$

where $n(\omega) = 1/(e^{\beta\omega} - \zeta)$ is the Bose or Fermi distribution and we can get $\Sigma_R(\omega) = \Sigma(i\omega_n = \omega + i0)$. At zero temperature $\beta = \infty$ we can replace $n_{\mathfrak{b}}(\omega)$ by $-\theta(-\omega)$ and $n_f(\omega)$ by $\theta(-\omega)$. Though $n_{\mathfrak{b}}(\omega)$ is divergent for $\omega \to 0$, we assume that this divergence does not play any role. Functions $G_R(\omega)$ and $\Sigma_R(\omega)$ are complex valued and further we will adopt notations for their real and imaginary parts $G_R(\omega) = G'(\omega) + iG''(\omega)$ and $\Sigma_R(\omega) = \Sigma'(\omega) + i\Sigma''(\omega)$. So for $\beta = \infty$ using (A.66) we find

$$\Sigma''(\omega) = \begin{cases} \zeta\pi J^2 \int_0^{\omega_1+\omega_2\le\omega} d\omega_1 d\omega_2 \rho(\omega_1)\rho(\omega_2)\rho(\omega_1+\omega_2-\omega), & \omega > 0 \\ \zeta\pi J^2 \int_{\omega_1+\omega_2\ge\omega}^{0} d\omega_1 d\omega_2 \rho(\omega_1)\rho(\omega_2)\rho(\omega_1+\omega_2-\omega), & \omega < 0\,. \end{cases} \qquad \text{(A.67)}$$

Below in all formulas we set $J = 1$ for brevity. We anticipate that at zero temperature the functions $\rho(\omega)$ and $\Sigma''(\omega)$ will have discontinuity. So it will be convenient to use a new set of functions defined separetely for $\omega > 0$ and $\omega < 0$

$$\rho(\omega) = \begin{cases} \frac{g_+(\omega)}{\sqrt{\omega}}, & \omega > 0 \\ \frac{g_-(-\omega)}{\sqrt{-\omega}}, & \omega < 0 \end{cases}, \quad \Sigma''(\omega) = \begin{cases} 4\pi\sqrt{\omega}s_+(\omega), & \omega > 0 \\ 4\pi\sqrt{-\omega}s_-(-\omega), & \omega < 0 \end{cases}. \qquad \text{(A.68)}$$

We make change of variables $\omega_1 = \omega \sin^2 u \cos^2\varphi$ and $\omega_2 = \omega \sin^2 u \sin^2\varphi$ in (A.67) and obtain

$$s_\pm(\omega) = \zeta \int_0^{\frac{\pi}{2}} du \sin u \int_0^{\frac{\pi}{2}} d\varphi\, g_\pm(\omega \sin^2 u \cos^2\varphi) g_\pm(\omega \sin^2 u \sin^2\varphi) g_\mp(\omega \cos^2 u)\,, \qquad \text{(A.69)}$$

and we notice that $s_\pm(x)$ and $g_\pm(x)$ are defined only for a positive argument. Now it is left to find a real part $\Sigma'(\omega)$ of the self-energy. For this we use the Kramers-Kronig relation

$$\Sigma'(\omega) = \fint_{-\infty}^{+\infty} \frac{d\nu}{\pi} \frac{\Sigma''(\nu) - \Sigma''(\omega)}{\nu - \omega} \,. \tag{A.70}$$

Defining $\Sigma'_\pm(\omega)$ as $\Sigma'(\omega) = \Sigma'_+(\omega)\theta(\omega) + \Sigma'_-(-\omega)\theta(-\omega)$ we find

$$\Sigma'_\pm(\omega) = \pm \fint_0^{+\infty} \frac{d\nu}{\pi} \left(\frac{\Sigma''_\pm(\nu) - \Sigma''_\pm(\omega)}{\nu - \omega} - \frac{\Sigma''_\mp(\nu) - \Sigma''_\pm(\omega)}{\nu + \omega} \right) . \tag{A.71}$$

At zero temperature we set chemical potential $\mu = \Sigma'(\omega = 0)$, so introducing $h_\pm(\omega)$ as

$$\Sigma'(\omega) - \Sigma'(0) = \begin{cases} 4\sqrt{\omega} h_+(\omega), & \omega > 0 \\ 4\sqrt{-\omega} h_-(-\omega), & \omega < 0 \end{cases} \tag{A.72}$$

and simplifying expressions we finally obtain

$$h_\pm(\omega) = \pm \fint_0^{+\infty} d\nu \left(\frac{\sqrt{\omega} s_\pm(\nu) - \sqrt{\nu} s_\pm(\omega)}{\sqrt{\nu}(\nu - \omega)} + \frac{\sqrt{\omega} s_\mp(\nu) + \sqrt{\nu} s_\pm(\omega)}{\sqrt{\nu}(\nu + \omega)} \right) . \tag{A.73}$$

Now using the first Dyson-Schwinger equation we can get $g_\pm$ from $s_\pm$ and $h_\pm$

$$g_\pm(\omega) = -\frac{4 s_\pm(\omega)}{(4 h_\pm(\omega) \mp \sqrt{\omega})^2 + 16\pi^2 (s_\pm(\omega))^2} \,. \tag{A.74}$$

We solve Dyson-Schwinger equations iteratively using (A.69), (A.73) and (A.74) and also imposing the initial conditions coming from the conformal solution (2.53)

$$g_{\pm}(0) = \frac{C\sin\left(\frac{\pi}{4} \pm \theta\right)}{\pi},\ s_{\pm}(0) = -\frac{\sin\left(\frac{\pi}{4} \pm \theta\right)}{4\pi C},\ h_{\pm}(0) = \mp\frac{\cos\left(\frac{\pi}{4} \pm \theta\right)}{4C},\ C = \left(\frac{-\zeta\pi}{\cos 2\theta}\right)^{1/4}. \tag{A.75}$$

We can compute the chemical potential numerically using that $\mu = \Sigma'(\omega = 0)$ and eq. (A.71):

$$\mu = 4\int_0^{+\infty} d\omega \frac{s_+(\omega) - s_-(\omega)}{\sqrt{\omega}}\,. \tag{A.76}$$

In the random rotor model defined in the Section 2.6 the spectral density $\rho(\omega)$ is an odd function due to the particle-hole symmetry. Thus we have $g_-(\omega) = -g_+(\omega)$ and $s_-(\omega) = -s_+(\omega)$, where equation for $s_+(\omega)$ is written in (A.69) ($\zeta = 1$ in this case). Also $h_-(\omega) = h_+(\omega)$ and from (A.73) we find

$$h_+(\omega) = \int_0^{+\infty} d\nu \frac{2\omega(\sqrt{\omega}s_+(\nu) - \sqrt{\nu}s_+(\omega))}{\sqrt{\nu}(\nu^2 - \omega^2)}\,. \tag{A.77}$$

The first Schwinger-Dyson equation in the random rotor model reads

$$g_+(\omega) = -\frac{4s_+(\omega)}{(\omega^{3/2} - 4h_+(\omega))^2 + 16\pi^2 s_+(\omega)^2} \tag{A.78}$$

and the boundary conditions are obtained from (A.75) for $\theta = \pi/2$.

B

Supplementary Information for Chapter 3

B.1 Zero temperature numerics for $t-J$ model

We consider Dyson-Schwinger equations for the retarded Green's function for $t-J$ model, which is obtained by analytic continuation from the Matsubara frequency $i\omega_n \to \omega + i0$. The first pair of the

Dyson-Schwinger equations reads

$$G_{f,R}(\omega)^{-1} = \omega + i0 + \mu_f - \Sigma_{f,R}(\omega)\,; \tag{B.1}$$

$$G_{b,R}(\omega)^{-1} = \omega + i0 + \mu_b - \Sigma_{b,R}(\omega)\,. \tag{B.2}$$

As before, we define analytic in the upper half plane Green's functions $G(z)$ and self energy $\Sigma(z)$, which are expressed through the spectral densities $\rho(\omega)$ and $\sigma(\omega)$ as

$$G(z) = \int_{-\infty}^{+\infty} d\omega \frac{\rho(\omega)}{z-\omega}\,, \quad \Sigma(z) = \int_{-\infty}^{+\infty} d\omega \frac{\sigma(\omega)}{z-\omega}\,. \tag{B.3}$$

The Matsubara and retarded Green's functions can be obtained from these functions by taking $z = i\omega_n$ and $z = \omega + i0$. We can find the spectral density as $\rho(\omega) = -\frac{1}{\pi}\mathrm{Im}G_R(\omega)$. Also using the representation (B.3) we can obtain Green's function in imaginary time expressed through integral over the spectral density

$$G_a(\tau) = \frac{1}{\beta}\sum_n G_a(i\omega_n)e^{-i\omega_n\tau} = -\int_{-\infty}^{+\infty} d\omega \frac{\rho(\omega)e^{-\omega\tau}}{1-\zeta e^{-\beta\omega}}, \quad \tau \in (0,\beta)\,, \tag{B.4}$$

where $a = f, b$ and $\zeta_f = -1, \zeta_b = 1$. We notice that $G(0^+) - \zeta G(\beta^-) = -1 = -\int_{-\infty}^{+\infty} d\omega\rho(\omega)$ for arbitrary temperature.

Here we consider an original model with fermionic spinon and bosonic holon, that gives the following second pair of the Dyson-Schwinger equations

$$\Sigma_f(\tau) = J^2 G_f^2(\tau)G_f(\beta-\tau) + kt^2 G_f(\tau)G_b(\tau)G_b(\beta-\tau)\,; \tag{B.5}$$

$$\Sigma_b(\tau) = t^2 G_f(\tau)G_f(\beta-\tau)G_b(\tau)\,. \tag{B.6}$$

To obtain the second Dyson-Schwinger equation for the retarded self-energy $\Sigma_R(\omega)$ we consider

the equations in the Matsubara space above and use (B.4) to write it in terms of the spectral densities for fermions

$$\Sigma_f(i\omega_n) = -J^2 \int_{-\infty}^{+\infty} \prod_{i=1}^{3} (d\omega_i \rho_f(\omega_i)) \frac{n_f(\omega_1) n_f(\omega_2) n_f(-\omega_3) + n_f(-\omega_1) n_f(-\omega_2) n_f(\omega_3)}{\omega_1 + \omega_2 - \omega_3 - i\omega_n} \tag{B.7}$$

$$+ kt^2 \int_{-\infty}^{+\infty} \prod_{i=1}^{3} d\omega_i \rho_f(\omega_1) \rho_b(\omega_2) \rho_b(\omega_3) \frac{n_f(\omega_1) n_b(\omega_2) n_b(-\omega_3) + n_f(-\omega_1) n_b(-\omega_2) n_b(\omega_3)}{\omega_1 + \omega_2 - \omega_3 - i\omega_n} \tag{B.8}$$

and for bosons

$$\Sigma_b(i\omega_n) = t^2 \int_{-\infty}^{+\infty} \prod_{i=1}^{3} d\omega_i \rho_f(\omega_1) \rho_b(\omega_2) \rho_f(\omega_3) \frac{n_f(\omega_1) n_b(\omega_2) n_f(-\omega_3) + n_f(-\omega_1) n_b(-\omega_2) n_f(\omega_3)}{\omega_1 - \omega_2 + \omega_3 - i\omega_n} \tag{B.9}$$

where $n_a(\omega) = 1/(e^{\beta\omega} - \zeta)$ is the Bose or Fermi distribution and we can get $\Sigma_R(\omega) = \Sigma(i\omega_n = \omega + i0)$. At zero temperature $\beta = \infty$ we can replace $n_b(\omega)$ by $-\theta(-\omega)$ and $n_f(\omega)$ by $\theta(-\omega)$. Though $n_b(\omega)$ is divergent for $\omega \to 0$, we assume that this divergence does not play any role. Functions $G_R(\omega)$ and $\Sigma_R(\omega)$ are complex valued and further we will adopt notations for their real and imaginary parts $G_R(\omega) = G'(\omega) + iG''(\omega)$ and $\Sigma_R(\omega) = \Sigma'(\omega) + i\Sigma''(\omega)$. So for $\beta = \infty$ for fermions we find

$$\rho_{bf}(\omega_1, \omega_2, \omega) = kt^2 \rho_b(\omega_2) \rho_b(\omega_1 + \omega_2 - \omega) - J^2 \rho_f(\omega_2) \rho_f(\omega_1 + \omega_2 - \omega) \tag{B.10}$$

$$\Sigma''_f(\omega) = \begin{cases} \pi \int_0^{\omega_1 + \omega_2 \leq \omega} d\omega_1 d\omega_2 \rho_f(\omega_1) \rho_{bf}(\omega_1, \omega_2, \omega), & \omega > 0 \\ \pi \int_{\omega_1 + \omega_2 \geq \omega}^{0} d\omega_1 d\omega_2 \rho_f(\omega_1) \rho_{bf}(\omega_1, \omega_2, \omega), & \omega < 0 \end{cases} \tag{B.11}$$

and for bosons

$$\Sigma''_b(\omega) = \begin{cases} -\pi t^2 \int_0^{\omega_1+\omega_2\leq\omega} d\omega_1 d\omega_2 \rho_f(\omega_1)\rho_b(\omega_2)\rho_f(\omega_2+\omega_1-\omega), & \omega > 0 \\ -\pi t^2 \int_{\omega_1+\omega_2\geq\omega}^0 d\omega_1 d\omega_2 \rho_f(\omega_1)\rho_b(\omega_2)\rho_f(\omega_2+\omega_1-\omega), & \omega < 0\,. \end{cases} \tag{B.12}$$

We anticipate that at zero temperature the functions $\rho(\omega)$ and $\Sigma''(\omega)$ will have discontinuity. So it will be convenient to use a new set of functions defined separately for $\omega > 0$ and $\omega < 0$

$$\rho_a(\omega) = \begin{cases} \frac{g_a^+(\omega)}{\sqrt{\omega}}, & \omega > 0 \\ \frac{g_a^-(-\omega)}{\sqrt{-\omega}}, & \omega < 0 \end{cases}, \quad \Sigma''_a(\omega) = \begin{cases} 4\pi\sqrt{\omega}s_a^+(\omega), & \omega > 0 \\ 4\pi\sqrt{-\omega}s_a^-(-\omega), & \omega < 0 \end{cases}. \tag{B.13}$$

We make change of variables $\omega_1 = \omega \sin^2 u \cos^2\varphi$ and $\omega_2 = \omega \sin^2 u \sin^2\varphi$ in (B.11) and obtain

$$\begin{aligned} s_f^{\pm}(\omega) = \int_0^{\frac{\pi}{2}} du \sin u \int_0^{\frac{\pi}{2}} d\varphi\, g_f^{\pm}(\omega \sin^2 u \cos^2\varphi)(kt^2 g_b^{\pm}(\omega \sin^2 u \sin^2\varphi) g_b^{\mp}(\omega \cos^2 u) \\ - J^2 g_f^{\pm}(\omega \sin^2 u \sin^2\varphi) g_f^{\mp}(\omega \cos^2 u))\,, \end{aligned} \tag{B.14}$$

and for bosons

$$s_b^{\pm}(\omega) = -t^2 \int_0^{\frac{\pi}{2}} du \sin u \int_0^{\frac{\pi}{2}} d\varphi\, g_f^{\pm}(\omega \sin^2 u \cos^2\varphi) g_b^{\pm}(\omega \sin^2 u \sin^2\varphi) g_f^{\mp}(\omega \cos^2 u)\,, \tag{B.15}$$

and we notice that $s_{\pm}(x)$ and $g_{\pm}(x)$ are defined only for a positive argument. Now it is left to find a real part $\Sigma'(\omega)$ of the self-energy. For this we use Kramers-Kronig transform

$$\Sigma'(\omega) = \fint_{-\infty}^{+\infty} \frac{d\nu}{\pi} \frac{\Sigma''(\nu) - \Sigma''(\omega)}{\nu - \omega}\,. \tag{B.16}$$

Defining $\Sigma_a'^{(\pm)}(\omega)$ as $\Sigma_a'(\omega) = \Sigma_a'^{(+)}(\omega)\theta(\omega) + \Sigma_a'^{(-)}(-\omega)\theta(-\omega)$ we find

$$\Sigma_a'^{(\pm)}(\omega) = \pm\!\!\!\!\!\!\int_0^{+\infty} \frac{d\nu}{\pi}\left(\frac{\Sigma_a''^{(\pm)}(\nu) - \Sigma_a''^{(\pm)}(\omega)}{\nu - \omega} - \frac{\Sigma_a''^{(\mp)}(\nu) - \Sigma_a''^{(\pm)}(\omega)}{\nu + \omega}\right). \tag{B.17}$$

At zero temperature we set chemical potential $\mu_a = \Sigma_a'(\omega = 0)$, so introducing $h_a^{\pm}(\omega)$ as

$$\Sigma_a'(\omega) - \Sigma_a'(0) = \begin{cases} 4\sqrt{\omega}h_a^{+}(\omega), & \omega > 0 \\ 4\sqrt{-\omega}h_a^{-}(-\omega), & \omega < 0 \end{cases}. \tag{B.18}$$

and simplifying expressions we finally obtain

$$h_a^{\pm}(\omega) = \pm\!\!\!\!\!\!\int_0^{+\infty} d\nu\left(\frac{\sqrt{\omega}s_a^{\pm}(\nu) - \sqrt{\nu}s_a^{\pm}(\omega)}{\sqrt{\nu}(\nu - \omega)} + \frac{\sqrt{\omega}s_a^{\mp}(\nu) + \sqrt{\nu}s_a^{\pm}(\omega)}{\sqrt{\nu}(\nu + \omega)}\right). \tag{B.19}$$

Now using the first pair of the Dyson-Schwinger equations (B.1),(B.2) we can get $g_a^{\pm}$ from $s_a^{\pm}$ and $h_a^{\pm}$

$$g_a^{\pm}(\omega) = -\frac{4s_a^{\pm}(\omega)}{(4h_a^{\pm}(\omega) \mp \sqrt{\omega})^2 + 16\pi^2(s_a^{\pm}(\omega))^2}. \tag{B.20}$$

We solve Dyson-Schwinger equations iteratively using (B.14), (B.15), (B.19) and (B.20) and also imposing the initial conditions

$$g_a^{\pm}(0) = \frac{C_a}{\pi J}\sin\Big(\frac{\pi}{4} \pm \theta_a\Big), \quad s_a^{\pm}(0) = -\frac{1}{4\pi C_a}\sin\Big(\frac{\pi}{4} \pm \theta_a\Big), \quad h_a^{\pm}(0) = \mp\frac{1}{4C_a}\cos\Big(\frac{\pi}{4} \pm \theta_a\Big). \tag{B.21}$$

where the constants C_a are given in (3.23).

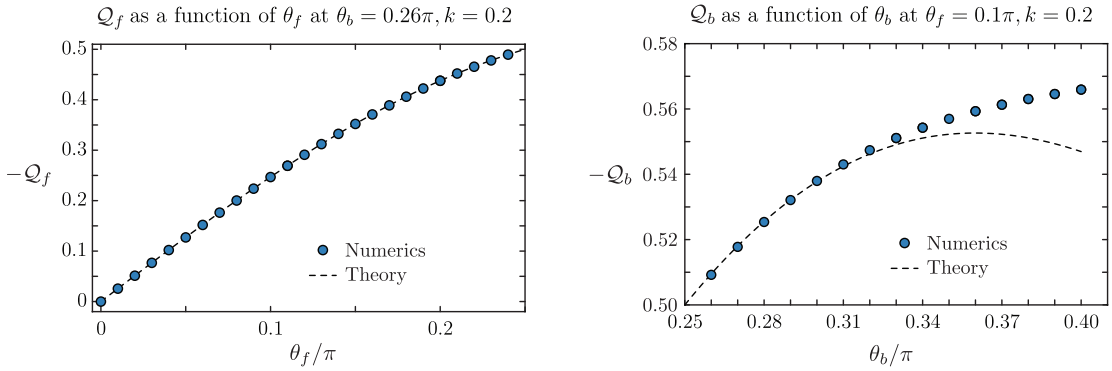

Figure B.1: The Luttinger constraints for fermions (left) and bosons (right). Blue dots are numerically computed Luttinger constraints and the dashed black lines are the analytical functions (B.22),(B.23). Here we fix the parameters $k = 0.2$, and $\theta_b = 0.26\pi$ (left), $\theta_f = 0.1\pi$ (right). We note that the precision for each point is in the range of $10^{-5} - 10^{-7}$.

B.1.1 Luttinger constraints and fermionic charge vs chemical potential

We can numerically investigate the solution similarly to the previous paper [174] computing the Luttinger constraints (3.92),(3.93) both numerically and analytically that we rewrite as follows

$$\mathcal{Q}_f(\theta_f) = -\frac{\theta_f}{\pi} - \frac{1}{4}\sin(2\theta_f) = \left\langle f^\dagger f \right\rangle - \frac{1}{2}\,, \tag{B.22}$$

$$\mathcal{Q}_b(\theta_b) = -\frac{\theta_b}{\pi} - \frac{1}{4}\sin(2\theta_b) = -\frac{1}{2} - \left\langle b^\dagger b \right\rangle\,. \tag{B.23}$$

Numerically we compute the areas under fermionic and bosonic spectral density curves respectively at fixed parameters. We show the comparison of the analytical and numerical results in the Fig.B.1.

In addition to the Luttinger constraints, we numerically compute the fermionic charge as a function of the chemical potential that is given by the real part of the self energy at zero frequency $\mu = \Sigma'(\omega = 0)$. The result is presented in the Fig.B.2.

The behavior of the fermionic charge as a function of chemical potential is similar to the SYK case [174]. We do not see special features in the bosonic charge $\mathcal{Q}_b$.

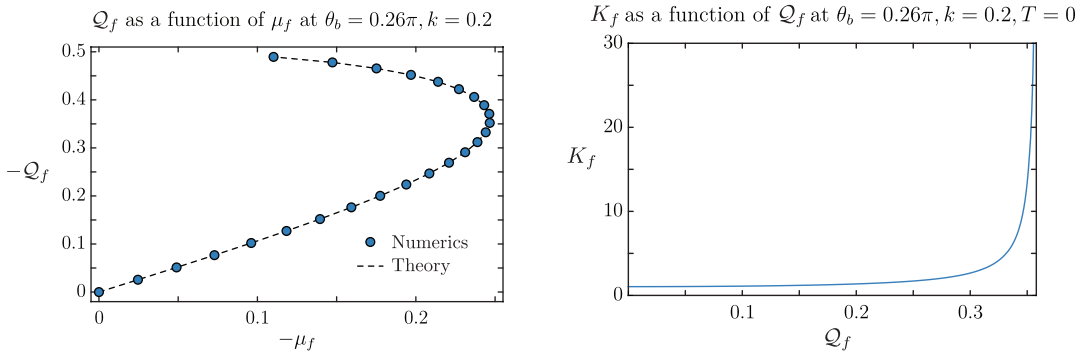

Figure B.2: Left: Charge as a function of fermionic chemical potential at $T = 0$. The function $\mathcal{Q}_f$ depends on μ_f through θ_f. Right: Compressibility as a function of charge at $T = 0$. Parameters for both plots: $\theta_b = 0.26\pi, k = 0.2, J = 1$ and $t = 1$. Dashed line on the left plot is numerical line connecting the blue points. The divergence of compressibility happens at $\theta_f \sim 0.15\pi$.

B.2 Corrections to Conformality

The notation we adopt here is the same as[78,81,174], where we represent the functions as a four-component vector indexed by boson/fermion and $\pm\tau$ branches. We use the following basis for the UV-source and the corrections of Green's function and self-energy:

$$\sigma_b(\tau) = \begin{pmatrix} \delta\sigma_{b+}\Sigma_b^c(\tau) \\ \delta\sigma_{b-}\Sigma_b^c(\tau) \\ \delta\sigma_{f+}\Sigma_f^c(\tau) \\ \delta\sigma_{f-}\Sigma_f^c(\tau) \end{pmatrix} |J\tau|^{1-b}, \tag{B.24}$$

$$\delta G(\tau) = \begin{pmatrix} \delta G_{b+}G_b^c(\tau) \\ \delta G_{b-}G_b^c(\tau) \\ \delta G_{f+}G_f^c(\tau) \\ \delta G_{f-}G_f^c(\tau) \end{pmatrix} |J\tau|^{1-b}, \qquad \delta\Sigma(\tau) = \begin{pmatrix} \delta\Sigma_{b+}\Sigma_b^c(\tau) \\ \delta\Sigma_{b-}\Sigma_b^c(\tau) \\ \delta\Sigma_{f+}\Sigma_f^c(\tau) \\ \delta\Sigma_{f-}\Sigma_f^c(\tau) \end{pmatrix} |J\tau|^{1-b}. \tag{B.25}$$

Here $\pm$ means positive/negative τ branches, and b, f denote boson and fermion respectively.

Kernel of the *t-J* Model in the bosonic spinon + fermionic holon case

In this part we compute the kernel K_G of the *t-J* model in bosonic spinon + fermionic holon case. The basic ingredient is W_Σ and W_G as defined in[78,81]. We elaborate the definition by explicitly writing down on indices

$$\begin{aligned} W_\Sigma(\tau_1,\tau_2;\tau_3,\tau_4)_{a\tilde{a}} &= \left.\frac{\delta G_{*a}(\tau_1,\tau_2)}{\delta \Sigma_{\tilde{a}}(\tau_3,\tau_4)}\right|_{\Sigma^c}, \\ W_G(\tau_1,\tau_2;\tau_3,\tau_4)_{a\tilde{a}} &= \left.\frac{\delta \Sigma_{*a}(\tau_1,\tau_2)}{\delta G_{\tilde{a}}(\tau_3,\tau_4)}\right|_{G^c}, \end{aligned} \tag{B.26}$$

where $a,\tilde{a} = \mathfrak{f},\mathfrak{b}$ denote fermion and boson. Using Eq.(B.26) and the conformal saddle point equations, we obtain

$$W_\Sigma(1,2;3,4) = \begin{pmatrix} G^{13}_{\mathfrak{f}} G^{42}_{\mathfrak{f}} & 0 \\ 0 & G^{13}_{\mathfrak{b}} G^{42}_{\mathfrak{b}} \end{pmatrix}, \tag{B.27}$$

and diagramatically

$$W_\Sigma(1,2;3,4) = \begin{pmatrix} \begin{matrix} 1 \text{ - - -}\!\!\leftarrow\!\!\text{ - - - } 3 \\ 2 \text{ - - -}\!\!\rightarrow\!\!\text{ - - - } 4 \end{matrix} & \begin{matrix} 0 \\ 1 \longleftarrow 3 \\ 2 \longrightarrow 4 \end{matrix} \\ 0 & \end{pmatrix}. \tag{B.28}$$

Here we use dashed line to denote fermion and solid line to denote boson.

W_G differs from the other scheme by a switching $\mathfrak{b} \leftrightarrow f$, $\mathfrak{f} \leftrightarrow b$ and an overall minus sign.

$$\tilde{G}_{\mathfrak{b}} = 2G^{12}_{\mathfrak{b}} G^{21}_{\mathfrak{b}} \delta^{24;13} + (G^{12}_{\mathfrak{b}})^2 \delta^{23;14} \tag{B.29}$$

$$W_G(1,2;3,4) = \begin{pmatrix} t^2 G^{12}_{\mathfrak{b}} G^{21}_{\mathfrak{b}} \delta^{24;13} & t^2 G^{43}_{\mathfrak{b}} G^{12}_{\mathfrak{f}} (\delta^{24;13} + \delta^{23;14}) \\ -kt^2 G^{43}_{\mathfrak{f}} G^{12}_{\mathfrak{b}} (\delta^{24;13} + \delta^{23;14}) & -kt^2 G^{12}_{\mathfrak{f}} G^{21}_{\mathfrak{f}} \delta^{24;13} + J^2 \tilde{G}_{\mathfrak{b}} \end{pmatrix} \tag{B.30}$$

where notation $\delta^{ij;kl} = \delta(\tau_i - \tau_j)\delta(\tau_k - \tau_l)$. Diagrammatically, W_G has the following representation

$$W_G(1,2;3,4) = \begin{pmatrix} t^2 \; \text{ 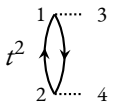 } & t^2 \left(\text{ 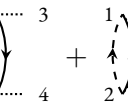 } + \text{ 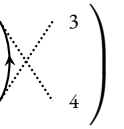 } \right) \\ -kt^2 \left(\text{ 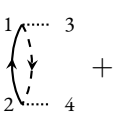 } + \text{ 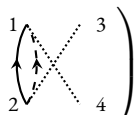 } \right) & -kt^2 \; \text{ 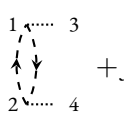 } + J^2 \left(2 \; \text{ 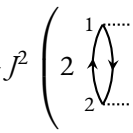 } + \text{ 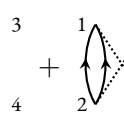 } \right) \end{pmatrix}, \tag{B.31}$$

where a dotted line without arrow represents a δ-function. In the basis given by (B.24) and (B.25) W_Σ and W_Σ take the familiar form

$$\begin{aligned} W_\Sigma(h) &= w(\Delta_\mathfrak{f}, \theta_\mathfrak{f}; h) \oplus w(\Delta_\mathfrak{b}, \theta_\mathfrak{b}; h), \\ w(\Delta, \theta; h) &= \frac{\Gamma(2\Delta - 1 + h)\Gamma(2\Delta - h)}{\Gamma(2\Delta)\Gamma(2\Delta - 1)\sin(2\pi\Delta)} \begin{pmatrix} \sin(\pi h + 2\theta) & -\sin(2\pi\Delta) + \sin(2\theta) \\ -\sin(2\pi\Delta) - \sin(2\theta) & \sin(\pi h - 2\theta) \end{pmatrix}, \end{aligned} \tag{B.32}$$

and

$$W_G(h) = \begin{pmatrix} 1 & 0 & 1 & 1 \\ 0 & 1 & 1 & 1 \\ -k\frac{\cos 2\theta_\mathfrak{f}}{\cos 2\theta_\mathfrak{b}} & -k\frac{\cos 2\theta_\mathfrak{f}}{\cos 2\theta_\mathfrak{b}} & k\frac{\cos 2\theta_\mathfrak{f}}{\cos 2\theta_\mathfrak{b}} + 2 & k\frac{\cos 2\theta_\mathfrak{f}}{\cos 2\theta_\mathfrak{b}} + 1 \\ -k\frac{\cos 2\theta_\mathfrak{f}}{\cos 2\theta_\mathfrak{b}} & -k\frac{\cos 2\theta_\mathfrak{f}}{\cos 2\theta_\mathfrak{b}} & k\frac{\cos 2\theta_\mathfrak{f}}{\cos 2\theta_\mathfrak{b}} + 1 & k\frac{\cos 2\theta_\mathfrak{f}}{\cos 2\theta_\mathfrak{b}} + 2 \end{pmatrix}. \tag{B.33}$$

Finally $K_G(h) = W_\Sigma(h) W_G(h)$ and $K_\Sigma(h) = W_G(h) W_\Sigma(h)$. It turns out that in this scheme the kernel is identical to that of the fermionic spinon + bosonic holon theory if we substitute $\theta_f \to \theta_\mathfrak{b}$, $\theta_b \to \theta_\mathfrak{f}$.

Linear order correction at zero temperature

Following derivations in [174], the first order conformal corrections at zero temperature take the following form :

$$\begin{aligned} \delta G(\tau) &= \sum_h \delta_h G(\tau)\,, \\ \delta_h G(\tau) &= -\alpha_h v_h \frac{G^c(\tau)}{|J\tau|^{h-1}}\,, \quad \alpha_h = -\frac{w_h W_\Sigma(h)\vec{\sigma}_h}{k'_G(h)}\,. \end{aligned} \tag{B.34}$$

Here the sum is over the operator spectrum of the *t-J* model determined by (2.58), and v_h and w_h are the corresponding right and left eigenvectors of $K_G(h)$ respectively which have eigenvalue $k_G(h) = 1$ and normalized as $w_h v_h = 1$, and $\vec{\sigma}_h = (\delta\sigma_{b+}, \delta\sigma_{b-}, \delta\sigma_{f+}, \delta\sigma_{f-})^T$.

It can be verified that the eigenspace corresponding to the two $h = 1$ operators are spanned by $\delta G^c_a/\delta\theta_b$ and $\delta G^c_a/\delta\theta_b$ (i.e. changes of θ_b and θ_f) which by the Luttinger relations (3.31),(3.32) are related to $\delta\mathcal{Q}_f$ and $\delta\mathcal{Q}_b$ respectively. Therefore, there is no need to include these corrections if we use the renormalized value of θ_f, θ_b.

Nonlinear order correction at zero temperature

It is also possible to obtain corrections of higher order in α following derivations in [174]. The result takes the form

$$G(\tau) = G^c(\tau)\left(1 - \sum_h \frac{\alpha_h v_h}{|J\tau|^{h-1}} - \sum_{h,h'} \frac{a_{hh'}\alpha_h\alpha_{h'}}{|J\tau|^{h+h'-2}} - \sum_{h,h',h''} \frac{a_{hh'h''}\alpha_h\alpha_{h'}\alpha_{h''}}{|J\tau|^{h+h'+h''-3}} - \dots\right), \tag{B.35}$$

where v_h, $a_{hh'}$, $a_{hh'h''}$, etc are four-component vectors. The coefficients $a_{hh'}$, $a_{hh'h''}$ can be calculated using the recursion procedure described in [174]. As an example, we perform a calculation for $a_{hh'}$, using

Eq. (4.32) of[174]:

$$\delta^2 G = \frac{1}{1 - W_\Sigma W_G}\left[W_\Sigma \bar{\delta}^2 \Sigma_*[G] + \bar{\delta}^2 G_*[\Sigma]\right], \tag{B.36}$$

where $\Sigma_*[G]$ and $G_*[\Sigma]$ denote the RHS of Schwinger-Dyson equations (3.15)-(3.18) with $(i\omega_n + \mu)$ dropped. The meaning of $\bar{\delta}^2\Sigma_*[G]$ is that we compute the second-order variation of Σ_* using only first-order variation of G.

The second term in the bracket of (B.36) can be computed using the same procedure as[174], with the result

$$\frac{\bar{\delta}^2 G_*(\tau)}{G^c(\tau)} = \sum_{h,h'} F(h+h'-1)^{-1}\big(F(h)v_h \cdot F(h')v_{h'}\big)\frac{\alpha_h \alpha_{h'}}{|J\tau|^{h+h'-2}}, \tag{B.37}$$

where "$\cdot$" means multiply two vectors entry-wise and $F(h)$ is a 4 by 4 matrix that acts on v_h:

$$\begin{aligned} F(h) &= f(h,\theta_b) \oplus f(h,\theta_f), \\ f(h,\theta) &= -\frac{\Gamma(3/2-h)}{2\sqrt{\pi}}\begin{pmatrix} -e^{-\frac{1}{2}i\pi h}\left(e^{2i\theta}+i\right) & -e^{\frac{i\pi h}{2}}\left(e^{2i\theta}-i\right) \\ i\left(e^{2i\theta}+i\right)e^{\frac{1}{2}i(\pi h-4\theta)} & \left(-1-ie^{2i\theta}\right)e^{-\frac{1}{2}i(\pi h+4\theta)} \end{pmatrix}. \end{aligned} \tag{B.38}$$

The first term in the bracket of (B.36) can be computed by expanding the Schwinger-Dyson equation $\Sigma = \Sigma_*[G]$ to second order, with the result

$$\frac{\bar{\delta}^2 \Sigma_*(\tau)}{\Sigma^c(\tau)} = \sum_{h,h'} \frac{\alpha_h \alpha_{h'}}{|J\tau|^{h+h'-2}} d_{hh'}, \tag{B.39}$$

and $d_{hh'}$ is a four-component vector whose entries are

$$
\begin{aligned}
d_{hh';b+} &= \frac{1}{2}(v_{hb+}(v_{h'f-}+v_{h'f+})+v_{hf-}(v_{h'b+}+v_{h'f+})+v_{hf+}(v_{h'b+}+v_{h'f-}))\,, && \text{(B.40)}\\
d_{hh';b-} &= \frac{1}{2}(v_{hb-}(v_{h'f-}+v_{h'f+})+v_{hf-}(v_{h'b-}+v_{h'f+})+v_{hf+}(v_{h'b-}+v_{h'f-}))\,, && \text{(B.41)}\\
d_{hh';f+} &= \frac{1}{2}\eta\Big(v_{hb-}(v_{h'b+}+v_{h'f+})+v_{hb+}(v_{h'b-}+v_{h'f+})-2v_{hf-}v_{h'f+} && \text{(B.42)}\\
&\quad +v_{hf+}(v_{h'b-}+v_{h'b+}-2(v_{h'f-}+v_{h'f+}))\Big)+v_{hf-}v_{h'f+}+v_{hf+}(v_{h'f-}+v_{h'f+})\\
d_{hh';f-} &= \frac{1}{2}\eta\Big(v_{hb-}(v_{h'b+}+v_{h'f-})+v_{hb+}(v_{h'b-}+v_{h'f-})-2v_{hf+}v_{h'f-}\,, && \text{(B.43)}\\
&\quad +v_{hf-}(v_{h'b-}+v_{h'b+}-2(v_{h'f-}+v_{h'f+}))\Big)+v_{hf-}(v_{h'f-}+v_{h'f+})+v_{hf+}v_{h'f-}\,.
\end{aligned}
$$

We remind the reader that $\eta = -k\cos(2\theta_b)/\cos(2\theta_f)$. Combining (B.37) and (B.39), we obtain

$$
\begin{aligned}
a_{hh'} = &-\left(1-W_\Sigma(h+h'-1)W_G\right)^{-1}\\
&\times\left(F(h+h'-1)^{-1}\big(F(h)v_h\cdot F(h')v_{h'}\big)+W_\Sigma(h+h'-1)d_{hh'}\right). \qquad \text{(B.44)}
\end{aligned}
$$

B.3 Qualitative analysis of potentially relevant operators in the $t-J$ model

The goal of this analysis is to determine the range of parameters regarding the existence and stability of the saddle conformal solution, and to study the relevance of time-reparameterization mode $h=2$. The outcome of the analysis is in Fig. 3.2 and Fig. 3.4. We will mainly discuss the fermionic spinon + bosonic holon model. The analysis of the fermionic holon + bosonic spinon model is completely parallel as the kernel is related to by $\theta_f \to \theta_{\mathfrak{b}}$, $\theta_b \to \theta_{\mathfrak{f}}$.

We will be analyzing the function

$$
F(h) \equiv \det(K_G(h)-1) = 0, \qquad \text{(B.45)}
$$

whose zeroes determine the scaling dimension of irrelevant operators appearing in the corrections. The conformal saddle exists if the Eq.(3.22) has real solutions for C_f and C_b, which implies

$$\cos\left(2\theta_f\right) + k\cos(2\theta_b) > 0. \tag{B.46}$$

Here $\theta_f \in [-\pi/4, \pi/4]$ and $\theta_b \in [\pi/4, \pi/4]$ are assumed to respect unitarity constraint.

By numerically inspecting the function $F(h)$, we found that there is almost always a solution with scaling dimension $\mathrm{Re}\, h_1 < \frac{3}{2}$. Depending on parameters, this solution may be on the real axis within the range $\frac{1}{2} < h_1 < \frac{3}{2}$, or it may move onto the imaginary axis such that $h_1 = 1/2 \pm is,\ s > 0$.

Qualitative behaviors of the solution can be described by simple inequalities, which we describe below. First, whether the solution h_1 is real or complex depends on the sign of $F(h)$ near the pole $h = 1/2$. When h_1 moves from real to complex, the pole switches sign. Therefore the existence of a complex solution corresponds to

$$\begin{aligned} 0 >& 16\pi^2 \lim_{h\to 1/2} (h-\frac{1}{2})^4 F(h) = 8\left(4\cos\left(2\theta_b\right)+\pi\right)\cos\left(2\theta_f\right) + 16k\cos\left(4\theta_b\right) + 16k + \pi(3\pi-4) \\ &+ 2(\pi-2)k\cos\left(2\theta_b\right)\left(8\cos\left(2\theta_b\right)+3\pi-4\right)\sec\left(2\theta_f\right) + 4(3\pi-4)(k+1)\cos\left(2\theta_b\right). \end{aligned} \tag{B.47}$$

Second, generically $F(h)$ has a double zero at $h = 1$, corresponding two gauge charges $\mathcal{Q}_f,\ \mathcal{Q}_b$ which have scaling dimension 1. When h_* crosses 1, $F(1)$ will be a triple zero such that

$$0 = F''(1) = 16\left(\pi\cos\left(2\theta_b\right)+2\right)\left(\pi\cos\left(2\theta_f\right)+2\right)\sec\left(2\theta_f\right)\left(k\cos\left(2\theta_b\right)+\cos\left(2\theta_f\right)\right). \tag{B.48}$$

Assuming, (B.46) holds, the only factor that could change sign is $2 + \pi\cos(2\theta_b)$, so the condition for $1/2 < h_1 < 1$ is

$$\theta_b > \frac{1}{2}\arccos\left(\frac{-2}{\pi}\right) \simeq 0.3598\pi. \tag{B.49}$$

We also remark that this is the maximum of the LHS of Luttinger constraint (3.32). When $h_1 = \frac{3}{2}$, it will be absorbed by the pole of $F(h)$ at $h = \frac{3}{2}$, so the mode disappears (it has zero OPE with the f and b). Physically, this corresponds to $\theta_b = \pi/4$, i.e. the holon density is zero.

Additionally, there can be a second solution near h_2 near $h = 2$. When this mode crosses $h = 2$, $F'(2)$ changes sign. The condition that $h_2 < 2$ is

$$\begin{aligned} 0 > F'(2) = \frac{16}{81} \sec\left(2\theta_f\right) \\ \times \left(-4k\cos\left(2\theta_b\right) - 3\pi k\cos\left(4\theta_b\right) + 4\cos\left(2\theta_f\right) + 3\pi\cos\left(4\theta_f\right) - 3\pi k + 3\pi\right). \end{aligned} \tag{B.50}$$

The above constraints define all the boundaries in Fig. 3.2. Same inequalties with $\theta_f \to \theta_\mathfrak{b}$, $\theta_b \to \theta_\mathfrak{f}$ define the boundaries in Fig. 3.4.

B.4 Calculation of Optical Conductivity

In this appendix we give details on the evaluation of (3.80). For convenience, we will work in units where $\beta = 2\pi$. Our starting point is the Kubo formula (3.77), recast into the following form

$$\mathrm{Re}\sigma(\omega) = \frac{\sigma_0}{C_e^2/J^2}\int_{-\infty}^{+\infty} \mathrm{d}\Omega \frac{1}{\omega}\left(\frac{1}{e^{2\pi\Omega}+1} - \frac{1}{e^{2\pi(\Omega+\omega)}+1}\right)\rho_e(\Omega)\rho_e(\Omega+\omega)\,, \tag{B.51}$$

here the prefactors are chosen such that the conformal contribution is σ_0. The electron spectral weight is given in (3.73),

$$\rho_e(\omega) = \rho_e^c(\omega)\left(1 - \sum_b V_b^{\mathrm{A}}\mathcal{R}_b^{\mathrm{A}}\left(\omega - \mathcal{E}_e\right) - V_b^{\mathrm{S}}\mathcal{R}_b^{\mathrm{S}}\left(\omega - \mathcal{E}_e\right)\right), \tag{B.52}$$

where

$$V_b^{\mathrm{A/S}} = \frac{\alpha_b}{2(\beta J)^{b-1}}\left(v_{bf+} \pm v_{bf-} \pm v_{bb+} + v_{bb-}\right). \tag{B.53}$$

The conformal contribution is

$$\mathrm{Re}\sigma_0(\omega) = \sigma_0 I(\omega)\,, \tag{B.54}$$

where the integral $I(\omega)$ is

$$I(\omega) = \int \mathrm{d}\Omega \frac{e^{\varepsilon\Omega}}{\omega}\left(\frac{1}{e^{2\pi\Omega}+1} - \frac{1}{e^{2\pi(\Omega+\omega)}+1}\right)\frac{\cosh(\pi\Omega)\cosh(\pi(\Omega+\omega))}{\cosh(\pi(\Omega-\mathcal{E}_e))\cosh(\pi(\Omega+\omega-\mathcal{E}_e))}\,. \tag{B.55}$$

We have added a convergence factor $e^{\varepsilon\Omega}$ with $\varepsilon \to 0$, which allows to split the two terms in the parentheses. The individual integrands are periodic under $\Omega \to \Omega + i$, so we can use an rectangular contour with infinite sides at $\mathrm{Im}\Omega = 0$ and at $\mathrm{Im}\Omega = 1$. The encircled poles are at $\Omega = \mathcal{E}_e + \frac{i}{2}$ and $\Omega = \mathcal{E}_e - \omega + \frac{i}{2}$. We obtain

$$I(\omega) = \frac{1-e^{-\varepsilon\omega}}{2\omega\sin\frac{\varepsilon}{2}}e^{\varepsilon\mathcal{E}_e}, \tag{B.56}$$

and in the limit $\varepsilon \to 0$ we get

$$\mathrm{Re}\sigma_0(\omega) = \sigma_0 I(\omega) = \sigma_0, \tag{B.57}$$

which is independent of frequency as expected from scaling analysis.

Next we look at contribution due to corrections

$$\begin{aligned}\mathrm{Re}\delta_b\sigma(\omega) = -\sigma_0 \int \mathrm{d}\Omega \frac{e^{\varepsilon\Omega}}{\omega}\left(\frac{1}{e^{2\pi\Omega}+1} - \frac{1}{e^{2\pi(\Omega+\omega)}+1}\right)\frac{\cosh(\pi\Omega)\cosh(\pi(\Omega+\omega))}{\cosh(\pi(\Omega-\mathcal{E}_e))\cosh(\pi(\Omega+\omega-\mathcal{E}_e))} \\ \times\left(V_b^{\mathrm{A}}\mathcal{R}_b^{\mathrm{A}}(\Omega-\mathcal{E}_e) + V_b^{\mathcal{S}}\mathcal{R}_b^{\mathrm{S}}(\Omega-\mathcal{E}_e) + V_b^{\mathrm{A}}\mathcal{R}_b^{\mathrm{A}}(\Omega+\omega-\mathcal{E}_e) + V_b^{\mathcal{S}}\mathcal{R}_b^{\mathrm{S}}(\Omega+\omega-\mathcal{E}_e)\right)\,.\end{aligned} \tag{B.58}$$

Using explicit expression (3.75) for $\mathcal{R}_h^{\mathrm{A/S}}$, we need the following auxilary integral ($\varepsilon \to 0$)

$$\begin{aligned} J(\omega) &= \int \mathrm{d}\Omega \frac{e^{\varepsilon\Omega}}{\omega}\left(\frac{1}{e^{2\pi\Omega}+1}-\frac{1}{e^{2\pi(\Omega+\omega)}+1}\right)\frac{\cosh(\pi\Omega)\cosh(\pi(\Omega+\omega))}{\cosh(\pi(\Omega-\mathcal{E}_e))\cosh(\pi(\Omega+\omega-\mathcal{E}_e))} \\ &\quad \times {}_3\mathbf{F}_2\left(\begin{matrix} h, 1-h, \frac{1}{2}+i(\Omega-\mathcal{E}_e) \\ 1, 1 \end{matrix}; 1\right) \\ &= {}_3\mathbf{F}_2\left(\begin{matrix} h, 1-h, 1-i\omega \\ 1, 2 \end{matrix}; 1\right), \end{aligned} \tag{B.59}$$

which is evaluated by expanding the hypergeometric function in series, doing the integral term by term with the contour method as for the integral $I(\omega)$, and then resumming the series.

Using $J(\omega)$, we can express the correction as

$$\mathrm{Re}\delta_h\sigma(\omega) = -\sigma_0 \frac{2\left(\frac{\pi}{2}\right)^h \Gamma(h)}{\sqrt{\pi}\sin\left(\frac{\pi h}{2}\right)\Gamma(h-1/2)}\left(V_h^{\mathrm{A}}\mathrm{Re}(J(\omega)+J(-\omega)) + V_h^{\mathrm{S}}\mathrm{Im}(J(\omega)+J(-\omega))\right). \tag{B.60}$$

Here the $J(-\omega)$ terms come from integrating $\mathcal{R}_h^{\mathrm{A/S}}(\Omega+\omega-\mathcal{E}_e)$. Since $J(\omega) = J(-\omega)^*$, only the V_h^{A} terms are nonzero, and we obtain (3.80).

C

Supplementary Information for Chapter 4

C.1 Details of the eigenvalue equation

In what follows we derive the one dimensional eigenvalue equation that is solved in the main text. A similar analysis of the Feynman rules for the OTOC was done before *e.g.* in [30,145,166]. We will present explicit derivations for each diagram and describe how the final structure is obtained. The analysis is first done for the single patch theory, and we later on generalize to two antipodal patches, and show

that our results and conclusions do not change.

The object of interest is the regulated squared anticommutator of the fermion operators

$$\mathcal{C}_x(t,0) = \frac{1}{N^2}\,\theta(t)\sum_{n,m=1}^{N}\mathrm{Tr}\left[e^{-\beta H/2}\{\psi_n(\mathbf{x},t),\psi_m^\dagger(0)\}e^{-\beta H/2}\{\psi_n(\mathbf{x},t),\psi_m^\dagger(0)\}^\dagger\right], \tag{C.1}$$

where $\psi(x,t) = U_I^\dagger\psi_0(x,t)U_I$ and U_I is the interaction picture time evolution operator. The notation $\psi(0) \equiv \psi(0,0)$ is introduced for simplicity. In the following, we drop the subscript "o" on ψ, assuming that the fields are free.

A Taylor expansion of the evolution operator up to second order reads

$$\begin{aligned} U_I &= \exp\left(\frac{i}{N}\sum_{ijl}\int_y\int_0^t ds\, g_{ijl}\psi_i^\dagger(y,s)\psi_j(y,s)\varphi_l(y,s)\right) \qquad \text{(C.2)}\\ &= 1+\frac{i}{N}\sum_{ijl}\int_y\int_0^t ds\, g_{ijl}\psi_i^\dagger(y,s)\psi_j(y,s)\varphi_l(y,s)\\ &+\left(\frac{i}{N}\right)^2\sum_{\text{all indecies}}\int_{y,y'}\int_0^t ds\int_0^s ds' g_{ijl}g_{i'j'l'}\varphi_l(y,s)\varphi_{l'}(y',s')\psi_i^\dagger(y,s)\psi_j(y,s)\psi_{i'}^\dagger(y',s')\psi_{j'}(y',s')+\dots. \end{aligned}$$

An expansion of its conjugate is therefore given by

$$\begin{aligned} U_I^\dagger &= \exp\left(-\frac{i}{N}\sum_{ijl}\int_y\int_0^t ds\, g_{ijl}\psi_i^\dagger(y,s)\psi_j(y,s)\varphi_l(y,s)\right) \qquad \text{(C.3)}\\ &= 1-\frac{i}{N}\sum_{ijl}\int_y\int_0^t ds\, g_{ijl}\psi_i^\dagger(y,s)\psi_j(y,s)\varphi_l(y,s)\\ &+\left(\frac{-i}{N}\right)^2\sum_{\text{all indecies}}\int_{y,y'}\int_0^t ds\int_0^s ds' g_{ijl}g_{i'j'l'}\varphi_l(y,s)\varphi_{l'}(y',s')\psi_i^\dagger(y,s)\psi_j(y,s)\psi_{i'}^\dagger(y',s')\psi_{j'}(y',s')+\dots. \end{aligned}$$

We use the following definitions of retarded Green's functions and the symmetrized Wightman func-

tions for fermions and bosons:

$$G^R(\mathbf{x},t)\delta_{a,b} = -i\theta(t)\,\langle\{\psi_a(\mathbf{x},t),\psi_b^\dagger(0)\}\rangle, \tag{C.4}$$

$$D^R(\mathbf{x},t)\delta_{a,b} = -i\theta(t)\langle[\varphi_a(\mathbf{x},t),\varphi_b(0)]\rangle, \tag{C.5}$$

$$G^W(\mathbf{x},t)\delta_{a,b} = \mathrm{Tr}[\rho^{1/2}\psi_a(\mathbf{x},t)\rho^{1/2}\psi_b^\dagger(0)], \tag{C.6}$$

$$D^W(\mathbf{x},t)\delta_{a,b} = \mathrm{Tr}[\rho^{1/2}\varphi_a(\mathbf{x},t)\rho^{1/2}\varphi_b(0)]. \tag{C.7}$$

where $\rho = e^{-\beta H}$.

Leading contribution.

The zeroth order Taylor expansion of the evolution operator (C.2), along with the above definition of the retarded Green's function for fermions (C.4), gives us the leading contribution to the expression for the squared anticommutator

$$\begin{aligned}\mathcal{C}_x^{(0)}(t,0) = \frac{1}{N^2}\theta(t)\sum_{n,m=1}^{N}\mathrm{Tr}\left[\rho^{1/2}\{\psi_m(x,t),\psi_n^\dagger(0)\}\rho^{1/2}\{\psi_m(x,t),\psi_n^\dagger(0)\}^\dagger\right]\\ = \frac{1}{N}(iG^R(\mathbf{x},t))(-iG^{R*}(\mathbf{x},t)) = \frac{1}{N}|G^R(\mathbf{x},t)|^2,\end{aligned}$$

Diagrammatically, we represent it simply as

$$\mathcal{C}_x^{(0)}(t,0) = \quad . \tag{C.8}$$

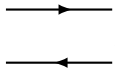

First order.

To derive the eigenvalue equation at the first order, we note that only the product of even numbers of the coupling constants g_{ijl} gives a non-zero result. The combination of the first term on one of the

time folds, and the expansion (C.2)-(C.3) to higher orders on the other time fold leads to corrections self energy corrections to the Green's function. Thus we are left with the expansion (C.2)-(C.3) to the first order on both time folds, and we obtain

$$\mathcal{C}_x^{(1)}(t,0) = \frac{1}{N^4}\theta(t)\int_{s,s'}\int_{\mathbf{y},\mathbf{y}'}\sum_{\text{all indices}} \mathrm{Tr}[\rho^{1/2} g_{ijl}\varphi_l(\mathbf{y},s)\{[\psi_m(\mathbf{x},t),\psi_i^\dagger(\mathbf{y},s)\psi_j(\mathbf{y},s)],\psi_n^\dagger(0)\}$$
$$\times\rho^{1/2} g_{i'j'l'}\ \varphi_{l'}(\mathbf{y}',s')\{[\psi_m(\mathbf{x},t),\psi_{i'}^\dagger(\mathbf{y}',s')\psi_{j'}(\mathbf{y}',s')],\psi_n^\dagger(0)\}^\dagger]$$

Using definitions (C.4)-(C.7), and counting the powers of N for each term, we obtain the following expression

$$\mathcal{C}_x^{(1)}(t,0) = \frac{g^2}{N}\int_{s,s'}\int_{\mathbf{y},\mathbf{y}'} G^R(\mathbf{x}-y,t-s)G^R(y,s)D^W(y-y',s-s')G^{R*}(x-y',t-s')G^{R*}(y',s'),$$

which gives the "rung" diagram

$$\mathcal{C}_x^{(1)}(t,0) = \quad . \tag{C.9}$$

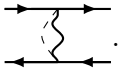

Second order.

At the second order we find three terms, but only one of them is both nonzero at large N and is not two ladders of type (C.9). This term is a "box" diagram and is similar to the one found in [145] and

reads

$$\mathcal{C}_x^{(2)}(t,0)$$
$$= \frac{g^4}{N}\int_{\{y\}}\int_0^t ds_1\int_0^{s_1} ds_2\int_0^t ds_3\int_0^{s_3} ds_4 G^R(x-y_1,t-s_1)D^R(y_1-y_2,s_1-s_2)G^W(y_1-y_3,s_1-s_3)$$
$$\times\, G^W(y_4-y_2,s_4-s_2)G^R(y_2,s_2)G^{R*}(x-y_3,t-s_3)D^{R*}(y_3-y_4,s_3-s_4)G^{R*}(y_4,s_4)$$

The diagram is

$$\mathcal{C}_x^{(2)}(t,0) = \quad . \tag{C.10}$$

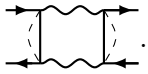

In the large N limit, we don't find any new types of diagrams other than boxes and rungs contributing to (C.1), after expanding the unitary operator (C.2) to higher orders.

The eigenvalue equation.

We now evaluate the ladder sum and work with the following function:

$$\mathcal{C}(\omega) = \frac{1}{N}\int \frac{d^3k}{(2\pi)^3}\mathcal{C}(k,\omega), \tag{C.11}$$

where $\mathcal{C}(\omega)$ is the Fourier transform of $\mathcal{C}_x(t,0)$ with respect to x and t. The spatial Fourier transform converts x to a momentum p_x that is taken to be along the x direction (normal to the patch Fermi surface), as the butterfly velocity is the largest along this direction [145].

The Bethe-Saltpeter equation (Fig. 4.2 of the main text) then reads

$$\mathcal{C}(k,\omega) = G^R(k)G^{R*}(k-p_x-\omega)\left[1+\int\frac{d^3k'}{(2\pi)^3}(g^2D^W(k-k')+K_2(k,k',\omega))\mathcal{C}(k',\omega)\right].$$

Each of the terms corresponds to Fourier transform of the perturbative expansion found above. The

exponential growth of the squared anticommutator in the chaos regime is expected if the eigenvalue equation is invariant under adding a ladder, and we can then write

$$\mathcal{C}(k,\omega) = G^R(k)G^{R*}(k-p_x-\omega)\int \frac{d^3k'}{(2\pi)^3}(g^2D^W(k-k') + K_2(k,k',\omega))\mathcal{C}(k',\omega), \quad \text{(C.12)}$$

where the function $K_2(k,k',\omega)$ is the kernel of the "box" diagram found above (C.10), which in Fourier space reads

$$K_2(k,k',\omega) = g^4\int \frac{d^3k_1}{(2\pi)^3}D^R(k_1)D^{R*}(k_1-p_x-\omega)G^W(k-k_1)G^W(k'-k_1). \quad \text{(C.13)}$$

We can now explicitly compute each term in (C.12). The fermion and boson Green's functions the single patch theory[49] are given by

$$G^R(k,\omega) = \frac{1}{k_x + k_y^2 - \Sigma^R(\omega) - i\mu(T)}, \quad \text{(C.14)}$$

$$G^W(k,\omega) = -\frac{\mathrm{Im}\Sigma^R(\omega)+\mu(T)}{\cosh\frac{\beta\omega}{2}\left([(k_x+k_y^2)+\mathrm{Re}\Sigma^R(\omega)]^2 + [\mathrm{Im}\Sigma^R(\omega)+\mu(T)]^2\right)}, \quad \text{(C.15)}$$

$$D^R(q,\Omega\neq 0) = \frac{|q_y|}{|q_y|^3 + m^2 - ic_b\Omega}, \quad \text{(C.16)}$$

$$D^W(q,\Omega) = \frac{c_b\Omega|q_y|}{\sinh\frac{\beta\Omega}{2}((|q_y|^3+m^2)^2 + c_b^2\Omega^2)}, \quad \text{(C.17)}$$

where we added a small mass term in the boson Green's function as an IR regulator that will eventually be carefully taken to zero, and

$$\Sigma^R(\omega) = ic_f T^{2/3}H_{1/3}\left(\frac{-i\omega-\pi T}{2\pi T}\right) \quad \text{(C.18)}$$

The function $H_{1/3}(z) = \zeta(1/3) - \zeta(1/3, z+1)$ is the Harmonic number function, as noted in the main text, and the constants take the values $c_f = 2^{5/3}g^{4/3}/(3\sqrt{3})$ and $c_b = g^2/(8\pi)$ in the single

patch theory.

Since our theory has sliding symmetry about the patch Fermi surface, the function $\mathcal{C}(k,\omega)$ depends on momentum as $\mathcal{C}(k,\omega) = \mathcal{C}(k_x + k_y^2, k_0, \omega)$. Our main goal further is to express the equation in terms of a momentum independent eigenfunction [145] (which we call $\mathcal{C}(k_0,\omega,i|p_x|)$ in the main text)

$$\tilde{\mathcal{C}}(k_0',\omega) = \int \frac{dk_x'}{2\pi}\mathcal{C}(k_x' + k_y^2, k_0', \omega), \tag{C.19}$$

which we will see is possible to do because of the special momentum dependence of $\mathcal{C}$ induced by the sliding symmetry.

We now compute each term in (C.12). The diagonal term in the equation is simply

$$\begin{aligned}\int \frac{dk_x}{2\pi} G^R(k)G^{R*}(k-p_x-\omega) &= \frac{i}{\Sigma^R(k_0) - \Sigma^{R*}(k_0-\omega) + 2i\mu(T) - p_x} \\ &= \frac{1}{c_f T^{2/3}} \frac{1}{H_{1/3}\left(\frac{-ik_0-\pi T}{2\pi T}\right) + H_{1/3}\left(\frac{-i(\omega-k_0)-\pi T}{2\pi T}\right) + 2\mu(T) + ip_x}.\end{aligned}$$

The "first order" term can be written as

$$\begin{aligned}&g^2 \int \frac{d^3k'}{(2\pi)^3} D^W(k-k')\mathcal{C}(k',\omega) \\ &= g^2 c_b \int \frac{dk_0' dk_y'}{(2\pi)^2} \frac{(k_0-k_0')|k_y'|}{(k_y'^3+m^2)^2 + c_b^2(k_0-k_0')^2} \frac{\tilde{\mathcal{C}}(k_0',\omega)}{\sinh\frac{k_0-k_0'}{2T}}.\end{aligned}$$

The second term in the eigenvalue equation, *i.e.* the K_2 - term can be evaluated as done in Ref. [145]

$$\begin{aligned}&\int \frac{d^3k'}{(2\pi)^3} K_2(k,k',\omega)\mathcal{C}(k',\omega) \\ &= g^4 \int \frac{d^3k_1 d^3k'}{(2\pi)^6} D^R(k_1) D^{R*}(k_1 - p_x - \omega) G^W(k-k_1) G^W(k'-k_1)\mathcal{C}(k',\omega) \\ &= \frac{g^{4/3}4\pi^{4/3}}{3\sqrt{3}} \int \frac{dk_0' dk_{01}}{(2\pi)^2} \frac{(ik_{01} + (-ik_{01})^{2/3}(i(k_{01}-\omega)))}{k_{01}(i(k_{01}-\omega))^{1/3}(2k_{01}-\omega)} \frac{\tilde{\mathcal{C}}(k_0',\omega)}{\cosh\frac{k_0-k_{01}}{2T}\cosh\frac{k_0'-k_{01}}{2T}}.\end{aligned} \tag{C.20}$$

The integration over frequencies has to be done numerically. Combining the above equations, we obtain the eigenvalue equation that we solve in the main text, for $p_x = i|p_x|$:

$$\left[c_f T^{2/3}\left(H_{1/3}\left(\frac{-ik_0-\pi T}{2\pi T}\right)+H_{1/3}\left(\frac{-i(\omega-k_0)-\pi T}{2\pi T}\right)\right)+2\mu(T)-|p_x|\right]\tilde{\mathcal{C}}(k_0,\omega)$$
$$=g^2\int\frac{dk_0'dk_y'}{(2\pi)^2}\frac{c_b(k_0-k_0')|k_y'|}{(|k_y'|^3+m^2)^2+c_b^2(k_0-k_0')^2}\frac{\tilde{\mathcal{C}}(k_0',\omega)}{\sinh\frac{k_0-k_0'}{2T}}$$
$$+\frac{g^{4/3}4\pi^{4/3}}{3\sqrt{3}}\int\frac{dk_0'dk_{01}}{(2\pi)^2}\frac{(ik_{01}+(-ik_{01})^{2/3}(i(k_{01}-\omega)))}{k_{01}(i(k_{01}-\omega))^{1/3}(2k_{01}-\omega)}\frac{\tilde{\mathcal{C}}(k_0',\omega)}{\cosh\frac{k_0-k_{01}}{2T}\cosh\frac{k_0'-k_{01}}{2T}}. \quad \text{(C.21)}$$

We then numerically solve the equation following Appendix D in [145].

Our numerical procedure is as follows. We first perform the integration over k_y with a small finite mass term $m = 0.02$. We then discretize the integration over k_0' as well as the variable k_0 in the region $k_0, k_0' \in [-15, 15]$ with the step size $dk_0 = 0.005$. We solve the eigenvalue equation for different ω on the positive imaginary axis, and look for ω at which eigenvalue of the equation (C.21) is closest to zero. Whenever we obtain a solution with multiple eigenvalues, we choose the largest one since it corresponds to the Lyapunov exponent λ_L. As a check, we find the value $\lambda_L \simeq 2.48T$ at $|p_x| = 0$, which is exactly the result that was found in [145].

Antipodal patches.

We now consider the evolution of the OTOC in the non-chiral theory with two antipodal patches. We will show that our conclusions about maximal quantum chaos are unaffected in the large N limit by the interactions induced between the two patches.

The action for the two patch model ((4.1) of the main text) tells us that the fermions in the $\pm$ patches disperse as $\pm k_x + k_y^2$ respectively. We therefore expect that the eigenfunctions for the two patches $\pm$ are given by $\mathcal{C}_\pm(k, k_0, \omega) = \mathcal{C}(\pm k_x + k_y^2, k_0, \omega)$, which is obvious at the non-interacting level (*i.e.* (C.8)), and can easily be shown to be self-consistent when interactions are included in the

Bethe-Salpeter equation.

In addition to the K_2 term in the eigenvalue equation, we now have a term that couples fermions from opposite patches at the two ends of the "box" diagrams. For the $+$ patch, it is given by (C.22),

$$\mathcal{C}_x'^{(2)}(t,0) = \tag{C.22}$$

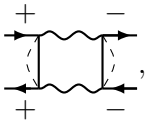

which yields

$$\int \frac{d^3k'}{(2\pi)^3} K_2'(k,k',\omega)\mathcal{C}_-(k',\omega) \;= \int \frac{d^3k'}{(2\pi)^3} K_2'(k,k_0',k_x',k_y',\omega)\mathcal{C}(-k_x'+k_y'^2,k_0,\omega). \tag{C.23}$$

Then, by exploiting the sliding symmetry and shifting $k_x' \to k_x' + k_y'^2$, we can complete the internal momentum (k_{x1}, k_{y1}) integrals just like Ref. [145] did with the K_2 term, followed by the (k_x', k_y') integrals. This yields

$$\begin{aligned}
&\int \frac{d^3k'}{(2\pi)^3} K_2'(k,k',\omega)\mathcal{C}_-(k',\omega) \\
&= g^4 \int \frac{d^3k_1 d^3k'}{(2\pi)^6} D^R(k_1) D^{R*}(k_1 - p_x - \omega) G_+^W(k-k_1) G_-^W(k'-k_1)\mathcal{C}_-(k',\omega) \\
&= \frac{g^{4/3}4\pi^{4/3}}{2^{4/3}3\sqrt{3}} \int \frac{dk_0' dk_{01}}{(2\pi)^2} \frac{(ik_{01} + (-ik_{01})^{2/3}(i(k_{01}-\omega)))}{k_{01}(i(k_{01}-\omega))^{1/3}(2k_{01}-\omega)} \frac{\tilde{\mathcal{C}}(k_0',\omega)}{\cosh\frac{k_0-k_{01}}{2T}\cosh\frac{k_0'-k_{01}}{2T}},
\end{aligned}$$

where $G_\pm^W$ are the Wightman fermion Green's functions for the $\pm$ patches respectively. This is just proportional to the action of the K_2 term on $\mathcal{C}_+$ (C.20). The sum of the action of the K_2 and K_2' terms therefore yields the RHS of (C.20) divided by a factor of $2^{1/3}$. However, since the two patch value of c_b is twice its one patch value, and the two patch value of c_f is $1/2^{1/3}$ times its one patch value, this extra factor of $1/2^{1/3}$ cancels out in the equivalent of (C.21) as m is taken to 0, leaving us with

the same final one dimensional integral equation to be solved numerically.

Therefore, at $i|p_x| = 0$, there is no difference between the solutions for the one-patch and two-patch OTOCs. For non-zero external momentum, we can see that if we apply $+i|p_x|$ to the $+$ patch and $-i|p_x|$ to the $-$ patch, corresponding to a pair of chiral scrambling modes traveling with the same speed but in opposite directions (one coming from each patch), we get the same $i|p_x|$ dependence for the OTOC as well. The only difference is that the value of $i|p_x|$ is rescaled by a factor of $2^{1/3}$, and therefore the butterfly velocity is rescaled by a factor of $1/2^{1/3}$. However, since this merely corresponds to a rescaling of the x-axes of Figs. 4.3, 4.4 of the main text, our conclusions regarding maximal chaos remain unchanged.

C.2 Generalization of the ladder identity

In this section we discuss the generalization of the single mode ansatz [104,77,79] to the spatially dependent case, and show that the result obtained by Gu and Kitaev[77] holds.

The "regular" OTOC we are considering consists of connected and disconnected parts

$$\begin{aligned}\mathrm{OTOC}_x(t_1,t_2,t_3,t_4) = \frac{1}{N^2}\sum_{n,m=1}^{N} (\langle \rho^{1/4}\psi_n(x,t_1)\rho^{1/4}\psi_m^\dagger(0,t_3)\rho^{1/4}\psi_n^\dagger(x,t_2)\rho^{1/4}\psi_m(0,t_4)\rangle \\ + \langle \psi_n(x,t_1)\psi_n^\dagger(x,t_2)\rangle\langle \psi_m^\dagger(0,t_3)\psi_m(0,t_4)\rangle).\end{aligned} \tag{C.24}$$

We consider the Fourier transform of the connected part:

$$\mathrm{OTOC}_x(t_1,t_2,t_3,t_4) = \int_{p,k,k'} e^{ipx}\,\mathrm{OTOC}_p,(t_1,t_2,t_3,t_4;k,k') \tag{C.25}$$

and use the assumption that the single mode ansatz works for every momentum eigenmode. The

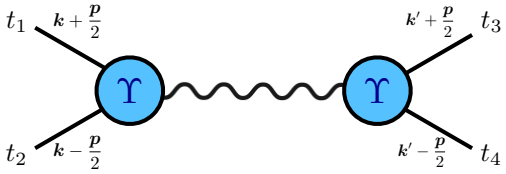

Figure C.1: Diagram representing the ansatz (C.26). The wavy line represents the scramblon. The figure is adapted from [77] for the momentum-dependent case.

OTOC then has the following form

$$\mathrm{OTOC}_p(t_1,t_2,t_3,t_4;k,k') \simeq \frac{e^{\kappa(p)(t_1+t_2-t_3-t_4)/2}}{C(p)}\Upsilon_p^R(t_{12},k)\Upsilon_p^A(t_{34},k'), \tag{C.26}$$

where we assume that the times are well separated $s = (t_1+t_2-t_3-t_4)/2 \gg \kappa(p)^{-1}$, the exponent represents the "scramblon", the momentum-dependent function $C(p)$ is to be determined below from the consistency condition, and $\Upsilon_p^{A,R}(t_{ij},k)$ are the momentum-dependent vertex functions. The diagram that represents the ansatz is shown in Fig. C.1.

Let us consider the following form of the regular OTOC, where we distinguish 2 ladders somewhere in the middle. We can then write down the self consistency condition as follows

$$\mathrm{OTOC}_p(t_1,t_2,t_3,t_4;k,k') \simeq \int_{t_5,t_6,t_7,t_8;q,q'} \mathrm{OTOC}_p^R(t_1,t_2,t_5,t_6;k,q) \times \quad \times \mathrm{OTOC}_p(t_7,t_8,t_3,t_4;\mathbf{q}',k'). \tag{C.27}$$

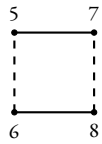

BOX

The points t_5 and t_6 have the same corresponding imaginary time components as t_1 and t_2. We therefore need to shift the coordinates on the Keldysh contour by $\pm i\pi/2$ to either direction as shown in

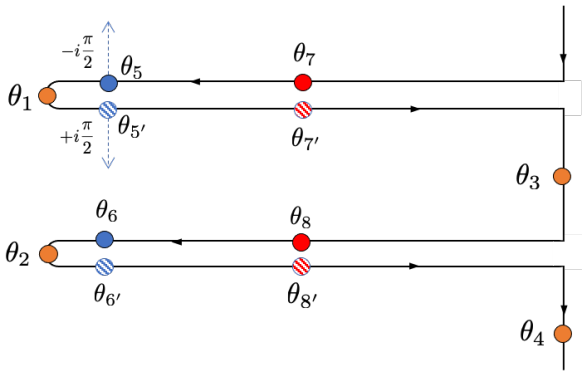

Figure C.2: Double Keldysh contour for the equation (C.27).

Fig.C.2. There are two choices

$$\mathrm{OTOC}_{p,A} = \mathrm{OTOC}_p\left(t_1, t_2, t_5 - i\frac{\pi}{2}, t_6 - i\frac{\pi}{2}; k, k'\right) \simeq \frac{e^{\kappa(p)(t_1+t_2-t_5-t_6+i\pi)/2}}{C(p)} \Upsilon_p^R(t_{12}, k)\Upsilon_p^A(t_{56}, k'),$$
$$\mathrm{OTOC}_{p,A'} = -\mathrm{OTOC}_p\left(t_1, t_2, t_6 + i\frac{\pi}{2}, t_5 + i\frac{\pi}{2}; k, k'\right) \simeq \frac{e^{\kappa(p)(t_1+t_2-t_5-t_6-i\pi)/2}}{C(p)} \Upsilon_p^R(t_{12}, k)\Upsilon_p^A(t_{56}, k'),$$

that we need to add together. The other OTOC in (C.27) is regular because the points t_3, t_4 and t_7, t_8 have different imaginary parts, and we obtain

$$\mathrm{OTOC}_p(t_7, t_8, t_3, t_4; k, k') \simeq \frac{e^{\kappa(p)(t_7+t_8-t_3-t_4)/2}}{C(p)} \Upsilon_p^R(t_{78}, k)\Upsilon_p^A(t_{34}, k'). \tag{C.28}$$

Plugging in the ansatzé for each OTOC on both sides in (C.27), we can schematically write

$$\begin{aligned}
&\frac{e^{\kappa(p)\frac{(t_1+t_2-t_3-t_4)}{2}}}{C(p)} \Upsilon_p^R(t_{12}, k)\Upsilon_p^A(t_{34}, k') = N\frac{2\cos\frac{\kappa(p)\pi}{2}}{C^2(p)} e^{\kappa(p)\frac{(t_1+t_2-t_3-t_4)}{2}} \\
&\times \int_{t_5,t_6,t_7,t_8;q,q'} e^{-\kappa(p)\frac{(t_5+t_6)}{2}} \Upsilon_p^R(t_{12}, k)\Upsilon_p^A(t_{56}, q) \\
&\cdot \mathrm{BOX}(t_5, t_6, t_7, t_8; q, q') \cdot e^{\kappa(p)\frac{(t_7+t_8)}{2}} \Upsilon_p^R(t_{78}, q')\Upsilon_p^A(t_{34}, k'),
\end{aligned}$$

where the dot product is a notation for the integration over the intermediate times and momentum.

The factor of N comes from the definition of the OTOC and needs to be compensated since we have two of them on the RHS. Simplifying the equation, we obtain

$$C(p) = 2N\cos\frac{\kappa(p)\pi}{2}\int_{t_5,t_6,t_7,t_8;q,q'} e^{\kappa(p)(t_7+t_8-t_5-t_6)/2}\Upsilon^A_p(t_{56},q) \tag{C.29}$$
$$\times\,\mathrm{BOX}(t_5,t_6,t_7,t_8;q,q')\times\Upsilon^R_p(t_{78},q').$$

We are interested in the fact that the momentum dependent coefficient $C(p)$ is proportional to

$$\frac{C(p)}{N}\sim\cos\frac{\kappa(p)\pi}{2}, \tag{C.30}$$

which becomes zero when $\kappa(p)=1$. In our case $\lambda_L(p)=2\pi T\kappa(p)$, which means that $\lambda_L=2\pi T$ corresponds to a pole in the regular OTOC (C.24).

C.3 Varying the dynamical critical exponent

In this section we derive the generalized eigenvalue equation for non-Fermi liquids with dynamical critical exponent $2<z\leq 3$. The retarded boson Green's function and boson Wightman function have the following forms:

$$D^R(q,\Omega\neq 0)=\frac{1}{|q_y|^{z-1}+ic_b\frac{\Omega}{|q_y|}}, \tag{C.31}$$

$$D^W(q,\Omega)=\frac{c_b\Omega|q_y|}{\sinh\frac{\beta\Omega}{2}(|q_y|^{2z}+c_b^2\Omega^2)}, \tag{C.32}$$

where $c_b = g^2/8\pi$ as before. The fermion self energy changes to

$$\begin{aligned}\Sigma(i\omega_n) &= ig^2\frac{T}{2}\sum_{\Omega_m\neq 0}\int_{q_y}\frac{\mathrm{sgn}(\omega_n+\Omega_m)}{|q_y|^{z-1}+\frac{g^2}{8\pi}\frac{|\Omega_m|}{|q_y|}} \\ &= 2^{2-\frac{6}{z}}g^{\frac{4}{z}}T\pi^{1-\frac{2}{z}}\frac{i}{z\sin\frac{2\pi}{z}}\sum_{\Omega_m\neq 0}\Omega_m^{\frac{2}{z}-1}\mathrm{sgn}(\omega_n+\Omega_m) \\ &= i\mathrm{sgn}(\omega_n)2^{2-\frac{4}{z}}g^{\frac{4}{z}}T^{\frac{2}{z}}\frac{1}{z\sin\frac{2\pi}{z}}H_{1-\frac{2}{z}}\left(\frac{|\omega_n|-\pi T}{2\pi T}\right).\end{aligned} \tag{C.33}$$

In a simpler form, the self energy is

$$\Sigma(i\omega_n) = i\mathrm{sgn}(\omega_n)c_{f,z}T^{\frac{2}{z}}H_{1-\frac{2}{z}}\left(\frac{|\omega_n|-\pi T}{2\pi T}\right), \tag{C.34}$$

$$c_{f,z} = 2^{2-\frac{4}{z}}g^{\frac{4}{z}}\frac{1}{z\sin\left(\frac{2\pi}{z}\right)}, \tag{C.35}$$

and the fermion Green's function reads

$$G(k,i\omega_n) = \frac{1}{k_x+k_y^2-ic_{f,z}\mathrm{sgn}(\omega_n)T^{2/z}H_{1-\frac{2}{z}}\left(\frac{|\omega_n|-\pi T}{2\pi T}\right)-i\mathrm{sgn}(\omega_n)\mu(T)}, \tag{C.36}$$

$$\mu(T) = \frac{g^2T}{2z\sin\left(\frac{2\pi}{z}\right)m^{2-\frac{4}{z}}}, \tag{C.37}$$

where $\mu(T)$, as before, is a term generated by a finite but small boson mass m. The derivation of the eigenvalue equation is the same as before, and it can be written as

$$\begin{aligned}&\left[T^{2/z}c_{f,z}\left(H_{1-2/z}\left(\frac{-ik_0-\pi T}{2\pi T}\right)+H_{1-2/z}\left(\frac{-i(\omega-k_0)-\pi T}{2\pi T}\right)\right)+2\mu(T)-|p_x|\right]\tilde{C}(k_0,\omega) \\ &= g^2\int\frac{dk_0'dk_y'}{(2\pi)^2}\frac{c_b(k_0-k_0')|k_y'|}{(|k_y'|^z+m^2)^2+c_b^2(k_0-k_0')^2}\frac{\tilde{C}(k_0',\omega)}{\sinh\frac{k_0-k_0'}{2T}} \\ &- \frac{ig^4}{8z\sin\left(\frac{2\pi}{z}\right)c_b^{2-\frac{2}{z}}}\int\frac{dk_0'dk_{01}}{(2\pi)^2}\frac{(-ik_{01})^{\frac{2}{z}-1}-(i(k_{01}-\omega))^{\frac{2}{z}-1}}{2k_{01}-\omega}\frac{\tilde{C}(k_0',\omega)}{\cosh\frac{k_0-k_{01}}{2T}\cosh\frac{k_0'-k_{01}}{2T}}.\end{aligned} \tag{C.38}$$

Checking this for $z = 3$, we obtain the result of the previous section. The numerical approach to solve this equation is the same as in the previous section; we vary the external momentum p_x on the imaginary axis and looking for a value of k_0 at which the equation has a solution. We present the result of $\lambda_L(i|p_x|)/T$ in the main text, and show that any theory with the dynamical critical exponent in a region $2 < z \leq 3$ is maximally chaotic.

C.3.1 Quasiparticles

Here, we would like to explore a Fermi liquid regime where quasiparticles appear, specifically when the dynamical critical exponent z is in the region $1 < z < 2$. We explicitly derive and solve the eigenvalue equation, and find and compare the saddle point and pole values. We show that the saddle point gives dominant contribution to the OTOC, and the theories are therefore not maximally chaotic as per the criteria of Ref.[77].

We first compute the fermion self energy with the dynamical critical exponent in the region $1 < z < 2$. As compared to the previous case, we set now the boson mass to zero, but have to include a finite UV cutoff Λ when integrating over k_y. The fermion self energy reads

$$\begin{aligned}\Sigma(i\omega_n) &= ig^2 \frac{T}{2} \sum_{\Omega_m} \int_{-\Lambda}^{\Lambda} \frac{dq_y}{2\pi} \frac{|q_y| \mathrm{sgn}(\omega_n + \Omega_m)}{|q_y|^z + c_b |\Omega_m|} \\ &= ig^2 \frac{T}{2\pi} \sum_{\Omega_m} \mathrm{sgn}(\omega_n + \Omega_m) \left[\frac{\Lambda^{2-z}}{2-z} + \frac{\pi c_b^{\frac{2}{z}-1} |\Omega_m|^{\frac{2}{z}-1}}{z \sin\left(\frac{2\pi}{z}\right)} \right] \\ &= i\omega_n \frac{g^2}{2\pi^2} \frac{\Lambda^{2-z}}{2-z} + ig^2 T^{\frac{2}{z}} \mathrm{sgn}(\omega_n) \frac{(2\pi c_b)^{\frac{2}{z}-1}}{z \sin\left(\frac{2\pi}{z}\right)} H_{1-\frac{2}{z}} \left(\frac{|\omega_n| - \pi T}{2\pi T} \right),\end{aligned} \tag{C.39}$$

where Λ is assumed to be large. The retarded self energy is therefore

$$\Sigma^R(\omega) = \omega \frac{g^2}{2\pi^2} \frac{\Lambda^{2-z}}{2-z} + ig^2 T^{\frac{2}{z}} \frac{(2\pi c_b)^{\frac{2}{z}-1}}{z \sin\left(\frac{2\pi}{z}\right)} H_{1-\frac{2}{z}} \left(\frac{-i\omega - \pi T}{2\pi T} \right). \tag{C.40}$$

The diagonal term in the eigenvalue equation reads

$$\int \frac{dk_x}{2\pi} G^R(k) G^{R*}(k - p_x - \omega) \qquad = \frac{i}{\Sigma^R(k_0) - \Sigma^{R*}(k_0 - \omega) + \omega - p_x}, \tag{C.41}$$

where we have retained the bare k_0 term in the fermion Green's functions, as it is no longer dominated by the self energy unlike the previously considered $2 < z \leq 3$ case. Combining (C.40) and (C.41), we obtain the diagonal term

$$\frac{1}{T^{2/z} c_{f,z} \left(H_{1-2/z}\left(\frac{-ik_0 - \pi T}{2\pi T}\right) + H_{1-2/z}\left(\frac{-i(\omega - k_0) - \pi T}{2\pi T}\right)\right) - i\omega(1 + \frac{g^2}{2\pi^2}\frac{\Lambda^{2-z}}{2-z}) + ip_x}. \tag{C.42}$$

The "first order" term is simply

$$g^2 \int \frac{dk_0' dk_y'}{(2\pi)^2} \frac{c_b |k_y'| (k_0 - k_0')}{|k_y'|^{2z} + c_b^2 (k_0 - k_0')^2} \frac{\tilde{\mathcal{C}}(k_0', \omega)}{\sinh \frac{k_0 - k_0'}{2T}} = \frac{g^2 c_b^{\frac{2}{z}-1}}{2z \sin \frac{\pi}{z}} \int \frac{dk_0'}{2\pi} \frac{(k_0 - k_0')^{\frac{2}{z}-1}}{\sinh \frac{k_0 - k_0'}{2T}} \tilde{\mathcal{C}}(k_0', \omega), \tag{C.43}$$

and we note that it is free of IR divergences. We also note that the K_2 term is the same as in the previous case (C.38) for $2 < z \leq 3$, and the eigenvalue equation becomes

$$\begin{aligned}
&\left[T^{2/z} c_{f,z} \left(H_{1-2/z}\left(\frac{-ik_0 - \pi T}{2\pi T}\right) + H_{1-2/z}\left(\frac{-i(\omega - k_0) - \pi T}{2\pi T}\right)\right) \right. \\
&\left. - i\omega \left(1 + \frac{g^2}{2\pi^2}\frac{\Lambda^{2-z}}{2-z}\right) - |p_x| \right] \tilde{\mathcal{C}}(k_0, \omega) \\
&= \frac{g^2 c_b^{\frac{2}{z}-1}}{2z \sin \frac{\pi}{z}} \int \frac{dk_0'}{2\pi} \left[\frac{(k_0 - k_0')^{\frac{2}{z}-1}}{\sinh \frac{k_0 - k_0'}{2T}} \right. \\
&\left. - \frac{ig^2}{8 \cos\left(\frac{\pi}{z}\right) c_b} \int \frac{dk_{01}}{2\pi} \frac{(-ik_{01})^{\frac{2}{z}-1} - (i(k_{01} - \omega))^{\frac{2}{z}-1}}{(2k_{01} - \omega) \cosh \frac{k_0 - k_{01}}{2T} \cosh \frac{k_0' - k_{01}}{2T}} \right] \tilde{\mathcal{C}}(k_0', \omega),
\end{aligned} \tag{C.44}$$

where the constants $c_{f,z}$ and c_b are defined above.

We solve the equation for parameters $z = 1.5, g = 0.5, T = 1$, and the UV cutoff $\Lambda = 50$. We

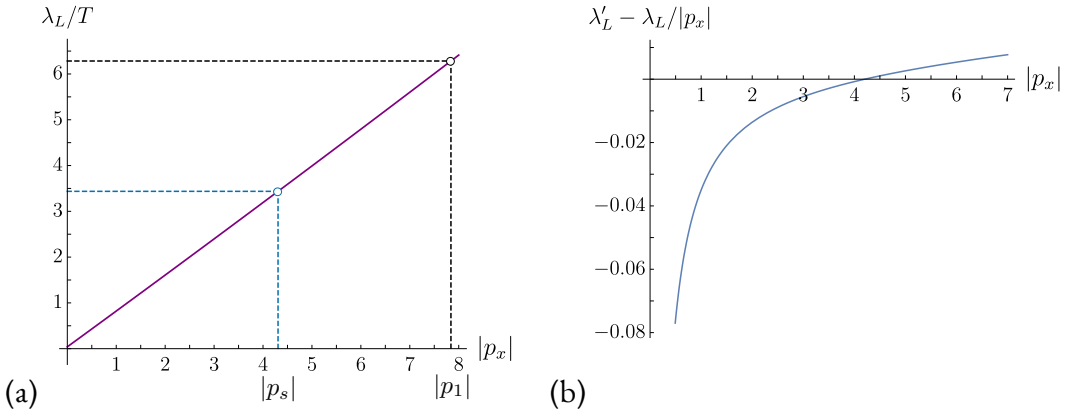

Figure C.3: Analysis of the eigenvalues numerically obtained from (C.44) for $z = 1.5, g = 0.5$ and $\Lambda = 50$. (a) Lyapunov exponent as a function of $|p_x|$ on the imaginary axis. The saddle point $|p_s|$ gives the dominant contribution as $|p_s| < |p_1|$[77]. In particular, we obtained $|p_s| = 4.28$ and $|p_1| = 7.84$. The butterfly velocity therefore is $v_B = (d\lambda_L(p_x)/d|p_x|)_{p_x=p_s} = 0.8 v_F$, where $v_F = 1$ is the Fermi velocity. The purple line is a fitting function $\lambda_L = 0.04 + 0.78|p_x| + 0.002|p_x|^2$ of the numerical data. The accuracy of the results is within $\sim 5\%$. (b) Finding the saddle point, which is given by the root of the plotted function.

find that the ballistic growth is present with the Lyapunov exponent $\lambda_L = 3.42$ and butterfly velocity $v_B = 0.8\, v_F$. Since the solution is numerical, we obtain the result with some error, that we estimate to be $\sim 5\%$. We show the behavior of eigenvalues upon changing the external momentum on the imaginary axis in Fig. C.3. We find that the magnitude of the saddle point momentum is $|p_s| = 4.28$, and that of the pole momentum is $|p_1| = 7.84$, which is much greater than $|p_s|$. Therefore, there is no maximal chaos according to the criteria set by Ref.[77].

We also solve the eigenvalue equation for several other values of the dynamical critical exponent in the range $1 < z < 2$, where quasiparticles are present. As in the main text, we compute the difference between the velocities v_1 and instantaneous slopes v_* at $p_x = p_1$. We show the result in Fig. C.4. Within our numerical accuracy ($\sim 5\%$), we find that the instantaneous slope v_* is always larger than the velocity v_1 at the pole $p = i|p_1|$. Since $\lambda_L(i|p_x|)$ is a positive, monotonically increasing, and convex function, this implies $|p_s| < |p_1|$. Therefore, following the criteria set by Ref.[77], we can argue that for $z < 2$, the theories are not maximally chaotic.

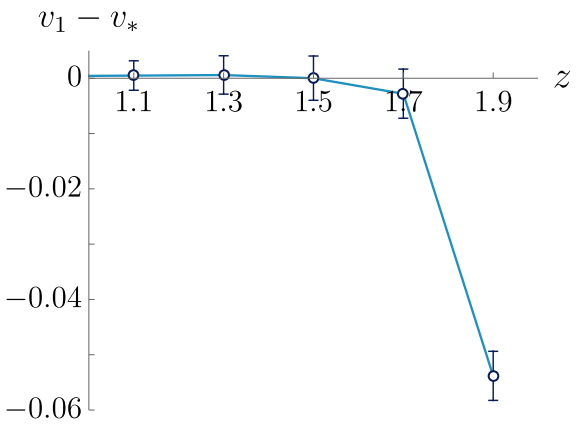

Figure C.4: Difference between v_1 and the instantaneous slopes v_* at $p_x = p_1$, for several dynamical critical exponents z in the region $1 < z < 2$. This difference is negative within numerical accuracy, and therefore there is no maximal chaos when $z < 2$. This is in contrast to the $2 < z \leq 3$ case, where the difference is always positive (Fig. 4.4 of the main text)

We also note that the leading behavior of the eigenvalues is controlled by the linear in frequency behavior in the diagonal term of the equation (C.44). Therefore, to first order, we see that $\lambda_L \sim T^{2/z} \ll 2\pi T$, and we can also estimate the butterfly velocity as

$$v_B \simeq \frac{1}{1 + \frac{g^2}{2\pi^2}\frac{\Lambda^{2-z}}{2-z}} v_F, \tag{C.45}$$

where $v_F = 1$ is the Fermi velocity. For the chosen parameters, this equation approximates $v_B \simeq 0.85\, v_F$, which is close to the actual numerical solution we obtained above. We therefore argue that, within the class of problems we are interested in, any theory with the dynamical critical exponent in the region $1 < z < 2$, *i.e.*, one that has quasiparticles, is not maximally chaotic.

D

Supplementary Information for Chapter 5

D.1 Real frequency equations for critical metal with fermionic spinons

In this appendix we present details related to solving the saddle-point equations in Eqs. (5.12)-(5.17) of the main text on the real-frequency axis. We shall focus our attention at zero temperature. In addition, we also present more details of our solution and present arguments for the absence of a Fermi-liquid solution.

D.1.1 Analytic continuation to real frequency

We can separate the zero frequency bosonic greens function into a part which is regular at $i\omega_n = 0$ and a part which diverges at zero temperature:

$$\beta\bar{r} = \beta r - \overline{G_b}(i\omega_n = 0) \tag{D.1}$$

We can then rewrite the saddle point equations in terms of r and $\overline{G}_b$ as:

$$\overline{G}_b(i\omega_n = 0) - \beta r = \frac{1}{\mu_b - \Sigma_b(i\omega_n = 0)} \tag{D.2}$$

$$\overline{G}_b(i\omega_n) = \frac{1}{i\omega_n + \mu_b - \Sigma_b(i\omega_n)} \tag{D.3}$$

$$\Sigma_b(\tau) = -t^2 G_f(\tau) G_f(-\tau)\left[-r + \bar{G}_b(\tau)\right] \tag{D.4}$$

$$\overline{G}_f(i\omega_n) = \frac{1}{i\omega_n + \mu_f - \Sigma_f(i\omega_n)} \tag{D.5}$$

$$\Sigma_f(\tau) = -J^2 G_f(\tau)^2 G_f(-\tau) + kt^2 G_f(\tau)\left[r^2 - r(\overline{G}_b(\tau) + \overline{G}_b(-\tau)) + \overline{G}_b(\tau)\overline{G}_b(-\tau)\right] \tag{D.6}$$

We wish to solve the above equations on the real frequency axis so that we may obtain physical observables like the electron and spin spectral functions. The above equations can be rewritten in terms of the spectral functions for fermions and bosons by analytically continuing the imaginary frequency greens functions to obtain the retarded greens function $G^R_{f/b}(\omega)$:

$$\rho_{f/b} = -\frac{1}{\pi}\mathrm{Im}[G_{f/b}(i\omega_n = \omega + i0^+)] = -\frac{1}{\pi}\mathrm{Im}[G^R_{f/b}(\omega)] \tag{D.7}$$

We can similarly define the retarded self energies as $\Sigma^R_{f/b}(\omega) = \Sigma_{f/b}(i\omega_n = \omega + i0^+)$, leading to the following real frequency expressions for the saddle point equations:

$$\rho_{f/b}(\omega) = -\frac{1}{\pi}\frac{\Sigma''^R_{f/b}(\omega)}{(\omega - \Sigma'^R_{f/b}(\omega))^2 + \Sigma''^R_{f/b}(\omega)^2} \tag{D.8}$$

Where we define the imaginary part of the retarded self energy for bosons as: $\Sigma''^R_b(\omega)$as follows:

$$\Sigma''^R_b(\omega) = \Sigma^1_b(\omega) + \Sigma^2_b(\omega) \tag{D.9}$$

with:

$$\Sigma^1_b(\omega) = t^2 r\pi \int d\omega_1 \rho_f(\omega_1)\rho_f(\omega_1 - \omega)\left[n_f(\omega_1)n_f(\omega - \omega_1) - n_f(-\omega_1)n_f(\omega_1 - \omega)\right] \tag{D.10}$$

$$\Sigma^2_b(\omega) = t^2\pi \int d\omega_1 d\omega_2 \rho_f(\omega_1)\rho_b(\omega_2)\rho_f(\omega_1 + \omega_2 - \omega) \tag{D.11}$$

$$\times \left[n_f(\omega_1)n_b(\omega_2)n_f(\omega - \omega_1 - \omega_2) + n_f(-\omega_1)n_b(-\omega_2)n_f(\omega_1 + \omega_2 - \omega)\right] \tag{D.12}$$

We also define the imaginary part of the retarded self energy for fermions as $\Sigma_f^{''R}(\omega)$ as follows:

$$\Sigma_f^{''R}(\omega) = \Sigma_f^1(\omega) + \Sigma_f^2(\omega) + \Sigma_f^3(\omega) + \Sigma_f^4(\omega) \tag{D.13}$$

$$\Sigma_f^1(\omega) = -J^2 \int d\omega_1 d\omega_2 \rho_f(\omega_1)\rho_f(\omega_2)\rho_f(\omega_1+\omega_2-\omega)$$

$$\times \left[n_f(\omega_1)n_f(\omega_2)n_f(\omega-\omega_1-\omega_2) + n_f(-\omega_1)n_f(-\omega_2)n_f(\omega_1+\omega_2-\omega)\right] \tag{D.14}$$

$$\Sigma_f^2(\omega) = -t^2 r^2 k\pi \rho_f(\omega) \tag{D.15}$$

$$\Sigma_f^3(\omega) = kt^2 r\pi \int d\omega_1 \rho_f(\omega_1) \left[\rho_b(\omega-\omega_1) - \rho_b(\omega_1-\omega)\right]$$

$$\times \left[n_b(\omega_1-\omega)n_f(-\omega_1) - n_b(\omega-\omega_1)n_f(\omega_1)\right] \tag{D.16}$$

$$\Sigma_f^4(\omega) = kt^2\pi \int d\omega_1 d\omega_2 \rho_f(\omega_1)\rho_b(\omega_2)\rho_b(\omega_1+\omega_2-\omega)$$

$$\times \left[n_f(\omega_1)n_b(\omega_2)n_b(\omega-\omega_1-\omega_2) + n_f(-\omega_1)n_b(-\omega_2)n_b(\omega_1+\omega_2-\omega)\right] \tag{D.17}$$

The constraints on the fermionic and bosonic fillings in real frequency can be rewritten as:

$$r + \int_{-\infty}^{\infty} d\omega \frac{\rho_b(\omega)}{e^{\beta\omega}-1} = p \qquad \int_{-\infty}^{\infty} d\omega \frac{\rho_f(\omega)}{1+e^{\beta\omega}} = \kappa - kp \tag{D.18}$$

The real parts of the bosonic and fermionic self energies are related to their imaginary self energies via the Kramers-Kronig relation. At zero temperature, the Fermi-Dirac and Bose-Einstein functions in the imaginary self energies are replaced by $\theta(-\omega)$ and $-\theta(-\omega)$ respectively. Then at zero temperature,

the saddle point equations become:

$$\Sigma_b''^R(\omega) = \Sigma_b^1(\omega) + \Sigma_b^2(\omega) \tag{D.19}$$

$$\Sigma_b^1(\omega) = \begin{cases} -t^2 r\pi \int_0^\omega d\omega_1 \rho_f(\omega_1)\rho_f(\omega_1 - \omega), & \text{for } \omega > 0 \\ t^2 r\pi \int_\omega^0 d\omega_1 \rho_f(\omega_1)\rho_f(\omega_1 - \omega), & \text{for } \omega < 0 \end{cases} \tag{D.20}$$

$$\Sigma_b^2(\omega) = \begin{cases} -t^2\pi \int_0^{\omega_1+\omega_2<\omega} d\omega_1 d\omega_2 \rho_f(\omega_1)\rho_b(\omega_2)\rho_f(\omega_1+\omega_2-\omega), & \text{for } \omega > 0 \\ -t^2\pi \int_{\omega_1+\omega_2>\omega}^0 d\omega_1 d\omega_2 \rho_f(\omega_1)\rho_b(\omega_2)\rho_f(\omega_1+\omega_2-\omega), & \text{for } \omega < 0 \end{cases} \tag{D.21}$$

$$\Sigma_f''^R(\omega) = \Sigma_f^1(\omega) + \Sigma_f^2(\omega) + \Sigma_f^3(\omega) + \Sigma_f^4(\omega) \tag{D.22}$$

$$\Sigma_f^1(\omega) = \begin{cases} -J^2\pi \int_0^{\omega_1+\omega_2<\omega} d\omega_1 d\omega_2 \rho_f(\omega_1)\rho_f(\omega_2)\rho_f(\omega_1+\omega_2-\omega), & \text{for } \omega > 0 \\ -J^2\pi \int_{\omega_1+\omega_2>\omega}^0 d\omega_1 d\omega_2 \rho_f(\omega_1)\rho_f(\omega_2)\rho_f(\omega_1+\omega_2-\omega), & \text{for } \omega < 0 \end{cases} \tag{D.23}$$

$$\Sigma_f^2(\omega) = -t^2 r^2 k\pi \rho_f(\omega) \tag{D.24}$$

$$\Sigma_f^3(\omega) = \begin{cases} -kt^2 r\pi \int_0^\omega d\omega_1 \rho_f(\omega_1)[\rho_b(\omega-\omega_1) - \rho_b(\omega_1-\omega)], & \text{for } \omega > 0 \\ kt^2 r\pi \int_\omega^0 d\omega_1 \rho_f(\omega_1)[\rho_b(\omega-\omega_1) - \rho_b(\omega_1-\omega)], & \text{for } \omega < 0 \end{cases} \tag{D.25}$$

$$\Sigma_f^4(\omega) = \begin{cases} kt^2\pi \int_0^{\omega_1+\omega_2<\omega} d\omega_1 d\omega_2 \rho_f(\omega_1)\rho_b(\omega_2)\rho_b(\omega_1+\omega_2-\omega), & \text{for } \omega > 0 \\ kt^2\pi \int_{\omega_1+\omega_2>\omega}^0 d\omega_1 d\omega_2 \rho_f(\omega_1)\rho_b(\omega_2)\rho_b(\omega_1+\omega_2-\omega), & \text{for } \omega < 0 \end{cases} \tag{D.26}$$

Subject to the filling constraints:

$$r - \int_{-\infty}^0 d\omega \rho_b(\omega) = p \qquad \int_{-\infty}^0 d\omega \rho_f(\omega) = \kappa - kp \tag{D.27}$$

D.1.2 Absence of a Fermi-liquid solution

In the above saddle point equations, the low frequency structure for $r > 0$ implies $\overline{G}_b(i\omega_n = 0) \sim 1/|\omega|$. Such low frequency behavior leads to a logarithmically diverging boson density and r, meaning that we must have $r = 0$ at $T = 0$. We then set $r = 0$ and begin looking for critical solutions to the above equations at $T = 0$ of the following form:

$$G_a(i\omega_n) = -iC_a \begin{pmatrix} e^{-i\theta_a} \\ -e^{i\theta_a} \end{pmatrix} \frac{1}{\omega^{1-2\Delta_a}} \tag{D.28}$$

and corresponding low frequency form for the spectral density:

$$\rho_a(\omega) = \frac{C_a}{\pi} \begin{pmatrix} \sin\left(\pi\Delta_a + \theta_{f/b}\right) \\ \sin(\pi\Delta_a - \theta_a) \end{pmatrix} \frac{1}{\omega^{1-2\Delta_a}} \tag{D.29}$$

where $a = f/b$ and with the additional constraint $\Delta_f + \Delta_b = \frac{1}{2}$. To resolve the low frequency divergences in the spectral densities in our numerical integration, we absorb the the low frequency ω dependence of the spectral functions into the numerical integration measure such that the numerical integrals do not contain any divergent pieces. We use 4×10^4 frequency points on our real ω axis and a frequency spacing which is smaller at small ω and larger at large ω.

D.1.3 Fixing the low energy solution

In this section we will detail how we fix the coefficients C_f, C_b, Δ_f, Δ_b, θ_f, and θ_b in Eq. D.29. The filling constraints for bosons and fermions will be imposed by the initial conditions we select for θ_f, θ_b, Δ_f, and Δ_b. In constraining these coefficients in the low energy solution, we first solve for θ_f and θ_b as a function of Δ_b at fixed doping. We do this for a given Δ_b and p by separately solving the two

Luttinger constraints for fermions and bosons to obtain corresponding values for θ_f and θ_b,

$$\begin{aligned}\frac{\theta_f}{\pi}+\left(\frac{1}{2}-\Delta_f\right)\frac{\sin\left(2\theta_f\right)}{\sin\left(2\pi\Delta_f\right)}&=\frac{1}{2}-\kappa+kp\,,\\ \frac{\theta_b}{\pi}+\left(\frac{1}{2}-\Delta_b\right)\frac{\sin(2\theta_b)}{\sin(2\pi\Delta_b)}&=\frac{1}{2}+p\,.\end{aligned}\tag{D.30}$$

For a fixed doping, we can then use θ_f and θ_b calculated as a function of Δ_b to compute the coefficient k as a function of Δ_b using its expression in terms of the self-consistency conditions,

$$k=-\frac{\Gamma(2-2\Delta_f)\Gamma(2\Delta_f)\sin\left(\pi\Delta_f+\theta_f\right)\sin\left(\pi\Delta_f-\theta_f\right)}{\Gamma(2-2\Delta_b)\Gamma(2\Delta_b)\sin(\pi\Delta_b+\theta_b)\sin(\pi\Delta_b-\theta_b)}\,,\tag{D.31}$$

We then fix Δ_b by selecting the value of Δ_b at which k attains its physical value $k=\frac{1}{2}$. We show for 3 different dopings the k we compute in this way as a function of Δ_b in Fig. D.2 and the values of θ_f, θ_b, Δ_f, Δ_b we obtain by choosing $k=\frac{1}{2}$ in Fig. D.3. We then have fixed every free parameter in Eq. D.29 except for C_b and C_f. C_f and C_b are parameters which are unconstrained in the original low frequency ansatz and generally have values which depend on the full ω dependent solutions $\rho_f(\omega)$ and $\rho_b(\omega)$. We solve for these constants at each step of our iterative procedure by taking the Hilbert transform of the spectral densities to obtain the bosonic and fermions greens functions from which we may extract the constant C_f at low frequency and a small temperature $T=10^{-5}$. C_b can then be obtained from C_f via the self consistency equations and these extracted values for C_f and C_b are then plugged in to the next step of numerical iteration. Their values are shown in Fig. D.3. Results for the boson and fermion spectral densities computed in this manner are shown in Fig. D.1.

We also compute the physical observables, the spin and electron spectral functions, $\rho_s(\omega)=\frac{1}{\pi}\chi''(\omega)$ and $\rho_c(\omega)$. In the limit $r=0$,these observables have the following expressions on the real frequency

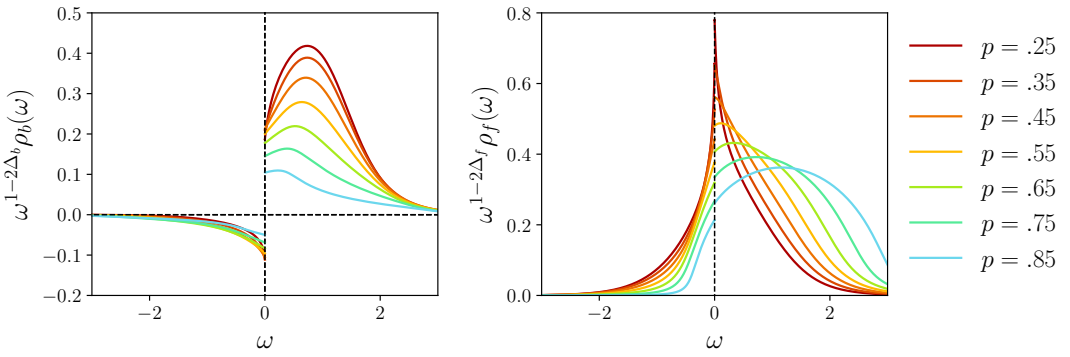

Figure D.1: Plot of the boson spectral density (left) and fermion spectral density (right) obtained at $t = J = 1$. Both the boson and fermion spectral densities show deviations from the conformal power law behavior for small frequencies.

axis:

$$\rho_c(\omega) = \int_{-\infty}^{\infty} \rho_f(\omega_1)\rho_b(\omega_1 - \omega)\left[n_f(\omega_1) + n_b(\omega_1 - \omega)\right] , \tag{D.32}$$

$$\chi''(\omega) = \pi\rho_s(\omega) = \pi \int_{-\infty}^{\infty} \rho_f(\omega_1)\rho_f(\omega_1 - \omega)\left[n_f(\omega_1 - \omega) - n_f(\omega_1)\right] . \tag{D.33}$$

Results for these spectral functions appeared in Fig. 5.3. The electron spectral density satisfies the sum rule,

$$\int_{-\infty}^{\infty} d\omega\, \rho_c(\omega) = \frac{1+p}{2} . \tag{D.34}$$

Note that for canonical fermions this sum rule results in unity. However, here the electron operator is being fractionalized and the Hilbert-space has only three states. Hence the sum rule is modified. There is a also a simple way to understand this modification. The electron spectral density sum is equal to $\langle\{c_\alpha, c_\alpha^\dagger\}\rangle$. For canonical fermions, $\{c_\alpha, c_\alpha^\dagger\} = 1$, but in our case $\{c_\alpha, c_\alpha^\dagger\} = b^\dagger b + f_\alpha^\dagger f_\alpha$, which gives the modified sum rule in Eq. D.34. The sum rule for the spin spectral density is not easy to obtain at

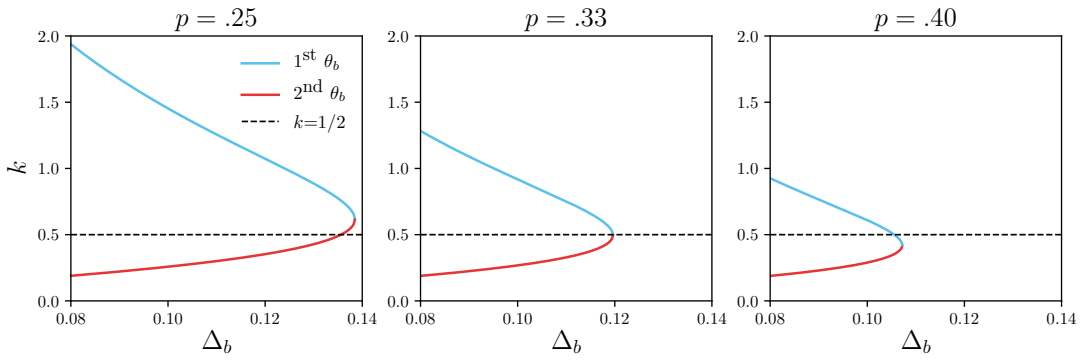

Figure D.2: Plot of the value of k as computed from the zero frequency self consistency conditions for three different dopings. The values of θ_f and θ_b are computed from the Luttinger relations at fixed Δ_b (and fixed $\Delta_f = \frac{1}{2} - \Delta_b$) and are then used to compute k via the self consistency condition. We find in general there are two possible values of θ_b which are compatible with the Luttinger constraints, leading to the two distinct branches of the function for k shown in red and blue above. The correct value of Δ_b is selected by choosing the value of Δ_b where $k = \frac{1}{2}$. The physical value $k = \frac{1}{2}$ is denoted with a dashed black line. As is shown in the above plot, for $p > \frac{1}{3}$, this leads to selecting the first (smallest) value of θ_b and for $p < \frac{1}{3}$ leads to selecting the second (largest) value of θ_b, with the two values of θ_b coinciding at $p = \frac{1}{3}$ and $k = \frac{1}{2}$.

finite temperature. But at zero temperature we have,

$$\int_0^\infty \rho_s(\omega) = \frac{1-p^2}{4}\,. \tag{D.35}$$

D.1.4 Varying J

In this section, we will discuss the behavior of the spectral functions as J is varied between $0 \leq J \leq t$. For the case where $0 < \Delta_b < \frac{1}{4}$ and $\frac{1}{4} < \Delta_f < \frac{1}{2}$, the Luttinger constraints and saddle point equations exactly at zero frequency have no dependence on J, meaning the values of Δ_b, Δ_f, θ_b, and θ_f we solve for do not depend on the value of J (though C_f and C_b which depend on the full ω dependent forms of $\rho_f(\omega)$ and $\rho_b(\omega)$ do depend on J). We then follow the same procedure as for $t = J = 1$ and solve the saddle point equations for $0 \geq J \geq t = 1$. We find mostly qualitative changes for high doping, however we find a curious feature in the electron spectral density at low doping as shown

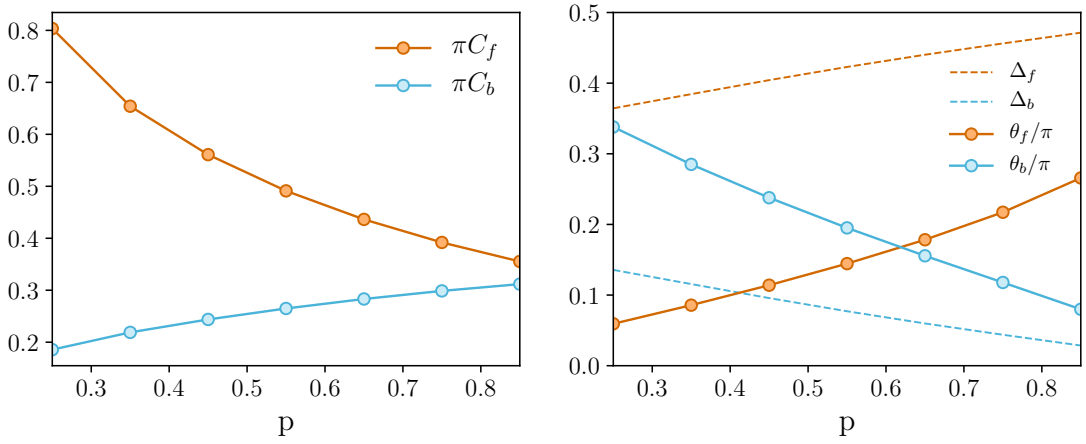

Figure D.3: In the left plot, we show the converged values of C_f and C_b as a function of doping for $t = J = 1$. In the right plot, we show the doping dependence of Δ_b, Δ_f, θ_b, and θ_f, obtained by simultaneously solving the two Luttinger relations and the two constraints, as discussed in the text.

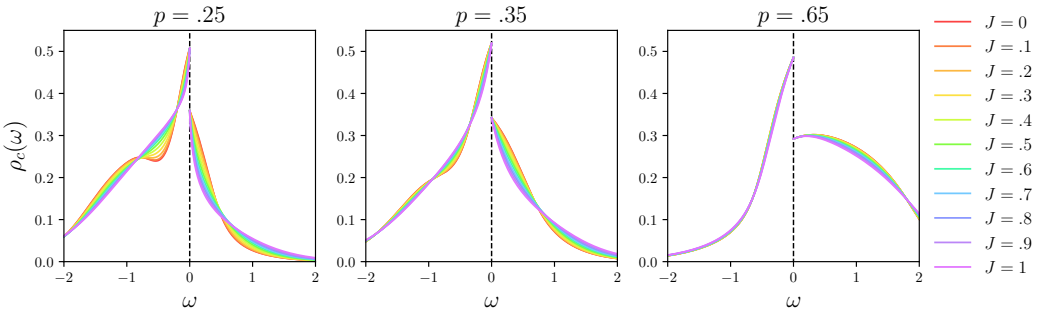

Figure D.4: Plot showing how the electron spectral density varies with J for three distinct dopings and $t = 1$.

in Fig. D.4. We find that for small enough doping around $p < .3$ that the electron spectral density acquires a second local maximum or peak at finite $\omega < 0$ for small J which does not appear for larger values of J or larger values of doping p. We find that this peak originates from a similar peak in the bosonic spectral density that occurs when $\omega = \Sigma_b'(\omega)$ and $\rho_b(\omega) = -\frac{1}{\pi\Sigma_b''(\omega)}$. While we do not have an analytic reason for this behavior of the boson and electron spectral functions, we reason that this feature originates from strong corrections to the conformal solutions for ρ_b and ρ_c away from $\omega = 0$.

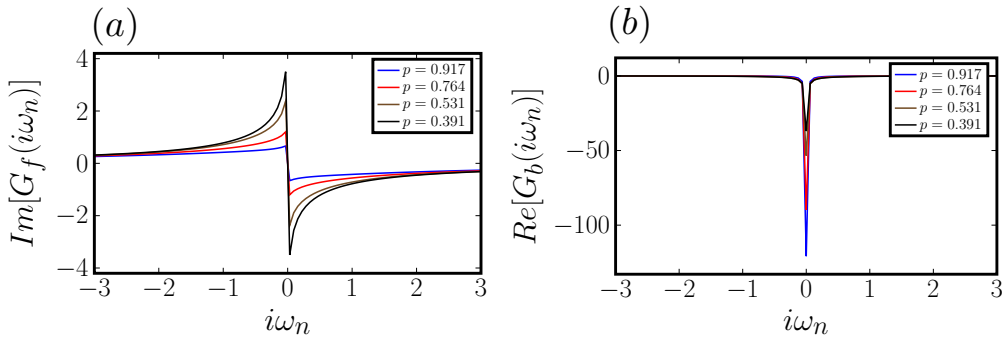

Figure D.5: (a) Imaginary part of the fermionic spinon Green's function on the Matsubara-frequency axis for different dopings at $T = 0.01$. (b) Real part of the bosonic holon Green's function on the Matsubara-frequency axis for different dopings at $T = 0.01$. We have used $t = J = 1$.

D.2 Additional results from imaginary-frequency calculation

In this appendix we present additional results obtained from the imaginary-frequency analysis. In particular, we will discuss an independent way to extract the exponent Δ_f and numerical analytic continuation to real frequencies.

D.2.1 Holon and spinon Green's function in the critical metal phase

The strategy to solve the saddle-point equations, Eqs. 5.12-5.17, is straightforward. We first fix $\bar{r}$ and solve Eqs. 5.12-5.15 until we find a converged solution. Then we check if these solutions give the same doping value using Eqs. 5.16 and 5.17. If it does then we have our final solution for a given doping. Else, we go back to step one and change $\bar{r}$, and repeat the next steps until we find the final solution. In this fashion, we obtain the holon and spinon Green's functions on the imaginary frequency axis, which are shown in Fig. D.5. Recall that in the critical metal phase, holon is a bosonic and spinons are fermionic operators. We have checked that these satisfy the respective sum rules: $G_a(0^+) - \zeta_a G_a(\beta^-) = -1 = -\int_{-\infty}^{\infty} \rho_a(\omega) d\omega$, where $\zeta_a = \pm 1$ for $a = b, f$ respectively. Once we have the holon and spinon Green's functions it is then straightforward to obtain the electron Green's

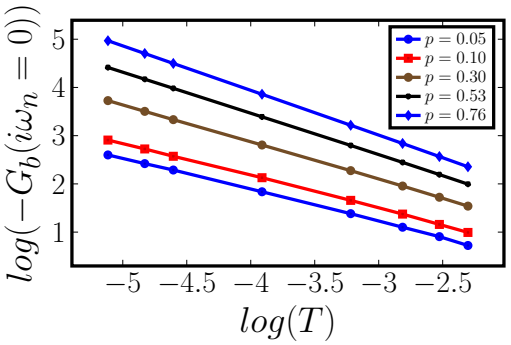

Figure D.6: Log-log plot of the relation in Eq. 5.25 for different dopings. We find that the data fits a linear curve to a good accuracy. Thus we can use the value of slopes of these curves to determine Δ_b, as discussed in Section 5.3.2.

function and the spin correlator.

As discussed in the main text, using the temperature dependence of the holon Green's function at $i\omega = 0$ we can estimate the exponent, Δ_b. In Fig. D.6 we show the data points used to estimated Δ_b at different dopings.

D.2.2 Spin-correlator in the critical metal phase

Let us consider the spin correlator,

$$\frac{\langle \vec{S}(\tau) \cdot \vec{S}(0) \rangle}{2} = Q(\tau) = G_f(\tau) G_f(-\tau) \,. \tag{D.36}$$

In the critical metal phase, the solution has a conformal form in the low-frequency or large-time limit. At a finite temperature, in terms of the imaginary time this limit corresponds to $\tau = \beta/2$, where we expect the conformal form,

$$\frac{Q(\tau)}{Q(\beta/2)} \sim \frac{1}{[\sin(\pi\tau/\beta)]^{4\Delta_f}} \,. \tag{D.37}$$

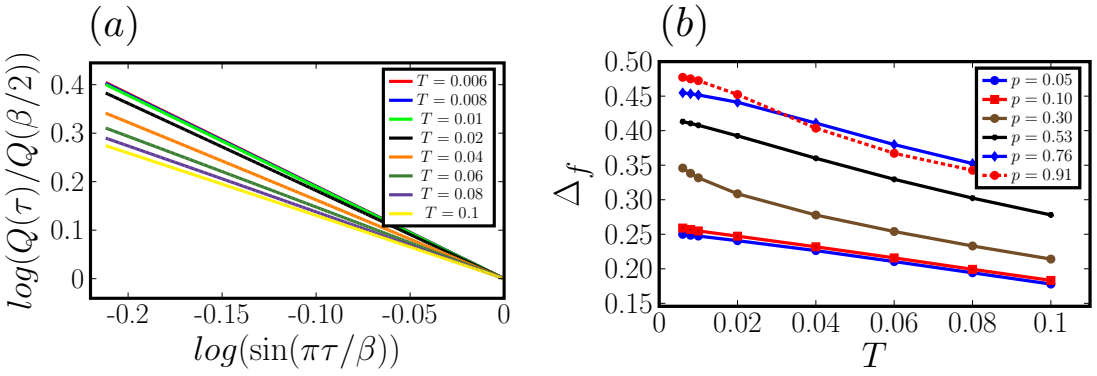

Figure D.7: (a) Log-log plot of Eq. D.37 near $\tau = \beta/2$ for different temperatures at $p = 0.91$. The data considered for the plot is in the range $1/2 \leq \tau/\beta \lesssim 0.7$. (b) Plot of Δ_f as a function of temperature T for different dopings. Note that $4\Delta_f$ is the exponent of the spin correlation.

Thus if we make a log-log plot then we can extract Δ_f from the slope of the resulting linear curve. In Fig. D.7*A* we show such a plot for several different temperatures at a fixed doping, $p = 0.91$. These curves fit to a linear curve. In Fig. D.7 (b) we plot the extracted value of Δ_f as a function of temperature for different dopings. Remarkably, the extrapolated zero-temperature values of Δ_f in the overdoping region for $p \gtrsim 0.3$ are in agreement with those found analytically earlier. At lower dopings we find some disagreement with the analytic result.

As discussed in Section 5.3.3, using the local spin susceptibility, $\chi(i\omega = 0)$, we can estimate the critical doping below which the spin-glass is stabilized. We therefore plot the coefficient of quadratic term in Eq. 5.26 as a function of doping for different temperatures in Fig. D.8. This gives the critical doping as a function of temperature, which is used to plot the phase diagram in Fig. 5.1*B*.

D.2.3 Numerical analytic continuation

We also perform numerical analytic continuation to real frequency. In general, performing analytic continuation is an ill-posed problem if the function on the imaginary axis is known only at a finite number of points. There are several techniques to do analytic continuation. But for simplicity we

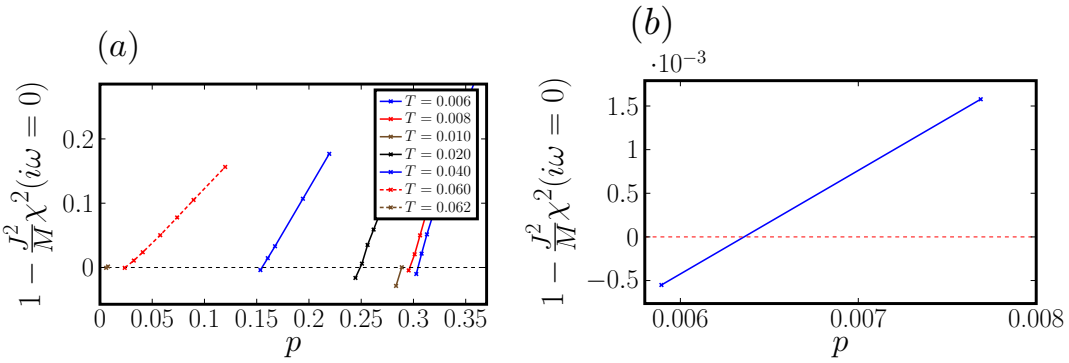

Figure D.8: (a) Coefficient of quadratic term in Eq. 5.26 as a function of doping for different temperature. As explained in the text, a sign change of this coefficient gives the critical doping. (b) Enlarged plot for T=0.062.

use the Pade approximation method. This technique parametrizes the function on imaginary axis as a ratio of two polynomials or by terminating a continued fraction. There are several ways for implementing Pade approximation. We adopt the simple strategy outlined in Ref.[179] of evaluating the coefficients of the two polynomials recursively, which is based on Thiele's reciprocal difference method. Details of the algorithm can be found in the Appendix of Ref.[179]. Briefly, we first solve the saddle-point equations on the imaginary-frequency axis to obtain the required Green's function, say $F(i\omega)$, at non-negative Matsubara frequencies. The number of Matsubara frequencies used in our calculation is 10^5. Then we evaluate the required polynomials, $A_n(z)$ and $B_n(z)$, to approximate the imaginary-frequency function, $F(z) = A_n(z)/B_n(z)$. The accuracy of these polynomials depends on the number of Pade points, n, and in our calculation we find that $n = 200$ points are sufficient to obtain accurate results. We have checked our results by increasing or decreasing n and it does not result in any significant improvement. The resulting ratio of polynomials then corresponds to the retarded Green's function on real-frequency axis, once we identify $z = \omega + i\eta$. Using the imaginary part of this function we then readily obtain the spectral densities.

In the critical non-Fermi-liquid metal phase, we find the electron and spin spectral densities using this approach. In Fig. D.9, we plot the results of analytic continuation at $T = 0.006$ alongside the

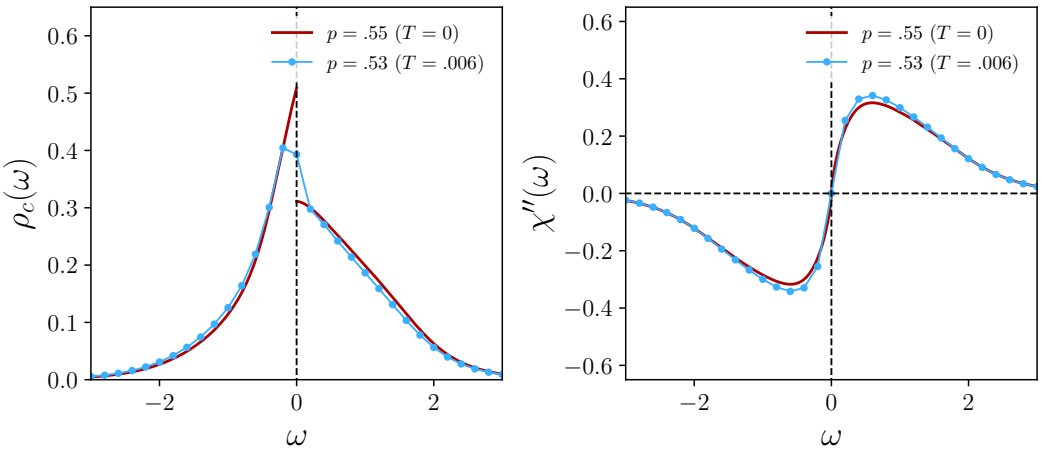

Figure D.9: Comparison of electron and spin spectral densities obtained for similar dopings from the $T = 0$ real-frequency numerics and analytic continuation of the imaginary frequency solution to real frequency at $T = 0.006$.

results from real-frequency analysis at zero temperature. The agreement is remarkably good. We have also checked that the electron and spin spectral densities obtained via numerical analytic continuation satisfy to a good accuracy the appropriate sum rules in Eqs. D.34 and D.35. In this phase, as shown earlier, the spinon and holon spectral densities have a $\omega^{1-2\Delta_a}$ divergence. In principle, we can adopt our method if we scale this divergence, as done in the real-frequency analysis. However, we do not attempt to do it here. Anyways, these quantities are not gauge-invariant observables.

In the spin-glass phase the holon and fermion spectral densities do not have divergences. So in this case we calculate the holon and spinon spectral densities in addition to the spin and electron spectral densities. In Figs. D.10 and D.11 we plot these spectral densities at $p = 0.027$ and $p = 0.2$ respectively, obtained by analytic continuation of imaginary-frequency results at $T = 0.01$. Alongside it we also plot the results obtained at $T = 0$ for a nearby doping value. The agreement is remarkable. The spectral densities obtained via numerical analytic continuation satisfy the respective sum rules listed in Eqs. D.80, D.83, and D.84.

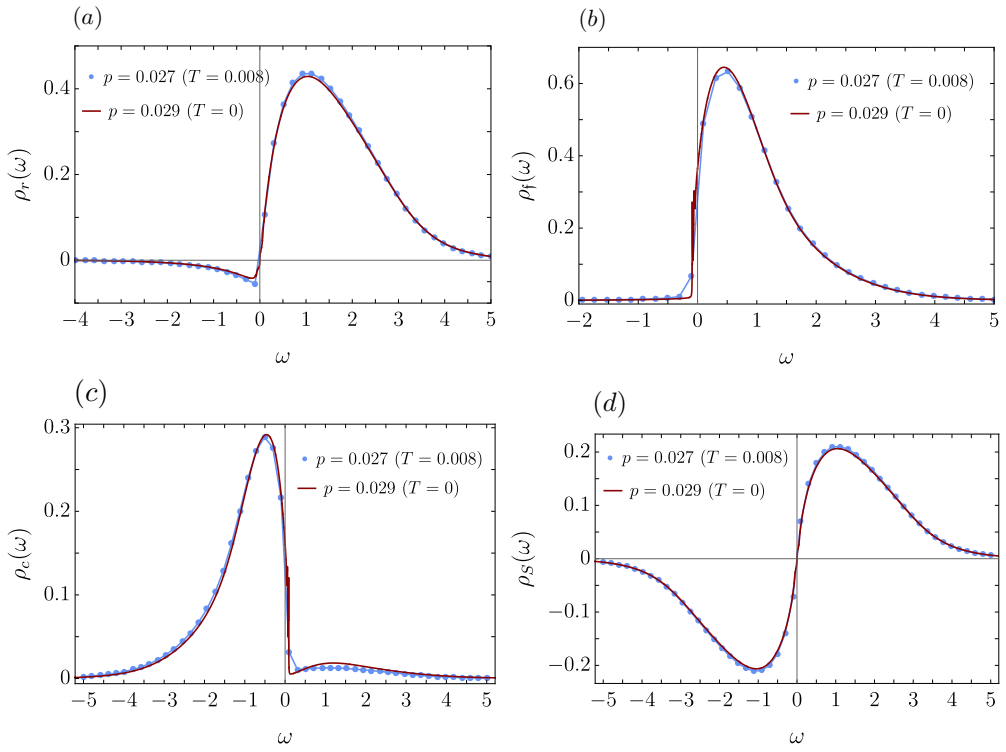

Figure D.10: Comparison of spectral densities in the spin glass phase at small doping obtained via analytic continuation at $T = 0.008$ for $p = 0.027$ and via real frequency analysis at zero temperature for $p = 0.029$. From (a) to (d), we plot the holon, spinon, electron, and spin spectral densities respectively.

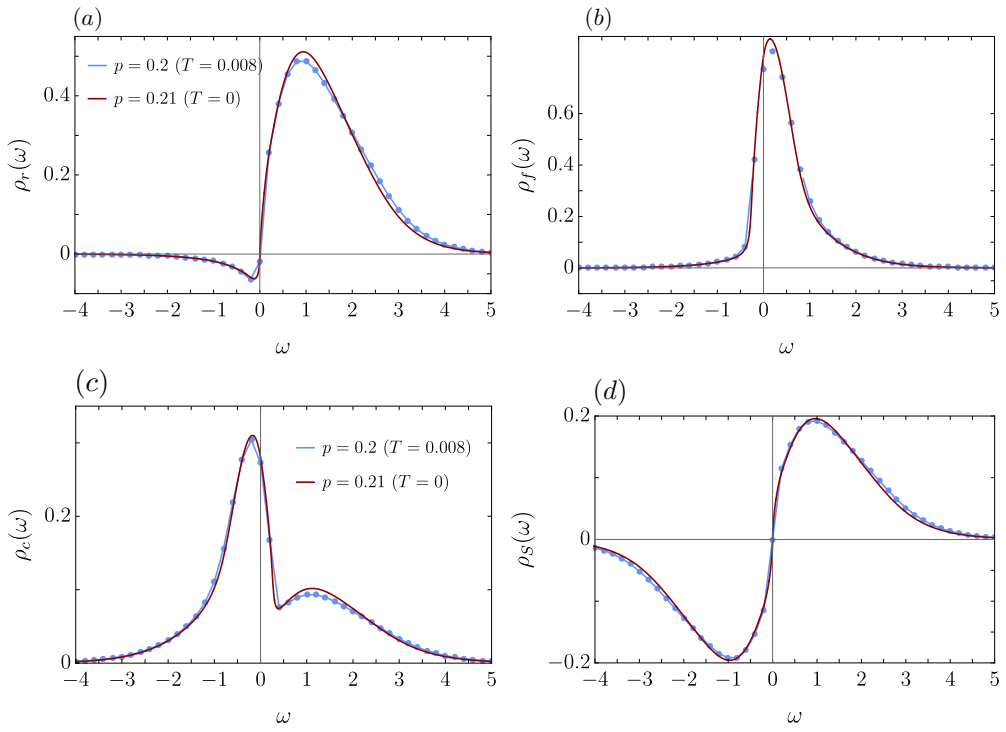

Figure D.11: Comparison of spectral densities in the spin glass phase at small doping obtained via analytic continuation at $T = 0.008$ for $p = 0.2$ and via real frequency analysis at zero temperature for $p = 0.21$. From (a) to (d), we plot the holon, spinon, electron, and spin spectral densities respectively.

D.3 Insulating SY model with bosonic spinons

This appendix will recall the solution of an insulating spin glass obtained using bosonic spinons in Ref.[63]. We consider the spin model

$$H = \frac{1}{\sqrt{NM}} \sum_{i<j=1}^{N} \sum_{\alpha,\beta=1}^{M} J_{ij} \mathcal{S}_{\beta}^{\alpha}(i) \mathcal{S}_{\alpha}^{\beta}(j) \tag{D.38}$$

where $\mathcal{S}_{\beta}^{\alpha}(i) = [\mathcal{S}_{\alpha}^{\beta}(i)]^{\dagger}$ are generators of SU(M) on each site i. Each site contains states corresponding to the symmetric product of κM fundamentals, and these are realized by bosonic spinons with

$$\mathcal{S}_{\beta}^{\alpha}(i) = s_{\beta}^{\dagger}(i) s^{\alpha}(i) - \kappa \delta_{\beta}^{\alpha}, \quad \sum_{\alpha} s_{\alpha}^{\dagger}(i) s^{\alpha}(i) = \kappa M \tag{D.39}$$

on each site i. We have made the spin operators traceless. The exchange constants J_{ij} are mutually uncorrelated and selected with probability $P(J_{ij}) \sim \exp\left(-J_{ij}^2/(2J^2)\right)$.

We introduce replicas $a = 1 \ldots n$, and average over J_{ij} to obtain the averaged, replicated partition function

$$\begin{aligned}
\overline{\mathcal{Z}^n} &= \int \mathcal{D} s_a^{\alpha}(i,\tau) \mathcal{D} \lambda_a(i,\tau) \exp\left[-S_B - S_J\right] \\
S_B &= \sum_i \int d\tau \left[s_{a\alpha}^{\dagger}(i) \partial_{\tau} s_a^{\alpha}(i) + i \lambda_a(i) \left(s_{a\alpha}^{\dagger}(i) s_a^{\alpha}(i) - \kappa M \right) \right] \\
S_J &= -\frac{J^2}{4NM} \int d\tau d\tau' \left[\sum_i \mathcal{S}_{a\beta}^{\alpha}(i,\tau) \mathcal{S}_{b\delta}^{\gamma}(i,\tau') \right] \left[\sum_j \mathcal{S}_{a\alpha}^{\beta}(j,\tau) \mathcal{S}_{b\gamma}^{\delta}(j,\tau') \right]
\end{aligned} \tag{D.40}$$

We can now decouple S_J with a Hubbard-Stratonovich field $Q_{ab,\beta\delta}^{\alpha\gamma}(\tau,\tau')$ and take the large N limit. Then the problem reduced to finding saddle points of the action

$$\frac{\mathcal{S}[Q]}{N} = \frac{J^2}{4M} \int d\tau d\tau' |Q_{ab,\beta\delta}^{\alpha\gamma}(\tau,\tau')|^2 - \ln \mathcal{Z}_f[Q] \tag{D.41}$$

where $\mathcal{Z}_f[Q]$ is the single site partition function

$$\begin{aligned}
\mathcal{Z}_b[Q] &= \int \mathcal{D}b_a^\alpha(\tau)\mathcal{D}\lambda_a(\tau)\exp\left[-S_B - S_b\right] && \text{(D.42)}\\
S_B &= \int d\tau\left[s_{a\alpha}^\dagger\partial_\tau s_a^\alpha + i\lambda_a\left(s_{a\alpha}^\dagger s_a^\alpha - \kappa M\right)\right] && \text{(D.43)}\\
S_b &= -\frac{J^2}{2M}\int d\tau d\tau' Q_{ab,\beta\delta}^{\alpha\gamma}(\tau,\tau')\left[s_{a\alpha}^\dagger(\tau)s_a^\beta(\tau) - \kappa\delta_\alpha^\beta\right]\left[s_{b\gamma}^\dagger(\tau')s_b^\delta(\tau') - \kappa\delta_\gamma^\delta\right] && \text{(D.44)}
\end{aligned}$$

Note that we have taken the $N\to\infty$ limit, and there is no remaining path integral over Q. We simply have to find the saddle points of $\mathcal{S}[Q]$ in Eq. D.41. Let us assume that the saddle point does not break spin rotation symmetry: this is true in both the spin glass, and spin liquid phases. So we take the ansatz

$$Q_{ab,\beta\delta}^{\alpha\gamma}(\tau,\tau') = \delta_\delta^\alpha\delta_\beta^\gamma Q_{ab}(\tau-\tau') \tag{D.45}$$

where $Q_{ab}(\tau)$ is a real function. Also, because there is no path integral over Q, we can also assume from now on that $Q_{ab}(\tau)$ is independent of τ for $a\neq b$. Then Eq. D.41 is replaced by

$$\frac{\mathcal{S}[Q]}{N} = \frac{J^2M}{4}\int d\tau d\tau'[Q_{ab}(\tau-\tau')]^2 - \ln\mathcal{Z}_b[Q] \tag{D.46}$$

while Eq. D.44 is replaced by

$$S_b = -\frac{J^2}{2M}\int d\tau d\tau' Q_{ab}(\tau-\tau')\left[s_{a\alpha}^\dagger(\tau)s_a^\beta(\tau)s_{b\beta}^\dagger(\tau')s_b^\alpha(\tau') - \kappa^2 M\right] \tag{D.47}$$

The saddle point equations for Q from Eqs. D.46 and D.47 are

$$Q_{ab}(\tau-\tau') = \frac{1}{M^2}\left\langle s_{a\alpha}^\dagger(\tau)s_a^\beta(\tau)s_{b\beta}^\dagger(\tau')s_b^\alpha(\tau')\right\rangle_{\mathcal{Z}_b[Q]} - \frac{\kappa^2}{M} \tag{D.48}$$

Now we need to evaluate $\mathcal{Z}_f[Q]$. This is conveniently done using G-Σ theory, where we define

$$G_{ab}(\tau,\tau') = -\frac{1}{M}\sum_{\alpha} s_a^{\alpha}(\tau)s_{b\alpha}^{\dagger}(\tau') \tag{D.49}$$

Then we can write

$$\begin{aligned}
\mathcal{Z}_b[Q] &= \int \mathcal{D}G_{ab}(\tau,\tau')\Sigma_{ab}(\tau,\tau')\mathcal{D}\lambda_a(\tau)\exp\left[-MI[Q] - \frac{\kappa^2 J^2}{2}\int d\tau d\tau' \sum_{a,b} Q_{ab}(\tau-\tau')\right] \\
I[Q] &= \ln\det\left[-\delta'(\tau-\tau')\delta_{ab} - i\lambda_a(\tau)\delta(\tau-\tau')\delta_{ab} - \Sigma_{ab}(\tau,\tau')\right] - i\kappa\int d\tau\lambda_a(\tau) \\
&\quad + \int d\tau d\tau' \left[\Sigma_{ab}(\tau,\tau')G_{ba}(\tau',\tau) - \frac{J^2}{2}Q_{ab}(\tau-\tau')G_{ab}(\tau,\tau')G_{ba}(\tau',\tau)\right]
\end{aligned} \tag{D.50}$$

Unlike the fermionic case, it is sufficient to work at $M = \infty$ to obtain the spin glass phase, and there is no need to consider $1/M$ corrections. The large M saddle-point equations of Eq. D.50 are

$$\Sigma_{ab}(\tau) = J^2 Q_{ab}(\tau)G_{ab}(\tau) \tag{D.51}$$

$$G_{ab}(i\omega) = \left[(i\omega+\overline{\lambda})\delta_{ab} - \Sigma_{ab}(i\omega)\right]^{-1} \tag{D.52}$$

where $i\lambda = -\overline{\lambda}$ at the saddle-point. The saddle-point equation Eq. D.48 now becomes

$$Q_{ab}(\tau) = G_{ab}(\tau)G_{ba}(-\tau) \tag{D.53}$$

Then Eqs. D.51, D.52 and D.53 combine to yield the bosonic SY equations[156] for replica diagonal case. We also have to include the saddle-point equation for $\overline{\lambda}$ which is

$$T\sum_{\omega_n} G_{aa}(i\omega_n) = -\kappa \tag{D.54}$$

D.3.1 Spin glass

The spin glass phase was described in Ref.[63]. In this phase, we must include replica off-diagonal components for $G_{ab}(\omega_n = 0)$, while other ω_n remain replica diagonal. We characterize the replica off-diagonal components of $G_{ab}(\tau)$ by a $n \times n$ matrix g_{ab} which is independent of τ. In other words, in frequency space

$$G_{ab}(i\omega_n) = -\beta g_{ab}\delta_{\omega_n,0}\,, \quad a \neq b \tag{D.55}$$

In Parisi's theory of the infinite-range spin glass, the $n \to 0$ limit of the matrix g_{ab} is defined by a function $g(u)$, with $u \in [0,1]$. We make the one-step replica symmetry breaking ansatz

$$\begin{aligned} g(u) &= g\,, \quad \text{for } x < u < 1 \\ &= 0\,, \quad \text{for } u < x. \end{aligned} \tag{D.56}$$

i.e. it is a step function at the 'breakpoint' $u = x$. The matrix g_{ab} is therefore fully defined by the values of g and x. For the replica diagonal components, it is convenient to define

$$G_{aa}(i\omega_n) = -\beta g\delta_{\omega_n,0} + G_r(\omega_n) \tag{D.57}$$

At the moment, there is no prescribed frequency dependence for G_r, and so this ansatz can be made without loss of generality. However, as we will see below, this ansatz is convenient because it leads to solutions in which G_r is a smooth function of frequency.

Similarly, for the self-energy, we have from Eqs. D.51 and D.53

$$\Sigma_{ab}(i\omega_n) = -\beta J^2 g_{ab}^3 \delta_{\omega_n,0}\,, \quad a \neq b\,, \tag{D.58}$$

and for the diagonal component we write

$$\Sigma_{aa}(i\omega_n) = -\beta J^2 g^3 \delta_{\omega_n,0} + \Sigma_r(\omega_n) \tag{D.59}$$

Now we need to insert the ansatz Eqs. (D.55), (D.56), (D.57), (D.58), (D.59) into Eqs. (D.51), (D.52), (D.53), (D.54) and obtain equations for the unknowns x, g, $G_r(\omega_n)$, $\Sigma_r(\omega_n)$ and $\overline{\lambda}$. To do this, we need an expression for the inverse of a matrix in replica space. To obtain this, we use the following results for the product of 2 matrices in replica space [125]. We consider the matrix A_{ab} whose off-diagonal elements are parameterized by the function $a(u)$, $u \in [0,1]$, and the diagonal element $A_{aa} = \tilde{a}$. Similarly, we have matrices B_{ab} and C_{ab}. Then if $C = AB$, we have

$$\begin{aligned} \tilde{c} &= \tilde{a}\tilde{b} - \langle ab \rangle \\ c(u) &= (\tilde{b} - \langle b \rangle)a(u) + (\tilde{a} - \langle a \rangle)b(u) - \int_0^u dv (a(u) - a(v))(b(u) - b(v)) \end{aligned} \tag{D.60}$$

where

$$\langle a \rangle = \int_0^1 du\, a(u) \tag{D.61}$$

So if $B = A^{-1}$ and $C = 1$, then $\tilde{c} = 1$ and $c(u) = 0$. Applying these results to the one-step replica symmetry breaking ansatz for $a(u)$ and $b(u)$, we obtain

$$\begin{aligned} b &= \frac{-a}{(a - \tilde{a})(a(1-x) - \tilde{a})} \\ \tilde{b} &= \frac{\tilde{a} + (x-2)a}{(a - \tilde{a})(a(1-x) - \tilde{a})} \end{aligned} \tag{D.62}$$

where $a(u)$ and $b(u)$ have the same breakpoint x.

Applying Eqs. D.62 to D.52 we obtain the equations

$$\begin{aligned} G_r(i\omega_n) &= \tfrac{1}{i\omega+\bar{\lambda}-\Sigma_r(i\omega_n)}\,, \quad \text{for all } \omega_n \\ [gJG_r(i\omega_n=0)]^2 &= 1+\beta J^2 g^3 x G_r(i\omega_n=0) \end{aligned} \tag{D.63}$$

Notice that same equation applies for $G_r(i\omega_n)$ for $\omega_n = 0$ and $\omega_n \neq 0$, and this was the rationale for ansatz in Eq. D.57.

It is useful to now introduce the dimensionless variable Θ, defined by

$$\Theta = -JgG_r(i\omega_n=0) \tag{D.64}$$

Using Eq. D.63, we see that Θ is related to x by

$$\beta x = \frac{1}{Jg^2}\left(\frac{1}{\Theta}-\Theta\right), \tag{D.65}$$

and so we eliminate x in favor of Θ. We also use the $\omega_n = 0$ equation in Eq. D.63 to express $\bar{\lambda}$ in terms of Θ and $\Sigma_r(i\omega_n = 0)$.

Now the saddle-point equations are expressed in terms of $G_r(i\omega_n)$, $\Sigma_r(i\omega_n)$, Θ, and g. The complete set of equations determining these parameters is

$$[G_r(i\omega_n)]^{-1} = i\omega_n - \frac{Jg}{\Theta} - [\Sigma_r(i\omega_n) - \Sigma_r(i\omega_n=0)] \tag{D.66}$$

$$\begin{aligned} \Sigma_r(\tau) &= J^2\Big([G_r(\tau)]^2 G_r(-\tau) - 2gG_r(\tau)G_r(-\tau) - g\,[G_r(\tau)]^2 \\ &\qquad + 2g^2 G_r(\tau) + g^2 G_r(-\tau)\Big) \end{aligned} \tag{D.67}$$

$$g - G_r(\tau = 0^-) = \kappa\,. \tag{D.68}$$

These equations leave the parameter Θ undetermined.

Following Appendix B.2 in Ref.[63], we determine the value of Θ by the requirement that G_r have a gapless spectrum. For a gapless spectrum, we expect the low frequency expansion for G_r for real ω

$$G_r(\omega + i\eta) = \frac{\Theta}{gJ} + (a + ib)\omega^\alpha \theta(\omega) + (a' + ib')|\omega|^\alpha \theta(-\omega) + \dots \tag{D.69}$$

where $\theta(\omega)$ is a step function, for some $\alpha > 0$, and with $b < 0$, $b' > 0$. Then from Eq. (D.67) we find that the leading singularity in Σ_r is given by the last 2 terms in Eq. (D.67)

$$\mathrm{Im}\,\Sigma_r(\omega + i\eta) = g^2 J^2 \left[(2b - b')\omega^\alpha \theta(\omega) + (2b' - b)|\omega|^\alpha \theta(-\omega)\right] \tag{D.70}$$

But from Eq. D.66 we have

$$\mathrm{Im}\,\Sigma_r(\omega + i\eta) = -\mathrm{Im}\left[G_r(\omega + i\eta)\right]^{-1} = \frac{g^2 J^2}{\Theta^2}\left[(b\,\omega^\alpha \theta(\omega) + b'\,|\omega|^\alpha \theta(-\omega)\right] \tag{D.71}$$

Comparing Eqs. D.70 and D.71 we have

$$\begin{aligned} (1/\Theta^2 - 2)b + b' &= 0 \\ b + (1/\Theta^2 - 2)b' &= 0 \end{aligned} \tag{D.72}$$

These equations are compatible only for $\Theta = 1, 1/\sqrt{3}$. The replica symmetric choice $\Theta = 1$ is excluded because it yields $b = b'$, which is not allowed by the positivity constraints on the spectral weight: b and b' need to have opposite signs. So the only choice is

$$\Theta = \frac{1}{\sqrt{3}}\,. \tag{D.73}$$

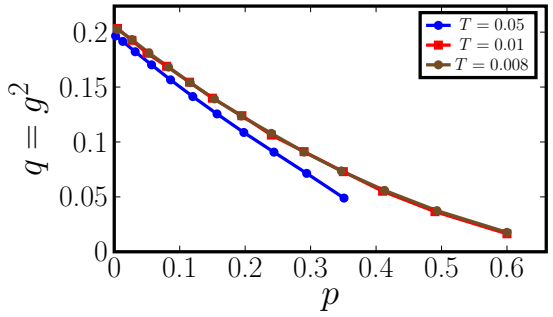

Figure D.12: Plot of spin-glass order parameter, $q = g^2$, as a function of doping at different temperatures.

D.4 Additional details for the metallic spin-glass phase

In this appendix we present details regarding the spectral densities in the metallic spin-glass phase. We show explicit form of the equations that are solved at zero temperature as well as details on spin and electron spectral densities at zero and finite temperatures.

D.4.1 Details of the solution at zero temperature

The analytic continuation of the equations (5.28)-(5.33) at zero temperature leads to the following equations for the spectral functions

$$\rho_r(\omega) = -\frac{1}{\pi}\frac{\Sigma_r''(\omega)}{(\omega - \frac{Jg}{\Theta} - (\Sigma_r'(\omega) - \Sigma_r'(0)))^2 + (\Sigma_r''(\omega))^2}; \tag{D.74}$$

$$\rho_{\mathfrak{f}}(\omega) = -\frac{1}{\pi}\frac{\Sigma_{\mathfrak{f}}''(\omega)}{(\omega - \mu_{\mathfrak{f}} - (\Sigma_{\mathfrak{f}}'(\omega) - \Sigma_{\mathfrak{f}}'(0)))^2 + (\Sigma_{\mathfrak{f}}''(\omega))^2}. \tag{D.75}$$

Equations for self energies are more cumbersome and we list them in several parts. For the imaginary part of the boson self energy we have three terms $\Sigma_r''(\omega) = \Sigma_{r,1}''(\omega) + \Sigma_{r,2}''(\omega) + \Sigma_{r,3}''(\omega)$. The linear

term reads

$$\begin{aligned}
\Sigma''_{r,1}(\omega) &= \pi J^2 g^2 [\rho_r(-\omega) - 2\rho_r(\omega)] \\
\Sigma''_{r,2}(\omega) &= \pi g \int_{-\infty}^{+\infty} d\omega_1 (\theta(-\omega_1)\theta(\omega_1 - \omega) - \theta(\omega_1)\theta(\omega - \omega_1)) \\
&\times \; (J^2 \rho_r(\omega_1)[-2\rho_r(\omega_1 - \omega) + \rho_r(\omega - \omega_1)] + kt^2 \rho_{\mathfrak{f}}(\omega_1)\rho_{\mathfrak{f}}(\omega_1 - \omega)) \\
\Sigma''_{r,3}(\omega) &= \pi \int_{-\infty}^{+\infty} d\omega_1 d\omega_2 (\theta(-\omega_1)\theta(-\omega_2)\theta(-\omega + \omega_1 + \omega_2) + \theta(\omega_1)\theta(\omega_2)\theta(-\omega_1 - \omega_2 + \omega)) \\
&\times \; (J^2 \rho_r(\omega_1)\rho_r(\omega_2)\rho_r(\omega_1 + \omega_2 - \omega) + kt^2 \rho_{\mathfrak{f}}(\omega_1)\rho_{\mathfrak{f}}(\omega_2)\rho_r(\omega_1 + \omega_2 - \omega))
\end{aligned}$$

Similarly, the imaginary part of the fermion self energy can be written as $\Sigma''_{\mathfrak{f}}(\omega) = \Sigma''_{\mathfrak{f},1}(\omega) + \Sigma''_{\mathfrak{f},2}(\omega) + \Sigma''_{\mathfrak{f},3}(\omega)$, in particular

$$\begin{aligned}
\Sigma''_{\mathfrak{f},1}(\omega) &= -\pi t^2 g^2 \rho_{\mathfrak{f}}(\omega) \\
\Sigma''_{\mathfrak{f},2}(\omega) &= \pi t^2 g \int_{-\infty}^{+\infty} d\omega_1 \rho_{\mathfrak{f}}(\omega_1)[\rho_r(\omega - \omega_1) - \rho_r(\omega_1 - \omega)] \\
&\times \; (\theta(-\omega_1)\theta(-\omega + \omega_1) - \theta(\omega_1)\theta(-\omega_1 + \omega)) \\
\Sigma''_{\mathfrak{f},3}(\omega) &= \pi t^2 \int_{-\infty}^{+\infty} d\omega_1 d\omega_2 (\theta(-\omega_1)\theta(-\omega_2)\theta(-\omega + \omega_1 + \omega_2) + \theta(\omega_1)\theta(\omega_2)\theta(-\omega_1 - \omega_2 + \omega)) \\
&\times \; \rho_{\mathfrak{f}}(\omega_1)\rho_r(\omega_2)\rho_r(\omega_1 + \omega_2 - \omega)
\end{aligned}$$

We obtain the real parts of the self energies by using the Kramers-Kronig relation. The filling constraints read

$$g - \int_{-\infty}^{0} d\omega \rho_r(\omega) = \kappa - kp \tag{D.76}$$

$$\int_{-\infty}^{0} d\omega \rho_{\mathfrak{f}}(\omega) = p \tag{D.77}$$

We fix parameters to $J = t = 1$ and $\kappa = k = 1/2$ everywhere for the spin glass phase. The solution of these equations is showns in Fig. 5.8 for different p. For the boson spectral density $\rho_r(\omega)$ we see linear in frequency behavior at small frequencies.

D.4.2 Spectral functions

In this section we find spectral functions of gauge invariant observables: spin and electron spectral densities. We also compute the sum rules for these functions at finite and zero temperatures. Recall that in the spin-glass phase we use the SU($M|M'$) representation where the holon is fermionic and spinons are bosonic operators. From Eq. 5.27,

$$G_c(\tau) = G_s(\tau) G_{\mathfrak{f}}(-\tau) = [G_r(\tau) - g]\, G_{\mathfrak{f}}(-\tau)\,. \tag{D.78}$$

Therefore the electron spectral density is

$$\begin{aligned}\rho_c(\omega) = -\frac{1}{\pi}\mathrm{Im}[G_c(\omega + i0^+)] = g\rho_{\mathfrak{f}}(-\omega) \\ + \int_{-\infty}^{\infty} d\omega_2 \rho_{\mathfrak{f}}(\omega_2)\rho_r(\omega+\omega_2)[n_B(\omega+\omega_2) + n_F(\omega_2)]\,.\end{aligned} \tag{D.79}$$

It is straightforward to obtain the sum rule,

$$\int_{-\infty}^{\infty} d\omega\, \rho_c(\omega) = \frac{1+p}{2}\,. \tag{D.80}$$

Recall that this is same as that obtained in the critical metal phase.

For the spin correlator we have,

$$\chi(\tau) = G_s(\tau) G_s(-\tau) = g^2 - g\,[G_r(\tau) + G_r(-\tau)] + G_r(\tau) G_r(-\tau)\,. \tag{D.81}$$

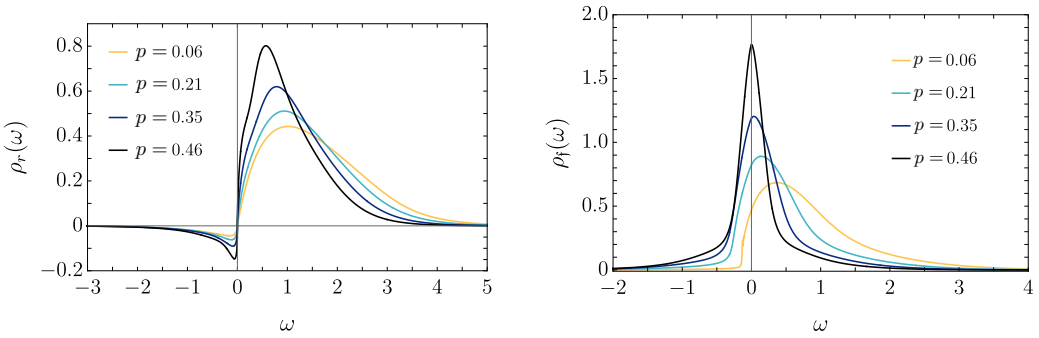

Figure D.13: Spectral functions obtained at zero temperature via real frequency analysis for several values of doping. Parameters are $J = t = 1$.

Here, $\chi'' = \mathrm{Im}[\chi(\tau)]$, where $\chi(\tau) = \langle \vec{S}(\tau) \cdot \vec{S}(0) \rangle$. This gives the spin spectral density,

$$\rho_s(\omega) = \frac{\chi''(\omega)}{\pi} = g^2 \beta \omega \delta(\omega) + g \left[\rho_r(\omega) - \rho_r(-\omega) \right] - \int_{-\infty}^{\infty} d\omega_2 \rho_r(\omega_2) \rho_r(\omega + \omega_2) \left[n_B(\omega + \omega_2) - n_B(\omega_2) \right] . \tag{D.82}$$

The sum rule for the spin spectral density at non-zero temperature is not easy to obtain and we do not have an exact expression for it. At zero temperature, however, we obtain

$$\int_0^{\infty} d\omega \rho_s(\omega) = \frac{(1-p)(3-p)}{4} - g^2 . \tag{D.83}$$

In addition, we have the usual sum rules,

$$\int_{-\infty}^{\infty} d\omega \rho_{\mathfrak{f}}(\omega) = \int_{-\infty}^{\infty} d\omega \rho_r(\omega) = 1 . \tag{D.84}$$

Solution of these equations for several values of doping is presented in Fig. D.13.

E

Supplementary Information for Chapter 6

E.1 Terms of order y^1 in $\mathcal{F}_Q$ for the Ising model

This appendix contains the $\mathcal{O}(y)$ corrections to the free energy and saddle-point values from the 'quantum' contribution to the free energy, $\mathcal{F}_Q$.

E.1.1 Zero longitudinal field

As in the main text, we first consider the $h = 0$ case of Sec. 6.2.4.

Paramagnet

Here, we continue the analysis of Sec. 6.2.4.

For the saddle point at order y^1, we write

$$Q_r(i\nu_n) = -\frac{\sqrt{\nu_n^2 + \Delta^2 + y\Delta_1^2 - y\Sigma(i\nu)}}{\kappa}\,, \tag{E.1}$$

where we can choose $\Sigma(0) = 0$ without loss of generality by adjusting the value of Δ_1^2. Then, from (6.30), we obtain

$$\begin{aligned} 0 = &-\left[y\Delta_1^2 - y\Sigma(i\nu_n)\right] - \frac{U}{\beta}\sum_{\nu'_n}\left[\sqrt{\nu_n'^2 + \Delta^2 + y\Delta_1^2 - y\Sigma(i\nu'_n)} - \sqrt{\nu_n'^2 + \Delta^2}\right] \\ &+ \frac{2y}{3\beta^2\kappa^2}\sum_{\nu'_n,\nu''_n}\sqrt{\nu_n'^2 + \Delta^2}\sqrt{\nu_n''^2 + \Delta^2}\sqrt{(\nu_n - \nu'_n - \nu''_n)^2 + \Delta^2}\,. \end{aligned} \tag{E.2}$$

After subtracting from (E.2) its value at $\nu_n = 0$, we determine

$$\Sigma(i\nu_n) = -\frac{2}{3\beta^2\kappa^2}\sum_{\nu'_n,\nu''_n}\sqrt{\nu_n'^2 + \Delta^2}\sqrt{\nu_n''^2 + \Delta^2}\left[\sqrt{(\nu_n - \nu'_n - \nu''_n)^2 + \Delta^2} - \sqrt{(\nu'_n + \nu''_n)^2 + \Delta^2}\right]\,. \tag{E.3}$$

Then, Δ_1^2 can be obtained from (E.2) as the solution of

$$\Delta_1^2 = \frac{2}{3\beta^2\kappa^2}\sum_{\nu_n,\nu_n'}\sqrt{\nu_n'^2+\Delta^2}\sqrt{\nu_n^2+\Delta^2}\sqrt{(\nu_n'+\nu_n)^2+\Delta^2} + \frac{U}{2\beta}\sum_{\nu_n}\frac{\Sigma(i\nu)}{\sqrt{\nu_n^2+\Delta^2}} - \lim_{y\to 0}\frac{U}{y\beta}\sum_{\nu_n}\left[\sqrt{\nu_n^2+\Delta^2+y\Delta_1^2}-\sqrt{\nu_n^2+\Delta^2}\right]. \tag{E.4}$$

At the critical point, where $\Delta^2 + y\Delta_1^2 = 0$ and $r = r_{c0} + yr_{c1}$, using (6.32) and (6.33), we can write the term proportional to u in (E.2) as

$$y\Delta_1^2 + yr_{c1} + \frac{Uy}{2\beta}\sum_{\nu_n}\frac{\Sigma(i\nu_n)|_{\Delta=0}}{|\nu_n|}, \tag{E.5}$$

where $\Sigma(i\nu_n)$ is to be evaluated from (E.3) at $\Delta = 0$. Then, (E.2) at $\nu = 0$ yields the shift in the position of the critical point at order y as

$$r_{c1} = -\frac{2}{3\beta^2\kappa^2}\sum_{\nu_n,\nu_n'}|\nu_n'||\nu_n||\nu_n'+\nu_n| - \frac{U}{2\beta}\sum_{\nu_n}\frac{\Sigma(i\nu_n)|_{\Delta=0}}{|\nu_n|}. \tag{E.6}$$

For the free energy at order y^1, with $\mathcal{F}_Q = \mathcal{F}_Q^0 + y\mathcal{F}_Q^1$, we can just insert the $\mathcal{O}(y^0)$ saddle-point values into the terms explicitly dependent upon y in (6.26):

$$\mathcal{F}_Q^1 = -\frac{1}{6\beta^3\kappa^4}\sum_{\nu_n,\nu_n',\nu_n''}\sqrt{\nu_n^2+\Delta^2}\sqrt{\nu_n'^2+\Delta^2}\sqrt{\nu_n''^2+\Delta^2}\sqrt{(\nu_n+\nu_n'+\nu_n'')^2+\Delta^2}. \tag{E.7}$$

Spin glass

We continue here the analysis of Sec. 6.2.4.

For the saddle-point aligns at order y^1, we write

$$\begin{aligned} q_{EA} &= \frac{1}{\kappa U}(r_{c0} - r) + y q_{EA1}, \\ Q_r(i\nu_n) &= -\frac{|\nu_n|}{\kappa} + y Q_{r1}(i\nu_n). \end{aligned} \tag{E.8}$$

Then, Eqs. (6.40) and (6.41) yield

$$\begin{aligned} 0 =& 2|\nu_n| Q_{r1}(i\nu_n) + \frac{U}{\beta}\sum_{\nu'_n} Q_{r1}(i\nu'_n) + u q_{EA1} + \frac{2}{3\kappa^3\beta^2}\sum_{\nu'_n,\nu''_n} |\nu'_n||\nu''_n||\nu_n - \nu'_n - \nu''_n| \\ &- \frac{2}{\kappa^2\beta} q_{EA0}\sum_{\nu'_n} |\nu'_n||\nu_n - \nu'_n| - 2Q_{r1}(0)|\nu_n|, \end{aligned} \tag{E.9}$$

$$q_{EA0}^2 = -\kappa Q_{r1}(0). \tag{E.10}$$

From (E.9,6.41), we determine that

$$q_{EA1} = -\frac{1}{\beta}\sum_{\nu_n} Q_{r1}(i\nu_n) - \frac{2}{3\kappa^3 U\beta^2}\sum_{\nu_n,\nu'_n} |\nu'_n||\nu_n||\nu'_n + \nu_n| + \frac{2}{\kappa^2 U\beta} q_{EA0}\sum_{\nu_n} |\nu_n|^2, \tag{E.11}$$

and

$$\begin{aligned} Q_{r1}(i\nu_n) =& -\frac{q_{EA0}^2}{\kappa} - \frac{1}{3\kappa^3\beta^2|\nu_n|}\sum_{\nu'_n,\nu''_n}\Big(|\nu'_n||\nu''_n||\nu_n - \nu'_n - \nu''_n| - |\nu'_n||\nu''_n||\nu'_n + \nu''_n|\Big) \\ &+ \frac{1}{\beta\kappa^2|\nu_n|} q_{EA0}\sum_{\nu'_n}\Big(|\nu'_n||\nu_n - \nu'_n| - |\nu'_n|^2\Big). \end{aligned} \tag{E.12}$$

At $T = 0$, we obtain, with a frequency cutoff $|\nu_n| < \Lambda$,

$$Q_{r1}(i\nu_n) = -\frac{q_{EA0}^2}{\kappa} - \frac{1}{6\pi\kappa^3}\Big(\frac{2\Lambda^3}{3}|\nu_n| - \frac{\Lambda^2}{3}|\nu_n|^2 + \frac{1}{20}|\nu_n|^4\Big) + \frac{1}{6\pi\kappa^2} q_{EA0}|\nu_n|^2. \tag{E.13}$$

The shift in the quantum critical point is obtained by setting $r = r_{c0} + y r_{c1}$ in (E.11) and (E.12), and this yields the same value of r_{c1} as that obtained from the vanishing gap condition on the paramagnetic side in (E.6).

For the free energy at order y^1, we now obtain from (6.26)

$$\mathcal{F}_Q^1 = -\frac{r q_{EA1}}{\kappa} - \frac{q_{EA0}^2}{\beta\kappa^2} \sum_{\nu_n} \nu_n^2 + \frac{2 q_{EA0}}{3\kappa^3\beta^2} \sum_{\nu_n, \nu_n'} |\nu_n||\nu_n'||\nu_n + \nu_n'| - \frac{1}{6\beta^3\kappa^4} \sum_{\nu_n, \nu_n', \nu_n''} |\nu_n||\nu_n'||\nu_n''||\nu_n + \nu_n' + \nu_n''|. \tag{E.14}$$

E.1.2 Nonzero longitudinal field

Next, we consider the case of $h \neq 0$ studied in Sec. 6.2.5.

Replica-symmetric solution

This section continues the analysis of Sec. 6.2.5.

For the saddle point at order y^1, we write as in (E.1)

$$Q_r(i\nu_n) = -\frac{\sqrt{\nu_n^2 + \Delta^2 + y\Delta_1^2 - y\Sigma(i\nu)}}{\kappa}, \qquad q_{EA} = q_{EA0} + q_{EA1}, \tag{E.15}$$

where we can again choose $\Sigma(0) = 0$ without loss of generality by adjusting the value of Δ_1^2. Then,

from (6.29), we obtain

$$
\begin{aligned}
0 = &- \left[y\Delta_1^2 - y\Sigma(i\nu_n)\right] - \frac{U}{\beta}\sum_{\nu'_n}\left[\sqrt{\nu'^2_n + \Delta^2 + y\Delta_1^2 - y\Sigma(i\nu'_n)} - \sqrt{\nu'^2_n + \Delta^2}\right] \\
&+ U\kappa y q_{EA1} + \frac{2y}{3\beta^2\kappa^2}\sum_{\nu'_n,\nu''_n}\sqrt{\nu'^2_n + \Delta^2}\sqrt{\nu''^2_n + \Delta^2}\sqrt{(\nu_n - \nu'_n - \nu''_n)^2 + \Delta^2} \\
&- \frac{2y}{\beta\kappa}q_{EA0}\sum_{\nu'_n}\sqrt{\nu'^2_n + \Delta^2}\sqrt{(\nu_n - \nu'_n)^2 + \Delta^2} + 2yq^2_{EA0}\sqrt{\nu_n^2 + \Delta^2}\,. \qquad \text{(E.16)}
\end{aligned}
$$

After subtracting from (E.16) its value at $\nu_n = 0$, we determine

$$
\begin{aligned}
\Sigma(i\nu_n) = &- \frac{2}{3\beta^2\kappa^2}\sum_{\nu'_n,\nu''_n}\sqrt{\nu'^2_n + \Delta^2}\sqrt{\nu''^2_n + \Delta^2}\left[\sqrt{(\nu_n - \nu'_n - \nu''_n)^2 + \Delta^2} - \sqrt{(\nu'_n + \nu''_n)^2 + \Delta^2}\right] \\
&+ \frac{2}{\beta\kappa}q_{EA0}\sum_{\nu'_n}\left[\sqrt{\nu'^2_n + \Delta^2}\sqrt{(\nu_n - \nu'_n)^2 + \Delta^2} - (\nu'^2_n + \Delta^2)\right] \\
&- 2q^2_{EA0}\left[\sqrt{\nu_n^2 + \Delta^2} - \Delta\right]\,. \qquad \text{(E.17)}
\end{aligned}
$$

Then, Δ_1^2 obeys, from (E.16),

$$
\begin{aligned}
\Delta_1^2 = &\; U\kappa q_{EA1} + \frac{2y}{3\beta^2\kappa^2}\sum_{\nu'_n,\nu''_n}\sqrt{\nu'^2_n + \Delta^2}\sqrt{\nu''^2_n + \Delta^2}\sqrt{(\nu_n - \nu'_n - \nu''_n)^2 + \Delta^2} \\
&- \frac{2y}{\beta\kappa}q_{EA0}\sum_{\nu'_n}\sqrt{\nu'^2_n + \Delta^2}\sqrt{(\nu_n - \nu'_n)^2 + \Delta^2} + 2yq^2_{EA0}\sqrt{\nu_n^2 + \Delta^2} \\
&+ \frac{U}{2\beta}\sum_{\nu_n}\frac{\Sigma(i\nu)}{\sqrt{\nu_n^2 + \Delta^2}} - \lim_{y\to 0}\frac{U}{y\beta}\sum_{\nu_n}\left[\sqrt{\nu_n^2 + \Delta^2 + y\Delta_1^2} - \sqrt{\nu_n^2 + \Delta^2}\right]\,. \qquad \text{(E.18)}
\end{aligned}
$$

Determination of q_{EA1} and Δ_1 requires solution of (E.16), along with a second align obtained from (6.51)

$$
-3q_{EA0}\frac{\Delta_1^2}{2\Delta} - 3\Delta q_{EA1} + q^3_{EA0} = 0\,. \qquad \text{(E.19)}
$$

For the free energy at order y^1, we now obtain from (6.26)

$$\mathcal{F}^1_Q = -\frac{yq^2_{EA0}}{\beta\kappa^2}\sum_{\nu_n}(\nu_n^2+\Delta^2)+\frac{2yq_{EA0}}{3\kappa^3\beta^2}\sum_{\nu_n,\nu'_n}\sqrt{\nu_n^2+\Delta^2}\sqrt{\nu_n'^2+\Delta^2}\sqrt{(\nu_n+\nu'_n)^2+\Delta^2}$$
$$-\frac{y}{6\beta^3\kappa^4}\sum_{\nu_n,\nu'_n,\nu''_n}\sqrt{\nu_n^2+\Delta^2}\sqrt{\nu_n'^2+\Delta^2}\sqrt{\nu_n''^2+\Delta^2}\sqrt{(\nu_n+\nu'_n+\nu''_n)^2+\Delta^2}. \tag{E.20}$$

E.2 Classical spherical p-rotor model

In the classical limit $g=0$, all components of $Q_{ab}(\tau)$ and $\Sigma_{ab}(\tau)$ are independent of τ, and the theory should reduce to that in Ref. [36]. So, we have $Q_{ab}(\omega_n)=\beta Q_{ab}(\tau)\delta_{\omega_n,0}\equiv\beta Q_{ab}\delta_{\omega_n,0}$, and similarly for Σ_{ab} and λ_{ab}. Then, the effective action in (6.74) becomes

$$\frac{S_{\text{eff}}}{N}=\frac{1}{2}\log\det\left[\frac{1}{\pi}\left(-i\delta_{ab}z^a+i\beta\lambda_{ab}\right)\right]+i\beta\sum_{a=1}^{n}z^a$$
$$-\sum_{a,b=1}^{n}\left(\beta^2\,i\lambda_{ab}Q_{ab}+\frac{\beta h^2}{4}\Big[-i\delta_{ab}z^a+i\beta\lambda_{ab}\Big]^{-1}_{ab}+\frac{\beta^2 J^2}{4}\left(Q_{ab}\right)^p\right). \tag{E.21}$$

Let us now change our notation a bit to obtain expressions similar to those in Ref. [155]. We define

$$-iz^a=\bar{z}\quad,\quad i\lambda_{ab}=-\sigma_{ab}. \tag{E.22}$$

Then, the effective action is

$$\frac{S_{\text{eff}}}{N}=\frac{1}{2}\log\det\left[\frac{1}{\pi}\left(\delta_{ab}\bar{z}-\beta\sigma_{ab}\right)\right]-\beta\sum_{a=1}^{n}\bar{z}$$
$$+\sum_{a,b=1}^{n}\left(\beta^2\,\sigma_{ab}Q_{ab}-\frac{\beta h^2}{4}\Big[\bar{z}\delta_{cd}-\beta\sigma_{cd}\Big]^{-1}_{ab}-\frac{\beta^2 J^2}{4}\left(Q_{ab}\right)^p\right). \tag{E.23}$$

Now, as before, we use the identity (E.96) to absorb the h^2 term into the log det

$$\frac{S_{\text{eff}}}{N} = \frac{1}{2}\log\det\left[\frac{1}{\pi}\left(\delta_{ab}\bar{z} - \beta\sigma_{ab} - \frac{\beta h^2}{2}\right)\right] - \beta\sum_{a=1}^{n}\bar{z} + \sum_{a,b=1}^{n}\left(\beta^2\,\sigma_{ab}Q_{ab} - \frac{\beta^2 J^2}{4}\,(Q_{ab})^p\right). \tag{E.24}$$

The saddle-point align with respect to σ_{ab} is

$$\beta Q_{ab} = \frac{1}{2}\left[\delta_{ab}\bar{z} - \beta\sigma_{ab} - \frac{\beta h^2}{2}\right]^{-1}_{ab}. \tag{E.25}$$

Inserting this back into (E.24), we obtain an effective action just for Q_{ab} and $\bar{z}$,

$$\frac{S_{\text{eff}}}{N} = -\frac{1}{2}\log\det Q - \beta\sum_{a=1}^{n}\bar{z} + \sum_{a,b=1}^{n}\left(\beta\bar{z}\delta_{ab}Q_{ab} - \frac{\beta^2 h^2}{2}Q_{ab} - \frac{\beta^2 J^2}{4}\,(Q_{ab})^p\right). \tag{E.26}$$

Then, the remaining saddle-point aligns are

$$\begin{aligned} 1 &= Q_{aa}, \\ Q^{-1}_{ab} &= 2\beta\bar{z}\delta_{ab} - \beta^2 h^2 - \frac{p\beta^2 J^2}{2}\,(Q_{ab})^{p-1}. \end{aligned} \tag{E.27}$$

E.2.1 Replica-symmetric solution

Now, we use the replica-symmetric ansatz

$$\begin{aligned} Q_{ab} &= q + Q_r\delta_{ab}, \\ \sigma_{ab} &= \varrho + \sigma_r\delta_{ab}. \end{aligned} \tag{E.28}$$

Then, using the identities in Appendix E.5, the aligns in (E.27) become

$$1 = q + Q_r, \tag{E.29}$$

$$\sigma_r = \frac{pJ^2}{4}(q+Q_r)^{p-1} - \frac{pJ^2}{4}q^{p-1}, \tag{E.30}$$

$$\varrho = \frac{pJ^2}{4}q^{p-1}, \tag{E.31}$$

$$\frac{1}{\beta Q_r} = 2(\beta\bar{z} - \beta\sigma_r), \tag{E.32}$$

$$\frac{q}{Q_r^2} = \beta^2 h^2 + \frac{p\beta^2 J^2}{2}q^{p-1}. \tag{E.33}$$

Focusing on $p = 2$ first, we can simplify the above to

$$1 = q + Q_r, \tag{E.34}$$

$$\beta Q_r = \frac{1}{\bar{z} + \sqrt{\bar{z}^2 - J^2}}, \tag{E.35}$$

$$q = \frac{J^2 q + h^2}{(\bar{z} + \sqrt{\bar{z}^2 - J^2})^2}. \tag{E.36}$$

These aligns are easily seen to be equivalent to the classical limit of Eqs. (E.49,E.53,E.55) derived for the quantum model later. Figure E.1 showcases the temperature dependence of the order parameter q for nonzero h. For $p = 2$, $h = 0$, it is known [111] that the replica-symmetric solution is stable and optimal, and we expect that this statement continues to hold for any $h \neq 0$ as well [36].

E.2.2 One-step replica symmetry breaking

The classical spherical p-rotor model can be solved exactly for all p, temperatures, and fields, and hosts a one-step RSB phase for any $p > 2$ [36] (akin to the model without the spherical constraint [60]). In this

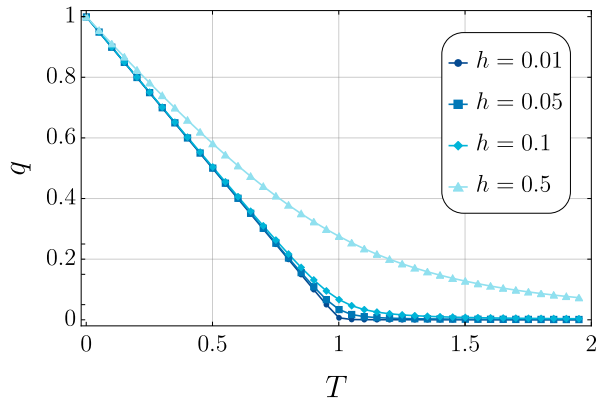

Figure E.1: Spin glass order parameter q of the classical spherical $p = 2$-rotor model (with $J=1$), as a function of the temperature T for several values of the longitudinal field h. For the replica-symmetric solution considered here, the spin glass phase transition occurs at $T = 1$.

case, for the diagonal elements of Q_{ab} and σ_{ab}, we use the ansatz

$$\begin{aligned} Q_{aa} &= q_1 + Q_r, \\ \sigma_{aa} &= \varrho_1 + \sigma_r, \end{aligned} \tag{E.37}$$

while the off-diagonal elements are as in (6.98). The aligns analogous to (6.84)–(6.88) are

$$1 = q_1 + Q_r, \tag{E.38}$$

$$\sigma_r = \frac{pJ^2}{4}(q_1 + Q_r)^{p-1} - \frac{pJ^2}{4}q_1^{p-1}, \tag{E.39}$$

$$\varrho_1 = \frac{pJ^2}{4}q_1^{p-1}, \tag{E.40}$$

$$\varrho_0 = \frac{pJ^2}{4}q_0^{p-1}, \tag{E.41}$$

$$\frac{1}{\beta Q_r} = 2(\bar{z} - \beta\sigma_r), \tag{E.42}$$

$$\frac{q_1 Q_r + x(q_1 - q_0)^2}{Q_r(Q_r + x(q_1 - q_0))^2} = \beta^2 h^2 + \frac{p\beta^2 J^2}{2}q_1^{p-1}, \tag{E.43}$$

$$\frac{q_0}{(Q_r + x(q_1 - q_0))^2} = \beta^2 h^2 + \frac{p\beta^2 J^2}{2}q_0^{p-1}. \tag{E.44}$$

We are mainly interested in the $\beta \to \infty$ limit. From the aligns above, we see that this limit exists if we write

$$q_1 = \widehat{q} - \frac{\theta}{\beta}, \quad x = \frac{\mu}{\beta}, \tag{E.45}$$

where $\widehat{q}$ is a β-independent constant, and θ and μ are finite as $\beta \to \infty$. For the present classical theory, $\widehat{q} = 1$, but we will see that $\widehat{q} < 1$ in the $g \neq 0$ theory.

Gapless condition

The gapless condition, obtained in the $g \to 0$ limit of (6.109) is

$$\frac{1}{\beta^2 Q_r^2} = \frac{p(p-1)J^2}{2}q_1^{p-2}. \tag{E.46}$$

Free energy

The classical limit of the action (6.110) is

$$\frac{S_{\text{eff}}}{Nn} = -\frac{1}{2}\log[Q_r] - \frac{1}{2}\frac{q_0}{Q_r + x(q_1 - q_0)} + \frac{1}{2x}\ln\frac{Q_r}{Q_r + x(q_1 - q_0)} \tag{E.47}$$
$$-\beta\bar{z} + \beta\bar{z}(Q_r + q_1) - \frac{\beta^2 h^2}{2}\left[Q_r + x(q_1 - q_0)\right] - \frac{\beta^2 J^2}{4}\left[(Q_r + q_1)^p - q_1^p(1-x) - q_0^p x\right].$$

We can now confirm that the aligns (E.38)–(E.44) are indeed the saddle-point aligns obtained from Eq. (E.47).

The stationarity condition with respect to the breakpoint yields

$$\frac{\partial S_{\text{eff}}}{\partial x} = 0 \quad \Rightarrow \quad \frac{J^2\beta^2}{4}(q_1^p - q_0^p) - \frac{1}{2x^2}\log\left[1 + \frac{x(q_1 - q_0)}{Q_r}\right]$$
$$+ \frac{\beta^2 h^2}{2}(q_1 - q_0) + \frac{(q_1 - q_0)(Q_r + q_1 x - 2q_0 x)}{2x(Q_r + x(q_1 - q_0))^2} = 0. \tag{E.48}$$

One can use either (E.46) or (E.48) to determine x.

E.3 Replica-symmetric solution for the $h \neq 0$ quantum spherical $p = 2$ model

We now consider the quantum version of the spherical $p = 2$-rotor model in a longitudinal field h. As discussed in Ref. [183], for $h = 0$, the replica-symmetric solution is the optimal one. Anticipating the same conclusion to hold for the case of $h \neq 0$, in what follows, we focus on the replica-symmetric solution.

For $p = 2$, the aligns (6.81), combined with the replica-symmetric ansatz (6.83), reduce to

$$1 = q + \frac{1}{\beta}\sum_{\omega_n} Q_r(\omega_n), \tag{E.49}$$

$$\varrho = gJ^2 q, \tag{E.50}$$

$$Q_r(\omega_n) = \frac{g}{\omega_n^2 + \overline{\lambda} - gJ^2 Q_r(\omega_n)}, \tag{E.51}$$

$$q = \frac{g\varrho + g^2 h^2}{[\overline{\lambda} - gJ^2 Q_r(\omega_n = 0)]^2}. \tag{E.52}$$

Specifically, the align for $Q_r(\omega_n)$ can be written as

$$Q_r(\omega_n) = \frac{2g}{\omega_n^2 + \overline{\lambda} + \sqrt{(\omega_n^2 + \overline{\lambda})^2 - 4g^2J^2}}, \tag{E.53}$$

$$Q_r(\omega_n = 0) = \frac{1}{2gJ^2}\left(\overline{\lambda} - \sqrt{\overline{\lambda}^2 - 4g^2J^2}\right). \tag{E.54}$$

Then, the order parameter is given by

$$q = 4g^2 \frac{J^2 q + h^2}{\left[\overline{\lambda} + \sqrt{\overline{\lambda}^2 - 4g^2J^2}\right]^2}. \tag{E.55}$$

From the align above, we observe that the condition $\overline{\lambda} \geq 2gJ$ has to be satisfied for the order parameter to be a real number. Note that for $h = 0$, we find

$$\overline{\lambda}|_{h=0} = 2Jg, \tag{E.56}$$

which is consistent with Eq. (33.41) of Ref.[155]. For $h \neq 0$, the align for the order parameter can be

formulated as

$$q = \frac{4g^2h^2}{\left[\overline{\lambda} + \sqrt{\overline{\lambda}^2 - 4g^2J^2}\right]^2 - 4g^2J^2} = \frac{2g^2h^2}{\overline{\lambda}^2 - 4g^2J^2 + \overline{\lambda}\sqrt{\overline{\lambda}^2 - 4g^2J^2}}. \tag{E.57}$$

We can simplify the expression above further to

$$q = -\frac{h^2}{2J^2}\frac{\overline{\lambda}^2 - 4g^2J^2 - \overline{\lambda}\sqrt{\overline{\lambda}^2 - 4g^2J^2}}{\overline{\lambda}^2 - 4g^2J^2} = -\frac{h^2}{2J^2}\frac{\lambda^{*2} - \overline{\lambda}\lambda^*}{\lambda^{*2}} = -\frac{h^2}{2J^2}\frac{\lambda^* - \overline{\lambda}}{\lambda^*} = \frac{h^2}{2J^2}\left(\frac{\overline{\lambda}}{\lambda^*} - 1\right), \tag{E.58}$$

where we introduce the notation

$$\lambda^{*2} = \overline{\lambda}^2 - 4g^2J^2. \tag{E.59}$$

We note that the order parameter has to be positive, $q > 0$, so $\overline{\lambda} > \lambda^*$. In addition, we require $\overline{\lambda} > 2gJ$ such that $\lambda^* > 0$.

Finally, we rewrite the correlator $Q_r(\omega_n)$ in terms of our new notation as

$$Q_r(\omega_n) = \frac{2g}{\omega_n^2 + \overline{\lambda} + \sqrt{\omega_n^4 + 2\omega_n^2\overline{\lambda} + \lambda^{*2}}}. \tag{E.60}$$

Since $\lambda^* > 0$, there is always a gap in the spectrum. The gap is given by the value of the frequency at which the square root in the Green's function (analytically continued to the real frequency) changes sign. This value is simply

$$\Delta = \sqrt{\overline{\lambda} - 2gJ}, \tag{E.61}$$

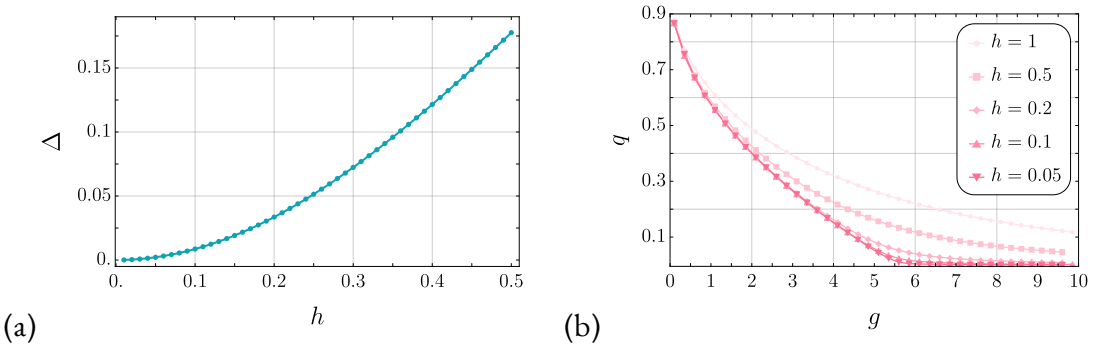

Figure E.2: (a) Gap in the spectrum (E.61) as a function of the longitudinal field strength h for the quantum spherical $p = 2$-rotor model, taking $g = 1$. The system is gapless in the limit $h \to 0$. (b) The order parameter q as a function of the transverse magnetic field for several values of h, illustrating the absence of a sharp phase transition at any nonzero g and h.

which is always greater than zero in the presence of a nonzero field h. The resulting behavior of the gap as a function of the longitudinal field is shown in Fig. E.2(a).

To find the value of the spin glass order parameter, we need to find $\overline{\lambda}$ according to

$$q = \frac{h^2}{2J^2}\left(\frac{\overline{\lambda}}{\lambda^*} - 1\right), \tag{E.62}$$

$$Q_r(\omega_n) = \frac{2g}{\omega_n^2 + \overline{\lambda} + \sqrt{\omega_n^4 + 2\omega_n^2\overline{\lambda} + \lambda^{*2}}}, \tag{E.63}$$

$$1 = q + \frac{1}{\beta}\sum_{\omega_n} Q_r(\omega_n). \tag{E.64}$$

The numerical solution for q as a function of g is shown in Fig. E.2(b). For $h = 0$, one can also compute the critical point, g_c, analytically to find

$$g_c = \frac{9\pi^2 J}{16} \simeq 5.55J, \tag{E.65}$$

which reproduces the result obtained in Ref. [155].

E.4 Replica-symmetric solution for the $h = 0$ quantum spherical $p = 3$ model at large g

In the limit of large longitudinal fields g, one can analytically solve the aligns (6.84)–(6.88) at $h = 0$. We first note that in this limit, the order parameter q is zero, *i.e.*, the system is in a paramagnetic phase as shown in Fig. 6.7. To obtain the solution in this phase, we rewrite the saddle-point aligns in the following form:

$$1 = Q_r(\tau = 0), \tag{E.66}$$

$$\Sigma_r(\tau) = \frac{3}{2} g J^2 Q_r^2(\tau), \tag{E.67}$$

$$Q_r(\omega_n) = \frac{g}{\omega_n^2 + \overline{\lambda} - \Sigma_r(\omega_n)}. \tag{E.68}$$

We numerically solve these aligns for several values of g and infer that λ grows faster with g than Σ_r, which can be seen in Fig. E.3(a). In addition, $\Sigma_r(\omega_n)$ is close to a constant in this limit as evidenced by Fig. E.3(b). We can therefore assume that, to leading order,

$$Q_r(\omega_n) = \frac{g}{\omega_n^2 + \overline{\lambda}}. \tag{E.69}$$

The resulting analytical solution yields

$$\overline{\lambda} = \frac{g^2}{4}, \;\; Q_r(\omega_n) = \frac{g}{\omega_n^2 + \overline{\lambda}}, \;\; \Sigma_r(\tau) = \frac{3g}{2} e^{-g|\tau|}, \;\; \Sigma_r(\omega_n) = \frac{3g^2}{g^2 + \omega_n^2} \simeq \frac{3}{g^2}(g^2 - \omega_n^2). \tag{E.70}$$

To improve upon our earlier approximation, we compute the Green's function to second order in

$1/g$. At this order, we obtain the following result:

$$\overline{\lambda} = \frac{g^2}{4} + \frac{9}{4}, \tag{E.71}$$

$$Q_r(\omega_n) = \frac{g}{\omega_n^2(1+3/g^2) + (\overline{\lambda}-3)}, \tag{E.72}$$

$$\Sigma_r(\tau) = \frac{3g^5}{2(g^4-9)} e^{-g|\tau|\sqrt{\frac{g^2-3}{g^2+3}}}, \tag{E.73}$$

$$\Sigma_r(\omega_n) = \frac{3g^6}{\sqrt{g^4-9}} \frac{1}{g^2(g^2-3)+\omega_n^2(g^2+3)}. \tag{E.74}$$

We therefore conclude that at large g, the spectral function has the form of a delta function

$$\rho(\omega) = \frac{g^3}{g^2+3} \delta\left(\omega^2 - \frac{g^2}{4}\frac{g^2-3}{g^2+3}\right), \tag{E.75}$$

with a finite gap. Thus, within this approximate framework, we expect the replica-symmetric solution to persist up to $g \simeq \sqrt{3}$.

E.5 Replica identities

We consider $n \times n$ replica matrices A_{ab} whose off-diagonal elements are parametrized by the Parisi function $a(u)$, $u \in [0,1]$, and the diagonal element $A_{aa} = \tilde{a}$ (similarly for B_{ab} and C_{ab}). We find it useful to define

$$\langle a \rangle \equiv \int_0^1 du\, a(u), \tag{E.76}$$

and

$$[a](u) \equiv -\int_0^u dv a(v) + ua(u)\,. \tag{E.77}$$

For the replica-symmetric case, we take

$$a(u) = a, \qquad \tilde{a} = a + \sigma_a \,. \tag{E.78}$$

For the case of one-step replica symmetry breaking, we take

$$\begin{aligned} \tilde{a} &= a_1 + \sigma_a, \\ a(u) &= \begin{cases} a_1 \,, & x < u < 1 \\ a_0 \,, & 0 < u < x \end{cases} . \end{aligned} \tag{E.79}$$

Then, we have $\langle a \rangle = a_1 - x(a_1 - a_0)$, and

$$[a](u) = \begin{cases} x(a_1 - a_0) \,, & x < u < 1 \\ 0 \,, & 0 < u < x \end{cases} . \tag{E.80}$$

We now present some useful identities for matrix operations in the limit $n \to 0$.

E.5.1 Term-by-term sum

$$\frac{1}{n} \sum_{a,b=1}^{n} A_{ab} = \tilde{a} - \langle a \rangle. \tag{E.81}$$

E.5.2 Matrix product

For

$$C_{ab} = \sum_{c=1}^{n} A_{ac} B_{cb} \,, \tag{E.82}$$

we have [125]

$$\begin{aligned} \tilde{c} &= \tilde{a}\tilde{b} - \langle ab \rangle, \\ c(u) &= (\tilde{b} - \langle b \rangle) a(u) + (\tilde{a} - \langle a \rangle) b(u) - \int_0^u dv (a(u) - a(v))(b(u) - b(v)). \end{aligned} \tag{E.83}$$

E.5.3 Matrix inverse

To determine $B = A^{-1}$, we set $C = 1$ in the matrix product to obtain the relations

$$\begin{aligned} 1 &= \tilde{a}\tilde{b} - \langle ab \rangle, \\ 0 &= (\tilde{b} - \langle b \rangle) a(u) + (\tilde{a} - \langle a \rangle) b(u) - \int_0^u dv (a(u) - a(v))(b(u) - b(v)). \end{aligned} \tag{E.84}$$

With replica-symmetric matrices, we have

$$\begin{aligned} \sigma_b &= \frac{1}{\sigma_a}, \\ b &= -\frac{a}{\sigma_a^2}. \end{aligned} \tag{E.85}$$

For the case of one-step replica symmetry breaking, we have

$$
\begin{aligned}
1 &= \tilde{a}\tilde{b} - a_0 b_0 x - a_1 b_1 (1-x), \\
0 &= (\tilde{b} - b_0 x - b_1(1-x))a_0 + (\tilde{a} - a_0 x - a_1(1-x))b_0, \\
0 &= (\tilde{b} - b_0 x - b_1(1-x))a_1 + (\tilde{a} - a_0 x - a_1(1-x))b_1 - x(a_1 - a_0)(b_1 - b_0).
\end{aligned} \tag{E.86}
$$

Solving these aligns, we obtain

$$
\begin{aligned}
\sigma_b &= \frac{1}{\sigma_a}, \\
b_1 &= -\frac{a_1 \sigma_a + x(a_1 - a_0)^2}{\sigma_a(\sigma_a + x(a_1 - a_0))^2}, \\
b_0 &= -\frac{a_0}{(\sigma_a + x(a_1 - a_0))^2}.
\end{aligned} \tag{E.87}
$$

E.5.4 Term-by-term inverse sum

If $A^{-1} = B$, then from (E.81)

$$
\frac{1}{n}\sum_{ab} A^{-1}_{ab} = \tilde{b} - \langle b \rangle. \tag{E.88}
$$

From (E.84), we have

$$
\begin{aligned}
1 &= \tilde{a}\tilde{b} - \langle ab \rangle, \\
0 &= (\tilde{b} - \langle b \rangle)\langle a \rangle + (\tilde{a} - \langle a \rangle)\langle b \rangle - \langle ab \rangle + \langle a \rangle \langle b \rangle.
\end{aligned} \tag{E.89}
$$

Taking the difference, we obtain

$$\frac{1}{n}\sum_{ab} A^{-1}_{ab} = \frac{1}{\tilde{a} - \langle a \rangle}. \tag{E.90}$$

E.5.5 Term-by-term product

For the product

$$D_{ab} = \sum_{c,d=1}^{n} A_{ac} B_{db}\,, \tag{E.91}$$

we use the fact that $\sum_c A_{ac}$ is independent of the index a for replica matrices. This yields a replica-symmetric matrix D_{ab}, which is of independent a, b and using (E.81) we have

$$\tilde{d} = d(u) = (\tilde{a} - \langle a \rangle)(\tilde{b} - \langle b \rangle). \tag{E.92}$$

For the replica-symmetric case, $\tilde{d} = d = \sigma_a \sigma_b$, and $\sigma_d = 0$. With one-step replica symmetry breaking $\tilde{d} = d_0 = d_1 = (\sigma_a + x(a_1 - a_0))(\sigma_b + x(b_1 - b_0))$, and $\sigma_d = 0$.

E.5.6 Trace log

The trace log is needed in the computation of the free energy. We have [125]

$$\frac{1}{n}\mathrm{Tr}\ln A = \ln(\tilde{a} - \langle a \rangle) + \frac{a(0)}{\tilde{a} - \langle a \rangle} - \int_0^1 \frac{du}{u^2} \ln \frac{\tilde{a} - \langle a \rangle - [a](u)}{\tilde{a} - \langle a \rangle}\,. \tag{E.93}$$

In the replica-symmetric case, we have

$$\frac{1}{n}\mathrm{Tr}\ln A = \ln(\sigma_a) + \frac{a}{\sigma_a}\,. \tag{E.94}$$

With one-step replica symmetry breaking, we have

$$\frac{1}{n}\mathrm{Tr}\ln A = \ln(\sigma_a) + \frac{a_0}{\sigma_a + x(a_1 - a_0)} - \frac{1}{x}\ln\frac{\sigma_a}{\sigma_a + x(a_1 - a_0)}\,. \tag{E.95}$$

Let us now consider $\mathrm{Tr}\ln(A+B)$, where B is a constant matrix, *i.e.*, $\tilde{b} = b(u) = b$, and $\sigma_b = 0$. Then, we have

$$\frac{1}{n}\mathrm{Tr}\ln(A+B) = \frac{1}{n}\mathrm{Tr}\ln A + \frac{b}{\tilde{a} - \langle a\rangle}. \tag{E.96}$$

E.5.7 Cubic term

According to (3.72) in Ref. [53], for the matrix q_{ab} with $\tilde{q} = 0$,

$$\frac{1}{n}\mathrm{Tr}q^3 = \int_0^1 du\left[u[q(u)]^3 + 3q(u)\int_0^u dv[q(v)]^2\right]. \tag{E.97}$$

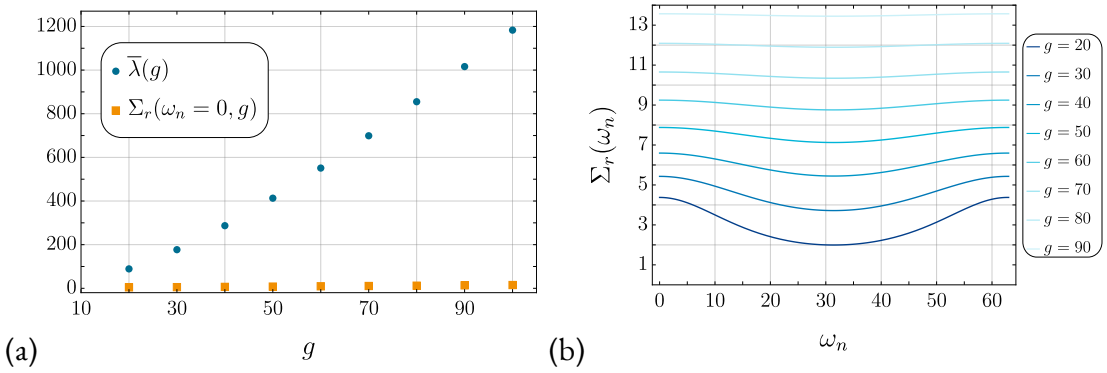

Figure E.3: (a) Behavior of $\overline{\lambda}$ and $\Sigma_r(\omega_n = 0)$ as a function of g for the quantum spherical $p = 3$-rotor model; $\overline{\lambda}$ grows significantly faster with g than Σ_r. In addition, $\Sigma_r(\omega_n = 0) \ll \overline{\lambda}$, which justifies the leading-order approximation made in (E.69). (b) Self-consistent solution of the paramagnetic aligns (E.66)-(E.68) for the self-energy, Σ_r, for large values of g. The self-energy becomes a constant in the limit $g \to \infty$.

References

[1] Abanov, A. & Chubukov, A. V. (2020). Interplay between superconductivity and non-Fermi liquid at a quantum critical point in a metal. I. *Phys. Rev. B*, 102, 024524.

[2] Aeppli, G., Mason, T. E., Hayden, S. M., Mook, H. A., & Kulda, J. (1997). Nearly Singular Magnetic Fluctuations in the Normal State of a High-T_c Cuprate Superconductor. *Science*, 278(5342), 1432–1435.

[3] Albash, T. & Lidar, D. A. (2018). Adiabatic quantum computation. *Rev. Mod. Phys.*, 90, 015002.

[4] Aldape, E. E., Cookmeyer, T., Patel, A. A., & Altman, E. (2022). Solvable theory of a strange metal at the breakdown of a heavy fermi liquid. *Phys. Rev. B*, 105(23), 235111.

[5] Altieri, A., Biroli, G., & Cammarota, C. (2020). Dynamical mean-field theory and aging dynamics. *J. Phys. A: Math. Gen.*, 53(37), 375006.

[6] Andreanov, A. & Müller, M. (2012). Long-Range Quantum Ising Spin Glasses at T=0: Gapless Collective Excitations and Universality. *Phys. Rev. Lett.*, 109, 177201.

[7] Anous, T. & Haehl, F. M. (2021). The quantum p-spin glass model: a user manual for holographers. *J. Stat. Mech.*, 2021(11), 113101.

[8] Aronson, M. C., Osborn, R., Robinson, R. A., Lynn, J. W., Chau, R., Seaman, C. L., & Maple, M. B. (1995). Non-Fermi-Liquid Scaling of the Magnetic Response in $UCu_{5-x}Pd_x$ ($x = 1, 1.5$) . *Phys. Rev. Lett.*, 75, 725–728.

[9] Arrachea, L. & Rozenberg, M. J. (2001). Dynamical Response of Quantum Spin-Glass Models at $T = 0$. *Phys. Rev. Lett.*, 86, 5172–5175.

[10] Arrachea, L. & Rozenberg, M. J. (2002). Infinite-range quantum random Heisenberg magnet. *Phys. Rev. B*, 65(22), 224430.

[11] Ayres, J., Berben, M., Čulo, M., Hsu, Y. T., van Heumen, E., Huang, Y., Zaanen, J., Kondo, T., Takeuchi, T., Cooper, J. R., Putzke, C., Friedemann, S., Carrington, A., & Hussey, N. E. (2021). Incoherent transport across the strange-metal regime of overdoped cuprates. *Nature*, 595(7869), 661–666.

[12] Azeyanagi, T., Ferrari, F., & Schaposnik Massolo, F. I. (2018). Phase Diagram of Planar Matrix Quantum Mechanics, Tensor, and Sachdev-Ye-Kitaev Models. *Phys. Rev. Lett.*, 120(6), 061602.

[13] Badoux, S., Tabis, W., Laliberté, F., Grissonnanche, G., Vignolle, B., Vignolles, D., Béard, J., Bonn, D., Hardy, W., Liang, R., et al. (2016). Change of carrier density at the pseudogap critical point of a cuprate superconductor. *Nature*, 531(7593), 210–214.

[14] Bagrets, D., Altland, A., & Kamenev, A. (2016). Sachdev–Ye–Kitaev model as Liouville quantum mechanics. *Nucl. Phys. B*, 911, 191–205.

[15] Basso, J., Farhi, E., Marwaha, K., Villalonga, B., & Zhou, L. (2022). The Quantum Approximate Optimization Algorithm at High Depth for MaxCut on Large-Girth Regular Graphs and the Sherrington-Kirkpatrick Model. *Leibniz Int. Proc. Inf.*, 232, 7:1–7:21.

[16] Biroli, G. & Cugliandolo, L. F. (2001). Quantum Thouless-Anderson-Palmer equations for glassy systems. *Phys. Rev. B*, 64(1), 014206.

[17] Biroli, G. & Parcollet, O. (2002). Out-of-equilibrium dynamics of a quantum Heisenberg spin glass. *Phys. Rev. B*, 65(9), 094414.

[18] Bouchaud, J.-P., Marsili, M., & Nadal, J.-P. (2023). Application of spin glass ideas in social sciences, economics and finance. In *Spin Glass Theory and Far Beyond: Replica Symmetry Breaking After 40 Years* (pp. 561–579). World Scientific.

[19] Brooke, J., Bitko, D., Rosenbaum, T. F., & Aeppli, G. (1999). Quantum annealing of a disordered magnet. *Science*, 284, 779–781.

[20] Bruin, J. A. N., Sakai, H., Perry, R. S., & Mackenzie, A. P. (2013). Similarity of Scattering Rates in Metals Showing *T*-Linear Resistivity. *Science*, 339(6121), 804–807.

[21] Büttner, G. & Usadel, K. D. (1990). Stability analysis of an Ising spin glass with transverse field. *Phys. Rev. B*, 41, 428–431.

[22] Byun, A., Kim, M., & Ahn, J. (2022). Finding the Maximum Independent Sets of Platonic Graphs Using Rydberg Atoms. *PRX Quantum*, 3, 030305.

[23] Cain, M., Chattopadhyay, S., Liu, J.-G., Samajdar, R., Pichler, H., & Lukin, M. D. (2023). Quantum speedup for combinatorial optimization with flat energy landscapes.

[24] Camjayi, A. & Rozenberg, M. J. (2003). Quantum and Thermal Fluctuations in the SU(N) Heisenberg Spin-Glass Model near the Quantum Critical Point. *Phys. Rev. Lett.*, 90(21), 217202.

[25] Cardy, J. L. (1985). Conformal Invariance and the Yang-Lee Edge Singularity in Two Dimensions. *Phys. Rev. Lett.*, 54, 1354–1356.

[26] Castellani, T. & Cavagna, A. (2005). Spin-glass theory for pedestrians. *J. Stat. Mech.*, 2005(5), 05012.

[27] Cavagna, A., Garrahan, J. P., & Giardina, I. (1999). Quenched complexity of the mean-field *p*-spin spherical model with external magnetic field. *J. Phys. A: Math. Gen.*, 32(5), 711.

[28] Chen, S.-D., Hashimoto, M., He, Y., Song, D., Xu, K.-J., He, J.-F., Devereaux, T. P., Eisaki, H., Lu, D.-H., Zaanen, J., et al. (2019). Incoherent strange metal sharply bounded by a critical doping in bi2212. *Science*, 366(6469), 1099–1102.

[29] Chowdhury, D., Georges, A., Parcollet, O., & Sachdev, S. (2022). Sachdev-ye-kitaev models and beyond: Window into non-fermi liquids. *Reviews of Modern Physics*, 94(3), 035004.

[30] Chowdhury, D. & Swingle, B. (2017). Onset of many-body chaos in the $O(N)$ model. *Phys. Rev. D*, 96, 065005.

[31] Chowdhury, D., Werman, Y., Berg, E., & Senthil, T. (2018). Translationally invariant non-Fermi liquid metals with critical Fermi-surfaces: Solvable models. *Phys. Rev. X*, 8(3), 031024.

[32] Christos, M., Haehl, F. M., & Sachdev, S. (2022a). Spin liquid to spin glass crossover in the random quantum Heisenberg magnet. *Phys. Rev. B*, 105(8), 085120.

[33] Christos, M., Joshi, D. G., Sachdev, S., & Tikhanovskaya, M. (2022b). Critical metallic phase in the overdoped random t-J model. *Proc. Nat. Acad. Sci.*, 119(29), e2206921119.

[34] Cooper, R. A., Wang, Y., Vignolle, B., Lipscombe, O. J., Hayden, S. M., Tanabe, Y., Adachi, T., Koike, Y., Nohara, M., Takagi, H., Proust, C., & Hussey, N. E. (2009). Anomalous Criticality in the Electrical Resistivity of $La_{2-x}Sr_xCuO_4$. *Science*, 323(5914), 603–607.

[35] Cotler, J. S., Gur-Ari, G., Hanada, M., Polchinski, J., Saad, P., Shenker, S. H., Stanford, D., Streicher, A., & Tezuka, M. (2017). Black Holes and Random Matrices. *JHEP*, 05, 118. [Erratum: JHEP 09, 002 (2018)].

[36] Crisanti, A. & Sommers, H. J. (1992). The spherical *p*-spin interaction spin glass model: the statics. *Z. Physik B - Condensed Matter*, 87(3), 341–354.

[37] Cugliandolo, L. F., Grempel, D. R., & da Silva Santos, C. A. (2000). From second to first order transitions in a disordered quantum magnet. *Phys. Rev. Lett.*, 85, 2589–2592.

[38] Cugliandolo, L. F., Grempel, D. R., & da Silva Santos, C. A. (2001). Imaginary-time replica formalism study of a quantum spherical p-spin-glass model. *Phys. Rev. B*, 64, 014403.

[39] Cugliandolo, L. F. & Kurchan, J. (1993). Analytical solution of the off-equilibrium dynamics of a long-range spin-glass model. *Phys. Rev. Lett.*, 71(1), 173–176.

[40] Cugliandolo, L. F. & Kurchan, J. (1994). On the out-of-equilibrium relaxation of the Sherrington-Kirkpatrick model. *J. Phys. A: Math. Gen.*, 27(17), 5749–5772.

[41] Cugliandolo, L. F. & Lozano, G. (1999). Real-time nonequilibrium dynamics of quantum glassy systems. *Phys. Rev. B*, 59(2), 915–942.

[42] Davison, R. A., Fu, W., Georges, A., Gu, Y., Jensen, K., & Sachdev, S. (2017). Thermoelectric transport in disordered metals without quasiparticles: The Sachdev-Ye-Kitaev models and holography. *Phys. Rev. B*, 95(15), 155131.

[43] de Almeida, J. R. L. & Thouless, D. J. (1978). Stability of the sherrington-kirkpatrick solution of a spin glass model. *Journal of Physics A: Mathematical and General*, 11(5), 983.

[44] Derrida, B. (1980). Random-Energy Model: Limit of a Family of Disordered Models. *Phys. Rev. Lett.*, 45, 79–82.

[45] Derrida, B. (1981). Random-energy model: An exactly solvable model of disordered systems. *Phys. Rev. B*, 24, 2613–2626.

[46] Dumitrescu, P. T., Wentzell, N., Georges, A., & Parcollet, O. (2022). Planckian metal at a doping-induced quantum critical point. *Phys. Rev. B*, 105(18), L180404.

[47] Dupont, M., Evert, B., Hodson, M. J., Sundar, B., Jeffrey, S., Yamaguchi, Y., Feng, D., Maciejewski, F. B., Hadfield, S., Alam, M. S., et al. (2023). Quantum-enhanced greedy combinatorial optimization solver. *Science Advances*, 9(45), eadi0487.

[48] Ebadi, S., Keesling, A., Cain, M., Wang, T. T., Levine, H., Bluvstein, D., Semeghini, G., Omran, A., Liu, J. G., Samajdar, R., Luo, X. Z., Nash, B., Gao, X., Barak, B., Farhi, E., Sachdev, S., Gemelke, N., Zhou, L., Choi, S., Pichler, H., Wang, S. T., Greiner, M., Vuletić, V., & Lukin, M. D. (2022). Quantum optimization of maximum independent set using Rydberg atom arrays. *Science*, 376(6598), 1209–1215.

[49] Esterlis, I., Guo, H., Patel, A. A., & Sachdev, S. (2021). Large N theory of critical Fermi surfaces. *Phys. Rev. B*, 103(23), 235129.

[50] Farhi, E., Goldstone, J., Gutmann, S., Lapan, J., Lundgren, A., & Preda, D. (2001). A Quantum Adiabatic Evolution Algorithm Applied to Random Instances of an NP-Complete Problem. *Science*, 292(5516), 472–476.

[51] Fei, L., Giombi, S., Klebanov, I. R., & Tarnopolsky, G. (2015). Generalized F-Theorem and the ε Expansion. *JHEP*, 12, 155.

[52] Ferrari, F. & Schaposnik Massolo, F. I. (2019). Phases Of Melonic Quantum Mechanics. *Phys. Rev. D*, 100(2), 026007.

[53] Fischer, K. & Hertz, J. (1993). *Spin Glasses*. Cambridge University Press, Cambridge.

[54] Fisher, M. E. (1978). Yang-Lee Edge Singularity and φ^3 Field Theory. *Phys. Rev. Lett.*, 40, 1610–1613.

[55] Frachet, M., Vinograd, I., Zhou, R., Benhabib, S., Wu, S., Mayaffre, H., Krämer, S., Ramakrishna, S. K., Reyes, A. P., Debray, J., Kurosawa, T., Momono, N., Oda, M., Komiya, S., Ono, S., Horio, M., Chang, J., Proust, C., LeBoeuf, D., & Julien, M.-H. (2020). Hidden magnetism at the pseudogap critical point of a cuprate superconductor. *Nature Physics*, 16(10), 1064–1068.

[56] Franz, S., Mézard, M., Parisi, G., & Peliti, L. (1998). Measuring Equilibrium Properties in Aging Systems. *Phys. Rev. Lett.*, 81(9), 1758–1761.

[57] Fu, W., Gu, Y., Sachdev, S., & Tarnopolsky, G. (2018). $\mathbb{Z}_2$ fractionalized phases of a solvable, disordered, *t-J* model. *Phys. Rev. B*, 98(7), 075150.

[58] Fuhs, M. C. & Touretzky, D. S. (2006). A spin glass model of path integration in rat medial entorhinal cortex. *Journal of Neuroscience*, 26(16), 4266–4276.

[59] Gannon, W. J., Wu, L. S., Zaliznyak, I. A., Xu, W. H., Tsvelik, A. M., Qiu, Y., Rodriguez-Rivera, J. A., & Aronson, M. C. (2018). Local quantum phase transition in YFe_2Al_{10}. *Proceedings of the National Academy of Science*, 115(27), 6995–6999.

[60] Gardner, E. (1985). Spin glasses with *p*-spin interactions. *Nucl. Phys. B.*, 257, 747–765.

[61] Georges, A. & Mravlje, J. (2021). Skewed non-Fermi liquids and the Seebeck effect. *Phys. Rev. Research*, 3, 043132.

[62] Georges, A., Parcollet, O., & Sachdev, S. (2000). Mean Field Theory of a Quantum Heisenberg Spin Glass. *Phys. Rev. Lett.*, 85(4), 840–843.

[63] Georges, A., Parcollet, O., & Sachdev, S. (2001). Quantum fluctuations of a nearly critical Heisenberg spin glass. *Phys. Rev. B*, 63(13), 134406.

[64] Giombi, S., Klebanov, I. R., Popov, F., Prakash, S., & Tarnopolsky, G. (2018). Prismatic Large *N* Models for Bosonic Tensors. *Phys. Rev. D*, 98(10), 105005.

[65] Giombi, S., Klebanov, I. R., & Tarnopolsky, G. (2016). Conformal QED_d, *F*-Theorem and the ε Expansion. *J. Phys. A*, 49(13), 135403.

[66] Giombi, S., Klebanov, I. R., & Tarnopolsky, G. (2017). Bosonic tensor models at large N and small ε. *Phys. Rev. D*, 96(10), 106014.

[67] Goldschmidt, Y. Y. (1990). Solvable model of the quantum spin glass in a transverse field. *Phys. Rev. B*, 41, 4858–4861.

[68] Gorbenko, V., Rychkov, S., & Zan, B. (2018). Walking, Weak first-order transitions, and Complex CFTs. *JHEP*, 10, 108.

[69] Gourgout, A., Grissonnanche, G., Laliberté, F., Ataei, A., Chen, L., Verret, S., Zhou, J.-S., Mravlje, J., Georges, A., Doiron-Leyraud, N., et al. (2022). Seebeck coefficient in a cuprate superconductor: particle-hole asymmetry in the strange metal phase and fermi surface transformation in the pseudogap phase. *Physical Review X*, 12(1), 011037.

[70] Greene, R. L., Mandal, P. R., Poniatowski, N. R., & Sarkar, T. (2020). The strange metal state of the electron-doped cuprates. *Annual Review of Condensed Matter Physics*, 11(1), 213–229.

[71] Grissonnanche, G., Fang, Y., Legros, A., Verret, S., Laliberté, F., Collignon, C., Zhou, J., Graf, D., Goddard, P. A., Taillefer, L., & Ramshaw, B. J. (2021). Linear-in temperature resistivity from an isotropic Planckian scattering rate. *Nature*, 595(7869), 667–672.

[72] Gross, D. & Mézard, M. (1984). The simplest spin glass. *Nucl. Phys. B.*, 240(4), 431–452.

[73] Gross, D. J. & Rosenhaus, V. (2017a). A Generalization of Sachdev-Ye-Kitaev. *JHEP*, 02, 093.

[74] Gross, D. J. & Rosenhaus, V. (2017b). A line of CFTs: from generalized free fields to SYK. *JHEP*, 07, 086.

[75] Gross, D. J. & Rosenhaus, V. (2017c). All point correlation functions in SYK. *JHEP*, 12, 148.

[76] Gross, D. J. & Rosenhaus, V. (2017d). The Bulk Dual of SYK: Cubic Couplings. *JHEP*, 05, 092.

[77] Gu, Y. & Kitaev, A. (2019). On the relation between the magnitude and exponent of OTOCs. *JHEP*, 02, 075.

[78] Gu, Y., Kitaev, A., Sachdev, S., & Tarnopolsky, G. (2020). Notes on the complex Sachdev-Ye-Kitaev model. *JHEP*, 02, 157.

[79] Gu, Y., Kitaev, A., & Zhang, P. (2021). A two-way approach to out-of-time-order correlators.

[80] Gu, Y., Qi, X.-L., & Stanford, D. (2017). Local criticality, diffusion and chaos in generalized sachdev-ye-kitaev models. *JHEP*, 2017(5), 125.

[81] Guo, H., Gu, Y., & Sachdev, S. (2020). Linear in temperature resistivity in the limit of zero temperature from the time reparameterization soft mode. *Annals Phys.*, 418, 168202.

[82] Haehl, F. M., Reeves, W., & Rozali, M. (2019). Reparametrization modes, shadow operators, and quantum chaos in higher-dimensional CFTs. *JHEP*, 2019(11), 1–44.

[83] Haehl, F. M. & Rozali, M. (2018). Effective field theory for chaotic CFTs. *JHEP*, 2018(10), 1–32.

[84] Hartnoll, S. A. & Mackenzie, A. P. (2022). Colloquium: Planckian dissipation in metals. *Reviews of Modern Physics*, 94(4), 041002.

[85] Haule, K., Rosch, A., Kroha, J., & Wölfle, P. (2002). Pseudogaps in an Incoherent Metal. *Phys. Rev. Lett.*, 89(23), 236402.

[86] Haule, K., Rosch, A., Kroha, J., & Wölfle, P. (2003). Pseudogaps in the *t-J* model: An extended dynamical mean-field theory study. *Phys. Rev. B*, 68(15), 155119.

[87] Hopfield, J. J. (1982). Neural networks and physical systems with emergent collective computational abilities. *Proceedings of the national academy of sciences*, 79(8), 2554–2558.

[88] Husain, A. A., Mitrano, M., Rak, M. S., Rubeck, S., Uchoa, B., March, K., Dwyer, C., Schneeloch, J., Zhong, R., Gu, G. D., & Abbamonte, P. (2019). Crossover of Charge Fluctuations across the Strange Metal Phase Diagram. *Phys. Rev. X*, 9, 041062.

[89] Iliesiu, L., Kos, F., Poland, D., Pufu, S. S., Simmons-Duffin, D., & Yacoby, R. (2016). Bootstrapping 3D Fermions. *JHEP*, 03, 120.

[90] Iliesiu, Luca and Koloğlu, Murat and Mahajan, Raghu and Perlmutter, Eric and Simmons-Duffin, David (2018). The Conformal Bootstrap at Finite Temperature. *JHEP*, 10, 070.

[91] Jeong, S., Kim, M., Hhan, M., Park, J., & Ahn, J. (2023). Quantum programming of the satisfiability problem with rydberg atom graphs. *Phys. Rev. Research*, 5(4), 043037.

[92] Joshi, D. G., Li, C., Tarnopolsky, G., Georges, A., & Sachdev, S. (2020). Deconfined critical point in a doped random quantum Heisenberg magnet. *Phys. Rev. X*, 10(2), 021033.

[93] Joshi, D. G. & Sachdev, S. (2020). Anomalous density fluctuations in a random t-j model. *Phys. Rev. B*, 102(16), 165146.

[94] Kaplan, D. B., Lee, J.-W., Son, D. T., & Stephanov, M. A. (2009). Conformality Lost. *Phys. Rev. D*, 80, 125005.

[95] Katz, E., Sachdev, S., Sørensen, E. S., & Witczak-Krempa, W. (2014). Conformal field theories at nonzero temperature: Operator product expansions, Monte Carlo, and holography. *Phys. Rev. B*, 90, 245109.

[96] Keimer, B., Birgeneau, R. J., Cassanho, A., Endoh, Y., Erwin, R. W., Kastner, M. A., & Shirane, G. (1991). Scaling Behavior of the Generalized Susceptibility in $La_{2-x}Sr_xCuO_{4+y}$. *Phys. Rev. Lett.*, 67, 1930–1933.

[97] Kennett, M. P., Chamon, C., & Ye, J. (2001). Aging dynamics of quantum spin glasses of rotors. *Phys. Rev. B*, 64(22), 224408.

[98] Kim, J., Altman, E., & Cao, X. (2021). Dirac fast scramblers. *Phys. Rev. B*, 103, L081113.

[99] Kim, J., Klebanov, I. R., Tarnopolsky, G., & Zhao, W. (2019). Symmetry Breaking in Coupled SYK or Tensor Models. *Phys. Rev. X*, 9(2), 021043.

[100] Kim, M., Kim, K., Hwang, J., Moon, E.-G., & Ahn, J. (2022). Rydberg quantum wires for maximum independent set problems. *Nat. Phys.*, 18(7), 755–759.

[101] King, A. D., Raymond, J., Lanting, T., Harris, R., Zucca, A., Altomare, F., Berkley, A. J., Boothby, K., Ejtemaee, S., Enderud, C., et al. (2023). Quantum critical dynamics in a 5,000-qubit programmable spin glass. *Nature*, 617(7959), 61–66.

[102] Kiss, A., Zaránd, G., & Lovas, I. (2023). Exact Solution for the Transverse Field Sherrington-Kirkpatrick Spin Glass Model with Continuous-Time Quantum Monte Carlo Method.

[103] Kitaev, A. (2018). Notes on $\widetilde{\mathrm{sl}}(2,\mathbb{R})$ representations.

[104] Kitaev, A. & Suh, S. J. (2018). The soft mode in the Sachdev-Ye-Kitaev model and its gravity dual. *JHEP*, 05, 183.

[105] Kitaev, A. Y. (2015). Talks at KITP, University of California, Santa Barbara. *Entanglement in Strongly-Correlated Quantum Matter*.

[106] Klebanov, I. R., Popov, F., & Tarnopolsky, G. (2018). TASI Lectures on Large N Tensor Models. *PoS*, TASI2017, 004.

[107] Klebanov, I. R., Pufu, S. S., & Safdi, B. R. (2011). F-Theorem without Supersymmetry. *JHEP*, 10, 038.

[108] Klebanov, I. R. & Tarnopolsky, G. (2017). Uncolored random tensors, melon diagrams, and the Sachdev-Ye-Kitaev models. *Phys. Rev. D*, 95(4), 046004.

[109] Kobrin, B., Yang, Z., Kahanamoku-Meyer, G. D., Olund, C. T., Moore, J. E., Stanford, D., & Yao, N. Y. (2021). Many-body chaos in the sachdev-ye-kitaev model. *Phys. Rev. Lett.*, 126(3), 030602.

[110] Kopeć, T. K., Usadel, K. D., & Büttner, G. (1989). Instabilities in the quantum Sherrington-Kirkpatrick Ising spin glass in transverse and longitudinal fields. *Phys. Rev. B*, 39, 12418–12421.

[111] Kosterlitz, J. M., Thouless, D. J., & Jones, R. C. (1976). Spherical Model of a Spin-Glass. *Phys. Rev. Lett.*, 36, 1217–1220.

[112] Kroeze, R. M., Marsh, B. P., Schuller, D. A., Hunt, H. S., Gopalakrishnan, S., Keeling, J., & Lev, B. L. (2023). Replica symmetry breaking in a quantum-optical vector spin glass. *arXiv preprint arXiv:2311.04216*.

[113] Kruchkov, A., Patel, A. A., Kim, P., & Sachdev, S. (2020). Thermoelectric power of Sachdev-Ye-Kitaev islands: Probing Bekenstein-Hawking entropy in quantum matter experiments. *Phys. Rev. B*, 101(20), 205148.

[114] Lee, S.-S. (2009). Low energy effective theory of Fermi surface coupled with U(1) gauge field in 2+1 dimensions. *Phys. Rev. B*, 80(16), 165102.

[115] Lee, S.-S. (2018). Recent Developments in Non-Fermi Liquid Theory. *Annual Review of Condensed Matter Physics*, 9, 227–244.

[116] Leschke, H., Manai, C., Ruder, R., & Warzel, S. (2021). Existence of Replica-Symmetry Breaking in Quantum Glasses. *Phys. Rev. Lett.*, 127, 207204.

[117] Li, C., Valentinis, D., Patel, A. A., Guo, H., Schmalian, J., Sachdev, S., & Esterlis, I. (2024). Strange metal and superconductor in the two-dimensional yukawa-sachdev-ye-kitaev model. *Physical Review Letters*, 133(18), 186502.

[118] Lisewski, A. M. & Lichtarge, O. (2010). Untangling complex networks: risk minimization in financial markets through accessible spin glass ground states. *Physica A: Statistical Mechanics and its Applications*, 389(16), 3250–3253.

[119] Maciejewski, F. B., Hadfield, S., Hall, B., Hodson, M., Dupont, M., Evert, B., Sud, J., Sohaib Alam, M., Wang, Z., Jeffrey, S., Sundar, B., Lott, P. A., Grabbe, S., Rieffel, E. G., Reagor, M. J., & Venturelli, D. (2023). Design and execution of quantum circuits using tens of superconducting qubits and thousands of gates for dense Ising optimization problems.

[120] Maldacena, J., Shenker, S. H., & Stanford, D. (2016a). A bound on chaos. *JHEP*, 08, 106.

[121] Maldacena, J. & Stanford, D. (2016). Remarks on the Sachdev-Ye-Kitaev model. *Phys. Rev. D*, 94(10), 106002.

[122] Maldacena, J., Stanford, D., & Yang, Z. (2016b). Conformal symmetry and its breaking in two dimensional Nearly Anti-de-Sitter space. *PTEP*, 2016(12), 12C104.

[123] Manai, C. & Warzel, S. (2021). The de Almeida–Thouless Line in Hierarchical Quantum Spin Glasses. *Journal of Statistical Physics*, 186(1), 14.

[124] Mao, D., Chowdhury, D., & Senthil, T. (2020). Slow scrambling and hidden integrability in a random rotor model. *Phys. Rev. B*, 102, 094306.

[125] Marc Mézard & Giorgio Parisi (1991). Replica field theory for random manifolds. *J. Phys. I France*, 1(6), 809–836.

[126] Maskara, N., Ostermann, S., Shee, J., Kalinowski, M., McClain Gomez, A., Araiza Bravo, R., Wang, D. S., Krylov, A. I., Yao, N. Y., Head-Gordon, M., Lukin, M. D., & Yelin, S. F. (2023).

Programmable Simulations of Molecules and Materials with Reconfigurable Quantum Processors.

[127] Mertens, T. G., Turiaci, G. J., & Verlinde, H. L. (2017). Solving the Schwarzian via the Conformal Bootstrap. *JHEP*, 08, 136.

[128] Metlitski, M. A. & Sachdev, S. (2010). Quantum phase transitions of metals in two spatial dimensions. I. Ising-nematic order. *Phys. Rev. B*, 82(7), 075127.

[129] Mézard, M. & Montanari, A. (2009). *Information, Physics, and Computation*. Oxford Graduate Texts. Oxford University Press, Oxford.

[130] Michon, B., Girod, C., Badoux, S., Kačmarčík, J., Ma, Q., Dragomir, M., Dabkowska, H. A., Gaulin, B. D., Zhou, J.-S., Pyon, S., Takayama, T., Takagi, H., Verret, S., Doiron-Leyraud, N., Marcenat, C., Taillefer, L., & Klein, T. (2019). Thermodynamic signatures of quantum criticality in cuprate superconductors. *Nature*, 567(7747), 218–222.

[131] Miller, J. & Huse, D. A. (1993). Zero-temperature critical behavior of the infinite-range quantum Ising spin glass. *Phys. Rev. Lett.*, 70, 3147–3150.

[132] Mitrano, M., Husain, A. A., Vig, S., Kogar, A., Rak, M. S., Rubeck, S. I., Schmalian, J., Uchoa, B., Schneeloch, J., Zhong, R., Gu, G. D., & Abbamonte, P. (2018). Anomalous density fluctuations in a strange metal. *Proceedings of the National Academy of Science*, 115(21), 5392–5396.

[133] Mukherjee, S., Rajak, A., & Chakrabarti, B. K. (2015). Classical-to-quantum crossover in the critical behavior of the transverse-field Sherrington-Kirkpatrick spin glass model. *Phys. Rev. E*, 92(4), 042107.

[134] Mukherjee, S., Rajak, A., & Chakrabarti, B. K. (2018). Possible ergodic-nonergodic regions in the quantum Sherrington-Kirkpatrick spin glass model and quantum annealing. *Phys. Rev. E*, 97(2), 022146.

[135] Murugan, J., Stanford, D., & Witten, E. (2017). More on Supersymmetric and 2d Analogs of the SYK Model. *JHEP*, 08, 146.

[136] Nguyen, M.-T., Liu, J.-G., Wurtz, J., Lukin, M. D., Wang, S.-T., & Pichler, H. (2023). Quantum Optimization with Arbitrary Connectivity Using Rydberg Atom Arrays. *PRX Quantum*, 4(1), 010316.

[137] Nobili, R. (1973). Conformal covariant wightman functions. *Nuovo Cim. A*, 13, 129–143.

[138] Panagopoulos, C., Petrovic, A. P., Hillier, A. D., Tallon, J. L., Scott, C. A., & Rainford, B. D. (2004). Exposing the spin-glass ground state of the nonsuperconducting $la_{2-x}sr_xcu_{1-y}zn_yo_4$ high-T_c oxide. *Phys. Rev. B*, 69, 144510.

[139] Parcollet, O. & Georges, A. (1999). Non-Fermi-liquid regime of a doped Mott insulator. *Phys. Rev. B*, 59, 5341–5360.

[140] Parisi, G. (1979). Infinite Number of Order Parameters for Spin-Glasses. *Phys. Rev. Lett.*, 43, 1754–1756.

[141] Patel, A. A., Guo, H., Esterlis, I., & Sachdev, S. (2023). Universal theory of strange metals from spatially random interactions. *Science*, 381(6659), 790–793.

[142] Patel, A. A., Lunts, P., & Albergo, M. S. (2024a). Strange metals and planckian transport in a gapless phase from spatially random interactions. *arXiv preprint arXiv:2410.05365*.

[143] Patel, A. A., Lunts, P., & Sachdev, S. (2024b). Localization of overdamped bosonic modes and transport in strange metals. *Proceedings of the National Academy of Sciences*, 121(14), e2402052121.

[144] Patel, A. A., McGreevy, J., Arovas, D. P., & Sachdev, S. (2018). Magnetotransport in a model of a disordered strange metal. *Phys. Rev. X*, 8(2), 021049.

[145] Patel, A. A. & Sachdev, S. (2017). Quantum chaos on a critical Fermi surface. *Proc. Nat. Acad. Sci.*, 114, 1844–1849.

[146] Patel, A. A. & Sachdev, S. (2019). Theory of a Planckian metal. *Phys. Rev. Lett.*, 123(6), 066601.

[147] Polchinski, J. & Rosenhaus, V. (2016). The Spectrum in the Sachdev-Ye-Kitaev Model. *JHEP*, 04, 001.

[148] Proust, C. & Taillefer, L. (2019). The remarkable underlying ground states of cuprate superconductors. *Annual Review of Condensed Matter Physics*, 10(1), 409–429.

[149] Ray, P., Chakrabarti, B. K., & Chakrabarti, A. (1989). Sherrington-Kirkpatrick model in a transverse field: Absence of replica symmetry breaking due to quantum fluctuations. *Phys. Rev. B*, 39, 11828–11832.

[150] Read, N., Sachdev, S., & Ye, J. (1995). Landau theory of quantum spin glasses of rotors and Ising spins. *Phys. Rev. B*, 52(1), 384–410.

[151] Rozenberg, M. J. & Grempel, D. R. (1998). Dynamics of the Infinite-Range Ising Spin-Glass Model in a Transverse Field. *Phys. Rev. Lett.*, 81, 2550–2553.

[152] Sachdev, S. (1999). *Quantum Phase Transitions*. Cambridge, UK: Cambridge University Press.

[153] Sachdev, S. (2001). Static hole in a critical antiferromagnet: field-theoretic renormalization group. *Physica C Superconductivity*, 357, 78–81.

[154] Sachdev, S. (2015). Bekenstein-Hawking Entropy and Strange Metals. *Phys. Rev. X*, 5(4), 041025.

[155] Sachdev, S. (2023). *Quantum Phases of Matter*. Cambridge University Press, Cambridge.

[156] Sachdev, S. & Ye, J. (1993). Gapless spin-fluid ground state in a random quantum Heisenberg magnet. *Phys. Rev. Lett.*, 70, 3339.

[157] Schiffer, B. F., Wild, D. S., Maskara, N., Cain, M., Lukin, M. D., & Samajdar, R. (2024). Circumventing superexponential runtimes for hard instances of quantum adiabatic optimization. *Phys. Rev. Research*, 6(1), 013271.

[158] Schindler, P. M., Guaita, T., Shi, T., Demler, E., & Cirac, J. I. (2022). Variational Ansatz for the Ground State of the Quantum Sherrington-Kirkpatrick Model. *Phys. Rev. Lett.*, 129, 220401.

[159] Schröder, A., Aeppli, G., Bucher, E., Ramazashvili, R., & Coleman, P. (1998). Scaling of Magnetic Fluctuations near a Quantum Phase Transition. *Phys. Rev. Lett.*, 80(25), 5623–5626.

[160] Shackleton, H., Wietek, A., Georges, A., & Sachdev, S. (2021). Quantum Phase Transition at Nonzero Doping in a Random t–J Model. *Phys. Rev. Lett.*, 126, 136602.

[161] Sherrington, D. & Kirkpatrick, S. (1975). Solvable model of a spin-glass. *Physical review letters*, 35(26), 1792.

[162] Sompolinsky, H. (1981). Time-Dependent Order Parameters in Spin-Glasses. *Phys. Rev. Lett.*, 47, 935–938.

[163] Sompolinsky, H. & Zippelius, A. (1981). Dynamic Theory of the Spin-Glass Phase. *Phys. Rev. Lett.*, 47, 359–362.

[164] Sompolinsky, H. & Zippelius, A. (1982). Relaxational dynamics of the Edwards-Anderson model and the mean-field theory of spin-glasses. *Phys. Rev. B*, 25, 6860–6875.

[165] Song, X.-Y., Jian, C.-M., & Balents, L. (2017). Strongly Correlated Metal Built from Sachdev-Ye-Kitaev Models. *Phys. Rev. Lett.*, 119(21), 216601.

[166] Steinberg, J. & Swingle, B. (2019). Thermalization and chaos in QED_3. *Phys. Rev. D*, 99, 076007.

[167] Taillefer, L. (2010). Scattering and pairing in cuprate superconductors. *Annu. Rev. Condens. Matter Phys.*, 1(1), 51–70.

[168] Takahashi, K. (2007). Quantum fluctuations in the transverse Ising spin glass model: A field theory of random quantum spin systems. *Phys. Rev. B*, 76, 184422.

[169] Talagrand, M. (2006). Free energy of the spherical mean field model. *Probab. Theory Relat. Fields*, 134(3), 339–382.

[170] Tarnopolsky, G. (2019). Large q expansion in the Sachdev-Ye-Kitaev model. *Phys. Rev. D*, 99(2), 026010.

[171] Tasseff, B., Albash, T., Morrell, Z., Vuffray, M., Lokhov, A. Y., Misra, S., & Coffrin, C. (2024). On the emerging potential of quantum annealing hardware for combinatorial optimization. *Journal of Heuristics*, (pp. 1–34).

[172] Thomson, S. J., Urbani, P., & Schiró, M. (2020). Quantum Quenches in Isolated Quantum Glasses out of Equilibrium. *Phys. Rev. Lett.*, 125(12), 120602.

[173] Thouless, D. J., de Almeida, J. R. L., & Kosterlitz, J. M. (1980). Stability and susceptibility in Parisi's solution of a spin glass model. *J. Phys. C: Solid State Physics*, 13, 3271.

[174] Tikhanovskaya, M., Guo, H., Sachdev, S., & Tarnopolsky, G. (2021a). Excitation spectra of quantum matter without quasiparticles. I. Sachdev-Ye-Kitaev models. *Phys. Rev. B*, 103(7), 075141.

[175] Tikhanovskaya, M., Guo, H., Sachdev, S., & Tarnopolsky, G. (2021b). Excitation spectra of quantum matter without quasiparticles. II: random *t-J* models. *Phys. Rev. B*, 103(7), 075142.

[176] Tulipman, E. & Berg, E. (2020). Strongly coupled quantum phonon fluid in a solvable model. *Phys. Rev. Research*, 2, 033431.

[177] Turiaci, G. J. & Verlinde, H. (2016). On CFT and quantum chaos. *Journal of High Energy Physics*, 2016(12), 1–22.

[178] Varma, C., Littlewood, P. B., Schmitt-Rink, S., Abrahams, E., & Ruckenstein, A. (1989). Phenomenology of the normal state of cu-o high-temperature superconductors. *Physical Review Letters*, 63(18), 1996.

[179] Vidberg, H. J. & Serene, J. W. (1977). Solving the Eliashberg equations by means of N-point Padé approximants. *Journal of Low Temperature Physics*, 29, 179–192.

[180] Vojta, M., Buragohain, C., & Sachdev, S. (2000). Quantum impurity dynamics in two-dimensional antiferromagnets and superconductors. *Phys. Rev. B*, 61(22), 15152–15184.

[181] Winer, M., Barney, R., Baldwin, C. L., Galitski, V., & Swingle, B. (2022). Spectral form factor of a quantum spin glass. *JHEP*, 09, 032.

[182] Yamamoto, T. & Ishii, H. (1987). A perturbation expansion for the Sherrington-Kirkpatrick model with a transverse field. *J. Phys. C: Solid State Phys.*, 20(35), 6053.

[183] Ye, J., Sachdev, S., & Read, N. (1993). Solvable spin glass of quantum rotors. *Phys. Rev. Lett.*, 70(25), 4011–4014.

[184] Young, A. P. (2017). Stability of the quantum Sherrington-Kirkpatrick spin glass model. *Phys. Rev. E*, 96(3), 032112.

[185] Zaanen, J. (2004). Why the temperature is high. *Nature*, 430(6999), 512–513.

[186] Zhang, P. (2017). Dispersive Sachdev-Ye-Kitaev model: Band structure and quantum chaos. *Phys. Rev. B*, 96(20), 205138.